



Colloid and Polymers Physic Group.
Department of condensed matter.
Faculty of Physics.

Structural Characterization and Analysis of the Biological Properties of New Amphiphilic Block Copolymers

Adriana Cambón Freire

PhD Thesis [2014]



Facultad de Física - Campus Vida
15782 Santiago de Compostela

Víctor Mosquera Tallón, Catedrático del Departamento de Física de la Materia Condensada de la Universidad de Santiago de Compostela; **Pablo Taboada Antelo**, Profesor Titular del Departamento de Física de la Materia Condensada de la Universidad de Santiago de Compostela; y **Silvia Barbosa Fernández**, Investigador Doctor del Programa Ramón y Cajal en el Departamento de Física de la Materia Condensada de la Universidad de Santiago de Compostela

Informan:

Que el trabajo de investigación titulado “**Structural Characterization and Analyses of the Biological Properties of New Amphiphilic Block Copolymers**” ha sido realizado bajo nuestra dirección por Adriana Cambón Freire en los laboratorios del Grupo de Física de Coloides y Polímeros del Departamento de Física de la Materia Condensada de la Universidad de Santiago de Compostela, y reúne los requisitos de calidad y rigor científicos necesarios para optar al Grado de Doctor en Ciencias Físicas.

Para que así conste a los efectos oportunos,

Santiago de Compostela, 10 de Abril de 2014.

Dr. V. Mosquera Tallón

Dr. P. Taboada Antelo

Dr. S. Barbosa Fernández

Index

Agradecimientos	vii
Summary	ix
Resumen	xvii
Listado de artículos	xxvii

Chapter 1: Introduction **1**

1.1 Nanotechnology	3
1.1.1 Nanopharmaceutics and nanomedicine	5
1.1.2 References	8
1.2. Nanoparticles as drug carriers	10
1.2.1 Influence of NP's properties on pharmaceutical performance	10
1.2.1.1 Drug solubility	11
1.2.1.2 Blood circulation time	12
1.2.1.3 Targeting	12
1.2.1.4 Cellular uptake	13
1.2.1.5 Release rate	13
1.2.1.6 Clearance mechanisms and excretion	14
1.2.2 NPs used in pharmaceutics	16
1.2.3 References	20
1.3. Polymeric micelles	23
1.3.1 Block copolymers	24
1.3.2 Block copolymers classification	25
1.3.3 Block copolymer micelles	27
1.3.4 Polymeric micelles as drug reservoirs	28
1.3.5 References	31

Chapter 2: EO_mSO_nEO_m copolymers as nanocarriers of hydrophobic drugs **33**

2.1 Aim of the work	35
2.1.1 Aim of the work	35
2.1.2 Methodology	35

2.1.3 References	37
2.2. EO _m SO _n EO _m copolymers: Micellization, drug solubilization and gelling features	39
2.2.1 Abstract	39
2.2.2 Introduction	39
2.2.3 Experimental section	41
2.2.3.1 Materials	41
2.2.3.2 Methods	42
2.2.4 Results and discussion	45
2.2.4.1 Characterization of the copolymer micelles	45
2.2.4.2 Phase behavior and rheological properties	48
2.2.4.3 Solubilization capacity studies	53
2.2.4.4. In vitro release of griseofulvin	55
2.2.5 Conclusions	57
2.2.6 References	57
2.3. Supporting information	61
2.3.1 Theoretical estimation of polymeric micelle shape	62
2.3.2 Rheological properties of copolymer EO ₃₈ SO ₁₀ EO ₃₈	
Temperature and concentration scans	63
2.3.3 References	64
2.4. EO _m SO _n EO _m copolymers: From “classical” chemotherapeutic nanocarriers to active cell-response inducers	65
2.4.1 Abstract	65
2.4.2 Introduction	65
2.4.3 Experimental section	67
2.4.3.1 Materials	67
2.4.3.2 Methods	68
2.4.4 Results and discussion	70
2.4.4.1 Solubilization capacity	70
2.4.4.2 Size distribution and physical stability of DOXO-polymeric micelles	71
2.4.4.3 In vitro release	72
2.4.4.4 Cytocompatibiity of EO ₃₃ SO ₁₄ EO ₃₃ and EO ₃₃ SO ₁₄ EO ₃₃	74
2.4.4.5 Inhibition of P-gp efflux pump and intracellular DOXO accumulation	75
2.4.4.6 Cellular uptke and in vitro cytotoxicity of	

DOXO-loaded polymeric micelles (P-gp evasion)	77
2.4.5 Conclusions	81
2.4.6 References	81

Chapter 3: BO_nEO_mEO_n copolymers as nanocarriers of hydrophobic drugs **95**

3.1. Aim of the work	97
3.1.1 Aim of the work	98
3.1.2 Methodology	98
3.1.3 References	100
3.2. Micellisation of triblock copolymers of ethylene oxide and 1,2-butylene oxide: Effect of BO-block length	101
3.2.1 Abstract	101
3.2.2 Introduction	101
3.2.3 Experimental section	103
3.2.3.1 Materials	103
3.2.3.2 Methods	104
3.2.4 Results and discussion	105
3.2.4.1 Determination of the critical micelle concentration	105
3.2.4.2 Influence of temperature on cmc	105
3.2.4.3 Correlation of cmc with hydrophobicity	109
3.2.5 Conclusions	111
3.2.6 References	111
3.3. Complex self-assembly of reverse poly(butylene oxide)-poly(ethylene oxide)-poly(butylene oxide) triblock copolymers with long hydrophobic and extremely lengthy hydrophilic blocks	114
3.3.1 Abstract	114
3.3.2 Introduction	115
3.3.3 Experimental section	116
3.3.3.1 Materials	116
3.3.3.2 Methods	117
3.3.4 Results and discussion	119
3.3.4.1 Clouding	119
3.3.4.2 Population size distributions	120
3.3.4.3 Micellar properties	122
3.3.4.4 Rheological behavior	124

3.3.5 Conclusions	133
3.3.6 References	133
3.4. Solution behavior of reverse poly(butylene oxide)-poly(ethylene oxide)-poly(butylene oxide) triblock copolymers with lengthy hydrophilic blocks	136
3.4.1 Abstract	136
3.4.2 Introduction	137
3.4.3 Experimental section	138
3.4.3.1 Materials	138
3.4.3.2 Methods	139
3.4.4 Results and discussion	141
3.4.4.1 Clouding	141
3.4.4.2 Population size distributions	142
3.4.4.3 Micellar properties	145
3.4.4.4 Rheological behavior	148
3.4.5 Conclusions	156
3.4.6 References	157
3.5. Supporting information	160
3.6. Doxorubicin-loaded micelles of reverse poly(butylene oxide)-poly(ethylene oxide)- poly(butylene oxide) block copolymers as efficient “active” chemotherapeutic agents	162
3.6.1 Abstract	162
3.6.2 Introduction	163
3.6.3 Experimental section	165
3.6.3.1 Materials	165
3.6.3.2 Methods	165
3.6.4 Results and discussion	169
3.6.4.1 Cytocompatibility of $BO_nEO_mBO_n$ copolymers	170
3.6.4.2 Solubilization capacity	170
3.6.4.3 Size and stability of the DOXO-loaded polymeric micelles	172
3.6.4.4 In vitro release	173
3.6.4.5 Intracellular DOXO accumulation by inhibition of Pg-P efflux pump	174
3.6.4.6. Cellular uptake of DOXO-loaded polymeric micelles (P-gp evasion)	175
3.6.5 Conclusions	180
3.6.6 References	181
3.7. Supporting information	184

Chapter 4: Linear copolymers **187**

4.1. Aim of the work	189
4.1.1 Aim of the work	189
4.1.2 Methodology	189
4.1.3 References	191
4.2. Cytocompatibility and P-glycoprotein inhibition of block copolymers: Structure-activity relationship	193
4.2.1 Abstract	193
4.2.2 Introduction	193
4.2.3 Experimental section	195
4.2.3.1 Materials	195
4.2.3.2 Methods	196
4.2.4 Results and discussion	198
4.2.4.1 Cytocompatibility of the block copolymers	198
4.2.4.2 Block copolymers as inhibitors of the P-gp efflux pump	203
4.2.5 Conclusions	209
4.2.6 References	209
4.3. Supporting information	213

Chapter 5: Experimental techniques **217**

5.1. Spectroscopy	219
5.1.1 EMR and light	219
5.1.2 Structure of matter	220
5.1.3 Light interaction with matter	221
5.2. Nuclear magnetic resonance spectroscopy	223
5.2.1 Nuclear magnetic properties	223
5.2.2 Nuclear magnetic resonance spectroscopy	223
5.2.3 Proton RMN spectroscopy (^1H)	225
5.3. UV-Vis spectroscopy	227
5.4. Fluorescence spectroscopy	231
5.4.1 The pyrene method	234
5.5. References	235
5.6. Gel permeation chromatography	237
5.6.1 References	238
5.7. Light scattering	239

5.7.1 Static light scattering	240
5.7.2 Dynamic light scattering	243
5.7.3 References	247
5.8. Isothermal titration calorimetry	239
5.8.1 References	250
5.9. Surface tension	251
5.9.1 Wihelmy plate method	252
5.9.2 References	253
5.10. Microscopy	254
5.10.1 Optical microscopy	255
5.10.2 Electronic microscopy	257
5.10.2.1 transmission electron microscopy (TEM)	257
5.10.2.2 Scanning electron microscopy (SEM)	258
5.10.2.3 Atomic force microscopy (AFM)	259
5.10.4 References	260
5.11. Rheology	262
5.11.1 Viscoelasticity	268
5.11.2 References	257

Agradecimientos

En primer lugar me gustaría agradecerle a mis directores de Tesis, Víctor Mosquera Tallón, Pablo Taboada Antelo y Silvia Barbosa Fernández, por brindarme la oportunidad de formar parte del Grupo de Física de Coloides y Polímeros de la Universidad de Santiago. Quiero agradecer especialmente a Víctor, por hacerme sentir parte de esta familia, y por sus consejos, tanto en lo profesional como en lo personal. A Pablo por contagiarme ese entusiasmo y pasión que siente en el trabajo, por guiarme en este camino así como por dejarme elegir, por todas las charlas que me han ayudado tanto a entender con claridad, por sus explicaciones y por poner todos los medios necesarios para llevar a cabo este trabajo. A Silvia le agradezco las horas juntas en el laboratorio, las charlas y los consejos, que me han servido a lo largo de este trabajo y seguro me seguirán siendo útiles en un futuro. A vosotros, muchísimas gracias por todo, porque estos años no se pueden resumir en unas líneas, ni lo que he aprendido aquí se puede resumir en una tesis.

Dedico esta tesis a todas aquellas personas que me han acompañado en este camino, porque todas ellas me han ayudado, de una u otra manera.

A mis compañeros en el Grupo de Física de Coloides y Polímeros, Josué, Sonia, Manuel y Emilio, vosotros me habéis enseñado y guiado, habéis compartido conmigo vuestros conocimientos y vuestro tiempo, los buenos y los malos momentos, muchas gracias por estar siempre ahí, muchas gracias por seguir estando ahí. A los compañeros que han llegado después a este laboratorio, como Antonio, Dolores, Eva, Miguel, Marta, Mateo y Alberto, que puedo decir, los buenos momentos quedan siempre en la memoria. He aprendido mucho con vosotros, dentro y fuera del lab. A todos los compañeros de los diversos grupos de investigación que han sido colegas y amigos, como Bieito, Goreti y Nati. Todos hemos compartido y celebrado los éxitos en el trabajo, pero también nos hemos ayudado siempre cuando las cosas no salían bien, por todo ello no puedo dejar de agradecer todo este tiempo, porque sin vosotros no habría sido posible.

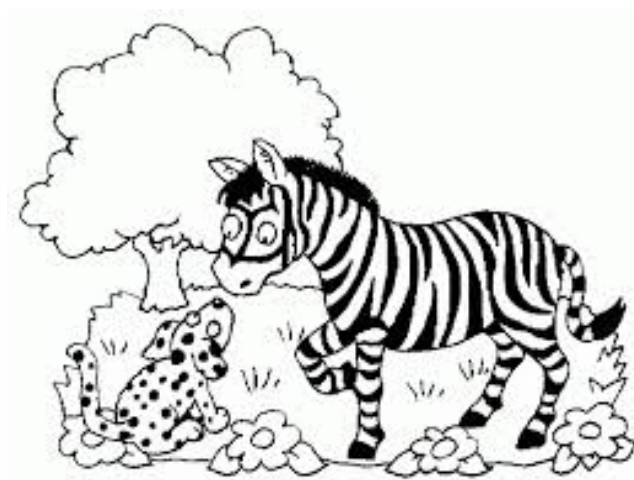
Quiero agradecer también a mis amigos, los que me han acompañado más directamente como Marta, Sergio y Claudia, y los que siempre están ahí, como Suso, Jose, Sergio y el resto del grupo, todos mis chicos, por interesarse por mi trabajo, por preguntar y preguntar.

Finalmente quiero agradecer a mis padres, porque de ellos lo he aprendido todo. A mis hermanas, por su apoyo incondicional y por animarme siempre que lo necesito. A mi hermano pequeño, ☺.

A Alberto y a Petra, porque son la alegría de mi casa.

Gracias,

muchas gracias !!!



SUMMARY

Nanotechnology is an emerging area that have allowed already the obtention and is expected to achieve new scientific breakthroughs through the manipulation of materials, their properties and their synthetic processes properties at the molecular level, ranging dimensions between 1 to 100 nm. However, the most promising aspects about nanotechnology is not the possibility to work with materials at small dimensions, but the radical change that undergo the physical and chemical properties of materials when working with them at the nanoscale: electrical conductivity, colour, strength or elasticity, amongst other properties. Hence, nanomaterials behave clearly different than the same material on the macroscopic scale, so these changes in the materials' properties can be used to be applied in different fields such as the synthesis of new materials, electronics, medicine or energy production, storage and recovery. There already exist nanotechnology products in the market as, for example, more effective and protective cosmetics, more flexible and resistant tennis rackets, anti-wrinkle or stain clothes or anti-scratch glasses and crystals.

The emergence of nanotechnology in health sciences has led to a new discipline called Nanomedicine, whose aim is the development of systems able to diagnose, prevent and treat diseases at early stages of their development. Nanomedicine includes three main areas: nanodiagnosis, controlled drug release (or nanotherapy) and regenerative medicine. *Nanodiagnosis* is the development of analytical and imaging systems for the detection and monitorization of diseases at the earliest possible stage. *Nanotherapy* aims to address active nanosystems containing recognition elements to induce biological responses, and to transport and release drugs exclusively in diseased areas in order to achieve a more effective treatment, minimizing adverse side effects. *Regenerative medicine* aims to repair or replace damaged tissues and organs by using nanotechnology tools.

The need for new diagnostic and therapeutic tools for various diseases such as cancer, diabetes, cardiovascular or neurodegenerative diseases, which do not have definitive treatments, have generated the progressive increase in Nanomedicine research. One of their biggest challenges is the development of "nanotherapies", that is therapies

based on nanoscale materials that can be directed selectively to diseased tissues and organs, avoiding the inevitable toxic side effects of current treatments. Amongst them we found the controlled drug delivery systems, which are nanostructures use as carriers for drugs. These nanocarriers transport drugs to selective damaged areas, enabling drug release only when they reach and recognized the target. To do this, it is previously necessary to encapsulate /protect the drug inside the nanocarrier to ensure the cargo inertness along the body while keeping intact its properties. Once the nanosystem has reached its target site, it must release the drug at an appropriate rate to be effective and, then, should allow its clearance from the body. Design and evaluation of these systems corresponds to the Pharmaceutical Nanotechnology area, which has been developed in parallel and in a complementary way to Nanomedicine .

In the present PhD Thesis we have focused on nanotherapy, creating controlled drug delivery systems for cancer treatment. The drug used was doxorubicin, which is one of the most widely used anticancer agents in the treatment of leukemias, Hodgkin lymphomas, as well as various cancers such as bladder, breast, stomach, lung and ovary, amongst others. The drug accumulates in the cell nucleus, where it intercalates with DNA provoking its cleavage, and then, cell death occurs.

To transport and protect the anticancer drug, nanocarriers based on amphiphilic block copolymers have been used. This class of polymers spontaneously aggregate giving rise to nanostructures called micelles at a certain concentration and/or temperature, with the hydrophobic blocks forming the micellar core and the hydrophilic ones the shell. Hydrophobic drugs hosted in the micellar core can increase its solubility, besides being protected against external degradation. The broad range of polymers available offers a wide range of possibilities, although water-soluble systems able to be dispersed in biological buffers are the main focus.

The molecular structure of a block copolymer consist of the chemical linkage between two or more macromolecules of different homopolymers. Considering the number of these blocks, polymers are called diblock, triblock or multiblock if they have two, three or more blocks, respectively. In addition, they are called linear if they are formed by a single unbranched chain, and are amphiphilic if their building blocks possess different affinity regarding the surrounding medium. Generally, ethylene oxide is the hydrophilic base unit (being water the surrounding medium) to construct block copolymers. Due to its hydrophilic nature, the other building blocks will have a more hydrophobic nature, giving the copolymer its amphiphilic character. The hydrophobic character of a copolymer can be increased by using more hydrophobic blocks or by increasing the number of hydrophobic units by block. Another important factor to consider is the temperature: for example, heating water makes it to become a poorer solvent for the hydrophilic ethylene oxide blocks. Furthermore, by

rising the temperature some polymers also modify their solubility due to changes in their intra-and inter- molecular interactions.

Amphiphilic block copolymers have the ability to self-associate in solution. This aggregation process for linear copolymers depends mainly on the solvent and the polymer concentration used. The simplest structure formed by copolymer chains self-association are micelles, nanostructures in which the polymer chains spontaneously reconfigure to form core-shell type structures. Copolymers bearing ethylene oxide units in their structure use these hydrophilic units to form the micellar shell (in water), while the hydrophobic units compose the core. Both polymolecular and unimolecular micelles can be used as drug carriers. The drug can be incorporated either in the shell, the core or the micellar interface, depending on the affinity of the drug regarding the different parts of the micelle. Furthermore, copolymers bearing ethylene oxide blocks lead to sterically stabilized micelles, which prolong the blood circulation time and avoid their recognition by macrophages, which constitute the reticuloendothelial system (RES). The drug loaded in the micellar core is also fully protected against dilution and other external factors. Regarding the role played by the nanocarrier size, it has been proved that the smaller the nanoparticles are the quicker their accumulation into the cells is, and longer particles are retained inside cells for longer periods. As a consequence, a compromise between internalization, accumulation and removal from the cell for a completely effective therapeutic action must be found.

The most widely studied copolymers for pharmaceutical applications are the so-called poloxamers (Pluronics®). Pluronics are copolymers whose structure is formed by a central poly(propylene oxide) block (PPO) and two side poly(ethylene oxide) (PEO) blocks. They are commercially available in a wide range of molecular weights and lengths, their solubilizing capacity has been fully demonstrated as well as their biocompatibility; even some of them have already entered in clinical trials. However, Pluronics also possess several drawbacks as drug delivery systems, as suffering of an incomplete micellization that usually gives rise to nanostructures with very limited stability upon dilution in the bloodstream.

The objective of the present thesis is to evaluate the properties and capabilities of new block copolymer micelles as drug delivery systems. Due to the need for the development of new drug delivery vehicles that allow an enhanced drug solubilization using polymer concentrations as low as possible, different copolymers were synthesized and characterized. To achieve this objective, this thesis was divided into the following chapters:

Basic notions regarding nanotechnology, nanotherapy and drug delivery systems are presented in **Chapter 1**. In order to understand the needs and objectives regarding delivery systems, a brief overview about different systems currently used in nanotherapy has been done, as well as a list of the requirements and expected benefits of these nanosystems. The chapter is fulfilled with a section concerning polymers and their aggregation properties,

mainly focused on the micellar systems and the advantages these possess as drug delivery vehicles .

Chapter 2 presents an analysis of copolymers $EO_{33}SO_{14}EO_{33}$ and $EO_{38}SO_{10}EO_{38}$ (where So denotes styrene oxide, and the subscripts the block lengths). Their structure and aggregation process in aqueous solution was tested as a preliminary step to be evaluated as drug carriers. These copolymers have been chosen as an alternative to the previous mentioned Pluronics, provided that they have the same molecular structure but a more hydrophobic central block, which should confer the micellar core with a higher solubilizing ability for hydrophobic drugs. The block length has been chosen to obtain the optimal compromise between chain solubility, micelle formation and micellar core size based on previous studies. These copolymers were synthesized by sequential anionic polymerization and their composition and block architecture was characterized by nuclear magnetic resonance (NMR) and gel permeation chromatography (GPC). Evaluation of polymeric micelles as nanocarriers for drug administration was performed by a detailed physico-chemical characterization in order to structural details, as well as their behavior in aqueous solution in a wide range of concentrations and temperatures, followed by *in vitro* studies to evaluate their ability to encapsulate hydrophobic drugs providing a suitable stability and protection to the cargo molecules, their biocompatibility and cytotoxic action.

The self-association process and subsequent micelle formation was followed by fluorescence spectroscopy, using the pyrene method. It was verified that the aggregation process starts at lower concentrations than for Pluronics having similar block lengths due to the larger hydrophobicity of the SO blocks.

Using static and dynamic light scattering techniques, (SLS and DLS, respectively) and analyzing a wide range of concentrations, information about the properties of the polymeric micelles formed (hydrodynamic radius, micellar aggregation number, micellar molecular weight, shell volume and hydration extent) was extracted. It was found that in aqueous solution $EO_mSO_nEO_m$ copolymers self-assemble at low concentrations to form micelles of sizes around ca. 15 nm, making them suitable for parenteral administration. Such micelles are spherical and have a hydrophobic core and a hydrophilic shell of PEO. To confirm the reliability of the DLS analysis regarding the micelle size, copolymer samples were also visualized by transmission electron microscopy (TEM) verifying, at the same time, the spherical symmetry of the micelles. The behavior of these block copolymers in a wide range of concentrations and temperatures was also analyzed by rheometry, gaining a detailed knowledge about the phase behavior and associated flow properties.

Next, the solubilization ability of poorly aqueous soluble drugs within $EO_{33}SO_{14}EO_{33}$ and $EO_{38}SO_{10}EO_{38}$ copolymer micelles was tested by varying the drug/copolymer ratio at polymer concentrations above their critical micelle concentration. To do that, two poorly

water-soluble drugs were tested: the antifungal griseofulvin and the anticancer doxorubicin. It was observed that the increase in solubility for both drugs was higher for EO₃₃SO₁₄EO₃₃ as a result of its larger and more hydrophobic core being, therefore, more compatible with the drug. Stability tests show that the polymeric micelles formed by these copolymers maintain their initial size after one freeze-drying-reconstitution cycle, which makes them suitable for storage. The temporal evolution of both empty and drug-loaded micelles under high dilution conditions show that these nanosystems are physically stable for at least 12 days, keeping almost invariable their size and cargo loading during first 5 days.

Another important point for the potential use of EO_mSO_nEO_m copolymers as delivery systems is the drug release rate once the nanocarrier reaches its target site. Drug-loaded micelles exhibited a rapid cumulative release *in vitro* at short incubation times, to become more sustained at later stages. It was also verified that the release rate depends on the pH of the surrounding medium in which the vehicle is located. To verify this point buffered solutions of pH 4.0, 5.5 and 7.4 were used, which mimic the acidic environment of cancer cells, lysosomes and cytoplasm, respectively. Thus, it was observed that griseofulvin release was higher and faster as more alkaline the medium is. Griseofulvin-loaded EO₃₃SO₁₄EO₃₃ copolymer micelles released the largest amount at pH 4.0, whereas those of EO₃₈SO₁₀EO₃₈ released faster at pH 7.4, reaching 80 % drug released before 10 hours of incubation. In the case of doxorubicin, the observed behavior was just the opposite: the drug release was smaller at pH 7.4 than at pH 5.5 as a result of the reprotonation of the amino group of the anticancer drug at acidic pH, which increases its aqueous solubility and accelerates the release; in this case, amount released was larger for EO₃₈SO₁₀EO₃₈ than for EO₃₃SO₁₄EO₃₃ copolymer.

To test the potential viability of these copolymers, biological tests *in vitro* were performed in order to ascertain the biocompatibility of the bare and drug-loaded nanocarriers and their cytotoxicity into different cell lines. The non-toxic nature of the present EO₃₈SO₁₀EO₃₈ and EO₃₃SO₁₄EO₃₃ copolymers was revealed by testing their cytotoxicity by means of the lactate dehydrogenase (LDH kit) assay and the cellular proliferation by measuring the formation of formazan crystals (MTT assay) in a BALB-3T3 fibroblast mouse cell line. These copolymers showed viabilities of ca. 100% except at the highest polymer concentrations tested (1.66 wt.%), at which the viabilities were slightly lower.

To achieve efficient nanocarriers, in particular for their use in antineoplastic therapy, it is necessary to accumulate the required amount of drug inside the cell in order to exert its cytotoxic activity. This concentration depends on efflux pump mechanisms through the cell membrane, which are those that cells use to expel foreign substances. In tumor cells these mechanisms are much more active, usually giving rise to sub-optimal drug concentrations inside cells which derive in inefficient therapeutic actions. In previous studies it has been

demonstrated that certain copolymers modify the cellular response inhibiting the efflux pump mechanisms in some cases. The NCI-ADR-RES cell line corresponds to drug multi-resistant ovarian tumor cells, that is a suitable model to test the effect of efflux pumps on the accumulation of anticancer drugs, in this case, of the P-glycoprotein pump (Pg-P) which is highly overexpressed in this cell line. For comparison and control, a MCF-7 cell line was used which corresponds to a breast cancer cell line highly sensitive to doxorubicin, and which shows no overexpression of Pg-P. To verify whether the present copolymers have a potential inhibitory effect of the Pg-P efflux pump, several copolymer concentrations were added to cell cultures. Strikingly, the inhibition of the Pg-P efflux pump in the NCI-ADR-RES cell line was found whilst for the MCF-7 cell line no variations in doxorubicin were found compared to the administration of free drug. To corroborate these results, other well-known Pg-P inhibitors were also tested as verapamil and Pluronic P85, which do not increase the levels of the anti-cancer drug on MCF-7 cells, but duplicate their levels in the NCI-ADR-RES cell line. The greater accumulation of doxorubicin in the NCI-ADR-RES cell line when administered within polymeric micelles was also confirmed by confocal microscopy, also revealing a slower drug accumulation inside cells as a consequence of the time delay associated with its release from micelle cores. The fluorescent pattern found for drug-loaded micelles was typical of cytoplasmic cargo release, that is, the loaded micelles accumulate in the cytoplasm where the acidic environment favoured drug release, allowing free doxorubicin to enter the nucleus and subsequently bind DNA strands.

Finally, to complete the study as well as to verify the suitability and efficacy of the present copolymers as drug delivery vehicles, the cytotoxicity of doxorubicin-loaded polymeric micelles of the present copolymers was evaluated using the crystal violet method. MCF-7 and NCI-ADR-RES tumor cell lines were used to test the effect of: the free drug, and empty and drug-loaded micelles of the two copolymers and Pluronic P85 used as a control,. It was found that the effect of the loaded nanocarriers is exclusively due to the release of the drug inside the cell, since the cell inhibition was not originated from empty micelles. Cell growth inhibition levels obtained for doxorubicin-loaded micelles in the NCI-ADR-RES cell line (that overexpresses the Pg-P efflux pump) were higher than for the free drug, approximately twice. Growth inhibition on the MCF-7 cell line (that not overexpresses the P-Pg efflux pump) showed similar results, which additionally confirms the sustained drug release over time after 14 h incubation previously observed.

In **Chapter 3**, reverse triblock copolymers bearing long poly(butylene oxide) and very lengthy poly(ethylene oxide) blocks were evaluated (PBO and PEO, respectively). These copolymers are of great interest due to the shortage of copolymers of this family possessing such structures, which can largely influence their solution properties. Their high hydrophobicity and their block length allows the formation of more polymeric micelles at lower concentrations, with the subsequent increase in drug solubilization ability. Hence, five copolymers were synthesized using PBO side blocks with a central PEO block. They were

designed having different block lengths, allowing to compare their properties as a function of block length or the block ratio. As $EO_nSO_mEO_n$, these copolymers were obtained by oxyanionic sequential polymerization and their molecular structure was determined using GPC and NMR techniques. Their self-assembly properties in aqueous solution were also studied. Micellization curves were obtained by fluorescence spectroscopy using the pyrene method. Critical micelle concentration values obtained for the present $BO_nEO_mBO_n$ copolymers are lower as the BO/EO ratio increased. As in Chapter 2, the aggregation properties in aqueous solution were obtained using SLS, DLS and TEM techniques. Also, the formation of both unimolecular and polymolecular micelles was confirmed at concentrations below their critical concentration, as well as the existence of micellar bridging as observed by atomic force microscopy (AFM) and rheometric analysis. Their phase and rheological behavior was studied at high concentrations due to their potential use as associative thickeners. First, the tube inversion method enabled to visualize the macroscopic phase behavior under temperature increases, allowing to identify three different regions (sol/soft gel/hard gel). To complete the phase diagram, the cloud temperature was obtained by UV-vis spectroscopy. The copolymers' behavior under controlled stress or strain was also analyzed and master curves constructed that enabled to analyze the flow behavior in a range of frequencies not achievable using conventional instrumentation. It was also observed that the thickening character of these copolymers is present despite the storage moduli (G') is lower than the loss moduli (G'') in a relatively narrow concentration range, as opposed to other widely used thickeners used as HEUR. Furthermore, their behavior does not conform to that of Maxwell fluids.

Evaluation of polymeric micelles of this type of copolymers as nanocarriers for drug administration was performed by the physical characterization of the drug-loaded micelles, followed by cargo release *in vitro* studies in the dilute concentration regime. In aqueous solution these copolymers form micelles of 10-40 nm in diameter with a hydrophobic core (BO) and a hydrophilic shell (EO), which makes them suitable for parenteral administration. Their ability to encapsulate hydrophobic drugs was tested by varying the drug/copolymer ratio, being doxorubicin the drug used. The encapsulation efficiency of these copolymers was higher than that found for other copolymers such as Pluronic, but smaller than the $EO_nSO_mEO_n$ systems previously reported in Chapter 2.

Concerning the stability and protection of their loading cargo, these copolymers maintain the initial size after one freeze - drying - reconstitution cycle; their temporal evolution in solution showed that these systems are physically stable up to 20 days of incubation, keeping the micellar size virtually unchanged and the loaded cargo at 90% of the initial value. Like $EO_nSO_mEO_n$ copolymers, $BO_nEO_mBO_n$ ones exhibited a burst release phase *in vitro* at short incubation times, becoming more sustained later. Drug release also depended on the surrounding medium, that is, of the solution pH: the lower the pH the higher the release was as in the case of $EO_nSO_mEO_n$ copolymers.

Biological assays were performed following the same scheme commented in the previous chapter. Three of the copolymers with different block lengths were selected in order to correlate their effectiveness with the molecular structure. Cytocompatibility assays for bare copolymers were made using the BALB-3T3 cell line by means of the MTT and LDH tests which revealed cell viabilities up to 100% at the studied concentrations, except for copolymer $\text{BO}_8\text{EO}_{90}\text{BO}_8$, which was 75%. In any case, all of the copolymers verified their non-toxicity and cytocompatibility (viability $\geq 50\%$).

As the previous chapter, the ability of $\text{BO}_n\text{EO}_m\text{BO}_n$ copolymers to behave as biological response modifiers was tested and, in particular, as inhibitors of the P-Pg efflux pump in the NCI-ADR-RES cell line. Their inhibitory capacity was confirmed, allowing a greater accumulation of the antitumor drug inside cells, as observed directly by confocal microscopy.

Chapter 4 extends the study of block copolymers as drug delivery systems in cancer therapy to a wide range of linear block copolymers, with diblock and triblock architecture as well as copolymers with the same constituent blocks and different block lengths. The objective was to determine the role played by copolymer structure and composition on the viability and cellular response in different cell lines. Over 30 polymers with similar structures possessing PEO as the common hydrophilic unit were analyzed in terms of their cytocompatibility and their influence on the inhibition of the Pg-P efflux pump. An empirical threshold of the ratio $\text{EO}/\text{PO}_{\text{effective}} = 1.5$ for cell viability was found for triblocks, whereas the inherent larger cytotoxicity enables precluded such finding at the concentrations studied. Furthermore, it was observed that some of the studied polymers such as $\text{EO}_{57}\text{PO}_{46}\text{EO}_{57}$ or $\text{C}_{16}\text{EO}_{455}\text{C}_{16}$ acted as inhibitors of the Pg-P efflux pump, promoting a greater accumulation of doxorubicin within NCI-ADR-RES cells.

Chapter 5 is a summary of the experimental techniques used along this thesis. Particular emphasis on operation principles and experimental accessible data was made in order to clarify the results. The different equipments are also shown, in some cases accompanied by diagrams of their most relevant parts/configurations.

RESUMEN

La nanotecnología es un área emergente en la que ya se han obtenido y se esperan conseguir nuevos avances revolucionarios mediante la manipulación de materiales, sus propiedades y los procesos de obtención a nivel molecular, abarcando dimensiones entre 1 nm hasta los 100 nm aproximadamente. Pero lo más interesante de la nanotecnología no es la posibilidad de trabajar con materiales de reducidas dimensiones, sino el cambio radical que sufren las propiedades físicas y químicas de la materia cuando se trabaja a escala nanométrica: la conductividad eléctrica, el color, la resistencia o la elasticidad, entre otras propiedades. Así, los nanomateriales se comportan de manera diferente a como lo hace el mismo material a escala macroscópica, por lo que estos cambios en las propiedades de los materiales pueden ser aplicados en diferentes campos entre los que destacan, por ejemplo, la producción de nuevos materiales, la electrónica, la medicina o la producción/almacenamiento/ recuperación de energía. Ya existen productos nanotecnológicos en el mercado como cosméticos más eficaces y protectores, raquetas de tenis más flexibles y resistentes, ropa que no se arruga ni se mancha, o gafas y cristales que no se rayan, por citar algunos ejemplos.

La irrupción de la nanotecnología en las ciencias de la salud ha dado lugar a una nueva disciplina denominada Nanomedicina, cuyo objetivo es el desarrollo de sistemas que permitan diagnosticar, prevenir y tratar enfermedades en el inicio de su desarrollo o en estados poco avanzados. La nanomedicina agrupa tres áreas principales: el nanodiagnóstico, la liberación controlada de fármacos (o nanoterapia) y la medicina regenerativa. El *nanodiagnóstico* consiste en el desarrollo de sistemas de análisis y de técnicas de imagen para la detección y monitorización de enfermedades en los estadios más tempranos posibles. La *nanoterapia* pretende dirigir nanosistemas activos que contengan elementos de reconocimiento para obtener respuestas biológicas y transportar y liberar medicamentos exclusivamente en las zonas afectadas a fin de conseguir un tratamiento más efectivo, minimizando los efectos secundarios adversos. La *medicina regenerativa* tiene como objetivo la reparación o sustitución de tejidos y órganos dañados usando herramientas nanotecnológicas.

La necesidad de encontrar nuevos métodos diagnósticos y terapéuticos para diversas dolencias como el cáncer, las enfermedades cardiovasculares, la diabetes o enfermedades neurodegenerativas para las que no existen tratamientos definitivos, ha generado el progresivo aumento del número de investigaciones en Nanomedicina. Uno de sus grandes retos consiste en el desarrollo de “nanoterapias”, terapias basadas en materiales nanométricos que se puedan dirigir de forma selectiva a los tejidos y órganos enfermos, evitando así los efectos secundarios inevitables en los tratamientos actuales. Entre ellas caben destacar los sistemas de liberación controlada de fármacos, que consisten en utilizar nanoestructuras que transporten el fármaco hasta la zona dañada, y sólo cuando la han reconocido, lo liberen. Para ello, es necesario la previa encapsulación o protección del fármaco para que este sea inerte en su recorrido por el cuerpo y mantenga intactas sus propiedades. Una vez que el nanosistema ha llegado a su destino, debe liberar el fármaco a una velocidad apropiada para que sea efectivo, y luego permitir la expulsión del nanotransportador del cuerpo humano.

En esta Tesis Doctoral nos hemos centrado en la nanoterapia, creando sistemas de liberación controlada de fármacos enfocados en el tratamiento del cáncer. El fármaco empleado ha sido la doxorubicina, que es uno de los agentes anticancerígenos más ampliamente empleados en el tratamiento de leucemias, linfomas de Hodking, así como en diversos cánceres de vejiga, pecho, estómago, pulmón u ovario, entre otros. El fármaco se acumula en el núcleo celular, donde se intercala con el ADN produciendo que se escinda y, por tanto, se produzca la muerte celular.

Para trasportar y proteger el fármaco anticancerígeno se han empleado nanotransportadores basados en copolímeros de bloque anfifílicos. Esta clase de polímeros a cierta concentración y/o temperatura se agregan de forma espontánea en estructuras denominadas micelas, de manera que los bloques hidróbobos configuran el núcleo y los hidrófilos la corona. Alojarse los fármacos hidrófobos en el núcleo micelar permite aumentar su solubilidad, además de protegerlo frente a la degradación externa. El amplio espectro de polímeros disponibles ofrece un amplio campo de posibilidades, aunque se prima que sean sistemas solubles en agua para que se pueda asegurar su redispersión en disoluciones tampón biológicas.

La estructura molecular de un copolímero de bloque consiste en la unión química de dos o más macromoléculas de homopolímeros diferentes. Atendiendo al número de bloques estos polímeros se denominan dibloque, tribloque o multibloque (si poseen dos, tres o más bloques, respectivamente), denominándose lineales a aquellos que forman una cadena simple, sin ramificaciones, y anfifílicos cuando presentan bloques constituyentes que poseen distinta afinidad por el medio continuo circundante. Generalmente, el óxido de etileno es la unidad base hidrófila (si consideramos que el medio circundante del

copolímero en cuestión es de base acuosa) para la construcción de los copolímeros de bloque. Debido a este carácter hidrófilo, los otros bloques que constituyen el copolímero tendrán un carácter más hidrófobo, dotando al copolímero de su carácter anfifílico. El carácter hidrófobo de un copolímero puede incrementarse mediante el uso de bloques más hidrófobos o aumentando el número de unidades hidrófobas por bloque. Otro factor importante a tener en cuenta es la temperatura: por ejemplo, al calentar agua ésta se vuelve un peor disolvente para los bloques hidrófilos de óxido de etileno. Además, incrementando la temperatura algunos polímeros modifican también su solubilidad debido a los cambios producidos en sus interacciones intra e inter-moleculares.

Una característica de los copolímeros de bloque anfifílicos es su capacidad para autoasociarse en disolución. Este proceso de agregación para los copolímeros lineales depende principalmente del disolvente empleado y de la concentración. Las estructuras más simples que se forman por autoasociación son las micelas, estructuras en las que las cadenas de polímero se reconfiguran espontáneamente para formar estructuras de tipo núcleo-coraza. Los copolímeros que tienen en su estructura unidades de óxido de etileno las usan para formar la coraza de la micela (en agua), mientras que las partes hidrófobas forman el núcleo. Tanto las micelas unimoleculares como las polimoleculares pueden ser empleadas como transportadores de fármaco. El fármaco puede incorporarse tanto en la coraza, el núcleo o la interfase, dependiendo de la afinidad de éste con cada parte. Además, los copolímeros con bloques de óxido de etileno dan lugar a micelas estéricamente estabilizadas, las cuales prolongan su circulación sanguínea al evitar ser reconocidas por los macrófagos que constituyen el sistema retículo-endotelial (SRE). El fármaco cargado en el núcleo micelar se encuentra asimismo completamente protegido frente a la dilución y a otros factores externos. Por otra parte, el tamaño del nanotransportador juega un papel clave. Así, se ha probado que la acumulación de nanopartículas dentro de las células es más rápida cuanto más pequeñas son, mientras que las partículas más largas son retenidas durante un tiempo mayor. Como consecuencia, se ha de encontrar un equilibrio entre la internalización, la acumulación y la expulsión de la célula para lograr una acción terapéutica efectiva.

Los copolímeros que más ampliamente se han estudiado para aplicaciones farmacéuticas son los llamados poloxámeros (Pluronic[®]). Los Pluronic son copolímeros cuya estructura está formada por un bloque central de poli(óxido de propileno) (PPO) y dos bloques laterales de poli(óxido de etileno), PEO; están comercialmente disponibles en un amplio rango de pesos moleculares y longitudes, su capacidad solubilizadora está sobradamente demostrada así como su biocompatibilidad; incluso, algunos están ya en fase de ensayos clínicos. Sin embargo, los Pluronic muestran también diferentes inconvenientes como nanosistemas de liberación farmacológica, como son una micelización incompleta en muchas ocasiones que, por lo general, conduce al auto-ensamblaje en nanoestructuras con una estabilidad limitada después de su dilución en el torrente sanguíneo.

El objetivo de esta tesis doctoral es analizar las propiedades y capacidades de nuevos copolímeros de bloque como sistemas de administración de fármacos mediante diferentes soportes micelares formados por estos. Debido a la necesidad de nuevos vehículos de administración de fármacos que permitan un aumento de la solubilización de medicamentos utilizando la concentración de polímero más baja posible, diferentes copolímeros fueron sintetizados y caracterizados. Para alcanzar este objetivo, la presente tesis se estructura en los siguientes capítulos:

En el **capítulo 1** se presentan unas nociones básicas en relación a la nanotecnología, la nanoterapia y a los sistemas de liberación de fármacos. Con la finalidad de entender las necesidades y objetivos de los sistemas de liberación, se ha realizado un resumen somero acerca de algunos de los distintos tipos de sistemas actualmente usados en nanoterapia, así como una relación de los requerimientos y ventajas que se esperan de estos sistemas. El capítulo se completa con un apartado referente a los polímeros y sus propiedades de agregación, enfocado principalmente a los sistemas micelares y las ventajas que presentan como vehículos de liberación de fármacos.

En el **capítulo 2** se presenta un análisis de los copolímeros $EO_{33}SO_{14}EO_{33}$ y $EO_{38}SO_{10}EO_{38}$ (SO = óxido de estireno, y los subíndices indican la longitud de los bloques). Se ha evaluado su estructura y su proceso de agregación en disolución acuosa como paso previo y necesario para su empleo como agentes transportadores y liberadores de fármacos. Estos copolímeros se han elegido como alternativa a los Pluronicos mencionados anteriormente, poseyendo la misma estructura molecular pero con el bloque central mucho más hidrófobo, lo que debiera conferirles una mayor capacidad de solubilización en el núcleo micelar. La longitud de los bloques ha sido elegida para obtener el mejor compromiso entre la solubilidad de la cadena polimérica, la formación de micelas y el tamaño del núcleo micelar en base a estudios previos. Estos copolímeros se sintetizaron mediante polimerización secuencial aniónica y se caracterizó su composición y arquitectura mediante resonancia magnética nuclear (RMN) y cromatografía de permeación en gel (GPC). La evaluación de las micelas como nanovehículos para la administración de fármacos se realizó mediante una caracterización física para conocer los detalles de su estructura, así como su comportamiento en disolución acuosa en un amplio rango de concentraciones y temperaturas, seguida por estudios *in vitro* para evaluar la capacidad para encapsular fármacos hidrófobos (proporcionándoles una debida estabilidad y protección), su biocompatibilidad y su acción citotóxica.

El proceso de autoasociación de los copolímeros y consiguiente formación de micelas se siguió mediante espectroscopía de fluorescencia, empleando el método del pireno. Se verificó que el proceso de agregación se inicia a concentraciones inferiores que para los

Pluronic de similar longitud de bloque al ser el bloque de óxido de estireno más hidrófobo que el de óxido de propileno.

Empleando las técnicas de dispersión estática y dinámica de luz (SLS y DLS, respectivamente) y analizando un amplio rango de concentraciones se extrajo la información necesaria para conocer las propiedades de las micelas poliméricas formadas: radio hidrodinámico, número de agregación micelar, peso molecular de las micelas, y el volumen de la corona micelar y su hidratación. Se encontró que en disolución acuosa los copolímeros $EO_mSO_nEO_m$ se autoensamblan a concentraciones muy bajas para formar micelas de tamaños entorno a ca. 15 nm, lo que los hace adecuados para la administración por vía parenteral. Tales micelas son esféricas y poseen un núcleo hidrófobo y una envoltura hidrófila de PEO. Para corroborar la fiabilidad de los análisis de los datos de DLS en cuanto a los tamaños micelares, las muestras se visualizaron también por microscopía electrónica de transmisión (TEM) verificándose, al mismo tiempo, la simetría esférica de las micelas. Asimismo, el comportamiento de estos copolímeros de bloque en un rango amplio de concentraciones y temperaturas también se analizó mediante reometría, de modo que nos permitió conocer en detalle el comportamiento físico y las propiedades asociadas a las distintas fases existentes en los mismos.

A continuación, la capacidad de solubilización de fármacos hidrófobos de los copolímeros $EO_{33}SO_{14}EO_{33}$ y $EO_{38}SO_{10}EO_{38}$ se probó mediante la variación de la relación de fármaco/copolímero, siempre a concentraciones de polímero por encima de su concentración micelar crítica. Para ello, se emplearon dos fármacos poco hidrosolubles, el antifúngico griseofulvina y el anticancerígeno doxorubicina. Se observó que el aumento de la solubilidad para ambos fármacos fue mayor cuando se emplea como vehículo el polímero $EO_{33}SO_{14}EO_{33}$ debido a tener un núcleo más grande y más hidrófobo y, por consiguiente, ser más afín con el fármaco. Las pruebas de estabilidad realizadas muestran que estos copolímeros en su forma micelar mantienen el tamaño inicial después de un ciclo de congelación - secado - reconstitución, lo que los hace adecuados para ser almacenados. La evolución en el tiempo bajo condiciones de fuerte dilución tanto de las micelas vacías como para las micelas cargadas de fármaco muestran que estos sistemas son físicamente estables hasta 12 días, manteniendo el tamaño prácticamente invariable y la carga al 100% de su valor inicial en los primeros 5 días.

Otro punto importante para el potencial empleo de los copolímeros del tipo $EO_mSO_nEO_m$ como sistemas de liberación es la velocidad de liberación del fármaco una vez ha llegado a su destino. Las micelas cargadas con el fármaco exhibieron una rápida liberación acumulada *in vitro* a tiempos cortos de incubación para, posteriormente volverse más sostenida. Se ha verificado también que la liberación depende del pH medio en el que se encuentre el vehículo. Para comprobar este punto se emplearon disoluciones tamponadas de pH 4.0, 5.5 y 7.4, las cuales imitan el ambiente ácido en las células

cancerígenas, los lisosomas y el citoplasma, respectivamente. De esta manera, se observó que para la griseofulvina la liberación fue mayor y más rápida cuanto más alcalino es el medio. Las micelas del copolímero $EO_{33}SO_{14}EO_{33}$ cargadas con griseofulvina fueron las que más carga liberaron a pH 4.0; sin embargo las de $EO_{38}SO_{10}EO_{38}$ liberaron su carga más rápidamente a pH 7.4, alcanzando el 80% del fármaco antes de las 10 horas de incubación. En el caso de la doxorubicina, el comportamiento observado es justamente el opuesto, siendo la liberación más reducida a pH 7.4 que a pH 5.5, como consecuencia de la reprotonación del grupo amino del anticancerígeno a pH ácido que incrementa su solubilidad acuosa y acelera su liberación, siendo superior para el $EO_{38}SO_{10}EO_{38}$ que para el $EO_{33}SO_{14}EO_{33}$.

Para comprobar la viabilidad biológica de estos copolímeros, se realizaron ensayos *in vitro* con el fin de conocer la biocompatibilidad del nanotransportador y la citotoxicidad del complejo fármaco-polímero en distintas líneas celulares. La naturaleza no tóxica de los presentes copolímeros $EO_{33}SO_{14}EO_{33}$ y $EO_{38}SO_{10}EO_{38}$ se reveló mediante los ensayos de citotoxicidad lactato-deshidrogenasa (LDH) y de proliferación celular mediante la medición de formación de formazán (MTT) en la línea celular BALB-3T3 de fibroblastos de ratón, mostrando viabilidades ca. 100% salvo a concentraciones altas de polímero (1.66 wt. %), en donde las viabilidades fueron ligeramente inferiores.

Para conseguir unos nanovehículos eficientes, en particular, para su empleo en la terapia antineoplásica, se necesita que se acumule la cantidad de fármaco necesaria dentro de la célula para así ejercer su actividad citotóxica. Esta concentración depende de los mecanismos de eflujo a través de la membrana celular, que son los que las células utilizan para expulsar sustancias extrañas. En las células tumorales estos mecanismos están mucho más activos, dando lugar a concentraciones por debajo de la adecuada para una eficiente acción terapéutica. Se ha comprobado en estudios previos que ciertos copolímeros modifican la respuesta celular inhibiendo en algunos casos la bomba de eflujo. La línea celular NCI-ADR-RES corresponde a células tumorales de ovario multiresistentes a fármacos, siendo un modelo adecuado para probar el efecto de las bombas de eflujo en la acumulación de fármacos antineoplásicos y, en particular, de la bomba de glicoproteína-P (Pg-P) pues presenta una alta expresión de esta última. A efectos de comparación y control, se empleó la línea celular MCF-7 correspondiente a células cancerígenas de tumores de mama sensibles a la doxorubicina, que no muestra sobreexpresión de la Pg-P. Para comprobar si los presentes copolímeros presentaban un potencial efecto inhibitorio de la bomba de flujo de la Pg-P, diferentes concentraciones de copolímero se añadieron a los cultivos celulares. Así, se verificó la inhibición de la bomba de eflujo en la línea celular NCI-ADR-RES, mientras que para la línea celular MCF-7 no se observó ninguna variación respecto a los niveles obtenidos cuando se aplicaba únicamente doxorubicina lib como control. Para corroborar estos resultados, otros inhibidores conocidos de la P-gp fueron también probados como el verapamilo y el Pluronic P85, que no aumentan los niveles del

anticancerígeno en la línea celular MCF-7, pero sí los duplican en la línea celular NCI-ADR-RES. La mayor acumulación de doxorubicina en la línea celular NCI-ADR-RES se corroboró también mediante microscopía confocal cuando se administra solubilizada con los copolímeros, revelándose que la acumulación del fármaco en el interior celular transcurre de forma más lenta como consecuencia directa del mecanismo de liberación desde el interior de las micelas poliméricas. El patrón de fluorescencia para las micelas cargadas con el fármaco es típico de localización citoplasmática, esto es, el vehículo se acumula en el citoplasma, donde el ambiente ácido favorece la liberación del fármaco, y permite que la doxorubicina ya libre penetre en el núcleo y se una al ADN.

Finalmente, para completar el estudio y verificar la idoneidad y eficacia de los presentes copolímeros como vehículos de liberación, se evaluó la actividad citotóxica de las micelas poliméricas cargadas con el fármaco doxorubicina empleando el método de cristalvioleta. Se emplearon las líneas celulares tumorales MCF-7 y NCI-ADR-RES para probar el efecto de: el fármaco solo y de las micelas vacías y cargadas, empleándose micelas de Pluronic P85 como control positivo. Así, se observó que el efecto de los nanovehículos cargados se debe exclusivamente a la liberación del fármaco dentro de la célula, ya que la inhibición celular no es debida a la micela vacía. En particular, los niveles de inhibición del crecimiento celular obtenidos para los nanovehículos cargados con la doxorubicina en la línea celular NCI-ADR-RES (que sobre-expresa la bomba de eflujo) fueron más altos que para el fármaco libre, aproximadamente el doble. En el análisis de la inhibición del crecimiento en la línea celular MCF-7 (que no sobre-expresa la bomba de eflujo de Pg-P) se obtuvieron resultados similares, lo que corrobora la liberación sostenida en el tiempo a partir de las 14 horas de incubación.

En el **capítulo 3** se evalúan los copolímeros tribloque reversos compuestos por bloques de poli(óxido de butileno), PBO, y de poli(óxido de etileno), PEO, $BO_nEO_mBO_n$ con longitudes de bloque tanto hidrófobos como hidrófilos muy largas. Estos copolímeros presentan un gran interés debido a la escasez de copolímeros de esta familia con bloques tan largos. Su hidrofobicidad y el tamaño de sus bloques permite obtener mayor número de micelas a concentraciones similares a las empleadas anteriormente, con el consecuente aumento en la solubilidad del fármaco. Por todo esto, se han sintetizado cinco copolímeros usando bloques de PBO como bloques laterales y bloques PEO como bloque central. Se han diseñado con longitudes de bloque distintas, lo que ha permitido comparar sus propiedades en función de la longitud de bloque o la razón entre ellos. Al igual que los copolímeros $EO_nSO_mEO_n$, estos polímeros se obtuvieron mediante polimerización oxianiónica secuencial y su estructura molecular se realizó empleando las técnicas de RMN y GPC. Sus propiedades de auto-ensamblaje en disolución acuosa han sido también estudiadas. Las curvas de micelización se han obtenido mediante espectroscopía de fluorescencia, empleando el método del pireno. Los valores de las concentraciones micelares críticas obtenidas para los copolímeros $BO_nEO_mBO_n$ son más bajos a medida que aumenta la relación BO/EO. Siguiendo

los mismos pasos que en el capítulo anterior, se obtuvieron las propiedades de agregación en disolución acuosa empleando las técnicas de SLS, DLS y TEM. Asimismo, se confirmó tanto la formación de micelas unimoleculares en estos copolímeros tribloque a concentraciones inferiores a sus respectivas concentraciones críticas, y de existencia de uniones (“bridging”) entre las micelas poliméricas a concentraciones superiores a la crítica gracias a las imágenes de microscopía de fuerza atómica (AFM) obtenidas y el análisis reométrico efectuado. Su comportamiento fásico y reológico ha sido también estudiado a altas concentraciones debido al potencial interés que presentan estos polímeros como agentes espesantes y como depósitos en forma de gel. En primer lugar, el método de inversión de tubo permitió visualizar el comportamiento fásico macroscópico bajo variaciones de temperatura, lo que permite diferenciar tres regiones (sol/gel blando/gel duro). Para completar el diagrama de fases, la temperatura de turbidez se obtuvo mediante espectroscopía UV-vis. También se ha analizado su comportamiento bajo un esfuerzo o tensión controlada y se han construido curvas maestras que permiten ver su comportamiento en un rango de frecuencias que no son alcanzables mediante instrumentación convencional. Asimismo, se ha obtenido que el carácter de espesante se demuestra a pesar de que el módulo de almacenamiento, G' , es inferior al de pérdida, G'' , sólo en un determinado rango de concentraciones, en oposición a espesantes ampliamente empleados como los HEUR. Además, su comportamiento no se ajusta a fluidos de Maxwell.

La evaluación de las micelas de este tipo de copolímeros como nanovehículos para la administración de fármacos se realizó mediante la caracterización física de las micelas cargadas seguida por los estudios de liberación *in vitro* en el rango de bajas concentraciones. En disolución acuosa estos copolímeros forman micelas de 10-40 nm de diámetro con núcleo hidrófobo (BO) y corona hidrófila (EO), lo que los convierte en adecuados para su administración por vía parenteral. Su capacidad para encapsular fármacos hidrófobos se probó mediante la variación de la relación fármaco/copolímero, siendo el fármaco empleado la doxorubicina. La eficiencia de encapsulación de estos copolímeros es mayor que la encontrada para otros copolímeros como los Pluronic, pero menor que los sistemas $EO_nSO_mEO_n$ previamente estudiados en el capítulo anterior.

En relación a la estabilidad y protección de su carga, estos copolímeros mantienen el tamaño inicial después de un ciclo de congelación - secado - reconstitución, y su evolución temporal en disolución muestra que estos sistemas son físicamente estables hasta 20 días de incubación, manteniendo el tamaño micelar prácticamente invariable y la carga al 90% del valor inicial. Al igual que los copolímeros $EO_nSO_mEO_n$, los polímeros $BO_nEO_mBO_n$ exhibieron una primera fase de liberación rápida *in vitro* del fármaco a tiempos de incubación cortos, para ser más sostenida posteriormente. La liberación dependió asimismo del medio en el que se encontraban las micelas cargadas, es decir, del pH, encontrándose que ésta fue superior a pH ácido, al igual que en el caso de los copolímeros $EO_nSO_mEO_n$.

Los ensayos biológicos se realizaron siguiendo las mismas pautas que en el Capítulo 2, seleccionándose tres de los copolímeros con longitudes de bloque diferentes con el fin de poder correlacionar su efectividad con la estructura molecular. Los ensayos de citocompatibilidad de los copolímeros vacíos se realizaron, en primer lugar, en la línea celular BALB-3T3 empleando los test MTT y LDH, revelando viabilidades entorno al 100% a las concentraciones estudiadas, salvo para el copolímero $\text{BO}_8\text{EO}_{90}\text{BO}_8$, que fue del 75%. En cualquier caso, todos los copolímeros han verificado que son no tóxicos y citocompatibles (viabilidad $\geq 50\%$).

Al igual que en capítulo anterior, se probó la capacidad potencial de los copolímeros $\text{BO}_n\text{EO}_m\text{BO}_n$ como modificadores de la respuesta biológica y, en particular, como inhibidores de la bomba de eflujo de la Pg-P en la línea celular NCI-ADR-RES, confirmándose su capacidad inhibidora. Este hecho permitió de nuevo una mayor acumulación del fármaco antitumoral en el interior de las células, como se observó directamente a través de microscopía confocal.

En el **capítulo 4** se ha extendido el estudio de los copolímeros como sistemas de liberación de fármacos en terapia anticancerígena a un amplio espectro de copolímeros de bloque lineales, tanto dibloque como tribloque, así como copolímeros con los mismos bloques constitutivos pero de diferentes longitudes. El objetivo que se ha tratado de lograr ha sido conocer el papel que juega la estructura y la composición de los copolímeros en la viabilidad y en la respuesta celular en diferentes líneas celulares. Más de 30 polímeros con estructuras comparables conteniendo como unidad hidrófila común el PEO fueron analizados en términos de su citocompatibilidad, así como su influencia sobre la capacidad de inhibición de la bomba de eflujo de Pg-P. Así, se encontró un umbral empírico para la viabilidad celular de los copolímeros tribloque entorno al valor $\text{EO}/\text{PO}_{\text{efectivo}} = 1.5$, mientras que para los dibloque su mayor toxicidad a las concentraciones estudiadas no permitió la determinación de ningún valor límite. Además, se ha observado que algunos de los polímeros estudiados (como el $\text{EO}_{57}\text{PO}_{46}\text{EO}_{57}$ y el $\text{C}_{16}\text{EO}_{455}\text{C}_{16}$) actúan como inhibidores de la bomba de eflujo de Pg-P, promoviendo una mayor acumulación del fármaco anticancerígeno doxorubicina dentro de las células NCI-ADR-RES.

El **capítulo 5** es un compendio de las técnicas experimentales empleadas en esta tesis. Se ha hecho especial hincapié en las bases de su funcionamiento y de las magnitudes que accesibles experimentalmente, con el fin de clarificar los resultados obtenidos. Se muestran asimismo los diferentes equipos, en algunos casos acompañados de diagramas de las piezas/configuraciones más relevantes que los constituyen.

Publicaciones derivadas de la presente tesis doctoral

1. Cambon, A.; Alatorre-Meda, M.; Juarez, J.; Topete, A., Mistry, D.; Attwood, D.; Barbosa, S.; Taboada, P.; Mosquera, V. Micellisation of triblock copolymers of ethylene oxide and 1,2-butylene oxide: Effect of B-block length. *J. Colloid&Interface Sci.*, **2011**, 361, 154-158.
2. Cambon, A.; Barbosa, S.; Rey-Rico, A.; Figueroa-Ochoa, E.B., Soltero, J.F.A.; Yeates, S.G.; Alvarez-Lorenzo, C.; Concheiro, A.; Taboada, P.; Mosquera, V. Poly(ethylene oxide)-poly(styrene oxide)-poly (ethylene oxide) copolymers: Micellization, drug solubilization and gelling features. *J. Colloid&Interface Sci.*, **2012**, 387, 275-284.
3. Cambon, A.; Rey-Rico, A.; Mistry, D.; Brea, J.; Loza, M. I.; Attwood, D.; Barbosa, S.; Alvarez-Lorenzo, C.; Concheiro, A.; Taboada, P.; Mosquera, V. Doxorubicin-loaded micelles of reverse poly(butylene oxide)-poly(ethylene oxide)-poly(butylene oxide) block copolymers as efficient “active” chemotherapeutic agents. *Int. J. Pharm.*, **2013**, 445, 47-57.
4. Cambon, A.; Rey-Rico, A.; Barbosa, S.; Soltero, J. F. A.; Yeates, S. G.; Brea, J.; Loza, M. I.; Alvarez-Lorenzo, C.; Concheiro, A.; Taboada, P.; Mosquera, V. Poly(styrene oxide)-poly(ethylene oxide) block copolymers: from “classical” chemotherapeutic nanocarriers to active cell-response inducers. *J.Control. Release*, **2013**, 167, 68-75.
5. Cambon, A.; Brea, J.; Loza, M.I.; Alvarez-Lorenzo, C.; Concheiro, A.; Barbosa, S.; Taboada, P.; Mosquera, V. Cytocompatibility and P-glycoprotein inhibition of block copolymers: structure-activity relationship. *Mol. Pharm.*, **2013**, 10, 3232-3241.
6. Cambon, A.; Figueroa-Ochoa, E.; Juárez, J.; Villar-Álvarez, E.; Pardo, A.; Barbosa, S.; Soltero, J.F.A.; Taboada, P.; Mosquera, V. Complex self-assembly of reverse poly(butylene oxide)-poly(ethylene oxide)-poly(butylene oxide) triblock copolymers with long hydrophobic and extremely lengthy hydrophilic blocks. *J. Phys. Chem. B*. In press.

7. Cambon, A.; Barbosa, S.; Yeates, S. G.; Taboada, P.; Mosquera, V. Solution behavior of reverse triblock reverse poly(butylene oxide)-poly(ethylene oxide)-poly(butylene oxide) copolymers with lengthy hydrophilic blocks. *Polymer*. Submitted.

Otras publicaciones realizadas durante el período doctoral

1. Juarez, J.; Goy-Lopez, S.; Cambon, A.; Taboada, P.; Mosquera, V. Influence of electrostatic interactions on the fibrillation process of human serum albumin. *J. Phys. Chem. B.*, **2009**, *113*, 10521-10529.

2. Juarez, J.; Taboada, P.; Goy-Lopez, S.; Cambon, A.; Madec, M.B.; Yeates, S.G.; Mosquera, V. Additional supra-self-assembly of human serum albumin under amyloid-like-forming solution conditions. *J. Phys. Chem. B.*, **2009**, *113*, 12391-12399.

3. Goy-Lopez, S.; Taboada, P.; Cambon, A.; Juarez, J.; Alvarez-Lorenzo, C.; Concheiro, A. Modulation of size and shape of Au nanoparticles using amino-S-shaped poly(ethylene oxide)-poly(propylene oxide) block copolymers. *J. Phys. Chem. B.*, **2010**, *114*, 66-76.

4. Goy-Lopez, S.; Juarez, J.; Cambon, A.; Botana, J.; Peeiro, M.; Baldomir, D.; Taboada, P.; Mosquera, V. Block copolymer-regulated synthesis of gold nanocrystals with sharp tips and edges. *J. Mat. Chem.*, **2010**, *20*, 6808-6814.

5. Juarez, J.; Goy-Lopez, S.; Cambon, A.; Valdez, M.A.; Taboada, P.; Mosquera, V. Surface properties of monolayers of amphiphilic poly(ethylene oxide)-poly(styrene oxide) block copolymers. *J. Phys. Chem. C*, **2010**, *114*, 15703-15712.

6. Juarez, J.; Cambon, A.; Goy-Lopez, S.; Topete, A.; Taboada, P.; Mosquera, V. Obtention of metallic nanowires by protein biotemplating and their catalytic application. *J. Phys. Chem. Lett.*, **2010**, *1*, 2680-2687.

7. Juarez, J.; Cambon, A.; Topete, A.; Taboada, P.; Mosquera, V. One-dimensional magnetic nanowires obtained by protein fibril biotemplating. *Chem. Eur. J.*, **2011**, *17*, 7366-7373.

8. Juarez, J.; Alatorre-Meda, M.; Cambon, A.; Topete, A.; Barbosa, S.; Taboada, P.; Mosquera, V. Hydration effects on the fibrillation process of a globular protein: the case of human serum albumin. *Soft Matter*, **2012**, *8*, 3608-3619.

9. Menzel, C.; Cambon, A.; Yeates, S. G. Double emulsion template suspension polymerization: towards the synthesis of polyelectrolyte core porous hydrophobic shell particles for environmental applications. *J. Mat. Chem. A.*, **2013**, 1, 12553-12559.

CHAPTER 1

INTRODUCTION

1.1 NANOTECHNOLOGY

Nanotechnology is a scientific field which primarily deals with the synthesis, characterization, exploration and exploitation of nanostructured materials. The National Nanotechnology Initiative (NNI) defines nanotechnology as the “understanding and control of matter at dimensions of roughly 1 to 100 nanometers, where unique phenomena enable novel applications,” allowing fabrication of devices on the nanoscale. Generally, nanomaterials are characterized by having at least one dimension in the nanometer range ($1 \text{ nm} = 10^{-9} \text{ m}$). Nanostructured materials constitute a bridge between molecules and infinite bulk systems. Individual nanostructures include clusters, quantum dots, nanocrystals, nanowires and nanotubes, amongst others, while collections of nanostructures involve arrays, assemblies and superlattices of individual nanostructures (1).

Nanotechnological devices offer a broad and exciting field of possibilities in a wide range of research areas: From the nanowires used in electronic devices to the ferrofluids used as contrast agents in magnetic resonance imaging (MRI), their potential applications are growing as the properties of each nanomaterial are discovered and characterized, and new combinations of different nanosystems emerge. The main advantage of nanotechnology is neither the inherent size of the building blocks themselves nor another step in miniaturization, it is in fact the generation of new or the enhancement of previous existing properties that materials exhibit in the nanoscale regime (from 1 to 1000 nm, the so-called mesoscale too). At this length scale, some materials properties are affected by the laws of atomic physics rather than behaving as traditional bulk materials do. Hence, the nanoworld lays midway between the scale of atomic and quantum phenomena and the scale of bulk materials.

In order to achieve materials in the mesoscale, there are two different approaches: top-down and bottom-up (see Figure 1). The top-down strategy uses physical engineering tools for carving of macro-size materials to obtain a mesoscale smaller material. Along this process, the lateral dimension of the material is reduced until a nanostructured material is obtained as occurred, for example, in the case of silicon integrated circuits fabricated by selective layer deposition. Conversely, the bottom-up strategy is based on the assembly of sub-units in a controlled and reproducible manner. These units can be in the atomic, molecular or colloidal regime. The bottom-up strategy also takes advantage of the self-association properties of nano-

sized building blocks as, for example, in the case of micelles formed by surfactants or polymers (2,3).

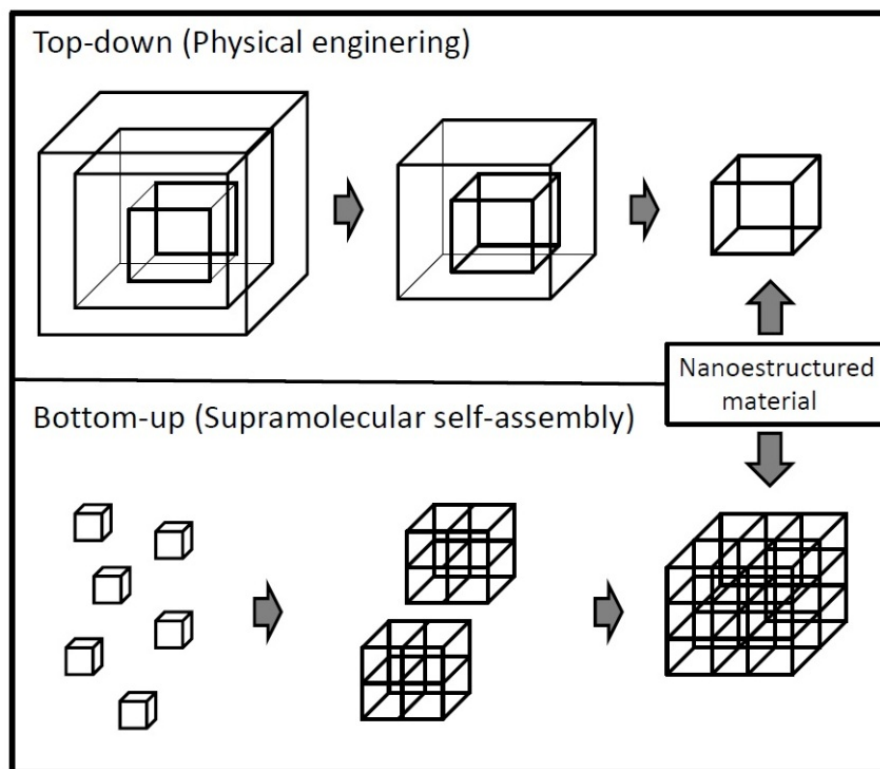


Figure 1. Schematic representation of two strategies used to get nanosized materials: a) Top-down and b) Bottom-up.

As commented previously, the physical and chemical properties of nanostructures are distinctly different from those of a single atom (molecule) and bulk matter with the same chemical composition (1). These differences between nanomaterials and the molecular and condensed-phase materials pertain to the spatial structures and shapes, phase changes, energetic, electronic structure, chemical reactivity, and catalytic properties of large, finite systems, and their assemblies. Some of the important issues in nanoscience are related to size and shape effects which affect, for example, the response to external electric and optical excitations of individual and coupled finite nanosystems through quantum confinement.

Surfaces and interfaces are also important in explaining nanomaterial behaviour. In bulk materials, only a relatively small percentage of atoms will be at or near a surface or interface (like a crystal grain boundary). In nanomaterials, the small feature size ensures that many atoms, more than a half in some cases, will be near interfaces. Surface/Interfacial properties such as energy levels, electronic structure, and reactivity

can be quite different from macrostates and may give rise to quite different material's properties as, for example, the fluorescent properties of quantum dots or the behaviour of superparamagnetic iron oxide nanoparticles (SPIONs) (4,5).

Nanomaterials are on the same scale as the critical size for many different physical phenomena to occur: For example, the tip radius of a crack in a material may be in the range 1-100 nm. The way a crack grows in a macro-sized material is different from a crack propagation in a nanomaterial, where crack and particle are comparable in size. As mentioned before, fundamental electronic, magnetic, optical, chemical, and biological processes are also different at this level. For example, proteins are 10-1000 nm in size, and the diameter of human cells spans from 10 to 20 μm being the organelles diameter ranging from a few nanometer to a few hundreds; as a consequence, the behaviour of biological entities when getting into contact a nanomaterial may be quite different from that observed when contacting to larger-scale materials (6). For this reason, nanotechnological devices may present new possibilities for drug delivery, gene therapy and medical diagnostics.

1.1.1 Nanopharmaceutics and nanomedicine

In relation to the pharmaceutical/medical aspects, the Federal Drug and Administration (FDA) Office of USA highlights that materials in the nanoscale often have different physical, chemical and biological properties than their bulk counterparts in complex biological media (7,8). As a consequence, their biological activities can also exhibit alterations. A very good example is silver: Silver atoms do not exhibit antibacterial activity, while ionic silver ions (Ag^+) are really effective antibactericidal, antimicrobial and antifungal agents. Because of their water solubility and ease of production, Ag^+ ions are a potential biocide, but their high toxicity exclude them to be used as a safe product. Other silver compounds are instead employed in external preparations as antiseptics, for example, silver nitrate. In addition, silver ions cannot be directly used inside the human body because they quickly combine with chloride to form silver chloride, an insoluble compound with reduced antimicrobial activity. To avoid this issue, colloidal silver nanoparticles (Ag NPs) were developed. Solid metallic Ag NPs are insoluble in water and can release ionic silver in a sustained rate once into the body but with suitable functionalization this problem can be overcome. However, concerns still remain regarding the long degradation time of this kind of particles inside living systems (9).

Nevertheless, nanotechnology offers a tremendous potential in applications such as biomedical diagnosis and therapy giving rise to a new field termed Nanomedicine, which nowadays constitutes one of the priority areas in most of the developed countries. For example, the National Institute of Health of USA offered a budget of 1443-M\$ for the period 2006-2011 to encourage and develop projects in this research field. The purpose of Nanomedicine is to follow, control, construct, repair, defend and improve biological human systems for different applications such as in imaging diagnosis and therapeutics. To do that, engineered nanodevices are used, these possess individual functions given by their individual components integrated in an single architecture and can even meet multiple functions; they work at the molecular level by interacting with cellular or sub-cellular structures and, at the same time, to look for producing effective responses at bigger scales. Hence, the final goal of nanomedicine is to overcome some or all of the drawbacks of current clinical practice as too short blood circulating times of active chemically-active compounds, lack of enough image resolution for an early detection of diseases like cancer, unspecific biodistribution, non-controlled release, unavailability to overcome biological barriers, cytotoxicity...

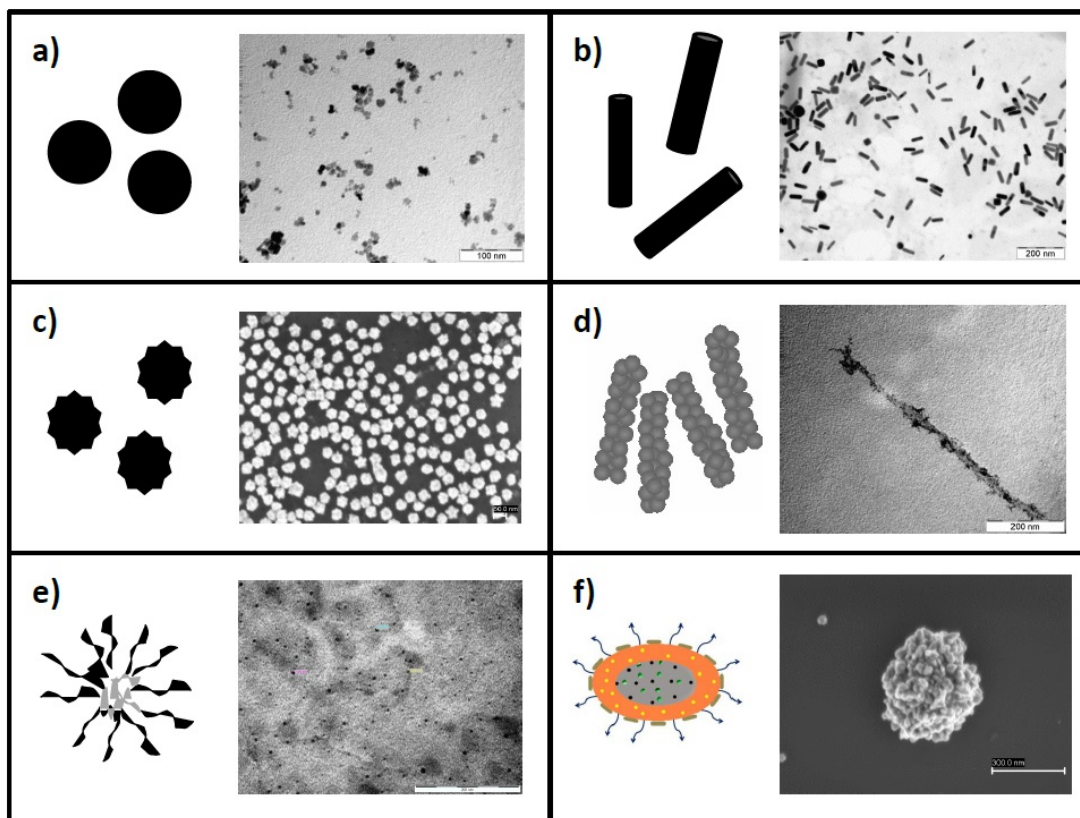


Figure 2. Examples of nanomaterials used in the nanopharmaceutical/nanomedical field: a) Fe_3O_4 SPION, b) gold nanorods, c) silver stars, d) metallic fibres, e) micelles and f) polymeric nanocapsules for simultaneous imaging and treatment.

To solve some of these problems, nanotechnology enabled the design and obtaining of the so-called drug delivery vehicles, also known as nanoplatforms or nanovectors—nanoparticles capable of carrying and delivering one or more bioactive molecules (4,10,11), giving rise to a field known as pharmaceutical nanotechnology. The main objective of these nanovectors is to transport the cargo by using nanoparticles composed of different materials (see Figure 2) as vehicles offering a protective environment until the target cell/tissue is reached and facilitating its controlled release. The ultimate goal of this strategy is to kill/cure an infected/tumour cells/organ/tissue without affecting healthy ones, avoiding adverse side effects. To exert the therapeutic function, drug carriers must be accumulated inside cells through the enhanced permeation and retention effect (EPR) and/or by specific targeting, should enable to cross the cell membrane in order to achieve the required concentration for enough time to carry out their optimal therapeutic activity levels.

Once reached the target, the release must be controlled to avoid under- or overdoses, which could derive in an ineffective treatment or toxicity. The degradation or excretion mechanism of the nanocarriers is also an important concern, because the accumulation in some organs could also derive in toxicity. To solve this issue, for example once into the cell the nanocarrier could undergo degradation whilst, at the same time, releases its cargo. On the other hand, if the nanovehicle remains unaltered after releasing the cargo it could be captured by the reticulo-endothelial system or degraded into smaller sizes, which would allow its excretion by renal clearance [8]. In this regard, the FDA demands an exhaustive control over the specifications and quality of the nanoparticles designed to pharmaceutical/medical applications, being the main requirements the control over (12):

- The particle size and their distribution.
- The surface area, the chemical properties of the surfaces, the porosity and the surface coverage.
- The hydrophobicity and the charge density of the surface.
- Purity and sterility.
- Stability (aggregation or protein adsorption).
- Cell internalization.
- Cytotoxicity.
- Drug release profile.
- Complete correlation between “in vitro” and “in vivo” behaviour.
- Excretion and biodegradability.
- Environmental impact.

Finally, just to mention that amongst the most well-known representatives of nanocarriers in clinical use, for example for cancer treatment, we can find liposomes (for example, DOXIL™, liposome loaded with the anticancer drug doxorubicin approved in 1995 for the treatment of Kaposi's sarcoma (13); albumin nanoparticles (as ABRAXANE™, approved in 2005 for the treatment of metastatic breast cancer) (14); or polymer nanoparticles (as GENEXOL-PM, a formulation of polymeric micelles loaded with the anticancer drug paclitaxel and free of Cremophor-El, which is a phase II trial for analyzing its efficacy in pancreatic tumours in USA) (15). However, the generation of nanovectors based on nanoparticles in the market nowadays, around a couple of dozens, are non-targeting passive systems whose biodistribution along the human body cannot be traced (8,11,16). The localization of these systems is addressed only by their size (in particular, by the enhanced retention and permeation effect, EPR, which leads to the nanovehicle to be localized in areas with uncontrolled increases of vascularity as occurred in solid tumours (17), and is not related with a specific recognition by the targeted cell or tissue. Hence, we can conclude that Nanomedicine is still in its infancy and there exist a huge number of challenges that this discipline can help to reach in next years.

1.1.2 References

1. Gogocij, J.G. *Nanomaterials Handbook*. Boca Raton: Taylor & Francis, 2006.
2. Booth, C.; Price C *Comprehensive Polymer Science*. Oxford: Pergamon Press, 1989.
3. Holmberg, K.; Jönsson, B.Kronberg, B. *Surfactants and Polymers in Aqueous Solution*. Nueva York: John Wiley & Sons, 1989.
4. Kim, K.Y. *Nanomedicine Nanotechnol. Biol. Med.* **2007**, 3, 103.
5. Arya, H.; Kaul, Z.; Wadhwa, R.; Taira, K. ; Hirano, T. ; Kaul, S. C. *Biochem. Biophys. Res. Commun.* **2005**, 329, 1173.
6. Yadav, A.K.; Mishra P.; Mishra A. K.; Mishra P.; Jain S.; Agrawal G. P. *Nanomedicine Nanotechnol. Biol. Med.* **2007**, 3, 246.
7. Preining, O. J. *Aerosol Sci.* **1998**, 29, 481.
8. Hagens, W.I.; Oomen, A. G.; de Jong, W. H.; Cassee, F. R.; Sips, A. J. A. M. *Regul. Toxicol. Pharmacol.* **2007**, 49, 217.
9. Maillard, J.-Y.; Hartemann, P. *Crit. Rev. Microbiol.* **2013**, 39, 373.
10. Koo, O.M.; Rubinstein, I.; Onyuksel, H. *Nanomedicine Nanotechnol. Biol. Med.* **2005**, 1, 193.
11. Mishra, B.; Patel, B.B; Tiwari, S. *Nanomedicine Nanotechnol. Biol. Med.* **2010**, 6, 9.
12. Tyner, K.; Sadrieh, N. *Methods Mol. Biol.* **2011**, 697, 17.
13. Working, P.K.; Newman, M. S.; Huang, S. K.; Mayhew, E.; Vaage, J.; Lasic, D. J. *Liposome Res.* **1994**, 4, 667.

14. Ibrahim, N.K., Samuels, B.; Page, R.; Doval, D.; Patel, K. M.; Rao, S. C.; Nair, M. K.; Bhar, Paul; Desai, N.; Hortobagyi, G. N. *J. Clin. Oncol.* **2005**, 23, 6019.
15. Werner, M.E., Cummings, N. D.; Sethi, M.; Wang, E. C.; Sukumar, R.; Moore, D. T.; Wang, A. Z. *Int. J. Radiation Oncol. Biol. Phys.* **2013**, 86, 463.
16. Chouly, C.; Pouliquen, D.; Lucet, I.; Jeune, J. J.; Jallet, P. J. *Microencapsulation* **1996**, 13, 245.
17. Heidel, J.; Davis, M. *Pharm. Res.* **2011**, 28, 187.

1.2 NANOPARTICLES as drug carriers...

As previously mentioned, nanoparticle (NP) technology in the pharmaceutical field started their development as a strategy to solve formulation issues related to the low aqueous solubility of different hydrophobic drugs. Novel approaches to drug delivery using nanotechnology are revolutionizing the future of medicine (18). Over recent years, achievements in drug delivery have facilitated the targeting of specific tissues and, with the advent of nanotechnology, these targeted tissues are now being even specific organelles within individualized cells. As a result, Nanomedicine has already converted into a billion-dollar industry because of these compounds' inherent ability to overcome solubility and stability issues, localized drug delivery, as well as to diagnose through in vivo imaging even generating multifunctional entities capable of simultaneously diagnosing, delivering therapeutic agents, and monitoring treatment. Coupled with genomic tailoring, nanomedicine should also soon lead to the so-called personalized medicine.

As commented previously, Nanomedicine is the medical application of a broad range of materials and devices on the nanoscale to assess, preserve, and restore health and welfare. It takes advantage of nanoscale formulations to optimize drug delivery and to facilitate non-invasive imaging; in particular, many different nanoscale drug delivery systems can be created from countless combinations of nanomaterials and molecules, and these carriers can be customized for working either in specific tissues or to be useful for an individual patient via attachment of suitable surface ligand molecules. However, new advancements are constantly being made that allow multifunctional nanoformulations to deliver drugs while simultaneously collecting diagnostic information (18).

In this chapter, the influence of NPs' properties on pharmaceutical applications has been briefly reviewed, followed by a short summary about diverse types of NPs that are being currently used in Nanomedicine and, specifically, in Nanopharmaceutics, with a special focus on their advantages regarding classical drug delivery systems.

1.2.1 Influence of NPs' properties on pharmaceutical performance

NPs show great promises as active vectors due to their capacity to release drugs, the relatively higher intracellular uptake thanks to their nanometer size, the improved stability and enhanced protection against degradation of loaded active substances, and

their potential biocompatibility with cells and tissues (19). As mentioned previously, some NPs properties are mandatory in the pharmaceutical field, as biostability and biocompatibility, while others are an added value, as active targetability.

Many of the physico-chemical properties of NPs used in pharmaceutical formulations or nanomedical devices are related to their inherent structural properties as size, shape, surface, as well as composition. These play a key role in drug solubilization, cargo protection and cell internalization, for example. Nevertheless, it is necessary to bear in mind that one NP's property can usually have some influence in more than one of the responses supplied by the nanosystem, or even different properties may influence/enhance its specific response. Hereafter, we will give a brief explanation about several important properties NPs should bear to be used as nanopharmaceutical tools.

1.2.1.1 Drug solubility

The use of nanocarriers to load active drugs increases their dissolution speed and their saturation solubility. Although saturation solubilisation only depends on temperature and the physico-chemical properties of the surrounding medium in bulk solution, below a size of ca. 1 μm the saturation solubility becomes also a function of the particle size (20). Common solubilisation levels of different poor soluble drugs has been reported (21). The antifungal drug griseofulvin has been one of the most employed hydrophobic drugs used as a standard for testing and comparing micellar hosts (22,23) owing to its low aqueous solubility, ca. 12 mg/g (24). Other common tested drugs are, for example, the anthracycline antibiotic doxorubicine (25) or the mitotic inhibitor Paclitaxel (26), with aqueous solubilities of ca. $1 \cdot 10^{-3}$ mg/g (0,5-1 mg/dm⁻³) (24) and $0,5 \cdot 10^{-6}$ mg/g (0,6 mM) (27), respectively. For example, Oliveira et al. have found that the solubility of griseofulvin increases using F127 micelles as nanocarriers, while by the addition of sub-micellar amounts of Pluronic F127 the solubility was not increased (28). NPs have also the ability to carry a large number of therapeutic molecules (small molecules, peptides, nucleic acids, and proteins) and protect them from degradation and dilution from the surrounding medium, to accumulate in the desired organ/tissue either by passive (enhanced permeation and retention effect, EPR) or active targeting, and to favour cell uptake and internalization (29). In this regard, cellular uptake of a single nanoparticle can achieve intracellular drug concentrations several orders of magnitude higher than that individual drug molecules or their molecular conjugate.

1.2.1.2 Blood circulation time

The pharmacokinetic profile of NPs incorporating drugs often includes a dramatic increase in circulation half-life ($t_{1/2}$) compared to the drug alone because of the carrier prevent from drug recognition by the body defence systems (30). This is particularly important for therapeutic molecules with very poor stability in blood, for which nanoparticle formulations allow the use of lower doses to achieve similar, if not enhanced, efficacies with much lower toxic side effects. To extended blood circulation half-life one of the most employed mechanisms is by pegylation of the nanocarrier (i.e., modifying the nanoparticles surfaces with polyethylene glycol, PEG) (31). Although the mechanism is not fully understood (32), surface PEG having relatively high molecular weights increases the systemic circulation time by preventing serum protein adsorption and subsequent opsonisation (33).

The nanoparticle surface (free available area, roughness, etc) is also a very important parameter in drug delivery systems (34). Indeed, once in the bloodstream conventional bare nanoparticles (with no surface modification/functionalization) can be rapidly opsonized and massively cleared by macrophages from the body. It is well known that the reticulo-endothelial system (RES), mainly the liver and spleen, is also a major obstacle because of its ability to recognize and entrap NPs, removing them from systemic circulation, and, consequently, avoiding their effective delivery to organs other than those of the reticuloendothelial system (35).

1.2.1.3 Targeting

To reach and enter the desired target cell or organ, two different approaches can be used, the so-called “passive” and “active” targeting, respectively (36). “Passive targeting” is based on drug accumulation in the areas around the diseased/cancerous cells via the enhanced permeation and retention (EPR) effect. Drug-loaded NPs are accumulated at higher concentrations than free drug molecules alone as a result of their largest size. In addition, the increased vascular permeability coupled with an impaired lymphatic drainage in tumours and/or inflamed tissues allows an enhanced permeability and retention effect of the nanosystems (37). Thus, this physiological alteration allows extravasations of the nanosystems and their selective localization in this kind of cells/tissues. The tendency of nanosystems to specifically localize in the reticulo-endothelial system also presents an excellent opportunity for passive targeting of drugs to macrophages present in the liver and spleen. Thus, this natural system can be used for targeting drugs for intracellular infections.

On the other hand, “active targeting” is usually referred to the specific recognition of receptors overexpressed on the surface of diseased (cancerous) cells and tissues by ligands attached on the nanocarrier’s surface (36). Nevertheless, both “active” and “passive targeting” enable the nanosystem to reach the target area as a result of blood circulation and extravasation followed by intratumoral retention and distribution. The term “active targeting” simply implies a specific “ligand–receptor type interaction” for intracellular localization which occurs only after blood circulation and extravasation (19). This is why increasing blood circulation time and/or improving the EPR effect is expected to enhance delivery to the tumour site.

1.2.1.4 Cellular uptake

It has been shown that cellular uptake is specifically dependent on NP size and shape. Nanocarrier sizes below 200 nm favour cellular uptake; in particular, the smaller the size the better and faster the internalization is, additionally allowing their evasion from RES and improving targeting capabilities (30). In particular, particles ranging from ca. 10 to 100 nm are optimal for intravenous injection and demonstrate the most prolonged blood circulation times: particles in this size range are small enough both to evade the RES as well as penetrate the very small capillaries within the body tissues and, therefore, may offer the most effective biodistribution (30). NPs with sizes below 10 nm are rapidly cleared from plasma through the pores within the glomerular capillary walls of kidneys (38,39). Conversely, particles with diameters greater than 200 nm are usually sequestered by the spleen and liver as a result of mechanical filtration and are eventually removed by the phagocyte system, resulting in decreased blood circulation times.

1.2.1.5 Release rate

Once one nanoparticle reaches the target area and cross the cell membrane, the loaded drug should be released in a sustained rate to avoid too low or too high doses, which could derive in an ineffective treatment and/or associated toxicity, as commented previously. In addition, NPs can also be prepared in order to have extended payload releases, covering the whole time period of the treatment from several days to weeks or even months. This feature should avoid the need of repetitive administrations and their associated toxicity, increasing therapy efficiency and the patients’ quality life, especially, when long-term treatments are required.

Drug conjugation to NPs can be done by physical (van der Waals) or chemical (covalent) means. Chemical bonds allow a better control over the amount of attached drug but it can give rise to changes on drug structure and/or activity that must be taken

into account. In addition, to release the drug at the desired place some stimulus inside (as pH, enzymes, temperature...) or outside (heat light, ultrasound, electric and magnetic fields...) cells/tissues has to promote such event (40). Conversely, physical bonding of the drug implies no changes in its structure, but fluctuations in both encapsulated and released drug concentrations, and the unspecific release by bond disturbance can be elevated (41,42). The release mechanism of physical entrapped drugs can be done by diffusion or by degradation of the carrier; even both mechanisms could take place.

The nanoparticles residence time inside a cell/tissue is also a key factor that will also determine the amount of drug release to produce the expected chemotherapeutical effect. NPs rapidly cleared out from the cell could derive in non-effective treatments because insufficient doses would be achieved, and adverse side reactions might appear by unspecific drug release out of the target cell/tissue.

1.2.1.6 Clearance mechanisms and excretion

The mechanisms that the body uses to defence itself from external agents are the same as those used to capture and excrete pharmaceutical nanoparticles after releasing their cargo. To avoid associated toxicity in the use of nanovehicles, this usually should be composed of biocompatible materials. In order to avoid adverse reactions promoted by NP opsonisation, macrophage recognition and RES uptake (inflammation, immune reactions...), the nanoparticles should be preferably composed of biodegradable materials too.

Biodegradable compounds initially behave as macromolecular agents and, then, degrade to low-molecular weight complexes that are rapidly excreted by kidneys (43). Renal clearance of intravascular agents is a multifaceted process involving glomerular filtration, tubular secretion, and finally elimination of the molecule through urinary excretion (44). Molecules with an hydrodynamic diameter (HD) < 6 nm are typically filtered, while those > 8 nm are not typically capable of glomerular filtration. Filtration of molecules within the intermediate range, 6-8 nm in HD depends on both size and charge of the NP. For example, quantum dots > 8 nm in size (HD = 8.65 nm) did not demonstrate renal filtration but instead exhibited uptake in the reticulo-endothelial system (RES) and lung (39). The hepato-biliary system represents the primary route of excretion for particles that do not undergo renal clearance. One of the physiological functions of the liver is to efficiently capture and eliminate particles on the scale of 10-20 nm. The liver provides the critical function of catabolism and biliary excretion of blood-borne particles as well as serves as an important site for the elimination of foreign substances and particles through phagocytosis (45). Phagocytic Kupffer cells are

part of the RES and rely exclusively on intracellular degradation for particle removal. They have ciliated borders and stellate branches that serve as highly adapted mechanical traps for the removal of unwanted substances from the blood including foreign colloidal or particulate substrates. Hepatocytes also play an important role in liver clearance through endocytosis and enzymatic breakdown of foreign particles, although the phagocytic capacity of hepatocytes is much less than that of Kupffer cells. Hepatocytes are within the pathway for biliary excretion and therefore particles processed by these cells are potentially excreted into the bile. For example, liposome-based nanoparticles (size > 25 nm) clearance has been shown to be governed by vesicle opsonization by serum proteins and subsequent uptake by the phagocytic cells of the RES (46).

Non-biodegradable NPs are expected to have different clearance behaviour owned to their inner nature. For example, clearance studies of metal NPs are nowadays under study. Mechanisms for Au NPs excretion primarily depend on particle size. The excretion of ultrasmall gold nanoparticles 1.9 nm in diameter suggest that kidneys are their primary site for clearance [30]. Other studies reveal that 10 nm-Au NP was greatly accumulated in the liver, followed by blood, spleen, kidney, lungs, brain, reproductive organs, thymus and heart; in contrast, 50, 100 and 250 nm Au NPs were only significantly deposited in the liver, spleen and blood (48). This predominance of liver accumulation suggests that the hepatobiliary system was the primary site for Au NPs clearance. Magnetic NPs (MNPs) demonstrate specific-uptake by the monocyte-macrophage system, being larger particles eliminated from the bloodstream faster than smaller-sized ones (49). Intravenously administered, small iron oxide nanoparticles (SPIONs) are primarily cleared from the blood by the RES system while the bigger ones demonstrate biodistribution to lymph nodes in addition to the RES (50). However, specific biodistribution and clearance parameters depend on particle properties such as surface functionalization, shape and size (51).

In summary, the use of drug carriers as reservoirs permits to enhance drug protection and dilution from the surrounding medium, to accumulate in the desired organ/tissue either by passive (enhanced permeation and retention effect, EPR) or active targeting and to favour cellular uptake and internalization (18,36,52). In this way, nanomaterials such as Pluronic copolymers, DOXIL (doxorubicin-loaded liposomes) or SPIONs, amongst others, were found to be safe and non-toxic to healthy tissues, allowing the FDA their use in clinics.

1.2.2 NPs used in pharmaceuticals

Different nanoparticles have been investigated as potential drug carriers with the aim of increasing the efficacy of the molecular cargo by the suitable simultaneous combination of the drug and vehicle's properties. As mentioned previously, this increase in effectiveness might be originated from drug protection, enhancement of drug solubility, passive or active targeting, accumulation in the targeted area and avoidance of natural excretion mechanisms. In addition, these nanoparticles must meet the condition of aqueous solubility to enable their transfer to biological media before administration to living systems.

Inorganic nanoparticles are those composed by inorganic materials, as silica or metals, which usually are presented as solid spheres, porous structures or hollow NPs (53). Their main advantages are related to their great aqueous stability and the possibility of choosing an appropriate size and shape on demand. Drugs are externally attached to solid structures while hollow NPs are used to encapsulate high doses into their inner cavities. Drugs are usually loaded onto the pores surface by physical adsorption (in porous NPs) because of their high surface area: the subsequent drug loading capacity and release profile results very different depending on pore diameter, pore topology, surface properties, etc (54). Regarding porous carriers, mesoporous silica NPs are the most extensively studied owing to the great amount of ordered uniform pores on their surface which enables a precise control of drug loading and release (55). Hollow nanocarriers provide an excellent isolated cavity for drug storage, which is made by removing the template used to create the NP. Amongst other inorganic materials used to prepare hollow NPs we should mention silica (56,57) and gold (58,59) as the most common found in literature. As examples, we could mention gold nanoparticles (Au NPs), which has been deeply studied because its unique physical (localized surface plasmon resonance, catalytic activity...) and chemical properties (chemical stability, ease of surface functionalization...) and allow controlled drug release strategies using internal or external stimuli, such as glutathione, pH, heat or light, amongst others (60-62); or iron oxide NPs (SPION), which were first successfully employed as contrast agents in magnetic resonance imaging (MRI) and now are being used to magnetically guide and deliver drugs taking advantage of their superb magnetic properties and biocompatibility (63).

On the other hand, **organic nanoparticles** are those composed by organic materials organized in supramolecular architectures. Amongst the most common employed organic materials composing drug delivery vehicles we can mention lipids, proteins, polymers or carbon nanotubes.

Some amphiphilic lipids can self-assemble to form vesicles, spherical bilayer structures whose cores comprise the same solvent as their surroundings. Therefore, these vesicles are suitable to deliver water-soluble drugs or biomaterials, including enzymes, antibodies or genes (53). Amongst these, liposomes are small artificial vesicles of spherical shape that can be produced from natural nontoxic phospholipids and cholesterol (64). Liposomes are particularly useful as drug and gene therapy devices because of their ability to pass through lipid bilayers and cell membranes. As an example, Doxil is a formulation carrying the chemotherapeutic drug doxorubicin loaded inside pegylated liposomes, where poly(ethylene oxide) chains provides the system with hydrophilic segments for aqueous dispensability. In addition, pegylated shells prevent the recognition of the liposomes by the reticulo-endothelial system (65), increasing the nanocarrier circulation time in the bloodstream and allowing the drug to be released for longer period times. Other well-studied lipid structure is solid lipid nanoparticles (SLN), which are composed by solid lipids both at ambient or body temperature (66,67). SLNs are composed by a solid lipid core matrix that can solubilise lipophilic molecules, while the used emulsifier prevent agglomeration between NPs and improve stability (50). SLN are produced by high-pressure homogenization, avoiding the use of organic solvents as well as allowing to be massively produced, a required condition for scalability and industrial production.

Proteins are large biological molecules constituted by one or more amino acid chains, which have several biological functions as well as play structural and mechanical functions in cells. As a result, their main advantages of their use as constituents of drug delivery systems are related to their biocompatibility into the human body, biodegradability, and their non-antigenic and metabolizable character (68). In addition, they can also be easily amenable for surface modification and covalent attachment of drugs and ligands. A relevant example of protein as a carrier is the use of albumin nanoparticles to transport and release, for example, the interferon-gamma (IFN- γ) (69,70), keeping active the bactericidal properties of IFN- γ . This system enhances the cellular uptake of the protein inside the protein nanocarrier, and even it exhibits a better therapeutic performance than liposomes concerning sustained drug release profiles.

Carbon nanotubes (CNTs) are a distinct molecular form of carbon atoms that was discovered in the late 1980s. Briefly, CNTs are hexagonally shaped arrangements of carbon atoms that have been rolled into tubes, with their diameter being within the nanometer scale. CNTs typically have diameters ranging from < 1 nm up to 50 nm while their lengths are typically of several microns. Their long, hollow structure with the walls formed by one-atom-thick sheets of carbon is called graphene. These sheets are rolled at specific and discrete ("chiral") angles, and the combination of the rolling angle and

particle radius control the nanotube's properties; for example, whether the individual nanotube shell is a metal or semiconductor. There has been tremendous enthusiasm over carbon nanotube applications in many industrial sectors, in part because they have been shown to be 100 times stronger than steel with only one-sixth of its weight, and with unusual heat and conductivity properties (71). In the area of nanomedicine, carbon nanotubes have been primarily used for transporting DNA cargos into the cell, and for thermal ablation therapy in cancer therapeutics. For example, Kam et al. have shown that single-walled carbon nanotubes of 1 to 2 nm in diameter carrying a 15-mer DNA chain adsorbed onto their surfaces as a cargo molecule can be internalized by cells and accumulate in their cytoplasm without causing cytotoxicity (72).

On the other hand, polymeric nanoparticles are those composed of polymers (from natural to synthetic polymers and from linear to branched or star copolymers), offering a huge field of possibilities. The most common structures formed are nanospheres and nanocapsules. Nanospheres have a matrix type-structure allowing drug absorption at the sphere surface or encapsulated within the particle. Nanocapsules are vesicular systems in which the drug is confined inside a cavity consisting of an inner liquid core surrounded by a polymeric membrane. In this case, the active substances are usually dissolved in the inner core but may also be adsorbed onto the capsule surface (34).

Polymeric particles are obtained by supramolecular assembly of polymeric chains. There exist two different approaches to obtain these type of nanoparticles: the first one involves the *in-situ* polymerization of monomers and their subsequent assembly; the second one is based on the dispersion and assembly of preformed polymeric chains (34). The methodologies to obtain NPs by monomer polymerization can be further classified into emulsion and interfacial polymerization (34). Besides, emulsion polymerization can be either organic or aqueous depending on the solvent used; the polymerization reaction starts when the monomer is dispersed or dissolved in the chosen solvent in the presence of initiators. Interfacial polymerization allows to obtain polymeric NPs whose surface corresponds to the contours of the inner phase of an oil/water or water/oil emulsion. Another type of interfacial polymerization is interfacial polycondensation, that relies on an interfacial reaction between two monomers. Nanoparticles can be also prepared directly from preformed synthetic or natural polymers and by desolvation of macromolecules. Recently, these polymeric systems have been also prepared by nebulization techniques.

Dispersion of preformed polymers can also be classified into two groups regarding the polymer nature, i.e synthetic or natural polymers. Synthetic preformed polymers can form nanoparticles by different techniques: emulsification/solvent

evaporation, solvent displacement, interfacial deposition, emulsification/solvent diffusion or salting out. Natural preformed polymers can be assembled by emulsion techniques or dropwise extrusion. Nevertheless, the main synthetic techniques used in the pharmaceutical field are those based in the spontaneous aggregation properties in solution (specially in aqueous solution) of the polymeric monomer chains such as micellisation, gelling or complex formation.

The general properties of polymeric NPs can be modulated by choosing the appropriate polymer monomeric chain and the chemical surface functionalization (73,74). Once the right polymer chain has been found, NP size can be tuned choosing between high or low molecular weight polymers and/or long or shorter block length composition (75). The employed synthetic technique also limits the NP size range, structure and stability (34). As an example, NPs obtained by in situ bulk monomer polymerization are solid NPs which cannot be degraded, while assembled polymeric NPs as micelles are reversibly dynamic systems. In the same way, physical gels progressively loss their structure under dilution conditions in contrast to chemical gels (crosslinked) which shrink while keeping intact their structure.

Drug encapsulation in polymeric NPs can be achieved by addition of the compound during the polymerization process, by its entrapment during NP formation, or by adsorption after the formation of the NP upon incubation (76). Entrapment efficiency depends primarily on the drug-reservoir affinity, but also on the encapsulation/incorporation method used.

On the other hand, one of the most employed strategies to enhance the circulation time of polymeric NPs in the bloodstream is the use of a hydrophilic coverage or shell around the polymeric NP core. The surface coverage can be made by physical adsorption upon NP obtainment or by covalent bonding to the polymer chains that form the polymeric core (77). In addition, polymeric NPs tend to accumulate in tumours through the EPR effect, which helps to ensure a sustained release inside a specific cell/tissue/organ. Other advantages of this type of nanocarriers are their great stability, scalability and their ease of functionalization to modulate their properties; by contrast, they also present several drawbacks such as the potential toxicity or non-biodegradability of some types of polymeric particles (34).

1.2.3 References

18. Bawarski, W.E., Chidlowsky E.; Bharali D. J.; Mousa S. A. *Nanomedicine Nanotechnol. Biol. Med.* **2008**, 4, 273.
19. Mora-Huertas, C.E.; Fessi, H.; Elaissari, A. *Int. J. Pharm.* **2010**, 385, 113.
20. Hurter, P.N.; Hatton, T.A. *Langmuir*, **1992**, 8, 1291.
21. Douroumis, D.F.A., *Drug Delivery Strategies for Poorly Water-Soluble Drugs*. Oxford: Wiley-Blackwell, 2013.
22. Taboada, P.; Velasquez, G.; Barbosa, S.; Yang, Z.; Nixon, S. K.; Zhou, Z.; Heatley, F.; Ashford, M.; Mosquera, V.; Attwood, D. *Langmuir* **2006**, 22, 7465.
23. Alvarez-Lorenzo, C., Gonzalez-Lopez, J.; Fernandez-Tarrio, M.; Sandez-Macho, I.; Concheiro, A. *Eur. J. Pharm. Biopharm.* **2007**, 66, 244.
24. Yalkowsky, S.H. He, Y. *Handbook of Aqueous Solubility Data*, Boca Raton, FL: CRC Press, 2003.
25. Jeong, Y.I., Kim, D. H.; Chung, C.-W.; Yoo, J.-J.; Choi, K. H.; Kim, C. H.; Ha, S. H.; Kang, D. Hwan. *Int. J. Nanomed.* **2011**, 6, 1415.
26. Dong, X., Mattingly, Cynthia A.; Tseng, M. T.; Cho, M. J.; Liu, Y.; Adams, V. R.; Mumper, R. J. *Cancer Res.* **2009**, 69, 3918.
27. Swindell, C.S., Krauss, N. E.; Horwitz, S. B.; Ringel, I. *J. Med. Chem.* **1991**, 34, 1176.
28. Oliveira, C.P., Vasconcellos, L. C. G.; Ribeiro, M. E. N. P.; Ricardo, N. M. P. S.; Souza, T. V. de P.; Costa, F. de M. L. L.; Chaibundit, C.; Yeates, S. G.; Attwood, D. *Int. J. Pharm.* **2011**, 409, 206.
29. Sahoo, S.K.; Parveen, S.; Panda, J.J. *Nanomedicine Nanotechnol. Biol. Med.* **2007**, 3, 20.
30. Heidel, J.; Davis, M. *Pharm. Res.* **2011**, 28, 187.
31. Harris J.M.; Martin, N. E.; Modi, M. *Clin. Pharmacokinetics*, **2001**, 40, 539.
32. Park, K. J. *Controlled Release* **2010**, 142, 147.
33. Yamaoka, T., Tabata, T.; Ikada, Y. *J. Pharm. Sci.* **1994**, 83, 601.
34. Pinto Reis, C.; Neufeld, R. J.; Ribeiro, A. J.; Veiga F. *Nanomedicine Nanotechnol. Biol. Med.* **2006**, 2, 8.
35. Kumar, N.; Ravikumar, M. N. V.; Domb, A. J. S. *Adv. Drug Deliv. Rev.* **2001**, 53, 23.
36. Bae, Y.H.; Park, H. J. *Controlled Release*, **2011**, 153, 198.
37. Maeda, H. *Adv. Enzyme Regul.* **2001**, 41, 189.
38. Venturoli, D.; Rippe, B. *Am. J. Physiol. Renal Physiol.* **2005**, 288, F605.
39. Choi H.S., Liu, W.; Misra, P.; Tanaka, E.; Zimmer, J. P.; Ipe, B. I.; Bawendi, M. G.; Frangioni, J. V. *Nature Biotechnol.* **2007**, 25, 1165.
40. Koo, O.M.; Rubinstein, I.; Onyuksel, H. *Nanomedicine Nanotechnol. Biol. Med.* **2005**, 1, 193.
41. Hagens, W.I.; Oomen, A. G.; de Jong, W. H.; Cassee, F.R.; Sips, A. J. A. M. *Regul. Toxicol. Pharmacol.* **2007**, 49, 217.
42. Greish, K.; Fang J.; Inutsuka T.; Nagamitsu A.; Maeda H. *Clin. Pharmacokinetics* **2003**, 42, 1089.
43. Feng, Y.; Zong, Y.; Ke, T.; Jeong, E.-K.; Parker, D. L.; Lu, R. Z. *Pharm. Res.* **2006**, 23, 1736.
44. Longmire, M.; Choyke, P. L.; Kobayashi, H. *Nanomedicine* **2008**, 3, 703.

45. Kuntz, E; Kuntz H.-D. *Hepatology Principles and Practice: History, Morphology, Biochemistry, Diagnostics, Clinic, Therapy*. Springer, 2006.
46. Ishida T.; Harashima, H.; Kiwada, H. *Biosci. Rep.* **2002**, 22, 197.
47. Hainfeld J.F.; Slatkin, D.N.; Focella, T.M.; Smilowitz, H.M. *Br. J. Radiol.* **2006**, 79, 248.
48. De Jong W.H.; Hagens, W.I.; Krystek, P.; Burger, M.C.; Sips, A. J. A. M.; Geertsma, R. E. *Biomaterials* **2008**, 29, 1912.
49. Neuberger, T.; Schoepf, B.; Hofmann, H.; Hofmann, M.; Von Rechenberg, B. J. *Magn. Magn. Mater.* **2005**, 293, 483.
50. Jain T.K., Reddy, M.K.; Morales, M.A.; Leslie-Pelecky, D.L.; Labhasetwar, V. *MolPharm.* **2008**, 5, 316.
51. Chouly, C.; Pouliquen, D.; Lucet, I.; Jeune, J.J.; Jallet, P. J. *Microencapsulation*, **1996**, 13, 245
52. Rejman, J.; Oberle, V.; Zuhorn, I.S.; Hoekstra, D. *Biochem. J.* **2004**, 377, 159.
53. Lim, E.-K.; Jang, E.; Lee, K.; Haam, S.; Huh, Y.-M. *Pharmaceutics* **2013**, 5, 294.
54. Vallet-Regí M., Balas, Francisco; Arcos, D. *Angew. Chem. Int. Ed.* **2007**, 46, 7548.
55. Tang F., Li, L.; Chen, D. *Adv. Mater.* **2012**, 42, 1504.
56. Park J.H.; Gu, Luo; V. M.; Geoffrey; R.; Erkki; B.; Sangeeta N.; Sailor, M.I.J. *Nature Mater.* **2009**, 8, 331.
57. Yang J.; Lee, Jaewon; K., Jinyoung; L., Kwangyeol; Suh, J.-S.; Yoon, H.-G.; Huh, Y.-M.; Haam, S. *Langmuir* **2008**, 24, 3417.
58. Yavuz M.S.; Cheng, Y.; Chen, J.; Cogley, C.M.; Zhang, Q.; Rycenga, M.; Xie, J.; Kim, C.; Song, Kwang H.; Schwartz, A.G. *Nature Mater.* **2009**, 8, 935.
59. Leung, J.; Wu, S.; Chou, K.C.; Signorell, R. *Nanomaterials* **2013**, 3, 86.
60. Duncan, B.; Kim, C.; Rotello, V.M. *J. Controlled Release* **2010**, 148, 122.
61. Rana S.; Bajaj, A.; Mout, R.; Rotello, V.M. *Adv. Drug Deliv. Rev.* **2012**, 64, 200.
62. Shukla, R., Bansal, V.; Chaudhary, M.; Basu, A.; Bhonde, R.R.; Sastry, M. *Langmuir* **2005**, 21, 10644.
63. Gupta, A.K.; Gupta, M. *Biomaterials* **2005**, 26, 3995.
64. Sahoo, S.K., Labhasetwar, V. *Drug Discov. Today* **2003**, 8, 1112.
65. Rösler, A.; Vandermeulen, G.W.M.; Klok, H.-A. *Adv. Drug Deliv. Rev.* **2012**, 64, 270.
66. Mishra, B.; Patel, B.B.; Tiwari, S. *Nanomedicine Nanotechnol. Biol. Med.* **2010**, 6, 9.
67. Mehnert, W.; Mäder, K. *Adv. Drug Deliv. Rev.* **2001**, 47, 165.
68. Wang, G.; Uludag, H. *Expert Opin. Drug Deliv.* **2008**, 5, 499.
69. Segura, S.; Espuelas, S.; Renedo, M. J.; Irache, J.M. *Drug Develop. Industr. Pharm.* **2005**, 31, 271.
70. Segura, S.; Gamazo, C.; Irache, J. M.; Espuelas, S. *Antimicrob. Agents Chemother.* **2007**, 51, 1310.
71. Kim, K.Y. *Nanomedicine Nanotechnol. Biol. Med.* **2007**, 3, 103.
72. Kam N.W.S.; O'Connell, M.; Wisdom, J.A.; Dai, H. *Proc. Natl. Acad. Sci. USA*, **2005**, 102, 11600.
73. Rao, J.P.; Geckeler, K.E. *Prog. Polym. Sci.* **2011**, 36, 887.

74. Cho, W.S.; Cho, W.-S.; Thielbeer, F.; Duffin, R.; Johansson, E.V.; Megson, I.L.; MacNee, W.; Bradley, M.; Donaldson, K. *Nanotoxicology*, **2014**, 8, 202.
75. Booth, C.; Price, C. *Comprehensive Polymer Science*, Oxford: Pergamon Press, 1989.
76. Soppimath, K.S.; Aminabhavi, T.M.; Kulkarni, A.R.; Rudzinski, W.E. J. *Controlled Release*, **2001**, 70, 1.
77. Shenoy, D.; Little, S.; Langer, Robert; A.; Amiji, M. *Mol. Pharm.* **2005**, 2, 357.

1.3 POLYMERIC MICELLES

Amphiphiles are small molecules or macromolecules that possess different domains in their structure, lyophilic and lyophobic, regarding their interactions with the surrounding medium, that is, the solvent becomes good for one part of the molecule while bad for the other (a selective solvent). The lyophobic part of the macromolecule tends to segregate and auto-associate with their neighbouring molecules to avoid direct contact with solvent ones. In aqueous media, amphiphiles usually tend to form supramolecular spherical colloidal particles termed micelles with a lyophobic interior (core) and a lyophilic exterior (shell), which is exposed toward the bulk solvent phase. Micelles can change their size from 5 to some hundreds of nanometers and can possess different geometries (spheres, worm-like, toroidal...) (78). Hydrophobic, electrostatic, and Van der Waals interactions are the predominant driving forces in the assembly of amphiphiles in aqueous medium (79). Furthermore, nanosized micelles have polarity gradients from the highly hydrated corona to the hydrophobic core (80) and, for example, can be used for solubilization of compounds of varying polarities by physical association with different regions within the micelles.

One of the most important types of nanosized micellar delivery systems are made of amphiphilic polymers (81-85). **Polymers** are macromolecules composed by the repetition of the same structural unit, known as monomer. Basically, they are hydrocarbon chains where the covalent bonds between C, H and O atoms constitute the main polymeric chain structure or backbone. The backbone can be flexible and may adopt different spatial configurations provided that polymer molecules are dynamic in nature, may continuously deform, and are able to return their original shape in solution. Other bonds present in polymeric molecules are weak bonds, which can be classified as non-polar and polar (hydrophobic and hydrophilic in aqueous solution). Hydrophilic bonds are formed, for example, by Van der Waals interactions and hydrogen bonding. Hydrophobic bonds are formed by repulsion of the hydrophobic counterparts and subsequent mutual interaction regarding the polar solvent molecules. Figure 1 shows the chemical structure of some monomers commonly found in many well-known polymers. Glucose is a monosaccharide found in plants along with fructose and galactose, being the starting monomer for the polymerization of starch and cellulose. Lysine is one of the twenty essential amino acids, which are the basic structural units for protein formation. Both monomers are the constitutive parts of these natural polymers. Conversely, ethylene is a natural molecule obtained from petrol and used as a monomer to polymerize polyethylene, which is one of the most worldwide extended plastics.

Although ethylene is natural, the subsequent manufacturing and processing processes make the produced polymer to be considered as synthetic.

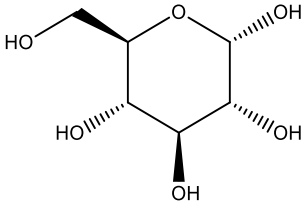
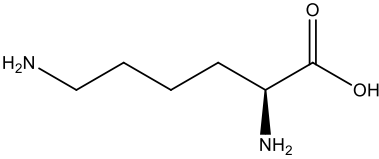
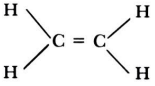
Name	Glucose	Lysine	Ethylene
Molecular structure			
Chemical formula	$C_6H_{12}O_6$	$C_6H_{14}N_2O_2$	C_2H_4
M_w (g/mol)	180.16	146.19	28.05

Figure 3. Chemical structures of some common monomers used in polymerization processes and their associated molecular weights (M_w).

1.3.1 Block copolymers

Amphiphilic polymers are those polymers that possess lyophobic and lyophilic monomers or chains (hydrophobic and hydrophilic in water) in their molecular structure. As a consequence, they can aggregate in a selective solvent, being this process dependent on the solvent employed as well as the polymer concentration, temperature, the presence of additives, etc (86). Some employed monomers can possess electrical charge, conferring the polymer a polar character that makes them water-soluble, but this also enhances their dependence with the medium properties (pH, ionic strength...) as in the case, for example, of DNA and proteins (87). Neutral polymers are those that do not bear electrical charges in their structure, being composed of non-charged monomers as, for example, ethylene oxide (EO). Aggregation properties for neutral polymers depend mainly on their affinity regarding the solvent used for their dissolution. As mentioned previously, amphiphilic polymers possess one soluble part in the chosen solvent, while the other tends to evade it; in aqueous solution this behaviour is called the hydrophobic effect.

Block copolymers are those polymers formed by two or more blocks, each block formed by the covalent bonding of the same repeating monomer. They are amphiphilic in nature because of the different affinity of the monomers that constitute each block regarding the solvent (88). Block copolymers exhibit those aggregation properties

characteristics of amphiphilic polymers and will be the main focus of the present PhD work.

There exists a critical concentration range where all amphiphilic polymers, and hence, amphiphilic block copolymers, change their state from singly dispersed molecules in solution to micellar aggregates denoted as the critical micellar concentration (CMC). Some block copolymers have also the ability to form micelles by increasing the temperature while keeping constant the copolymer concentration; this temperature is known as the critical micellar temperature (CMT) (see Figure 3). Both CMC and CMT depend on the nature and length of the copolymer blocks, solvent nature, presence of additives, and temperature much in the same way as small amphiphilic molecules do. Temperature-dependent amphiphilic polymers also exhibit a low critical solubility temperature, that appears when hydrophilic bonds start to break and hydrophobic ones become stronger and, as a consequence, water molecules are expelled from the micelle interior. Besides, some monomers are sensible to changes in the surrounding environment (pH, presence of additives, temperature...) modifying their solution behaviour as a consequence of variations in their intra- and intermolecular interactions.

Ethylene oxide is one of the most, if not the most, hydrophilic unit base to construct amphiphilic block copolymers. Common hydrophobic counterparts are ethylene, styrene, vinyl chloride, acrylonitrile, methyl methacrylate... (89). The relative hydrophobicity ratio of some different hydrophobic blocks commonly used in pharmaceutical applications has been studied previously in terms of the critical micelle concentration value of the obtained block copolymers being 1:4:5:6:10:12:12:15 for PO:L:C:BO:VL:CL:SO:G, where PO denotes propylene oxide, L lactide, C methylene, BO butylene oxide, VL valerolactone, CL caprolactone, SO styrene oxide and G glycidyl ether, respectively (90,91). Usually, the hydrophobic character of the polymer can be increased by using more hydrophobic monomers or increasing the hydrophobic/hydrophilic block ratio (90,91).

1.3.2 Block copolymers classification

The first classification for polymers which can be established is based on their origin: natural or synthetic ones. Other polymer classifications are related to the polymer chemical structure, their composition or spatial order. The simplest polymer structure is the homopolymer formed by the repetition of only one kind of monomer. Copolymers are those polymers formed by two or more different monomers. If the polymer has two or three blocks (each block formed by several repetitive monomers) is called diblock and triblock copolymer, respectively. Triblock copolymers can be formed

by two or three different monomers in each block (A-B-A or A-B-C structure). The conformation of the blocks along the chain can be alternating the sequence of monomers, or grafting the blocks (Figure 4a).








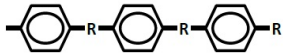

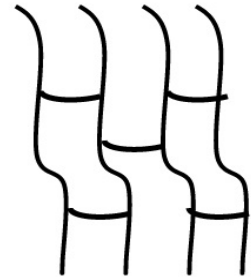
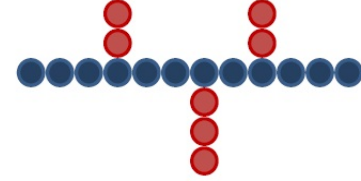
a)		b)	
Diblock copolymers		Linear	
Triblock copolymers		Branched	
Alternating copolymers		Crosslinked	
Periodic copolymers		Cyclolinear	
Statistical copolymers		Ladder	
Grafted copolymers			

Figure 4. Classification of polymers as a function of: a) the block distribution along the backbone, and b) as a function of the chain spatial conformation.

If the copolymer has no ramifications is called linear, if not it can be branched, crosslinked, cyclolinear or ladder. Non-linear copolymers are those that possess ramifications along the main backbone: Branched ones are those that have single ramifications; crosslinked ones are those whose ramifications are attached to other generating a random matrix; cyclolinear ones are those possessing cyclic compounds as ramifications; and, finally, ladder ones are those that form an ordered network joined by ramifications (see Figure 4b). Linear and branched block copolymers (depending on their composition) are usually soluble in most of solvents. Crosslinked and cyclolinear

polymers form an insoluble network (elastomers) which have the same properties as linear polymers except aqueous solubility; ladder polymers have also low solubility, but good thermal properties.

1.3.3 Block copolymer micelles

Neutral block copolymers are the main focus of the present work. Micellization of neutral block copolymers in aqueous medium is mainly driven by changes in solvation upon increasing temperature, especially for those bearing poly(ethylene oxide), PEO, as the hydrophilic block (88). Micellization of PEO-based copolymers largely depends on the chain length, architecture and composition of the blocks, temperature and the presence of additives such as cosolvents or added salts (92). As the solvent becomes poorer, the CMC decreases and the association number increases. The corresponding micellar sizes are not very temperature-dependent as a result of a compensation between the increase in association number and the decrease in the expansion of the hydrophilic block shell in the poorer solvent at high temperature. Micellization of triblock copolymers is entropically disfavoured if compared to that of diblocks (having the same block composition) due to looping either in the shell or in the core, which involves that two junctions are located at the core/shell boundary for triblocks compared to just one for a diblock one (90). This leads to larger CMC values and lower micellar aggregation numbers and sizes for triblock copolymers than for structurally related diblocks. In addition, the CMC of direct ABA triblock copolymers is lower than that of their reverse (BAB) counterparts (93). Micellization is also largely controlled by the hydrophobic block length and only slightly modified by the hydrophilic one (90). An increase in the number of hydrophilic EO units leads to a small increase in both of CMC and CMT, while an exponential decrease in CMC accompanied by important increases in both micellar size and aggregation number is observed upon changes in the hydrophobic block length (94). The enthalpy of micellization decreases to zero as the hydrophobic block length increases due to the shielding of the hydrophobic blocks from water in the unimer state, giving rise to the formation of the so-called unimolecular micelles in contrast to the interaction enthalpies of short-unit blocks, which are relatively extended in the molecular state (95).

The simplest structure that polymeric micelles can adopt is the spherical one provided that this geometry minimizes the interfacial free energy, but other shapes are also possible: elongated micelles, vesicles or lamellas. For spherical micelles, the average length of the hydrophobic block limits the attainable core volume and, hence, the final association number. This situation is reached at moderate temperatures for copolymers with lengthy hydrophobic blocks and relatively high association numbers.

Although micelles are stable at fixed conditions, their characteristics depend on the thermodynamic quality of the solvent and temperature: by increasing the polymer concentration or temperature the polymeric micellar solution could go through the following states: dispersed unimers in solution, unimolecular micelles, polymolecular micelles, micellar clusters, viscoelastic fluid (soft gel, see below) and gel (see Figure 3). The phase transition between states is gradual and there can exist an intermediate range where some states can coexist. Unimolecular micelles are composed of single polymer molecules spatially conformed in aqueous solution to avoid or reduce the contact between the hydrophobic block and the solvent. This is the first aggregation state found in block copolymers having very long hydrophilic blocks (90), but it is not found for all polymers. Polymolecular micelles are those formed by several copolymer molecules and conforms the common aggregation state for amphiphilic polymers. By increasing polymer concentration, intermicellar distances are reduced so that copolymer chains can start to act as bridges between micelles promoting cluster formation. The transition from diluted colloidal state to gel phase implies the change from sol to soft gel, that is, a viscoelastic fluid with localised very short local order. The term gel is used to mean a substance with a finite yield stress, being their storage modulus bigger than the loss modulus ($G' > G''$). The distinction between soft and hard gel relay on their rheological properties, being the soft phase a viscoelastic fluid as previously mentioned with $G' > 10$ Pa while the hard gel phase should have $G' > 1000$ Pa and a yield stress exceeding 40 Pa (92). The hard gel region is the highest structural order level that a polymer can reach in solution.

1.3.4 Polymeric micelles as drug reservoirs

Polymeric micelles as drug reservoirs have attracted much attention owing to their different structural domains (hydrophobic and hydrophilic ones). Drugs can be incorporated into the shell, into the core or into the core-shell interface. The simplest process to carry hydrophobic drugs in polymeric micelles is by exploiting drug affinity to the hydrophobic blocks forming the micellar core, while an alternative choice is by covalent attachment or complexation (97). In particular, the first method enables the incorporation of hydrophobic drug into an aqueous medium, leading to an increase in the extent of cargo solubilisation (98) as well as providing a protective environment. Although the micellization process is spontaneous, demicellisation in polymeric micelles is usually a slow process.

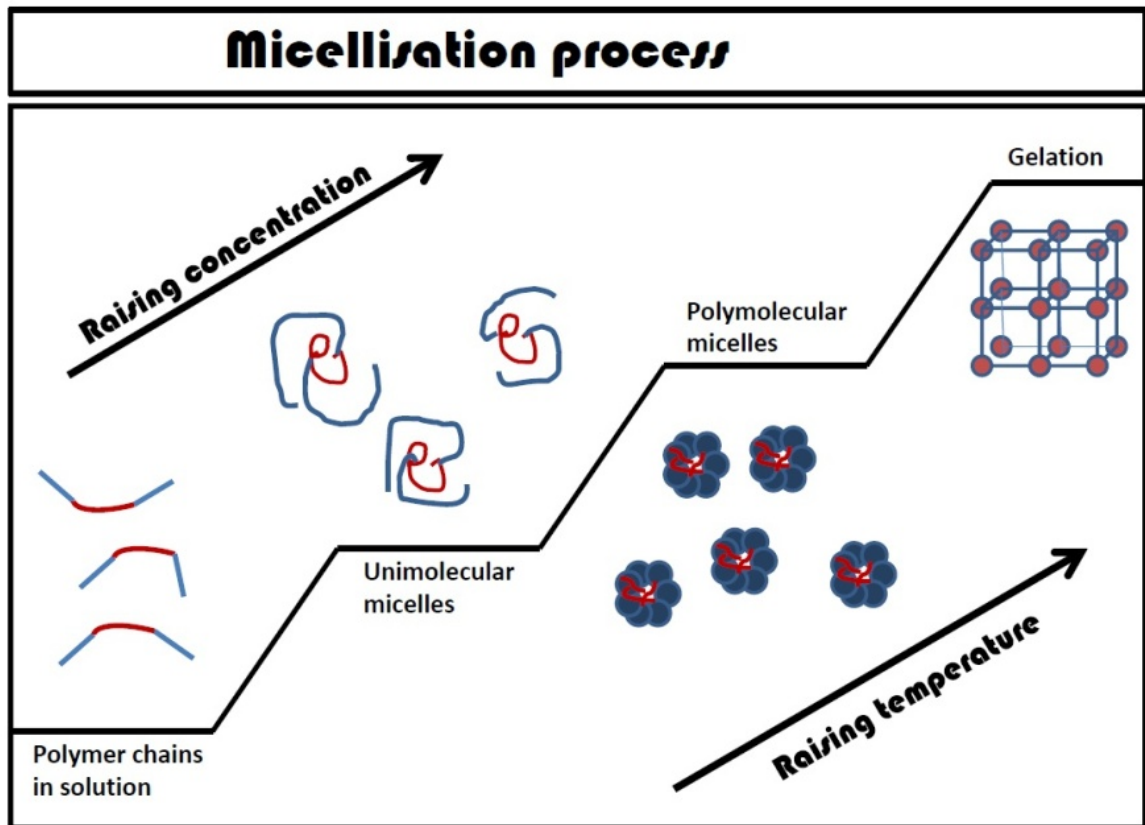


Figure 5. Polymeric aggregation process as a function of concentration or temperature. Plateau regions correspond to a unique phase, while the slopes correspond to the transition between the states, where coexistence takes place (96).

Most of copolymeric micelles already used as drug carriers in pharmaceutical devices are based on triblock copolymers (82,84,99). Since most pharmaceutical/nanomedical applications need to be performed in aqueous environments, PEO-based block copolymers have been the copolymers of choice on many drug solubilization studies (100). PEO is a water soluble polymer that provides aqueous solubility and stealthness to formed polymeric micelles, enabling long circulation times into the blood stream (88). As mentioned before, the protection of the drug from the surrounding medium is a very important constraint in drug delivery systems in order to avoid drug recognition by the reticulo-endothelial system (RES) and subsequent rapid clearance from the body, and to ensure drug chemical stability, two of the major drawbacks in drug-based therapies nowadays. Moreover, increasing the polymer concentration over the *cmc* usually involves an increase on the micelle's number in solution and, as a consequence, an increase in drug solubilisation (101). Another important feature to be considered in drug delivery is the size and surface properties of polymeric micelle carriers. These nanocarriers are in the size range of 10-100 nm, which is the optimal

window for effective treatments via intravenous injection. The particles in this size range are small enough both to evade the RES as well as penetrate in the small capillaries within the body tissues, as mentioned previously, achieving extremely long blood circulating times (102).

Once the loaded-drug polymeric micelles attain the target cell/tissue, the drug release mechanism is key in order to achieve the necessary and expected therapeutic response. Depending on copolymer composition, the release mechanism can be by diffusion through the micellar shell or by degradation and decomposition of the polymeric core; even both mechanisms can be simultaneously involved (103). The objective is to achieve a sustained drug release profile, usually characterized by an initial short burst release phase followed by a sustained release phase.

On the other hand, the excretion mechanisms of polymeric micelles largely depend on their composition and size. Biodegradable polymeric micelles are naturally decomposed in their monomeric units and subsequently excreted by renal clearance (80). The excretion mechanism for non-biodegradable ones depends on micellar size: those with smaller sizes can be also filtered off by kidney (ca. < 10n-15 nm) whilst bigger ones through the hepatobiliary system or even by RES (104,105).

A required condition polymeric micelles must fulfill to be used as drug delivery vehicles is their biocompatibility. Nowadays, the Federal Drug Administration (FDA) of USA has already approved some commercially available block copolymers that can be used in different pharmaceutical formulation in humans. Amongst them, the most widely studied and used are those composed of hydrophilic PEO blocks and hydrophobic propylene oxide (PPO) blocks, which can be classified in two families: the linear poloxamers (Pluronics[®]), and the X-shaped poloxamines (Tetronics[®]) (82,83,99).

PLURONICS are triblock copolymers whose backbone structure is formed by a central poly(propylene oxide) block (PPO) and two side PEO blocks (PEO-PPO-PEO). The commercial distribution of PLURONICS in a broad range of molecular weights makes them one of the most studied copolymers as drug nanocarriers (83,99). They are commercially available, for example from BASF in a broad range of block lengths: from 16 to 60 units for the inner PPO block, and from 6 to 265 for the hydrophilic PEO blocks (106,107). Their biocompatibility in different cellular lines has been proved for some of them, as PLURONIC F127 and F68 (83,99,108), as well as their ability to encapsulate many different drugs (for example, griseofulvin, doxorubicin or docetaxel) (83,84,109). Some PEO-PPO block copolymers have already entered clinical trials. For example, SP1049C (Supratek Pharma Inc., Montreal, Canada), a doxorubicin (DOXO)-loaded mixed micellar polymeric system composed of the hydrophobic Pluronic L61 and the

hydrophilic Pluronic F127, has successfully undergone phase I and II clinical trials, recently entered phase III studies and has been also granted orphan drug designation by the FDA for the treatment of oesophageal and gastric cancer (110). Nevertheless, Pluronic block copolymers also present some disadvantages as variation in their micellization behaviour from batch to batch (111) or an incomplete micellization of the unimers which could derive in other self-assembled structures but possessing different properties.

This thesis is focused on linear block copolymers owing to their outstanding self-assembly properties in aqueous solution. Bearing in mind the successful previous results obtained using Pluronic micelles as drug delivery vehicles but also their inherent drawbacks and limitations, several linear more hydrophobic block copolymers are going to be tested in order to evaluate from their aggregation properties to their cytotoxicity, going through their encapsulation efficiency and solution biostability with the objective of achieving more efficient block copolymer-based drug nanocarriers. Next chapters will go into detail in the types and properties of these deep new drug delivery vehicles.

1.3.5 References

78. Riess, G. *Prog. Polym. Sci.* **2003**, *28*, 1107.
79. Tanford, C. *The Hydrophobic Effect: Formation of Micelles and Biological Membranes*. 1980, New York: John Wiley & Sons.
80. Torchilin, V.P. *Nanoparticulates as Drug Carriers*. 2006, vol. 697.
81. Taboada, P.; Velasquez, G.; Barbosa, S.; Castelletto, V.; Nixon, S. K.; Yang, Z.; Heatley, F.; Hamley, I.W.; Ashford, M.; Mosquera, V. *Langmuir*, **2005**, *21*, 5263.
82. Alvarez-Lorenzo, C.; Sosnik, A.; Concheiro, A. *Curr. Drug Targets*, **2011**, *12*, 1112.
83. Batrakova, E.V.; Kabanov, A.V. *J. Controlled Release*, **2008**, *130*, 98.
84. Elsabahy, M.; Perron, M.-E.; Bertrand, N.; Yu, G.; Leroux, J.-C. *Biomacromolecules*, **2007**, *8*, 2250.
85. Ribeiro, M.E., Cavalcante, I. M.; Ricardo, N. M. P. S.; Mai, S.-M.; Attwood, D.; Yeates, Stephen G.; Booth, C. *Int. J. Pharm.*, **2009**, *369*, 196.
86. Hamley, I.W., *The Physics of Block Copolymers*. Oxford Science Publications. 1998, Oxford: Oxford University Press.
87. Hollander, F., *Charged Polymers*, in *Random Polymers*. 2009, Springer Berlin Heidelberg.
88. Alexandridis, P.; Lindman, B. *Amphiphilic Block Copolymers. Self-Assembly and Applications*. 2000, Amsterdam: Elsevier.
89. Hiemenz, P.C. *Polymer Chemistry: The Basic Concepts*. 1984, New York: M. Dekker.
90. Booth, C.; Attwood, D.; Price, C. *Phys. Chem. Chem. Phys.* **2006**, *8*, 3612.

91. Attwood, D.; Booth, C.; Yeates, S.G.; Chaibundit, C.; Ricardo, N.M.P.S. *Int. J. Pharm.* **2007**, 345, 35.
92. Hamley, I.W., *Block Copolymers in Solution: Fundamentals and Applications*. 2005, Chichester, England: John Wiley & Sons.
93. Yang, Y.-W.; Yang, Z.; Zhou, Z.-K.; Attwood, D.; Booth, C. *Macromolecules*, **1996**, 29, 670.
94. Nace, V.M., *Nonionic Surfactants: Polyoxyalkylene Block Copolymers*. Surfactant Science Series. 1996, New York: Marcel Dekker.
95. Booth, C.;Attwood, D. *Macromol. Rapid Commun.* **2000**, 21, 501.
96. Chiappetta, D.A.; Sosnik, A. *Eur. J. Pharm. Biopharm.* **2007**, 66, 303.
97. Croy, S.R.; Kwon, G.S; *Polymeric Micelles for Drug Delivery*. *Curr. Pharm. Des.* **2006**, 12, 4669.
98. Hurter, P.N.; Hatton, T.A. *Langmuir*, **1992**, 8, 1291.
99. Kabanov, A.V.; Alakhov, V.Y. *Crit. Rev. Ther. Drug Carrier Syst.* **2002**, 19, 1.
100. Tarcha , P.J. *Polymers for Controlled Drug Delivery*. 1991, CRC Press, Boca Raton.
101. Hadjichristidis, N.; Pispas, S.; Floudas, G. *Block Copolymers Synthetic Strategies, Physical Properties and Applications*. 2003, John Wiley & Sons.
102. Heidel, J.; Davis, M. *Pharm. Res.* **2011**, 28, 187.
103. Frisch, H.L. *J. Appl. Polym. Sci.* **1970**, 14, 1657.
104. De Jong W.H.; Hagens, W.I.; Krystek, P.; Burger, M.C.; Sips, A. J. A. M.; Geertsma, R. E. *Biomaterials* **2008**, 29, 1912.
105. Neuberger, T.; Schoepf, B.; Hofmann, H.; Hofmann, M.; Von Rechenberg, B. J. *Magn. Mater.* **2005**, 293, 483.
106. Batrakova, E.V.; Li, Shu; A.; Valery Y.; Miller, D.W.; Kabanov, A.V. *J. Pharmacol. Exp. Ther.* **2003**, 304, 845.
107. <http://worldaccount.basf.com/wa/Startpage>
108. Krupka, T.M.; Exner, A.A. *Int. J. Hyperthermia*, **2011**, 27, 663.
109. Wei, Z.; Hao, J.; Yuan, S.; Li, Y.; Wu, J.; Sha, X.; Fang, X. *Int. J. Pharm.* **2009**, 376, 176.
110. <http://www.supratek.com/rd/publications>
111. Yu, G.-E.; Altinok, H.; Nixon, S. K.; Booth, C.; Alexandridis, P.; Hatton, T. A. *Eur. Polym. J.* **1997**, 33, 673.

CHAPTER 2

$\text{EO}_m\text{SO}_n\text{EO}_m$ COPOLYMERS AS NANOCARRIERS OF HYDROPHOBIC DRUGS

2.1 AIM OF THE WORK

Styrene oxide (PSO)-based block copolymers are of particular interest as a consequence of their wide availability of architectures and molecular weights (1), their ability to self-assemble at very low concentrations into micelles of various shapes depending on relative block lengths (2,3), and their low glass transition temperatures (ca. 40 °C), which enables the incorporation of drugs at temperatures that are compatible with thermolabile agents (4,5). Despite the micellization process and solubilisation ability of some PSO-based block copolymers have been previously studied (5-11) and some of these copolymers are already commercially available from Goldschmidt AG, as far as we know only one study about diblock copolymers of styrene oxide and ethylene oxide (PSO-PEO) copolymer micelles as carriers of an anticancer drug (docetaxel) against tumour prostate cancer cells has been reported (12). Moreover, in contrast to the well-demonstrated inhibitory activity of several Pluronics® block copolymers against drug efflux transporters overexpressed in MDR cells and the subsequent bioavailability enhancement of their substrates in different tissues and organs (13-15), no reports are available about the potential capabilities of PSO-based copolymers as efflux-pump inhibitors. Therefore, the potential capability of this class of copolymers as potential P-glycoprotein efflux pump inhibitors to enhance drug accumulation in the NCI-ADR-RES which overexpressed P-glycoprotein is tested in this work for the first time, and compared to that observed for other types of PEO-based block copolymers, especially Pluronics®.

2.1.1 Aim of the work

In the present work, we report on the synthesis and characterization of the self-assembly properties of two new triblock PEO-PSO copolymers (see Figure 2), $EO_{33}SO_{14}EO_{33}$ and $EO_{38}SO_{10}EO_{38}$, where the subscripts denotes the block lengths.

2.1.2 Methodology

Physico-chemical characterization was performed by means of fluorescence spectroscopy, light scattering, transmission electron microscopy (TEM), confocal microscopy and rheometry. The triblock structure was selected for comparison with those data previously obtained for other triblock PEO-PPO-based block copolymers.

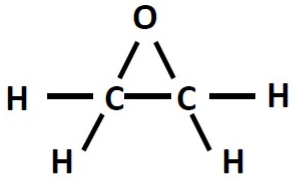
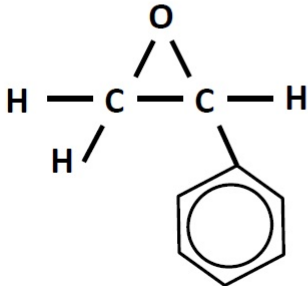
	$\text{OH} - \left[\text{C} - \text{C} \right]_n \text{OH}$
Ethylene oxide	Poly ethylene oxide
	$\text{OH} - \left[\text{C} - \text{C} \right]_n \text{OH}$
Styrene oxide	Poly styrene oxide

Figure 1. Constituent monomers of PEO-PSO-PEO block copolymers.

The aim of this work is to assess the ability of copolymers $\text{EO}_{33}\text{SO}_{14}\text{EO}_{33}$ and $\text{EO}_{38}\text{SO}_{10}\text{EO}_{38}$ to dissolve and chemically protect different hydrophobic drugs, evaluating: a) the colloidal stability of the drug-loaded polymer micelles, b) the drug release profile, c) the safety of the polymeric nanocarrier, and d) the *in vitro* efficacy as an antifungal/antitumor formulation. The EO/SO ratio (~ 1.5) and the block lengths of both block copolymers were selected with the objective of attaining an optimal compromise between chain solubility, micelle formation ability, and core size that leads to an enhanced drug solubility [16]. Previous studies have shown that shorter PEO blocks, as those of $\text{EO}_{10}\text{SO}_{10}\text{EO}_{10}$ copolymer, lead to reduced polymeric chain solubility (4), and longer hydrophobic blocks compromise copolymer solubility (3, 17). Conversely, longer PEO blocks and shorter PSO blocks may lead to larger cmc with i) the subsequent increase in material expense to form micelles able to solubilise the required amount of drug, and ii) the existence of possible adverse side effects due to an excess of polymer accumulated on cells/tissues (1). Triblock copolymers $\text{EO}_{33}\text{SO}_{14}\text{EO}_{33}$ and $\text{EO}_{38}\text{SO}_{10}\text{EO}_{38}$ may also enable to elucidate the possible influence of copolymer architecture in the solubilization and controlled release abilities by comparison with experimental data previously reported by Elsabathy *et al.* (12) for PEO-PSO diblock copolymers.

In summary, in this work two triblock copolymers have been designed and

synthesized to improve their drug solubility properties in the micellar range. These copolymers were physico-chemically characterized elucidating their structural composition, block length and purity (by means of the polydispersity index). Their behaviour in aqueous solution was tested in a broad range of concentrations in order to clearly define the micellar/gel regions and the properties that exhibit each copolymer in each state. In this regard, micellar parameters revealed the shape, size and aggregation number of the formed polymeric micelles, while the analysis of physical gels reported valuable information on their rheological properties and enable the construction of their corresponding phase diagrams. Once the physico-chemical behaviour of the block copolymers polymers was determined, their capability as drug reservoirs for two different drugs were studied, the antifungal compound griseofulvin and the anticancer drug doxorubicin. Spherical micelles were obtained in aqueous solution, having a highly hydrophobic core and a PEO shell. The PEO shell is expected to minimise the recognition by the RES in the blood stream, while the PSO core is expected to increase the drug entrapment respect Pluronic micelles owned to the higher affinity to hydrophobic drugs. The entrapment efficiency for these drugs was tested for both copolymers, as well as the drug loading capacity. Colloidal stability and release rates of the cargo from micelles into different buffer media were also performed in vitro, to mimic the different pH medium the system should go through. Stability test should permit to elucidate the drug release mechanism. Cellular toxicity and bioavailability were studied for empty and drug-loaded micelles in cell culture. Finally, the capability of both copolymers as potential P-glycoprotein efflux pump inhibitors to enhance drug accumulation in an ovarian MDR NCI-ADR/RES cell line was tested and compared to that observed for other different block copolymers.

2.1.3 References

1. Booth, C.; Attwood, D.; Price, C. *Phys. Chem. Chem. Phys.* **2006**, *8*, 3612.
2. Castro, E.; Barbosa S.; Juarez J.; Taboada P.; Katime I. A; Mosquera V. J. *Phys. Chem. B*, **2008**, *112*, 5296.
3. Juárez, J.; Taboada, P.; Valdez, M.A.; Mosquera, V. *Langmuir*, **2008**, *24*, 7107.
4. Crothers, M.; Zhou, Z.; Ricardo, N.M.P.S.; Yang, Z.; Taboada, P.; Chaibundit, C.; Attwood, D.; Booth, C. *Int. J. Pharm.* **2005**, *293*, 91.
5. Zhou, N.; Lodge, T.P.; Bates, F.S. *J. Phys. Chem. B*, **2006**, *110*, 3979.
6. Kabanov, A.V.; Alakhov, V.Y. *Crit. Rev. Ther. Drug Carrier Syst.* **2002**, *19*, 1.
7. Ribeiro, M.E.N.P.; Vieira, I.G.P.; Cavalcante, I.M.; Ricardo, N.M.P.S.; Attwood, D.; Yeates, S.G.; Booth, C. *Int. J. Pharm.* **2009**, *378*, 211.
8. Yang, Z.; Crothers, M.; Ricardo, N.M.P.S.; Chaibundit, C.; Taboada, P.; Mosquera, V.; Kellarakis, A.s; Havredaki, V.; Martini, L.; Valder, C. *Langmuir* **2003**, *19*, 943.
9. Yang, Z.; Crothers, M.; Attwood, D.; Collett, J.H.; Ricardo, N.M.P.S.; Martini, L. G.A.; Booth, C. *J. Colloid Interface Sci.* **2003**, *263*, 312

10. Chaibundit, C.; Ricardo, N.M.P.S.; Crothers, M.; Booth, C. *Langmuir* **2002**, *18*, 4277.
11. Crothers, M.; Ricardo, N.M.P.S.; Heatley, F.; Nixon, S.K.; Attwood, D.; Booth, C. *Int. J. Pharm.* **2008**, *358*, 303.
12. Elsabahy, M.; Perron, M.-E.; Bertrand, N.; Yu, G.; Leroux, J.-C. *Biomacromolecules*, **2007**, *8*, 2250.
13. Batrakova, E.V.; Kabanov, A.V. *J. Controlled Release*, **2008**, *130*, 98.
14. Kabanov, A.V.; Batrakova, E.V.; Alakhov, V.Y. *Adv. Drug Deliv. Rev.* **2002**, *54*, 759.
15. Alvarez-Lorenzo, C.; Rey-Rico, A.; Brea, J.; Loza, M. I.; Concheiro, A.; Sosnik, A. *Nanomedicine*, **2010**, *5*, 1371.
16. Yamamoto, Y.; Nagasaki, Y.; Kato, Y.; Sugiyama, Y.; Kataoka, K. *J. Controlled Release*, **2001**, *77*, 27.
17. Taboada, P.; Velasquez, G.; Barbosa, S.; Castelletto, V.; Nixon, S. K.; Yang, Z.; Heatley, F.; Hamley, I.W.; Ashford, M.; Mosquera, V. *Langmuir* **2005**, *21*, 5263.

2.2 POLY (ETHYLENE OXIDE) - POLY (STYRENE OXIDE) – POLY(ETHYLENE OXIDE) COPOLYMERS: MICELLIZATION, DRUG SOLUBILISATION AND GELLING FEATURES

2.2.1 Abstract

Two new poly(ethylene oxide)-poly(styrene oxide) triblock copolymers (PEO-PSO-PEO) with optimised block lengths selected on the basis of previous studies were synthesized with the aim of achieving a maximal solubilisation ability and a suitable sustained release, while keeping very low material expense and excellent aqueous copolymer solubility. The self-assembling and gelling properties of these copolymers were characterized by means of light scattering, fluorescence spectroscopy, transmission electron microscopy and rheometry. Both copolymers formed spherical micelles (12-14 nm) at very low concentrations. At larger concentration (> 25 wt%), copolymer solutions showed a rich phase behavior, with the appearance of two types of rheologically active (more viscous) fluids and of physical gels depending on solution temperature and concentration. The copolymer behaved notably different despite their relatively similar block lengths. The ability of the polymeric micellar solutions to solubilize the antifungal drug griseofulvin was evaluated and compared to that reported for other structurally-related block copolymers. Drug solubilization values up to 55 mg g⁻¹ were achieved, which are greater than those obtained by previously analyzed poly(ethylene oxide)-poly(styrene oxide), poly(ethylene oxide)-poly(butylene oxide), and poly(ethylene oxide)-poly(propylene oxide) block copolymers. The results indicate that the selected SO/EO ratio and copolymer block lengths were optimal for simultaneously achieving low critical micelle concentrations (cmc) values and large drug encapsulation ability. The amount of drug released from the polymeric micelles was larger at pH 7.4 than at acidic conditions, although still sustained over 1 day.

2.2.2 Introduction

Advances in materials science and nanotechnology offer novel approaches to address formulation issues and to regulate drug biodistribution and release patterns (1,2). Block or graft-copolymers consisting of hydrophilic and lipophilic domains are able to form polymeric micelles and nanocompartmentalized particles, via self-assembly in an aqueous environment, that exhibit a long circulation half-life due to the stabilization

provided by the hydrophilic shell. These core-shell-type nanostructures are particularly suitable to host poorly-soluble drugs and to target them to the required tissue or cells (3-9). As a consequence, the local drug bioavailability and the safety of the treatment are improved (10-12).

Probably, the most widely studied amphiphilic triblock copolymers are those composed of hydrophilic PEO blocks and hydrophobic propylene oxide (PPO) blocks, which can be classified in two families: the linear poloxamers (Pluronic[®]), and the X-shaped poloxamines (Tetronic[®]) (13-16). The reasons for their popularity can be summarized in: i) commercial availability in a very broad range of compositions (i.e., a wide variety of molecular weights, block lengths and PEO/PPO ratios); ii) proven solubilization capacity and sustained drug release; iii) high biocompatibility of most varieties; iv) enhancement of drug transport across cellular barriers; and v) approval of some varieties by US FDA and EMA to be used in pharmaceutical formulations and medical devices (13-16). Nevertheless, PEO–PPO block copolymers still present a number of limitations that could curtail their application, such as i) limited stability of the self-assembled nanostructures upon dilution in the bloodstream, particularly for derivatives with high EO/PO ratios, ii) incomplete micellization of the unimers, and iii) variability from batch to batch in micellar sizes, drug delivery capacities and release profiles.

To overcome some of these limitations, more hydrophobic block copolymer counterparts with similar architecture, but with the PPO segment replaced by a more hydrophobic one, such as poly(butylene oxide) (PBO), poly(styrene oxide) (PSO) or phenylglycidyl ether (PG), have been developed by the Attwood and Booth's group in collaboration with us during last years (17-21). Polystyrene oxide-based block copolymers are of particular interest due to i) their ability to self-assemble at very low concentrations into micelles with improved solubilization ability and stability (22-23) and ii) the low glass transition temperatures (ca. 40 °C) of the core-forming block, which enables the incorporation of drugs at temperatures that are compatible with thermolabile agents (22,24-25). In general, triblock PSO-based block copolymers show larger solubilization capacity of hydrophobic drugs if compared to commercially available Pluronic[®] or Tetronic[®] copolymers thanks to their more hydrophobic cores, although such an enhancement depends on copolymer structure, block length ratios, micellar shape and drug affinity for the block-forming micellar core (18,22-23). Some of these factors are also key in providing suitable polymeric chain solubility and stability; in fact, when designing styrene-oxide copolymers for enhancing drug solubility by increasing/decreasing the length of the hydrophobic/hydrophilic block, the copolymer chain solubility, the micelle stability and/or the drug solubilization capacity have been found to be compromised (18,24). Shorter EO and longer SO block lengths typically have led to reduced polymeric chain solubility, whereas copolymers with longer EO blocks

and/or very short SO block self-assemble at high concentrations and form micelles with lower drug entrapment abilities (20).

In the present work we report on the synthesis, the characterization of the self-assembling properties, and the drug solubilization and release profiles of two new triblock PEO-PSO copolymers, $\text{EO}_{33}\text{SO}_{14}\text{EO}_{33}$ and $\text{EO}_{38}\text{SO}_{10}\text{EO}_{38}$ (the subscripts denoting the block lengths) using fluorescence spectroscopy, light scattering, transmission electron microscopy (TEM) and rheometry. The main goals of the present work were to target optimized block lengths and hydrophilic/hydrophobic block molar ratios of the copolymers on the basis of previous studies to simultaneously achieve a compromise between polymer chain solubility and micelle formation at very low copolymer concentrations; and to study the effect of subtle differences on the copolymer block lengths to obtain a micellar core with a suitable size for hosting great amounts of a poorly-soluble drug such as the antifungal griseofulvin, used as a model for comparison purposes with other block copolymer structures. The micellar systems based on $\text{EO}_{33}\text{SO}_{14}\text{EO}_{33}$ and $\text{EO}_{38}\text{SO}_{10}\text{EO}_{38}$ block copolymers largely reach these goals, improving griseofulvin encapsulation and release. Hence, these results prove the potential benefits of this class of copolymers as components of drug delivery systems improving the performance of Pluronic and Tetronic block copolymers, while exhibiting the biocompatibility, cytocompatibility and capacity of inhibiting efflux pumps of the latter (26).

2.2.3 Experimental section

2.2.3.1 Materials

$\text{EO}_{33}\text{SO}_{14}\text{EO}_{33}$ and $\text{EO}_{38}\text{SO}_{10}\text{EO}_{38}$ copolymers were synthesized as previously described (27,28). Briefly, high vacuum and ampule techniques were used to eliminate unwanted moisture. Initiation of the bifunctional precursor was potassium hydroxide and 1,2-butanediol partly in the form of its potassium salt. The mole ratio OH/OK was ~ 9 , this being chosen to achieve a suitable polymerization rate. The monomers were distilled and dried immediately before use. Styrene oxide was added to the ampule by syringe, and for the second stage of polymerization, ethylene oxide was distilled through the vacuum line. The polymerization of styrene oxide at 85 °C was slow, taking as long as 8 weeks. Weight-averaged (M_w) to number-averaged (M_n) molecular weight ratios were determined at 25°C using a Waters gel permeation chromatography (GPC) system equipped with a 1515 isocratic pump and a 2410 refractive index detector (Waters, Milford, MA). Chloroform was used as the eluent, and monodisperse PEO was employed as standard. M_n values were estimated from ^1H NMR spectra recorded on a Bruker ARX400 spectrometer (Bruker, Milton, ON, Canada) in deuterated chloroform. Table 1 summarises the molecular characteristics of both copolymers. Water was

double distilled and degassed before use. Pyrene and griseofulvin were from Sigma-Aldrich.

Table 1. Molecular characteristics of the copolymers.

Polymer	M_n /g mol ⁻¹ (NMR)	wt % SO (NMR)	M_w/M_n (GPC)	M_w /g mol ⁻¹
EO ₃₃ SO ₁₄ EO ₃₃	4790	40.0	1.01	4850
EO ₃₈ SO ₁₀ EO ₃₈	5055	34.1	1.02	5130

Estimated uncertainty: M_n to ± 3 %; wt% S to ± 1 %, M_w/M_n to ± 0.01 . M_w calculated from M_n and M_w/M_n .

2.2.3.2 Methods

a. Characterization of block copolymer micelles

a1. Fluorescence measurements: Values of cmc were obtained from pyrene fluorescence measurements at 37 ± 0.1 °C (Cary Eclipse fluorescence spectrophotometer, Agilent., Germany) as described by Lee *et al.* (29). Stock solutions were prepared by dissolving the copolymers in water for 24 h before being diluted to the desired concentrations within the range 1-50 g dm⁻³. Pyrene dissolved in acetone was added to the copolymer solution and, after acetone evaporation, was allowed for equilibration during 24 h. The final copolymer solution contained 3×10^{-7} M pyrene. The fluorescence spectrum ($\lambda_{exc} = 335$ nm) was the average of three scans and was corrected for scattering using an equivalent blank solution before determining the ratio I_1/I_3 of the first and third vibronic peaks. Reproducibility was better than 2 %.

a2. Dynamic and static light scattering measurements: DLS and SLS intensities were measured at 37 °C by means of an ALV-5000F (ALV-GmbH, Germany) instrument with vertically polarized incident light ($\lambda = 488$ nm) supplied by a diode- pumped Nd:YAG solid-state laser (Coherent Inc., CA, USA) and operated at 2 W, and combined with an ALV SP-86 digital correlator with a sampling time of 25 ns to 100 ms (for DLS). The intensity scale was calibrated against scattering from toluene. Measurements were made at a scattering angle $\theta = 90^\circ$ to the incident beam, as appropriate for particles smaller than the light wavelength. Solutions were filtered through Millipore Millex filters (Triton free, 0.22 μ m porosity) directly into cleaned scattering cells and let to equilibrate at 37°C for 30 min before measurement. Experiment duration was in the range 5-10 min, and each experiment was repeated at least two times. The correlation functions from DLS runs were analyzed by the CONTIN method to obtain the intensity distributions of decay rates (Γ) (30). From the decay rate distributions the apparent diffusion coefficients ($D_{app} = \Gamma/q^2$, $q = (4\pi n_s/\lambda)\sin(\theta/2)$) were derived, being n_s the refractive index of solvent. Values of the apparent hydrodynamic radius ($r_{h,app}$, radius of

the hydrodynamically equivalent hard sphere corresponding to D_{app}) were calculated from the Stokes-Einstein equation

$$r_{h,app} = kT/(6\pi\eta D_{app}) \quad (1)$$

where k is the Boltzmann constant and η is the coefficient of viscosity of water at temperature T .

Static light scattering data were analysed in terms of scattering theory for hard spheres (31-33) whereby the interparticle structure factor (S) in the equation

$$K^*c/(I-I_s) = 1/S M_w \quad (2)$$

was approximated by

$$1/S = [(1 + 2\phi)^2 - \phi^2(4\phi - \phi^2)] (1 - \phi)^{-4} \quad (3)$$

where ϕ is the volume fraction of equivalent uniform spheres, I is the light scattering intensity from solution relative to that from toluene, I_s is the corresponding quantity for the solvent, c is the concentration (in g dm⁻³), M_w is the mass-average molar mass of the solute, and K^* is the appropriate optical constant which includes the specific refractive index increment, $dn/dc = 0.134 + 0.067w_s$, where w_s is the weight fraction of SO (27). Other quantities used were the Rayleigh ratio of toluene for vertically polarized light, $R_v = 2.57 \cdot 10^{-5}[1 + 3.68 \cdot 10^{-3}(t-25)]$ cm⁻¹ (t in °C) and the refractive index of toluene, $n = 1.4969[1 - 5.7 \cdot 10^{-4}(t-20)]$ (34-36). Values of ϕ were conveniently calculated by applying a thermodynamic expansion factor $\delta_t = v_t/v_a$, where v_t is the thermodynamic volume of a micelle (*i.e.* one of eighth of the volume, u , excluded by one micelle to another) and v_a is the anhydrous volume of a micelle ($v_a = M_w/N_A\rho_a$, where N_A is Avogadro's constant and ρ_a is the liquid density of the copolymer solute calculated assuming mass additivity of specific volumes) (37,38). The method is equivalent to using the virial expansion for the structure factor of effective hard spheres taken to its seventh term but requires just two adjustable parameters, *i.e.* M_w and ρ_t .

a3. Transmission electron microscopy (TEM): A drop of copolymer solution (0.2 wt% filtered through 0.2 μ m pore membrane) was placed on a copper grid and stained with 2% (v/v) of phosphotungstic acid. After drying, electron micrographs of the sample were recorded with a Phillips CM-12 electron microscope.

a4. Clouding and gel formation: Aqueous solutions of the copolymers at 10-80 wt % were prepared in tubes (10 mm in diameter, 0.5 cm³) and stored at 4°C. The tubes were immersed in a water bath and heated at 0.2 °C min⁻¹ from 5 to 90 °C. Clouding was detected by the naked eye. The tubes were inverted to check gel formation at 1 min intervals.

a5. *Rheometry*: Frequency scans of storage (G') and loss (G'') moduli of copolymer solutions at various temperatures were recorded using a controlled stress ARG2 rheometer (TA instruments, USA) fitted with a water bath temperature control and a cone-and-plate geometry (20 or 60 mm diameter at an angle of 1°). A solvent trap maintained a water-saturated atmosphere around the sample. The experiments were carried out in oscillatory shear mode, with the strain amplitude (A) maintained at a low value ($A < 0.5\%$) by means of the autostress facility of the software. This ensured that measurements of G' and G'' were in the linear viscoelastic region. Temperature scans were recorded from 5 to 95 °C (0.5°C/min) at 1 Hz. Measurements on solutions of low modulus ($G' = 1\text{--}10$ Pa), which fell outside the range for satisfactory autostress feedback, were rejected.

b. *Griseofulvin solubilisation*

Solubilisation of griseofulvin (solubility in water $< 10\text{ mg dm}^{-3}$ disregarding pH value (38)) in micellar copolymer solutions was tested in triplicate, as previously reported (17,38). Griseofulvin was chosen since it has been widely used as a comparative standard for solubilisation by many laboratories (6,22,38,39). Briefly, drug was added in excess to 0.2 wt% copolymer solution and the systems were kept under magnetic stirring at 37 °C for 3–5 days and then filtered (Millipore, 0.45 μm). The filtered solutions were diluted ca. 1000-times with methanol to disrupt the self-assembled structures, the amount of water after dilution being low enough to allow direct use of the calibration plot obtained in methanol. The amount of griseofulvin solubilised was determined by recording the absorbance at 292 nm (Cary 50 UV-Vis spectrophotometer, Agilent, Germany). Copolymer solutions at the same dilution were used as a blank. The method has been previously checked against analyses using NMR spectroscopy and, more recently, liquid chromatography (22). In order to check that solubilisation was predominantly in the core rather than in the EO-block corona, drug solubilisation in 5–30 wt% aqueous solutions of polyethylene glycol (M_n 6000 g mol^{-1}) was determined (22). Only residual solubilisation in the corona was found.

Drug loaded, D.L., and entrapment efficiency, E.E., of copolymer solutions were calculated as follows:

$$D.L.\% = \frac{\text{weight of the drug in micellar solution}}{\text{weight of polymer + drug}} \times 100\% \quad (4)$$

$$E.E.\% = \frac{\text{weight of the drug in micellar solution}}{\text{weight of feeding drug}} \times 100\% \quad (5)$$

The solubilisation capacity per gram of copolymer in solution (S_{CP}) was calculated as the amount of drug dissolved at 37 °C in 100 cm^3 of solution in excess of that dissolved in an equivalent volume of water.

c. In vitro griseofulvin release

Aliquots (4 mL) of griseofulvin-containing micellar systems (0.2 wt % copolymer in 0.01 M phosphate buffer pH 7.4, 0.01 M sodium citrate buffer pH 5.5 and 0.01 M acetic acid-sodium acetate buffer pH 4.0) were placed into dialysis tubes (SpectraPore®, MWCO 3500) that were immersed into the corresponding buffer (500 mL) at 37°C. The medium was replaced every 6 hours in order to maintain sink conditions. The drug concentration in the micellar solution (i.e., inside the dialysis bag) was UV-spectrophotometrically monitored at 292 nm over time by removing a small volume (20 µL) that was diluted in methanol in order to fit the calibration curve range (see above). Assays were carried out in triplicate.

2.2.4 Results and discussion

2.2.4.1 Characterization of the copolymer micelles

Steady-state pyrene fluorescence measurements were performed at 37 °C to estimate the cmc of $\text{EO}_{33}\text{SO}_{14}\text{EO}_{33}$ and $\text{EO}_{38}\text{SO}_{10}\text{EO}_{38}$ in water (Figure 1). Linear fitting of the two regions observed when the normalized I_1/I_3 pyrene fluorescence intensity ratio starts to abruptly decrease led to cmc values of $2.5 \cdot 10^{-3}$ and $3.7 \cdot 10^{-3}$ wt% for $\text{EO}_{33}\text{SO}_{14}\text{EO}_{33}$ and $\text{EO}_{38}\text{SO}_{10}\text{EO}_{38}$, respectively. The lower cmc of $\text{EO}_{33}\text{SO}_{14}\text{EO}_{33}$ can be attributed to the slightly longer hydrophobic block. The cmc values are in good agreement with those previously obtained for other EO/SO block copolymers (21) (see Figure S1).

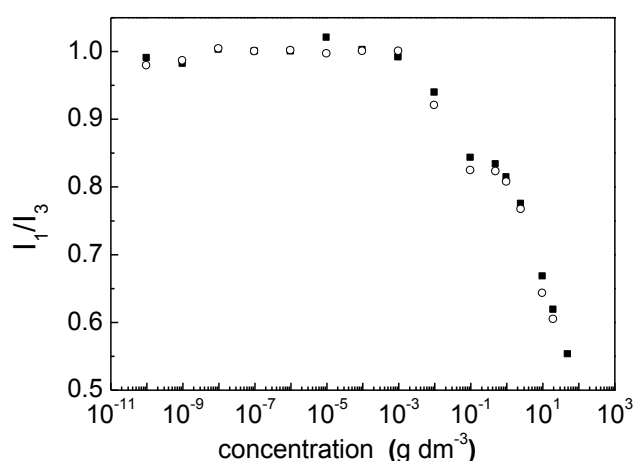


Figure 1: Dependence of the ratio of the first to third vibronic peaks of pyrene on the copolymer concentration for $\text{EO}_{33}\text{SO}_{14}\text{EO}_{33}$ (○) and $\text{EO}_{38}\text{SO}_{10}\text{EO}_{38}$ (■). Intensity data have been normalized to unity.

DLS and SLS measurements were performed at 37 °C for 1-9 % wt copolymer solutions to characterize the size and shape of the micelles. For both copolymers intensity fraction distributions of $\log r_{h,app}$ obtained by DLS (Figure 2a) were single narrow peaks indicative of a closed association process, and similar to those found previously for other EO/SO copolymers (27,28). The intercepts at $c=0$ of the linear plots of the reciprocal of $r_{h,app}$ vs. concentration (Figure 2b) allowed the determination of the micellar hydrodynamic radius, r_h , values (Table 2), which resulted to be very similar for both copolymers. Nearly spherical micelles were observed by TEM, as expected from the length of the theoretical stretched copolymer chains (see Supporting Information for details), whose diameters are in fair agreement with those obtained from DLS data, despite the usual shell dehydration and subsequent shrinking of the polymer structure upon solvent evaporation during TEM sample preparation (Figure 2c). It is worth noting that DLS gives an average size estimation, which is biased towards the larger-size elements of the population distribution. The sizes close to 10-20 nm and the external pegylated shell of $\text{EO}_{33}\text{SO}_{14}\text{EO}_{33}$ and $\text{EO}_{38}\text{SO}_{10}\text{EO}_{38}$ micelles should ensure their long systemic circulation and evasion from the reticulo-endothelial system (RES) (39).

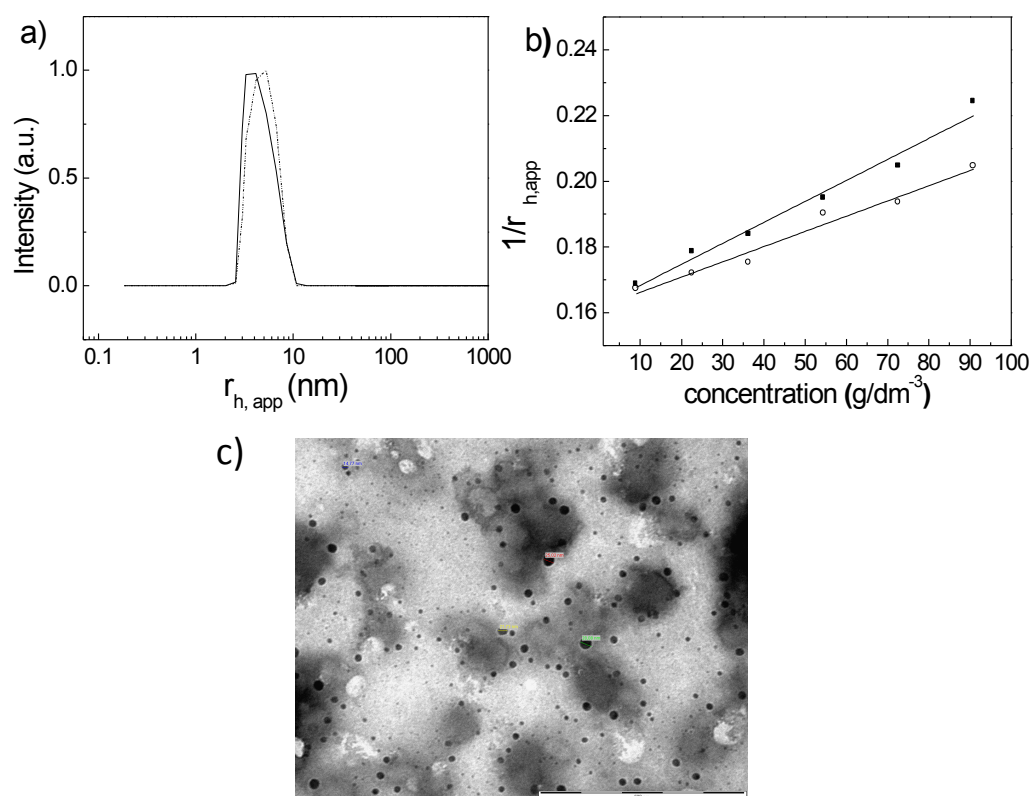


Figure 2: a) Intensity fraction size distributions of $\text{EO}_{33}\text{SO}_{14}\text{EO}_{33}$ (–) and $\text{EO}_{38}\text{SO}_{10}\text{EO}_{38}$ (····) at a concentration of 90 g dm^{-3} and 37 °C; b) plots of the reciprocal of the intensity average of $r_{h,app}$ (by using the Stokes-Einstein relation) for $\text{EO}_{33}\text{SO}_{14}\text{EO}_{33}$ (○) and $\text{EO}_{38}\text{SO}_{10}\text{EO}_{38}$ (■); c) TEM image of $\text{EO}_{38}\text{SO}_{10}\text{EO}_{38}$ micelles .

The SLS analysis data of the micellar solutions (angular dissymmetry factor, I_{45}/I_{135} , was 1.03 or less, which involves a small intraparticle scattering factor and, hence, a correction factor of r_g less than 1%) led to a maximum value of $r_g \sim 4.80$ nm ($r_g = 0.775r_h$; r_h values from Table 2) for EO₃₃SO₁₄EO₃₃ and EO₃₈SO₁₀EO₃₈. The existence of strong intermicellar interactions resulted in interparticle interference and caused both the curvature of SLS data plot even at low concentrations (Figure S2) and the positive slope observed in DLS data (Figure 2b), as also observed elsewhere (17-19, 27-28).

The values of the micelle molecular weight, M_w , and the swelling factor, δ_t , obtained from fitting of experimental SLS data are reported in Table 2. The mass-average association numbers of the micelles (estimated as the ratio of the M_w of the micelles and the M_w of the copolymer shown in Table 1) and the thermodynamic radius (r_t , calculated from the thermodynamic volume of the micelles, i.e., $v_t = \delta_t v_a$) were higher for EO₃₃SO₁₄EO₃₃ than for EO₃₈SO₁₀EO₃₈ (Table 2) as corresponds to a more hydrophobic copolymer with a larger hydrophobic core and stronger intermicellar interactions. According to the assumption that micelles have a spherical structure with a liquid-like core (40) free of solvent molecules, we can further evaluate the extent of drainage of the micellar corona. By subtracting the value of the core radius r_c (see Supplementary materials for its obtention) from the thermodynamic radius, r_t , the thickness of the micellar corona can be estimated and, hence, the volume of each water swollen EO unit, v_E , can be calculated from the relation:

$$(4/3)\pi(r_t^3 - r_c^3) = mN_w v_E = \langle L_h \rangle \quad (6)$$

where L_h is the micellar corona thickness and v_E the volume of each water swollen EO unit, which are listed in Table 2. Taking into account that the volume of an unswollen liquid EO unit is 0.073 nm³ and the volume of a water molecule close to 0.030 nm³, the number of water molecules associated with each EO-unit, n_{water} , can be estimated (see also Table 2). Raman spectroscopy has been used to show that there are six water molecules in the hydration shell of an EO unit: two H-bonded directly to the ether oxygen and four involved in hydration of the hydrophobic part of the unit (41). The rest will be essentially bulk water, restricted to the corona to some extent, which is determined by the balance of osmotic and dynamic forces in a given situation.

Table 2: Micellar and hydration properties at 37 °C of EO₃₃SO₁₄EO₃₃ and EO₃₈SO₁₀EO₃₈.

Polymer	cmc / 10^{-3} g dm ⁻³	δ_t	M_w / 10^4 mol g ⁻¹	r_h /nm	N_w	r_t /nm	v_E /nm ³	n_{water}
EO ₃₃ SO ₁₄ EO ₃₃	2.5	4.7	17.8	6.2	37	6.7	0.48	14
EO ₃₈ SO ₁₀ EO ₃₈	3.7	3.5	6.9	6.2	14	4.4	0.33	9

2.2.4.2 Phase behaviour and rheological properties

EO₃₃SO₁₄EO₃₃ and EO₃₈SO₁₀EO₃₈ (10-80 wt%) solutions remained clear when heated from 5°C to 90 °C. The temperature-composition phase diagrams for 0-50 wt% solutions were generated with data collected visually by the inverted tube method in combination with rheology measurements. The gel-like state is defined as an immobile fluid (Figure 3). To a good approximation, immobility in the tube inversion test requires the gel-like state to have a yield stress $\sigma_y \geq 30$ Pa (42). The insensitivity of storage moduli to frequency justifies our use of a single frequency (1 Hz) in the T scans done to confirm gel boundaries, as shown in detail below.

Physical block copolymer gels of the present type are formed by the enhancement of intermicellar interactions due to micellar crowding as the copolymer concentration in solution increases. SAXS studies on gels of PSO-based triblock copolymers have shown them to comprise spherical micelles packed in body-centered structures (43,44), which are favored due to softer intermicellar interactions as a result of a lower density of EO chains in the micelle corona if compared to diblock structure counterparts (28). For these cubic micellar arrays, it is known that $\sigma_y/G' \approx 0.1$ with G' measured at 1 Hz; this means that the storage modulus has to be above 1 kPa for successful physical gel formation. Such a gel-like state is referred to *hard* gel following Hvidt's *et al.* notation (45). On the other hand, qualitatively we also distinguish two mobile fluid phases in tube inversion experiments, one which flows immediately and freely on inversion from other (a viscous fluid), which flows very slowly. This viscous fluid has been named, for example, as *soft* gel by Hvidt *et al.* (45) and its boundaries can be well-determined by rheometry. This viscous fluid does not behave either as a sol or a proper gel, since it possess a low yield stress and a storage modulus larger than the loss modulus but with $G' < 1$ kPa, as shown in detail below.

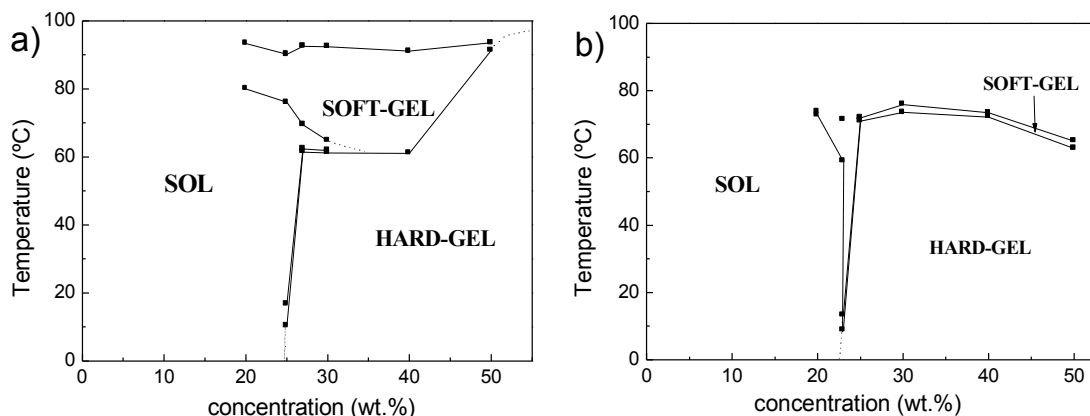


Figure 3: Gel boundaries of aqueous micellar solutions of a) EO₃₃SO₁₄EO₃₃ and b) EO₃₈SO₁₀EO₃₈.

As observed in Figure 3a, copolymer EO₃₃SO₁₄EO₃₃ at concentrations lower than 25 wt.% leads to a transparent and isotropic sol phase in the 0 to ca. 80 °C temperature range. At larger concentrations, the gel-like phase is formed, with an upper limit temperature of ca. 60 °C for concentrations lower than 40 wt.% which increases up to ca. 90 °C for a concentration of 50 wt.%. There was no low-temperature boundary for copolymer gels as a consequence of the stability of the polymeric micelles in water at low temperatures due to the water insolubility of PSO blocks, in agreement with their very low standard micellization enthalpy values (28). Also, the gel-viscous fluid spans from ca. 20 wt.% up to ca. 50 wt.%, with their lower temperature boundary concentration-dependent and the upper temperature limit close to 90 °C. This upper limit of the viscous fluid region reached within the temperature range investigated is consistent with a decrease in the stability of the hard gels of EO₃₃SO₁₄EO₃₃ as temperature increases, in contrast to other block sequences (21,24). At temperatures larger than 90 °C, the appearance of a new sol phase agrees with the melting of copolymer chains at such high temperature. The phase behavior of copolymer EO₃₈SO₁₀EO₃₈ is similar to that found for EO₃₃SO₁₄EO₃₃ but two main differences were detected: the viscous fluid-gel boundary was shifted to a lower concentration and the viscous fluid region became very narrow.

In order to get deeper insight on the rheological behavior of the present copolymers, temperature scans of storage and loss moduli at concentrations below and above their critical gel concentration, c_{gc} , (Figures 4 and 5) were used to verify and complete the phase diagrams. A c_{gc} of 19 wt% was estimated for both copolymers by means of the expression $c_{gc} = 10^2 \rho_a \phi_c / \delta_t$, where $\phi_c = 0.68$ is the volume fraction of spherical micelles packed in a body-centered structure. The rheological behavior of EO₃₃SO₁₄EO₃₃ and EO₃₈SO₁₀EO₃₈ copolymers at concentrations below 20 wt% exhibits a

predominant viscous behavior ($G'' > G'$) that is a characteristic feature of a sol phase (Figure 4a and Figure S3). At a temperature of ca. 70 °C, both G' and G'' increased in about two decades. This effect may be due to an increment in the number of micelles in solution due the insolubility of the PSO chains. The sample at 20 wt.% concentration exhibited a similar trend than that depicted for the 10 wt.% solution at a lower temperature. At higher temperatures two transitions were observed: the first at 78 °C, corresponding to the appearance of a sol-viscous fluid transition, and the second, at ca. 90 °C, due to the melting of the viscous fluid (Figure 4b). This area of the phase diagram is rather narrower for $\text{EO}_{38}\text{SO}_{10}\text{EO}_{38}$ (Figure S3). A more viscous fluid developed from a sol solution should originate from weak attractions of spherical micelles in water at elevated temperatures, where the solvent is poorer for the micelles. The transition from sol to viscous fluid may well occur when aggregates of spherical micelles well would reach a percolation threshold yielding sufficient structure to cause a characteristic rheological effect (46-47). This additional structuration is more important in the case of $\text{EO}_{38}\text{SO}_{10}\text{EO}_{38}$, which even formed a gel within this temperature range (Figure S3 and text in Supporting Information for further details). At 25 wt% (Figure 4c), the copolymer solution behaved as a gel below 10 °C due to the formation of cubic liquid crystals in a body centered structure (bcc); at higher temperatures two transitions were observed: the first one corresponding to a gel-viscous fluid at 10 °C, and a second one at 17 °C due to a viscous fluid-sol transition. The former transition can be assigned to a defective version of the cubic-packed gel as the temperature increases, i.e., small structured domains in an overall fluid matrix (gel-defective viscous fluids). This viscous region can be identified in Figure 4c as a narrow low- T shoulder on the $G(T)$ curve of the 25 wt% solution (or as a distinct high- T shoulder on the $G(T)$ curve of the 30 wt% in Figure S3d). Viscous fluids of the present type have been previously identified in aqueous micellar solutions of a wide range of block copolymers, including PEO-PPO, (18, 47-50) and other PEO-PSO block copolymers (21,24,51). In addition, G' and G'' increased in about three magnitude orders at ca. 70 °C to give a new viscous fluid region between 76 and 90 °C due to further copolymer micelle structuration. This additional structuration is more important in the case of $\text{EO}_{38}\text{SO}_{10}\text{EO}_{38}$ (Figure S3 and text in SI for further details).

On the other hand, an increase in polymer concentration (up to 30 wt%.) led to both a widening of the low-temperature gel region at the expense of the gel-defective viscous fluid region as a consequence of enhanced intermicellar interactions; also, a certain narrowing of the mild-temperature sol region took place until completely disappearance (Figure 4d for a 27 wt.% solution as an example), whilst the high- T viscous fluid region emerged at relatively lower temperatures (ca. 70 °C, see Figure 4d) and remained almost invariable in shape. This is in contrast to the behavior observed for $\text{EO}_{38}\text{SO}_{10}\text{EO}_{38}$, for which the high- T viscous fluid region was very narrow within this copolymer concentration range (Figure S3). At larger copolymer concentrations (> 30 wt.%), the attractive intermicellar interactions become much stronger. This involves

firstly the avoidance of the gel phase disruption in the temperature range 60-70°C (see Figure 4d) and, then, the widening of the gel phase at the expense of the gel-defective viscous fluid region (see Figure 4e) until it completely disappears at 50 wt.% for copolymer EO₃₃SO₁₄EO₃₃ (Figure 4f and Figure S3d).

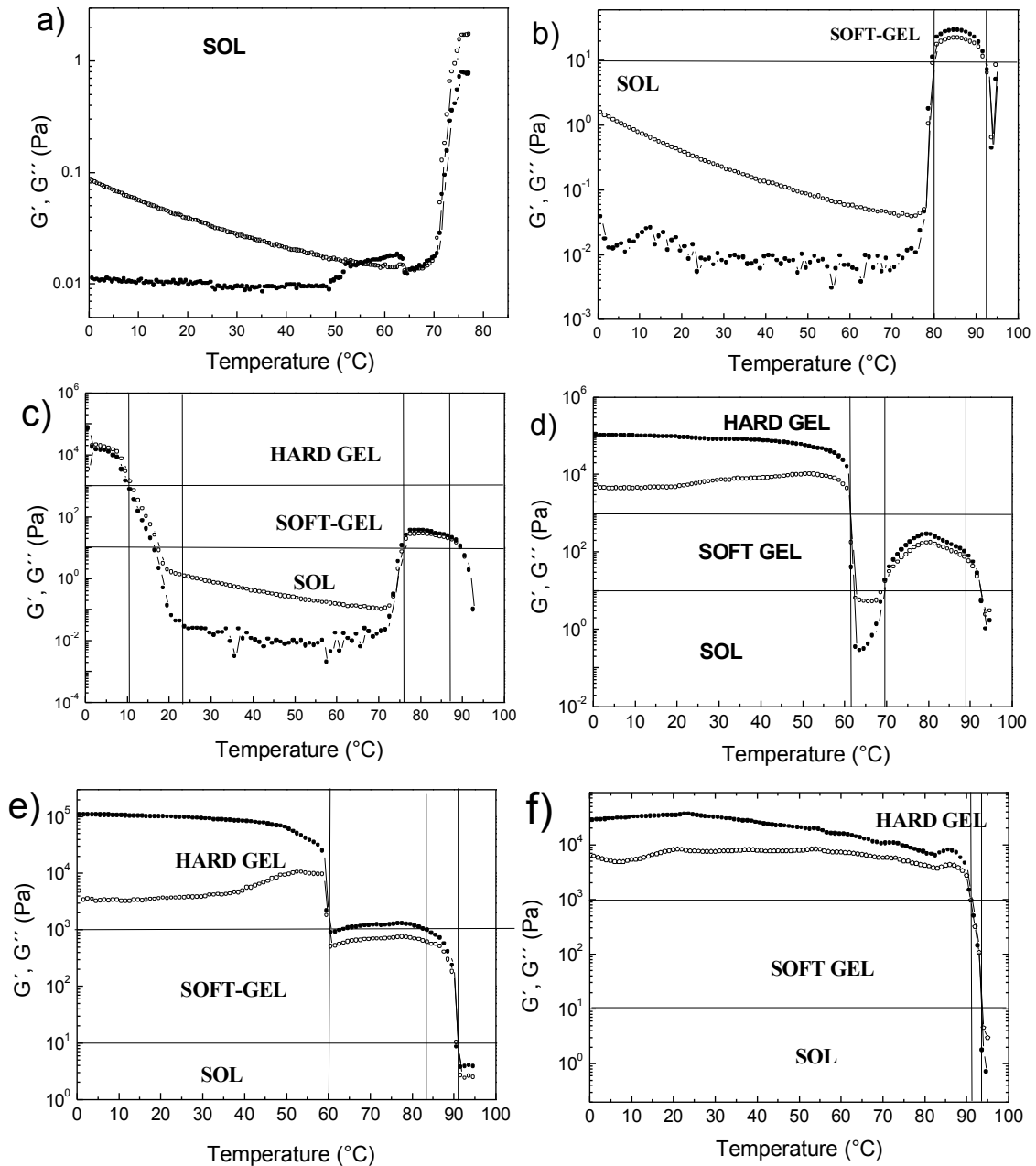


Figure 4: Temperature scans of (●) storage, G' , and (○) loss moduli, G'' , for a) 10 wt %.; b) 20 wt %.; c) 25 wt %.; d) 27 wt %.; e) 40 wt %.; and f) 50 wt % of EO₃₃SO₁₄EO₃₃.

To get a more detailed picture about the rheological behavior of the observed viscous fluids, frequency sweeps within the linear viscoelastic region of block copolymer

solutions were also performed. Frequency scans obtained for 20 and 30 wt%. solutions of copolymer EO₃₃SO₁₄EO₃₃ at different temperatures are shown in Figure 5. Similar plots were obtained for copolymer EO₃₈SO₁₀EO₃₈ (not shown). The 20 wt.% copolymer solution at 60 and 90 °C is a sol (Figure 3a); at these temperatures, the system exhibits a predominant viscous behavior ($G' < G''$) and only the terminal zone is observed, with increasing values of G' and G'' with frequency (see Figure 5a,c). In contrast, at 80 °C the solution behaves as a viscous fluid (or “soft gel”) and shows a viscoelastic behavior, with low G' values. G' and G'' exhibit a crossover at a characteristic frequency (ϕ_c) of 2 rad/s, which would correspond to a Maxwell fluid, at most, showing localized cubic order (Figure 5b); the reciprocal of the frequency crossover corresponds to the main relaxation time of the system, $\phi_c = 0.5$ s. At frequencies lower than ϕ_c the rheological behavior is predominantly viscous, and at higher frequencies the system exhibits a predominant elastic behavior ($G' > G''$). Both moduli increased with frequency but the plateau modulus (G_0) was not detected in the frequencies range studied. This behavior is a consequence of the weak attraction of spherical micelles in water at temperatures at which this is a poor solvent for micelles, as commented previously. Furthermore, the 30 wt.% solution at 20 °C is within the gel region, the G' , G'' crossover shifts to lower frequencies ($\phi_c = 0.2$ rad/s) increasing the predominant elastic behavior in almost the whole interval of frequencies studied. G' exhibits a plateau (G_0) with a value around of $4 \cdot 10^4$ Pa, and G' decreases in around one magnitude order indicating an increasing in the hardness of the sample with frequency (Figure 5d). The insensitivity of storage moduli to frequency justifies our use of a single frequency (6.28 rad/s) in the temperature scans done to confirm the gel boundary. As temperature rises, the copolymer solution becomes more fluid and transforms into a viscous fluid, as shown in Figure 5e. This plot shows again the characteristic moduli crossover and a predominant elastic behavior is observed in the interval of frequencies studied. As a consequence, temperatures at the soft-gel/sol boundary are dependent on the frequency used, and those drawn in Figure 3 give only an indication of the viscoelasticity of the systems.

From a pharmaceutical point of view, it is clear that at 37°C the transition between the sol and the gel state can be achieved through a tiny change in copolymer concentration around ca. 25% (see Figure 3). The present PEO-PSO-PEO copolymers could be suitable for preparing syringeable drug depots, which can easily flow from the syringe as a solution at a temperature some degrees above 37°C, but transform at the body temperature (for example, once injected in the subcutaneous tissue) in a viscoelastic gel that can sustain drug release. On the other hand, one can envision that if a polymeric physical gel is formed in the implantation site in the body, it can rapidly become a sol if the temperature raises some degrees above 37°C, as occurs when a pathological process is on-going or if an external source of heat is applied. Such a behaviour may enable to trigger drug release by a systemic or local increase in temperature. It should be noticed that although the micelles of both block copolymers

tested are too large to be directly cleared by renal filtration, the molecular weight of the unimers is much below the urinary threshold, so after drug release and micelle destabilization copolymer chains might be excreted through this route.

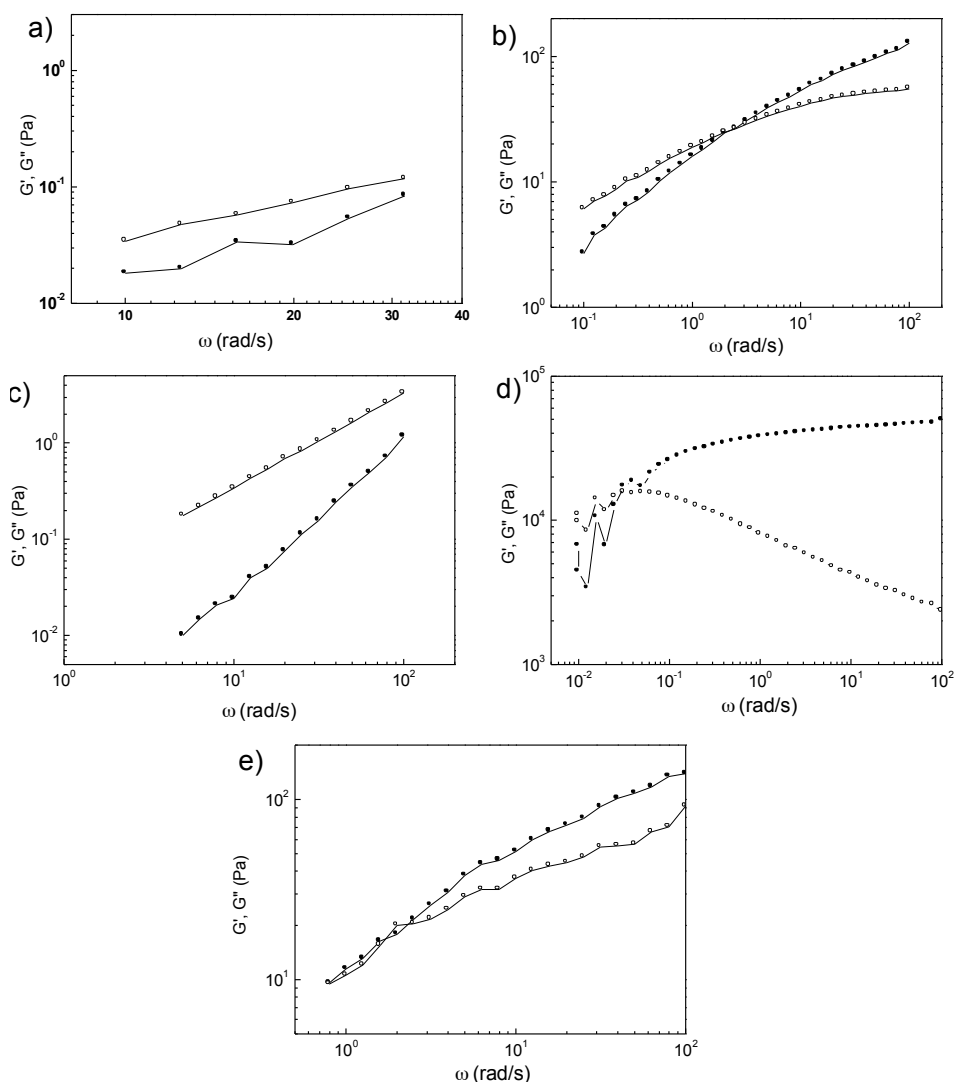


Figure 5: Frequency scans of storage (●) and loss (○) moduli obtained for 20 wt.% solutions of $EO_{33}SO_{14}EO_{33}$ at a) 60 °C; b) 80 °C; c) 90 °C; and 30 wt.% at d) 20 °C; and e) 90 °C.

2.2.4.3 Solubilization capacity studies

In order to establish the solubilization capability of the present copolymers as drug carriers, encapsulation experiments were carried out employing the antifungal drug griseofulvin. This drug is commonly used as a model for solubilization assays and, thus, it was chosen in order to compare the solubilization ability of $EO_{33}SO_{14}EO_{33}$ and $EO_{38}SO_{10}EO_{38}$ copolymers (at 0.2 wt%, far above the cmc) with that previously reported for other structure-related block copolymers. To investigate the impact of the amount

of feeding drug used to prepare the drug-loaded micelles, the entrapment efficiency and drug-loaded amount were determined in loaded micelles with varying drug/copolymer weight ratio. In general, the higher the feeding, the lower the entrapment efficiency was (Table 3) as a consequence of the saturation of the inner micellar core. Drug precipitation was also observed when very large griseofulvin feeding concentrations were used, which confirms that the micelles can enhance drug solubility but up to a maximum beyond which further addition of drug leads to precipitation. Comparing both copolymers, $EO_{33}SO_{14}EO_{33}$ exhibited a slightly larger solubilization capacity, which can be attributed to its longer hydrophobic block and the consequent higher affinity of the hydrophobic drugs for the micelle core. Also, the solubility per gram of copolymer (S_{CP} , Table 3, maximum uncertainty of $\pm 1 \text{ mg g}^{-1}$) was concentration-dependent, reaching values of up to 55 mg g^{-1} . These solubility values are larger than those previously reported for other triblock PSO-PEO block copolymer counterparts (22,23,39) and similar to related PSO-PEO diblocks despite the effective shorter block length of the present copolymers due to looping of the PSO blocks in the micellar core (22). This fact confirms that the selected EO:SO ratio and copolymer block lengths were optimal for efficient drug solubilization. In addition, $EO_{33}SO_{14}EO_{33}$ and $EO_{38}SO_{10}EO_{38}$ also display a notably much larger solubility than other types of block copolymers such as PEO-PPO, PEO-PBO and PEO-PG ones (18,19,23,52,53), or different surfactant and organic solutions (53). For example, we noted solubilization increases 10-fold larger than for Pluronic F127 [55] and Poloxamine T904 (38); these data highlight the importance of a judicious choice of both block composition and length to simultaneously minimize copolymer concentration (i.e. material expense) while maximizing solubilization ability without compromising polymeric micelles stability.

Table 3: Griseofulvin loaded amount (D.L.), entrapment efficiency (E.E.) and solubilisation capacity (S_{CP}) of the copolymers.

<i>Feeding</i> <i>Drug/Polymer</i> % (w/w)	<i>EO₃₃SO₁₄EO₃₃</i>			<i>EO₃₈SO₁₀EO₃₈</i>		
	<i>D.L.</i> %	<i>E.E.</i> %	<i>S_{cp}</i> /mg g ⁻¹	<i>D.L.</i> %	<i>E.E.</i> %	<i>S_{cp}</i> /mg g ⁻¹
4	3.8	98.0	39.6	3.5	91.4	36.6
10	2.4	24.4	34.7	2.2	22.2	32.4
15	2.2	4.3	43.1	2.8	5.5	55.6
25	1.4	8.6	17.2	1.2	6.9	13.8
50	1.2	3.7	18.4	1.3	4.0	19.9
100	1.2	2.4	23.5	1.1	2.3	22.8

2.2.4.4 In vitro release of griseofulvin

The *in vitro* release profiles of griseofulvin encapsulated inside EO₃₃SO₁₄EO₃₃ and EO₃₈SO₁₀EO₃₈ block copolymer micelles were monitored by dialysis at 37 °C in pH 4.0, 5.5 and 7.4 buffers (Figure 6). An initial burst release was observed in all cases, followed by a more gradual phase until equilibration was attained over 1 day. Based on this observation, it can be concluded that an important fraction of the drug probably existed at the interstices of the self-assembled micelles causing the burst release, while those drug molecules located at the micellar interior followed a slow and stepwise release kinetics (56). Furthermore, while roughly 35% and 45% of the loaded griseofulvin was released in 5 h at pH 4.0 and 5.5 respectively, the release at pH 7.4 was faster, and almost 75% of the drug diffused out the micelles.

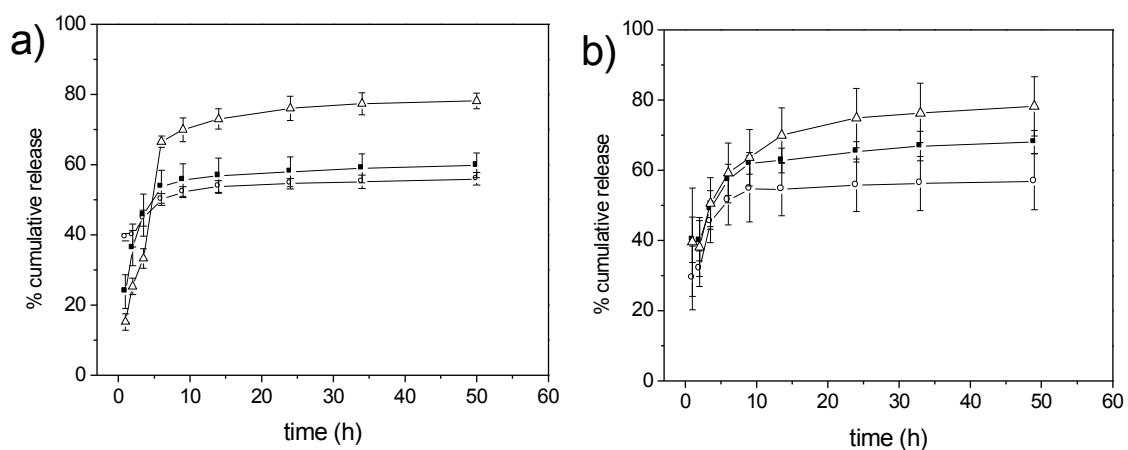


Figure 6. *In vitro* release kinetics of griseofulvin encapsulated inside a) EO₃₃SO₁₄EO₃₃ and b) EO₃₈SO₁₀EO₃₈ block copolymer micelles, under dialysis at 37 °C and pH 4.0 (○), 5.5 (■) and 7.4 (Δ).

Drug release profiles from the micellar systems were fitted to the typical square-root kinetics (57)

$$M_t/M_\alpha = k \cdot t^{0.5} \quad (9)$$

and to the Fickian diffusion model considering the micelles as perfect spheres (58)

$$M_t/M_\alpha = k_1 + k_2 \cdot t^{0.5} - k_3 \cdot t \quad (10)$$

Only the Fickian diffusion model fitted well the whole release profile (Table 4, correlation coefficient $R^2 > 0.90$). This model has been previously applied to swellable matrices to explain the coupling of the diffusion and relaxation events (57) and more recently to micellar systems to describe the radial diffusion of the drug through the

core-shell phases (58). Both conformational changes in the micellar structure during drug release and partial transfer of drug from one micelle to another may play a role in the release rate of the drug. Moreover, since the release data were obtained from the decay of the drug concentration in the micellar solution inside the dialysis bag, drug released from one micelle can enter in an already empty micelle nearby. That situation may mimic the drug release in a cellular environment, where the drug-loaded micelles would be at a short distance of the cellular acceptors (which can be simulated with empty micelles) (58). Thus, drug release from micelles to the aqueous buffer and from one micelle to another may likely occur. It should be noticed that the release tests were carried out using dialysis bags of MWCO 3500Da, which is below the molecular weight of the copolymer. Therefore, the copolymer concentration inside the dialysis bag should remain almost constant along the test and, consequently, the micelles breakdown may occur in a timescale considerably larger than that of the diffusion of the drug.

Table 4: Results of the fitting to equation 10 of the griseofulvin release profiles from the micellar solutions in aqueous buffer of different pH. The release rate constants are given as mean values, with standard deviations in parenthesis.

Formulation	Release medium	k_1	k_2	k_3	F	P-value	R^2
E ₃₃ SO ₁₄ EO ₃₃	pH 4	30.60 (2.12)	9.19 (1.28)	0.81 (0.16)	65.67	0.001	0.9563
	pH 5.5	12.39 (6.13)	19.22 (3.71)	1.84 (0.46)	26.35	0.002	0.8978
	pH 7.4	-18.07 (10.50)	37.88 (6.36)	3.53 (0.78)	38.19	0.001	0.9272
E ₃₈ SO ₁₀ EO ₃₈	pH 4	15.57 (5.28)	16.98 (3.22)	1.64 (0.40)	27.17	0.001	0.9005
	pH 5.5	25.18 (3.84)	15.25 (2.34)	1.34 (0.29)	58.16	0.001	0.9509
	pH 7.4	19.33 (3.76)	19.22 (2.28)	1.58 (0.28)	120.66	0.001	0.9757

The constant associated to drug diffusion (k_2) became larger as the pH raised from 4.0 to 7.4, particularly in the case E₃₃SO₁₄EO₃₃. The overall amount released in the first 24 h was larger at pH 7.4 (78 % for EO₃₃SO₁₄EO₃₃ and 71% for EO₃₈SO₁₀EO₃₈, respectively) than under acidic conditions (56 % at pH 4.0 for both copolymers). The reasons for this effect are unclear. One hypothesis is that at acid pH there is a strengthening of the hydrogen bonds between the PEO blocks and water molecules, resulting in the stretching of PEO chains and enlargement of the micellar shell (59), making the diffusion path longer. An effective increase in the SO/EO ratio might also

occur as the pH decreases, due to a partial hydrolysis of the EO chains (60), which may result in an enhanced drug/hydrophobic block affinity, hence, slowing drug release. The amount of drug released from $\text{EO}_{38}\text{SO}_{10}\text{EO}_{38}$ micelles was slightly larger than from the $\text{EO}_{33}\text{SO}_{14}\text{EO}_{33}$ ones, probably as a consequence of a slightly lower micellar stability (previously discussed) due to a less compact hydrophobic core of the former polymer, which may favour the formation of hydrophilic channels (61,62).

2.2.5 Conclusions

In aqueous solution, poly(ethylene oxide)-poly(styrene oxide) block copolymers $\text{EO}_{33}\text{SO}_{14}\text{EO}_{33}$ and $\text{EO}_{38}\text{SO}_{10}\text{EO}_{38}$ self-assembled at very low concentrations to form spherical micelles of sizes ca. 13-14 nm. Also, these copolymers present a rich phase behavior, with the formation of soft and hard gels. In this regard, two different types of soft gels were observed, one usually presented at high temperatures in the copolymer concentration range 20-30 wt% as a consequence of percolation between copolymer micelles acting as hard spheres, and other after hard gel regions originated by defective cubic structures. On the other hand, both copolymers display an important ability to solubilise hydrophobic drugs as observed by comparing the solubilisation extent of griseofulvin. Solubility factors up to ca. 55 mg g^{-1} , obtained by optimization of the SO/EO ratio and the copolymer block lengths, were not previously achieved in any other micellar system. Drug release profiles show an initial burst followed by a more sustained pH-dependent delivery. The slower release rate observed at acid pH may be the result of i) conformational changes in the EO blocks that lead to large shells and thus longer diffusional paths and ii) a more hydrophobic microenvironment inside the micelle, increasing the drug-hydrophobic copolymer chains affinity, due to partial hydrolysis of EO chains which leads to an effective increase in SO/EO ratio. Overall the results obtained indicate that $\text{EO}_{33}\text{SO}_{14}\text{EO}_{33}$ and $\text{EO}_{38}\text{SO}_{10}\text{EO}_{38}$ can act, at low concentrations, as suitable components of micellar carriers for drug administration by either parenteral or oral route, subsequent drug transport in the body and sustained release, and at higher concentrations, as components of gel systems that can undergo gel-to-sol transitions as a function of tiny increases in temperature above 37°C .

2.2.6 References

1. Ferrari, M. *Nat. Rev. Cancer*, **2005**, 5, 161.
2. Farozkhad, O.C.; Langer, R. *ACS Nano*, **2009**, 3, 16.
3. Letchford, K.; Burt, H. *Eur. J. Pharm. Biopharm.*, **2007**, 65, 259.

4. Alvarez-Lorenzo, C.; Concheiro, A. *Mini-Rev. Med. Chem.*, **2008**, 8, 1065.
5. Gaucher, G.; Satturwar, P.; Jones, M.-C.; Furtos, A.; Leroux, J.-C. *European J. Pharm. Biopharm.*, **2010**, 76,147.
6. Chiapetta, D.A.; Alvarez-Lorenzo, C.; Rey-Rico, A.; Taboada, P.; Concheiro, A.; Sosnik, A. *Eur. J. Pharm. Biopharm.*, **2010**, 76, 24.
7. Jeong, Y.I.; Kim, D.H.; Chung, C.W.; Yoo, J.J.; Choi, K.H.; Kim, C.H.; Ha, S.H.; Kang, D.H-. *J. Nanomed.* **2011**, 6, 1415.
8. Oerlemans, C.; Bult, W.; Bos, M.; Storm, G.; Nijssen, J.F.W.; Hennink, W.W.. *Pharm. Res.*, **2010**, 27, 2569.
9. Cao, Z.; Yu, Q.; Xue, H.; Cheng, G.; Jiang, S. *Angew. Chem. Int. Ed.* **2010**, 49, 3771.
10. Torchilin, V.P. *Pharm. Res.* **2007**, 24, 1.
11. Wiradharma, N.; Zhang, Y.; Venkataraman, S.; Hedrick, J.L.; Yang, Y.Y. *NanoToday*, **2009**, 4, 302.
12. Yang, T.F.; Chen, C.N.; Chen, M.C.; Lai, C.H.; Liang, H.F.; Sung, H.W. *Biomaterials*, **2007**, 28, 725.
13. Kabanov, AV.; Alakhov, V.Y. *Crit. Rev. Ther. Drug Carrier Syst.*, **2002**, 9, 1.
14. Batrakova, E.V.; Kabanov, A.V. *J. Controlled Release*, **2008**, 130, 98.
15. Alvarez-Lorenzo, C.; Rey-Rico, A.; Sosnik, S.; Taboada, P.; Concheiro, A. *Frontiers Biosci.*, **2010**, E2, 424.
16. Alvarez-Lorenzo, C.; Sosnik, A.; Concheiro, A. *Curr. Drug Targets*, **2011**,12, 1112.
17. Booth, C.; Attwood, D. *Macromol. Rapid Commun.*, **2000**, 21, 501.
18. Taboada, P.; Velasquez, G.; Barbosa, S.; Castelletto, V.; Nixon, S.K.; Yang, Z.; Heatley, F.; Hamley, I.W.; Ashford, M.; Mosquera, V.; Attwood, D.; Booth, C. *Langmuir*, **2005**, 21, 5263.
19. Taboada, P.; Velasquez, G.; Barbosa, S.; Yang, Z.; Nixon, S.K.; Zhou, K.;Heatley, F.; Ashford, M.; Mosquera, V.; Attwood, D.; Booth, C. *Langmuir*, **2006**, 22, 7465.
20. Booth, C.; Attwood, D.; Price, C. *Phys. Chem. Chem. Phys.*, **2006**, 8, 3612.
21. Barbosa, S.; Cheema, M.A.; Taboada, P.; Mosquera, V. *J. Phys. Chem. B*, **2007**, 11, 10920.
22. Crothers, M.; Zhou, Z.; Ricardo, N. M. P. S.; Yang, Z.; Taboada, P.; Chaibundit, C.; Attwood, D.; Booth, C. *Int. J. Pharm.*, **2005**, 293, 91.
23. Ribeiro, M. E. N. P.; Vieira, I. G. P.; Cavalcante, I.M.; Ricardo, N. M. P. S.; Attwood, D.; Yeates, S.G.; Booth, C. *Int. J. Pharm.*, **2009**, 378, 211.
24. Juarez, J.; Taboada, P.; Valdez, M.A.; Mosquera, V. *Langmuir*, **2008**, 24, 7107.
25. Zhou, N.; Lodge, T.P.; Bates, F.S. *J. Phys. Chem. B*, **2006**, 110, 3979.
26. Cambón, A.; Rey-Rico, A.; Barbosa, S.; Soltero, J.F.A.; Yeates, S.G.; Brea, J.;

- Loza, M.I.; Alvarez-Lorenzo, C.; Concheiro, A.; Taboada, P.; Mosquera, V. J. *Controlled Release* **2013**, 167, 68.
27. Crothers, M.; Attwood, D.; Collett, J.H.; Yang, Z.; Booth, C.; Taboada, P.; Mosquera, V.; Ricardo, N. M. P. S.; Martini, L.G.A. *Langmuir*, **2002**, 180, 8685.
 28. Yang, Z.; Crothers, M.; Ricardo, N. M. P. S.; Chaibundit, C.; Taboada, P.; Mosquera, V.; Kellarakis, A.; Havredaki, V.; Martini, L.; Valder, C.; Collett, J.H.; Attwood, D.; Heatley, F.; Booth, C. *Langmuir*, **2003**, 19, 943.
 29. Lee, K.; Shin, S.C.; Oh, O. *Arch. Pharm. Res.*, **2003**, 26, 653.
 30. Provencher, S.W. *Makromol. Chem.*, **1979**, 180, 201.
 31. Percus, J.K.; Yevick, G.J. *Phys. Rev.*, **1958**, 110, 1.
 32. Vrij, A. *J. Chem. Phys.*, **1978**, 69, 1742.
 33. Carnahan, N.F.; Starling, K.E.J. *J. Chem. Phys.*, **1969**, 51, 635.
 34. El-Kashef, H. *Rev. Sci. Instrum.* **1998**, 69, 1243.
 35. Liu, T.; Schuch, H.; Gerst, M.; Chu, M. *Macromolecules*, **1999**, 32, 6031.
 36. Huglin, M.B. *Light Scattering from Polymer Solutions* 1972, Plenum Press.
 37. Mai, S.M.; Booth, C.; Nace, V.N. *Eur. Polym J.*, **1997**, 33, 991.
 38. Alvarez-Lorenzo, C.; Gonzalez-Lopez, J.; Fernandez-Tarrio, M.; Sandez-Macho, I.; Concheiro, A. *Eur. J. Pharm. Biopharm.*, **2007**, 66, 255.
 39. Wei, Z.; Hao, J.; Yuan, S.; Li, Y.; Juan, W.; Sha, X.; Fang, X. *Int. J. Pharm.*, **2009**, 376, 176.
 40. Zhou, Z.; Chu, B.J. *J. Colloid Interface Sci.*, **1998**, 126, 171.
 41. Goutev, N.; Nickolov, Z.S.; Georgiev, g.; Matsuura, H. *Chem. Soc. Faraday Trans.*, **1997**, 93, 3167.
 42. Kellarakis, A.; Havredaki, V.; Booth, C.; Nace, V.M. *Macromolecules*, **2002**, 35, 5591.
 43. Castelletto, V.; Hamley, I.W.; Crothers, M.; Attwood, D.; Yang, Z.; Booth, C. *J. Macromol. Sci. Phys.* **2005**, 43, 13.
 44. Hamley, I.W.; Castelletto, V.; Ricardo, N. M. P. S.; Booth, C.; Attwood, D.; Yang, Z. *Polym. Int.*, **2007**, 56, 88.
 45. Hvidt, S.; Joergensen, E.B.; Brown, W.; Schillen, K. *J. Phys. Chem.* 1994, 98, 12320.
 46. Li, H.; Yu, G.E.; Price, C.; Booth, C.; Hecht, E.; Hoffmann, H. *Macromolecules*, **1997**, 30, 1347.
 47. Li, H.; Yu, G.E.; Price, C.; Booth, C.; Fairclough, J.P.A.; Ryan, A.J.; Mortensen, K. *Langmuir*, **2003**, 19, 1075.
 48. Kellarakis, A.; Havredaki, V.; Booth, C. *Macromol. Chem. Phys.*, **2003**, 204, 15.
 49. Chaibundit, C.; Ricardo, N.M.P.S.; Costa, F.M.L.L.; Wong, M.G.P.; Hermida-Merino, D.; Rodriguez-Perez, J.; Hamley, I.W.; Yeates, S.G.; Booth, C. *Langmuir*, **2008**, 24, 12260.
 50. Kellarakis, A.; Havredaki, V.; Booth, C. *Macromol. Chem. Phys.*, **2004**, 205, 1594.

51. Ricardo, N.M.P.S.; Pinho, M.E.N.; Yang, Z.; Attwood, D.; Booth, C. *Int. J. Pharm.*, **2005**, 300, 22.
52. Rekasas, C.J.; Mai, S.M.; Crothers, M.; Quinn, M.; Collett, J.H.; Attwood, D.; Heatley, F.; Martini, L.; Booth, C. *Phys. Chem. Chem. Phys.*, **2001**, 3, 4769.
53. Ribeiro, M.E.N.P.; Cavalcante, I.M.; Ricardo, N.M.P.S.; Mai, S.-M.; Attwood, D.; Yeates, S.G.; Booth, C. *Int J. Pharm.*, **2009**, 369, 196.
54. Balakrishnan, A.; Rege, B.D.; Amidon, G.L.; Polli, J.E. *J. Pharm. Sci.*, 2004, 93, 2064.
55. Oliveira, C.P.; Vasconcellos, L.C.G.; Ribeiro, M.E.N.P.; Ricardo, N.M.P.S.; Souza, T.C.P.; Costa, F.M.L.L.; Chaibundit, C.; Yeates, S.G.; Attwood, D. *Int. J. Pharm.*, **2011**, 409, 206.
56. Dutta, P.; Shrivastava, S.; Dey, J. *Macromol. Biosci.*, **2009**, 9, 1116.
57. Peppas, N.A.; Shalin, J.J. *Int. J. Pharm.*, **1989**, 57, 169.
58. Wang, H.; Xu, J.; Wang, J.; Chen, T.; Wang, Y.; Tan, Y.W.; Su, H.; Chan, K.L.; Chen, H. *Angew. Chem. Int. Ed.*, **2010**, 49, 8426.
59. Yang, B.; Guo, C.; Chen, S.; Ma, J.; Wang, J.; Liang, X.; Zheng, L.; Liu, H. *J. Phys. Chem. B*, **2006**, 110, 23068.
60. Morlat, S.; Gardette, J.L. *Polymer*, **2003**, 44, 7891.
61. Hu, Y.; Jiang, X.; Ding, Y.; Zhang, L.; Yang, C.; Zhang, J.; Chen, J.; Yang, Y. *Biomaterials*, **2003**, 24, 2395.
62. Wei, Z.; Hao, J.; Yuan, S.; Li, Y.; Juan, W.; Sha, X.; Fang, X. *Int. J. Pharm.*, **2009**, 376, 176.

2.3 SUPPORTING INFORMATION FOR POLY (ETHYLENE OXIDE) - POLY(STYRENE OXIDE) - POLY(ETHYLENE OXIDE) COPOLYMERS: MICELLIZATION, DRUG SOLUBILISATION AND GELLING FEATURES

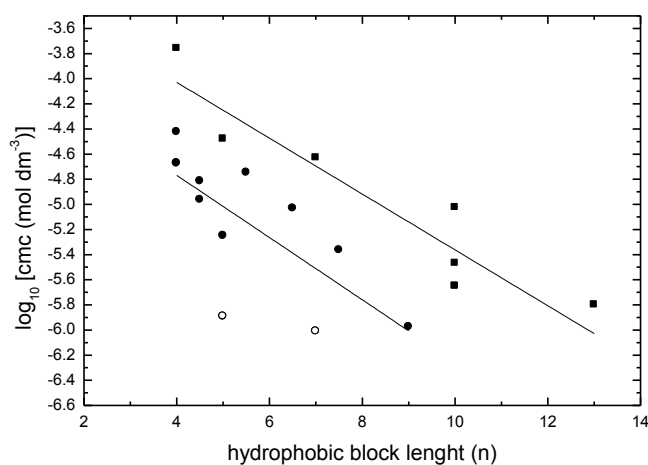


Figure S1. Logarithm of cmc (in mol dm⁻³) versus hydrophobic block length (*n*) for aqueous solutions at 30 °C of diblock copolymers (■) EO_mSO_n and triblock copolymers (●) EO_mSO_nEO_m plotted using half-length *n*/2 (S1-S3). Open symbols correspond to the copolymers studied in the present work.

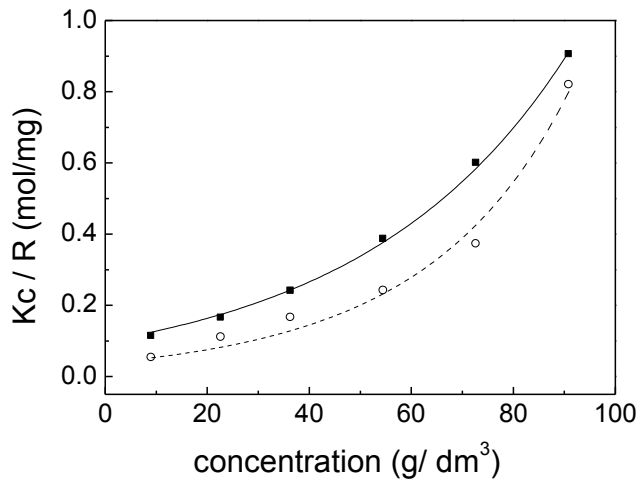


Figure S2: Debye plot for block copolymer EO₃₃SO₁₄EO₃₃ (○) and EO₃₈SO₁₀EO₃₈ (■).

2.3.1 Theoretical estimation of polymeric micelle shape

Taking the length of a SO unit to be 0.36 nm per chain unit (S4), the average length of the fully-stretched SO₁₀ and SO₁₄ blocks of the triblock copolymers are 3.6 and 4.7 nm, respectively. As the central block is looped in the micelle core, the effective length would be 1.8 and 2.3 nm, respectively. The average core volume (v_c) and core radius (r_c) can be estimated from the equation

$$v_c = (4/3)\pi r_c^3 = n v_s N_w \quad (1)$$

where v_s is the volume of a SO unit

$$v_s = M_{w,S} / \rho_s N_A \quad (2)$$

with $M_{w,S} = 120 \text{ g mol}^{-1}$ and $\rho_s = 1.13 \text{ g cm}^{-3}$ being the molar mass of a styrene oxide unit and the density of liquid oxystyrene, respectively, assuming spherical micelles cores with no penetration of water. Assuming that SO blocks have Poisson distributions, as expected in an ideal polymerization of an alkylene oxide (S4), and given the range of block lengths, we see that spherical (or near spherical) micelles are possible for both block copolymers.

2.3.2 Rheological properties of copolymer EO₃₈SO₁₀EO₃₈: Temperature and concentration scans

On the other hand, solutions of copolymer EO₃₈SO₁₀EO₃₈ display a rather similar behavior as those of EO₃₃SO₁₄EO₃₃ except at concentrations up to 20 % wt. The only difference is the narrow soft gel region at temperatures above 70 °C (see Figures S2a). At slightly larger polymer concentrations (23 % wt.) a hard gel region is present between 0 and 8 °C, followed by a soft gel region between 8-13 °C and an unstructured fluid between 13 and 59 °C. The soft gel region observed between 59 and 71 °C points to a further copolymer micelle structuration as temperature increases. The second peak at high temperatures (> 71 °C) does not correspond to a soft gel but to a hard gel region, which is present up to 95 °C (Figure S2b). At larger copolymer concentrations (> 23 % wt.) the $G'(T)$ profiles drastically change, and a wide hard gel region with a maximum G' values of ca. $2.0 \cdot 10^5$ Pa can be found from 0 up to ca. 70 °C. The soft gel region observed at high temperature (~70-80 °C) is very narrow and conducive to a non-structuring fluid (sol) at very high temperatures. This is in contrast with the behavior observed for copolymer EO₃₃SO₁₄EO₃₃, for which a wide high temperature-soft gel region could be observed.

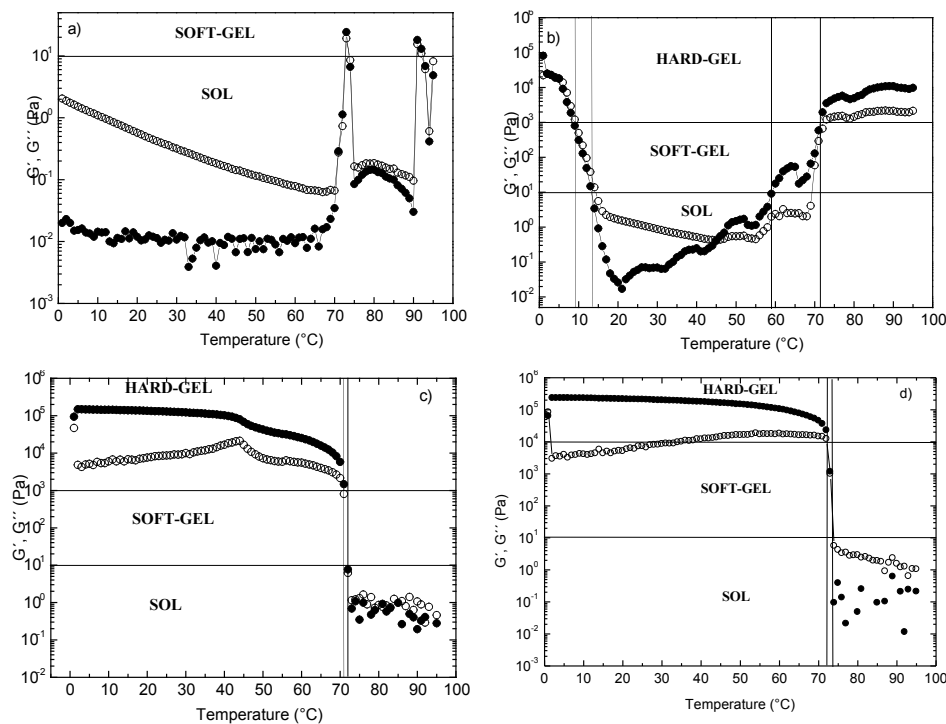


Figure S3: Temperature scans of (●) storage, G' , and (○) loss moduli, G'' , for a) 20 %wt.; b) 23 %wt.; c) 25 %wt.; and d) 40 %wt. of the block copolymer EO₃₈SO₁₀EO₃₈.

2.3.3 References

- S1. Booth, C.; Attwood, D.; Price, C. *Phys. Chem. Chem. Phys.*, 2006, 8, 3612.
- S2. Barbosa, S.; Cheema, M.A.; Taboada, P.; Mosquera, V. J. *Phys. Chem. B*, **2007**, 111, 10920.
- S3. Juarez, J.; Taboada, P.; Valdez, M.A.; Mosquera, V. *Langmuir*, **2008**, 24, 7107.
- S4. Flory, P.J. In *Principles of Polymer Chemistry*, 1953, Cornell UP, Ithaca, New York.

2.4 POLY (STYRENE OXIDE) - POLY(ETHYLENE OXIDE) BLOCK COPOLYMERS: FROM “CLASSICAL” CHEMOTHERAPEUTIC NANOCARRIERS TO ACTIVE CELL-RESPONSE INDUCERS

2.4.1 Abstract

Two poly(styrene oxide)-poly(ethylene oxide) (PSO-PEO) triblock copolymers with different chain lengths were analyzed as potential chemotherapeutic nanocarriers, and their ability to inhibit the P-glycoprotein (P-gp) efflux pump in a multidrug resistant (MDR) cell line were measured in order to establish possible cell-responses induced by the presence of the copolymer molecules. Thus, $EO_{33}SO_{14}EO_{33}$ and $EO_{38}SO_{10}EO_{38}$ polymeric micelles were tested regarding doxorubicin (DOXO) entrapment efficiency (solubilisation test), physical stability (DLS), cytocompatibility (fibroblasts), release profiles at various pHs (*in vitro* tests), as well as P-gp inhibition and evasion and cytotoxicity of the DOXO-loaded micelles in an ovarian MDR NCI-ADR/RES cell line and in DOXO-sensitive MCF-7 cells. $EO_{33}SO_{14}EO_{33}$ and $EO_{38}SO_{10}EO_{38}$ formed spherical micelles (~13 nm) at lower concentration than other copolymers under clinical evaluation (e.g. Pluronic[®]), exhibited 0.2 to 1.8% loading capacity, enhancing more than 60 times drug apparent solubility, and retained the cargo for long time. The copolymer unimers inhibited P-gp ATPase activity in a similar way as Pluronic P85, favoring DOXO accumulation in the resistant cell line, but not in the sensitive cell line. DOXO loaded in the micelles accumulated more slowly inside the cells, but caused greater cytotoxicity than free drug solutions in the NCI-ADR-RES cell line, which overexpressed P-gp. Hence, PSO-PEO block copolymers offer interesting features as new biological response modifiers to be used in the design of efficient nanocarriers for cancer chemotherapy.

2.4.2 Introduction

Advances in materials science offer tremendous opportunities to develop novel nanocarriers able to improve the pharmacokinetics and the local bioavailability of a variety of drugs, apart from providing additional functionalities (1-4). Among the diverse nanoparticulate systems suitable for encapsulating and delivering drugs, micelles formed by amphiphilic polymers occupy a relevant position (5,6). Self-assembly of

biocompatible copolymers consisting of two or more blocks with different hydrophobicity may result in the formation of micelles with a hydrophobic core and a hydrophilic shell. Copolymers bearing hydrophilic poly(ethylene oxide) (PEO) blocks lead to sterically stabilized micelles that show prolonged blood circulation, and passively accumulate in solid tumors (4). The most widely studied amphiphilic copolymers are those composed of PEO and poly(propylene oxide) (PPO) blocks, particularly the linear and bifunctional poloxamers (Pluronic[®]) and the X-shaped poloxamines (Tetronic[®]). PEO–PPO block copolymers have gained popularity over the last decades due to: *i*) their commercial availability; *ii*) proven fair solubilization capacity and sustained drug delivery; *iii*) high biocompatibility of most varieties; *iv*) inhibition of different efflux transporters overexpressed in multidrug resistant (MDR) cells; *v*) ability to enhance drug transport across cellular barriers; and *vi*) regulatory status, i.e., approval of some varieties by US FDA and EMA to be used in pharmaceutical formulations and medical devices (7-9). Nevertheless, PEO–PPO block copolymers display several drawbacks, such as uncomplete micellization of unimers and limited drug solubility and colloidal stability upon dilution in the bloodstream particularly when the EO/PO ratio is high.

To achieve a more efficient aggregation and micelle stability, a series of other block copolymer counterparts of similar architecture but with the PPO segment replaced by a more hydrophobic one such as poly(butylene oxide) (PBO), poly(styrene oxide) (PSO) or phenylglycidyl ether (PG) has been developed by the Attwood and Booth's group in collaboration with us during last years (10-13). The micelles of these copolymers showed improved solubilization capacity and stability (11,14-15). In particular, PSO-based block copolymers are of interest due to the wide availability of architectures and molecular weights (12), their ability to self-assemble into micelles of different shapes at very low concentrations depending on their relative block lengths (16), and their low glass transition temperature (ca. 40 °C), which enables the incorporation of termolabile drugs (11,17). Despite the micellization and solubilisation ability of some PSO-based copolymers have been previously studied (10,12,13,16), as far as we know only one study has analysed the role of PSO-PEO copolymer micelles as carriers of an anticancer drug (docetaxel) (18). Moreover, in contrast to the well-demonstrated inhibitory activity of several PEO-PPO Pluronic[®] and Tetronic[®] block copolymers against drug efflux transporters overexpressed in MDR cells (8,19-20), no reports are available about the potential capabilities of PSO-based copolymers as efflux-pump inhibitors.

Hence, we evaluate the ability of copolymers EO₃₃SO₁₄EO₃₃ and EO₃₈SO₁₀EO₃₈ to dissolve and chemically protect doxorubicin (DOXO), analyzing the colloidal stability, the drug release profiles, the safety, and the *in vitro* efficacy of the drug-loaded polymeric micelles as an antitumoral formulation. The EO/SO ratio and the block lengths of both copolymers were selected to attain an optimal compromise between chain solubility,

micelle formation ability, and core size that lead to enhanced drug solubility, while ensuring renal clearance of unimers as required for non-biodegradable polymers (21). Shorter PEO blocks, as those of EO₁₀SO₁₀EO₁₀ (16), and longer PSO blocks compromise copolymer solubility. By contrast, longer PEO and shorter PSO blocks may lead to greater cmcs with the subsequent increase in material expense to solubilise the required amount of drug (12). EO₃₃SO₁₄EO₃₃ and EO₃₈SO₁₀EO₃₈ may also help to elucidate the effect of copolymer architecture in solubilisation and controlled release performance by comparison with the data reported for PSO diblock copolymers (18). On the other hand, the ability of the present copolymers to inhibit the P-glycoprotein (P-gp) efflux pump was investigated for the first time. DOXO accumulation in an *in vitro* model of MDR cell line with high expression of P-gp (ovarian tumor cell line NCI-ADR-RES) was evaluated and compared with that achieved in a non-resistant cell line (breast cancer cell line MCF-7). Moreover, the effect of the copolymers on P-gp ATPase activity was analyzed and compared to that caused by Pluronic[®] P85, the most efficient cell sensitizing block copolymer so far described (8,19). Overall, the results indicate that the micellar systems based on PSO-PEO block copolymers improves DOXO encapsulation and its systemic delivery, resulting in lower cytotoxicity and enhanced chemotherapeutic activity by the combined effect of the controlled drug release and the inhibition of the P-gp efflux pump.

2.4.3 Experimental section

2.4.3.1 Materials

EO₃₃SO₁₄EO₃₃ and EO₃₈SO₁₀EO₃₈ (Table 1) were synthesized as previously described (10). Weight-averaged (M_w) to number-averaged (M_n) molecular weight ratios were determined at 25°C using a Waters gel permeation chromatography (GPC) system (Waters, Milford, MA). M_n values were estimated from ¹H NMR spectra recorded on a Bruker ARX400 spectrometer (Bruker, Milton, ON, Canada). Pluronic[®] P85 was supplied by BASF (New Milford, CT, USA). Verapamil (VER), calcein AM, and doxorubicin hydrochloride (DOXO·HCl) were from Sigma-Aldrich. DOXO base for solubilisation inside copolymer micelles was obtained by means of aqueous precipitation of DOXO·HCl (1 mg/ml) adding triethylamine (three moles per drug mol) and methylene chloride. Hereinafter, DOXO refers to DOXO base. Water was double distilled and degassed before use. All other reagents were analytical grade.

Table 1. Molecular characteristics of the copolymers.

	M_n^* (g mol ⁻¹)	SO content* (wt.%)	M_w/M_n^{**}	M_w (g mol ⁻¹)
EO ₃₃ SO ₁₄ EO ₃₃	4790	40.0	1.01	4850
EO ₃₈ SO ₁₀ EO ₃₈	5055	34.1	1.02	5130

*Estimated from NMR data; **Determined by GPC; M_w was calculated from M_n and M_w/M_n ratio. Uncertainty: M_n to ± 3 %; wt% SO to ± 1 %, M_w/M_n to ± 0.01 .

2.4.3.2 Methods

a. Drug solubilisation

Solubilization of DOXO (intrinsic solubility in water 0.1-0.5 mg dm⁻³) (22) in micellar copolymer solutions (0.2 wt%) was tested in triplicate following a methodology previously reported (15) (see Supplementary Material).

b. Physical stability of the drug-loaded micelles upon dilution

DOXO micellar solutions were diluted (1/50) with either 0.01 M phosphate buffer pH 7.4 or cell culture medium with 10% FBS and incubated at 37 °C, and the drug concentration was monitored over time by UV spectrophotometry. In parallel, changes in the size of drug-loaded micelles were monitored by dynamic light scattering at 37 °C using an ALV-5000F (ALV-GmbH, Germany) instrument with vertically polarized incident light ($\lambda = 488$ nm) supplied by a diode-pumped Nd:YAG solid-state laser (Coherent Inc., CA, USA) operated at 2 W, and combined with an ALV SP-86 digital correlator (sampling time 25 ns to 100 ms) as previously reported (10) (see Supplementary Material).

c. In vitro DOXO release

Aliquots (4 mL) of DOXO-loaded micellar systems (0.2 wt. % copolymer) in 0.01 M phosphate buffer pH 7.4, 0.01 M sodium citrate buffer pH 5.5, or cell culture media at pH 7.4 or 5.5 were placed into dialysis tubes (SpectraPore®, MWCO 3500), and immersed into the same medium (500 mL) used to prepare the micellar solutions. The medium was kept at 37°C and replaced every 6 hours to maintain *sink* conditions. The released drug concentration was spectrophotometrically monitored at 480 nm, by removing a small volume (20 μ L) that was diluted in methanol in order to fit the calibration curve range. Assays were carried out in triplicate.

d. Copolymer cytocompatibility evaluation

The cytocompatibility of the bare copolymer micelles was first assessed using BALB/3T3 clone A31 mouse embryonic fibroblast cells (CCL 163, ATCC), following a previously reported procedure (23) (see Supplementary Material for further details).

e. Cellular uptake of DOXO after incubation with unimers and empty polymeric micelles (P-gp inhibition)

MDR NCI-ADR/RES and drug-sensitive MCF-7 cells (American Type Culture Collection, MD, USA) were separately seeded in a 24-wells plate (1.5×10^5 cells/well, 1000 μ L/well) in supplemented RPMI 1640 and EMEM medium, respectively, for 48 h. The medium was replaced by serum-free one containing 4-(2-hydroxyethyl)-1-piperazineethanesulfonic acid (HEPES, 25 mM, pH 7.4). Polymer samples were added (20 μ L; final concentrations in the medium 0.001%, 0.01% and 0.2%) and cells incubated at 37°C for 30 min. Polymer-free medium and VER solution (100 μ M) were used as blank and positive control, respectively. Immediately after 30 min incubation, 50 μ L of a DOXO solution (100 mM in water) was added and the samples incubated for 60 additional min. The medium was removed and the cells washed (PBS, 3 x 500 μ L) to remove DOXO and copolymer residues. Quantification of DOXO inside the cells was carried out as previously reported (20) (see Supplementary Material for details). Confocal microscopy analysis (Leica TCS-SP2, LEICA Microsystems Heidelberg GmbH, Germany) was carried out upon cell staining with Bodipy® phalloidin (30 μ L/ml) in 0.2% Triton X-100 (permeabilizer), and subsequent washing and mounting on glass slides using anti-fading solution. Visualization was made at 20X and 63X using green channel for doxorubicin ($\lambda_{exc.}$ 561nm) and red channel for Bodipy® Phalloidin ($\lambda_{exc.}$ 633 nm, see Supplementary Material for details).

f. Cellular uptake of calcein AM after incubation with the polymers

The calcein AM assay was performed following the method described by Dong *et al.* (24) (see Supplementary Material for details).

g. P-gp ATPase assay

The effect of EO₃₃SO₁₄EO₃₃, EO₃₈SO₁₀EO₃₈ and Pluronic P85 at 0.001%, 0.01% and 0.2 wt% on the ATPase activity of Pgp was measured using Pgp-Glo™ Assay System with P-glycoprotein (V3601, Promega Biotech Ibérica, SL, Madrid, Spain) following the manufacturer's protocol. Na₃VO₄ and verapamil (12 mM) were used as controls of inhibition and stimulation, respectively. The luminescence of the samples detected

using a Tecan Ultra Evolution (Tecan, Switzerland) reflected the ATP level, which negatively correlated with the activity of P-gp ATPase.

h. Cellular uptake of DOXO-loaded polymeric micelles (P-gp evasion)

NCI-ADR/RES seeded in 24-wells plates (1×10^5 cells/well) in RPMI 1640 medium with 2 mM L-glutamine, 10% FBS and 1% penicillin/streptomycin over sterile glass covers. After 48 h, culture medium was replaced with RPMI 1640 medium with HEPES 25 mM (pH 7.4). Cells were incubated with formulations containing DOXO for 1 and 24 h at 37°C. Then, DOXO formulations were removed and the cells were washed and stained as explained above. As a control, the cells were incubated with DOXO solution (50 μ M) in PBS at pH 7.4.

i. In vitro cytotoxicity of drug loaded-polymeric micelles

Human NCI-ADR/RES and MCF-7 cells were seeded in 96-wells plates (15.000 cells/well) as described above. Then, DOXO-loaded micellar systems or DOXO-HCl solutions (100 μ M and 50 μ M final concentration) in PBS pH 7.4 were added. As controls, copolymers at 0.01 and 0.2% (final concentrations) were used. Cytotoxicity was evaluated at 24 and 48 h applying the crystal violet method (see Supplementary Material for details).

2.4.4 Results and discussion

The molecular characteristics of copolymers $EO_{33}SO_{14}EO_{33}$ and $EO_{38}SO_{10}EO_{38}$ and the physico-chemical properties of their micelles in diluted and concentrated regime were previously characterized in detail (25). Briefly, $EO_{33}SO_{14}EO_{33}$ and $EO_{38}SO_{10}EO_{38}$ displayed very low cmc in aqueous medium ($2.5 \cdot 10^{-3}$ and $3.7 \cdot 10^{-3}$ wt. %, respectively), and formed monodisperse spherical micelles of ca. 13 nm in diameter and association numbers of 37 and 14, respectively (Table S1 and Figure S1 in Supplementary Material).

2.4.4.1 Solubilization capacity

Some PSO-PEO block copolymers have shown superior solubilisation ability compared to Pluronic® and Tetronic® ones (14,15,17). Optimization of the SO/EO ratio and the blocks length can enhance their performance. Apparent solubility of DOXO was tested in 0.2 wt.% copolymer solutions (above the cmc) by adding different amounts of drug in order to evaluate the impact of the feeding amount on the entrapment efficiency and the total drug loaded. In general, the higher the drug/copolymer weight ratio, the lower the entrapment efficiency was (Table 2) due to drug saturation of the micelles. $EO_{33}S_{14}EO_{33}$ copolymer exhibited a slightly larger solubilisation capacity, which can be attributed to its longer hydrophobic block and subsequent higher affinity of the

micelle core for hydrophobic drugs. Nevertheless, both copolymers encapsulated DOXO very efficiently with a hydrosolubility excess of 30 mg/l; i.e, more than 60 times the aqueous solubility of free DOXO. The maximum loading capacity was ca. 1.8%, with entrapment efficiencies ranging from 20% to 50% depending on the drug feeding concentration. These values are also slightly larger than those reported for DOXO in previous solubilisation studies with other block copolymers, such as PEO-based poly(DL-lactic-co-glycolic acid), PEG-PLGA, poly(caprolactone), PEO-PCL, or poly[N-(2-hydroxypropyl) methacrylamide-lactate], PEG-p(HPMAm-Lac), that had entrapment efficiencies of ca. 23%, 48% or 5%, respectively (26-30).

Table 2: Doxorubicin loaded amount (D.L.), entrapment efficiency (E.E.) and solubilisation capacity (S_{CP}) of the copolymers at 0.2 wt.%.

<i>Feeding drug/polymer % (w/w)</i>	EO₃₃SO₁₄EO₃₃			EO₃₈SO₁₀EO₃₈		
	<i>D.L. %</i>	<i>E.E. %</i>	<i>S_{cp} mg g⁻¹</i>	<i>D.L. %</i>	<i>E.E. %</i>	<i>S_{cp} mg g⁻¹</i>
0.1	0.05	46.7	0.4	0.05	51.8	0.5
0.5	0.2	52.3	2.4	0.2	46.0	2.2
1	0.3	36.8	3.4	0.4	44.7	4.2
2.75	1.0	37.6	10.2	1.0	38.6	10.5
4.25	1.4	34.5	14.5	0.9	22.1	9.3
6	1.8	30.8	16.1	1.3	21.2	11.6

2.4.4.2 Size distribution and physical stability of DOXO-loaded polymeric micelles

Size is critical for the biodistribution profile and the interactions of micelles with cells. Drug incorporation could increase the micellar size due to either the enlargement of the core (31) and/or the fusion of drug-containing micelles into larger ones (32). However, both non-loaded and DOXO loaded-micelles showed similar narrow and monodisperse intensity distribution functions by DLS. The loaded micelles could be readily freeze-dried and their initial size distribution was recovered upon reconstitution in aqueous solution (Figure 1A). The micellar sizes also remained stable upon extensive incubation, which points to a great micelle stability and the capability of the PEO stealth layer to avoid protein binding and subsequent micellar aggregation (Figure 1B and Supplementary Material, Figure S2A).

DOXO-loaded-copolymer micellar solutions were strongly diluted (1/50) in medium with or without 10% FBS to mimic the events after body administration, and the drug concentration was monitored over time. In any tested medium, the loaded-

polymeric micelles were physically stable until 10-12 days. DOXO solubility remained above 86% of the initial value for $\text{EO}_{33}\text{S}_{14}\text{EO}_{33}$ and ca. 75% for $\text{EO}_{38}\text{SO}_{10}\text{EO}_{38}$ when incubating in the cell culture medium (Figure 1C). In the absence of proteins, DOXO solubility remained slightly larger: ca. 92% and 85% for $\text{EO}_{33}\text{S}_{14}\text{EO}_{33}$ and $\text{EO}_{38}\text{SO}_{10}\text{EO}_{38}$, respectively, at 20 days of incubation (Supplementary Material Figure. S2B). The observed slightly lower stability of $\text{EO}_{38}\text{SO}_{10}\text{EO}_{38}$ micelles possibly arises from a less compact/smaller hydrophobic core and higher cmc. In addition, the colloidal stability of $\text{EO}_{33}\text{S}_{14}\text{EO}_{33}$ and $\text{EO}_{38}\text{SO}_{10}\text{EO}_{38}$ micelles is apparently larger than that previously reported for $\text{EO}_{45}\text{SO}_{15}$ and $\text{EO}_{45}\text{SO}_{26}$ diblock copolymers (18); nevertheless, it is necessary to bear in mind that the latter copolymers were subjected to stronger destabilizing conditions which might accelerate their disintegration. Also, micellar stability of $\text{EO}_{33}\text{S}_{14}\text{EO}_{33}$ and $\text{EO}_{38}\text{SO}_{10}\text{EO}_{38}$ is greater than that of some structurally related PBO-PEO and PPO-PEO block copolymers, for which the drug solubilized decreased more than 60% upon extended incubation (18,23,32).

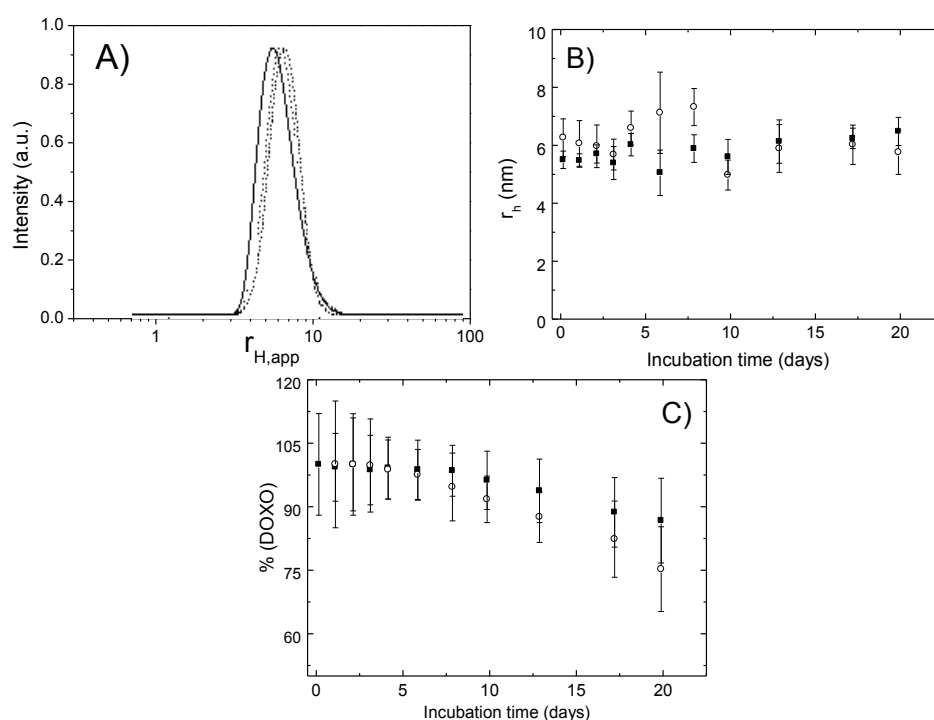


Figure 1: Intensity fraction size distribution of (–) non-loaded, (···) DOXO-loaded and (–) reconstituted freeze-dried DOXO-loaded $\text{EO}_{33}\text{S}_{14}\text{EO}_{33}$ micelles (A); temporal evolution of the size of DOXO-loaded $\text{EO}_{33}\text{S}_{14}\text{EO}_{33}$ (■) and $\text{EO}_{38}\text{SO}_{10}\text{EO}_{38}$ (○) micelles under strong dilution in cell culture medium (B); and %DOXO that remained solubilised in the polymeric micelles over time when diluted with cell culture medium at 37 °C (C).

2.4.4.3 In vitro release

DOXO-loaded micellar solutions (0.2 wt.% copolymer) were dialysed against pH 7.4 and 5.5 buffer and serum-containing (10 % FBS) media using dialysis tubing that

ensured that no micellar diffusion occurred. In general, *in vitro* cumulative DOXO release profiles at both neutral and acidic conditions in the presence of FBS showed a burst followed by a sustained release pattern (Figure 2). At pH 7.4, ca. 25% DOXO was released from both micellar systems in the first 5 h of incubation, and then a more sustained release was observed with ca. 35 % released at 60 h. In general, the amount of drug released from EO₃₈SO₁₀EO₃₈ micelles was slightly larger than from the EO₃₃SO₁₄EO₃₃ ones, probably as a consequence of the observed slightly lower micelle stability due to a less compact hydrophobic core of the former polymer, which may favor the formation of hydrophilic channels (32). The drug release rate was higher at pH 5.5, which is consistent with previous reports (27,33-34) (for modellization of release profiles, see Supplementary Material). At pH 5.5, EO₃₈SO₁₀EO₃₈ and EO₃₃SO₁₄EO₃₃ micelles released, respectively, ca. 39% and 47% of the initially loaded DOXO during the first 5 h and ca. 76% and 63 % at 60 h. As occurred for the stability micellar tests, no significant differences in the release profiles were observed when serum was not present in the medium (Supplementary Material, Figure S3). The faster release under acidic conditions is originated from the reprotonation of the amine group of DOXO, which involves an increase in its hydrophilicity and a decrease in the affinity for the hydrophobic blocks. This in turn favors its escape from the micellar core by an out-diffusion process through the core-shell structure whose diffusion rate depends on factors such as copolymer crystallinity, viscosity, and drug association state (35). Reprotonation would enable DOXO to be preferentially released in acidic tumor sites, compared to healthy tissues. In this regard, it is plausible that copolymer micelles are passively targeted to the tumor tissue through the EPR effect with minimised DOXO release along circulation in the bloodstream. After accumulation in the vicinity of the tumor cells, DOXO could be selectively released from the micelles in the acidic solid tumor microenvironment for passive cellular uptake (33). More importantly, intact copolymer micelles might be also taken up by tumor cells through nonspecific endocytosis and located preferentially at the acidic endosome compartments, in which the decreasing pH values might induce a faster DOXO release and a subsequent diffusion in the cytosol. This cellular uptake mechanism could bypass, to certain extent, the multidrug resistance (MDR) effect, which is often observed when free DOXO penetrates in the cell by passive diffusion.

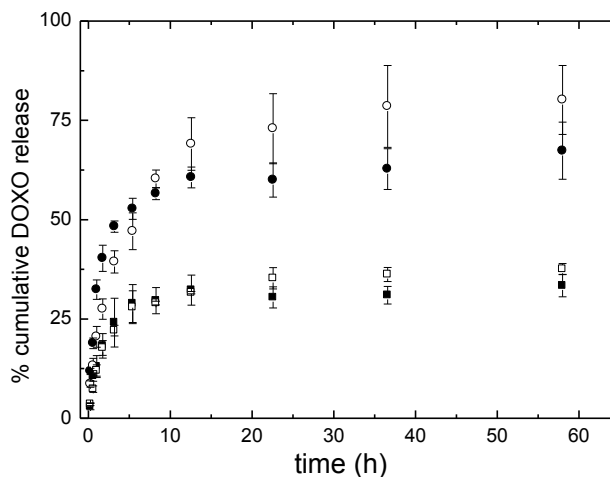


Figure 2: In vitro drug release from DOXO-loaded EO₃₃SO₁₄EO₃₃ (filled symbols) and EO₃₈SO₁₀EO₃₈ (open symbols) micelles in cell culture medium (10 % FBS) at pH 7.4 (squares) and 5.5 (circles).

2.4.4.4 Cytocompatibility of EO₃₃SO₁₄EO₃₃ and EO₃₈SO₁₀EO₃₈

Cytocompatibility tests were carried out against the BALB/3T3 fibroblast cell line because of its high sensitiveness to the presence of toxic species. The LDH assay enabled to measure if this cytosolic enzyme was released to the culture medium due to increased membrane permeability, indicating cell damage or lysis (36). For the lowest concentration tested (0.1 wt.%) viability extents of ca. 100 % were observed for both copolymers, decreasing up to ca. 92% (for EO₃₈SO₁₀EO₃₈) and 84% (for EO₃₃SO₁₄EO₃₃) when copolymer concentration increased up to 1.66 wt.% (Figure 3). In order to prevent false positives caused by possible delayed LDH release from cells after induction of cell apoptosis or necrosis, the activity of the mitochondrial dehydrogenase enzyme was studied by means of the MTT assay. Whilst cell viability for EO₃₃SO₁₄EO₃₃ was ca. 100% in the whole range of concentrations analyzed, proliferation in the presence of EO₃₈SO₁₀EO₃₈ was lower and slightly decreased as the copolymer concentration increased: 95% at 0.1 wt.%, 82.5% at 1.0 wt.%, to ca. 60% at a concentration of 1.66 wt.%, respectively. In any case, none of the copolymer concentrations led to cell viabilities below 50% (37). Therefore, both copolymers can be considered as safe and non-toxic, being even more cytocompatible than most of the commercially available and FDA-approved Pluronic® and Tetronic® block copolymers (20,32).

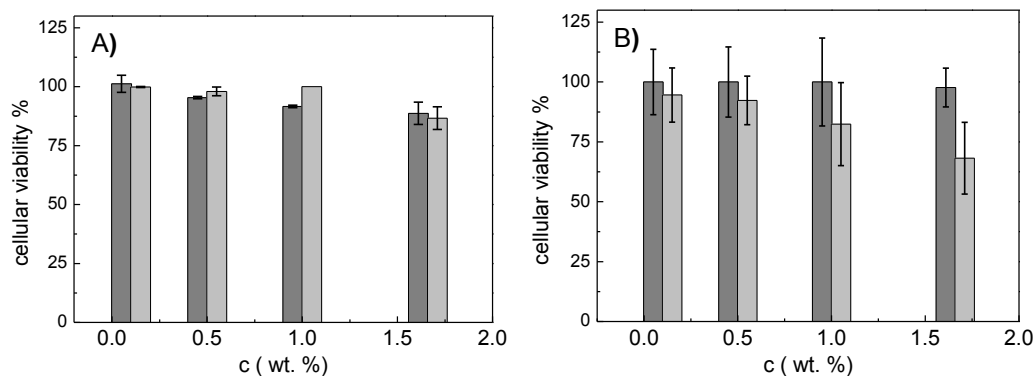


Figure 3: Viability of BALB/3T3 fibroblasts exposed to EO₃₃SO₁₄EO₃₃ (dark grey bars) and EO₃₈SO₁₀EO₃₈ (light grey bars) solutions, measured by means of LDH (A) and MTT (B) assay. Mean \pm SD (n = 3).

2.4.4.5 Inhibition of P-gp efflux pump and intracellular DOXO accumulation

Over-expression in cancer cells of efflux transporters belonging to the ATP-binding cassette proteins superfamily, such as P-gp and MDR-associated proteins (MDR phenotype), severely limits the efficacy of the chemotherapeutic treatments (19,38-39). Efflux of drug molecules in the basolateral-to-apical direction leads to drug removal from the target organ or tissue, and results in subtherapeutic concentrations and very often in therapeutic failure. It has been reported that different PEO-PPO copolymers, such as Pluronic® (8) or Tetronic® (20), PEO-PCL (40), and some natural polymers such as anionic gums and polysaccharides (41), effectively inhibit the activity of the efflux pumps and enhance the accumulation of their substrates in target tissues and organs. The interaction of the individual unimers with the lipid microenvironment surrounding P-gp and the copolymer induced-ATP depletion in MDR cells have been pointed out as possible mechanisms for chemosensitization of these cells (8). We have evaluated the P-gp inhibitory performance of EO₃₃SO₁₄EO₃₃ and EO₃₈SO₁₀EO₃₈ by measuring the intracellular accumulation of DOXO (an exclusive substrate of P-gp) in the ovarian tumor cell line NCI-ADR-RES, which is an adequate *in vitro* model of MDR cells with a relatively high expression of P-gp (42), and also, for comparative purposes, in the drug-sensitive breast cancer cell line MCF-7. The inhibitory P-gp performance of the copolymers at 0.001 (below cmc), 0.01 and 0.2 wt.% (concentration used in solubilisation and drug release experiments) was assessed and compared with that attained with the well-characterized selective and efficient P-gp inhibitors verapamil, VER, (43) and Pluronic® P85 (8,19). Preincubation of MCF-7 cells with any of the polymers or VER did not significantly increase (ANOVA, post-hoc T3 Dunnet) the intracellular accumulation of DOXO (Table S3 in Supplementary Material). Compared to the accumulation level achieved when DOXO solely solution was applied to the NCI-ADR-RES cells, the preincubation with VER 100 μ M led to a 2.12-fold increase in DOXO accumulation, f_{DOXO} . Preincubation of NCI-ADR-RES cells with EO₃₃SO₁₄EO₃₃ and EO₃₈SO₁₀EO₃₈ at 0.2 wt.% increased DOXO accumulation by 1.58 ± 0.18 and 1.34 ± 0.12 -fold, respectively.

Preincubation with the polymers at 0.001 and 0.01 wt.% led to similar DOXO accumulation levels (Table S3 in Supplementary Material). DOXO accumulation levels were statistically higher ($P < 0.01$, ANOVA test, post-hoc T3 Dunnet) than those achieved without preincubation (only DOXO). In contrast, $\text{EO}_{33}\text{SO}_{14}\text{EO}_{33}$ and $\text{EO}_{38}\text{SO}_{10}\text{EO}_{38}$ did not increase the accumulation of calcein-AM, a lipid soluble dye recognized as a substrate for both P-gp and MRP transporters (44), which highlights the complexity of the different efflux pumps mechanisms and their interrelation (see Supplementary Material for details on calcein-AM accumulation studies).

To gain further insight into the mechanism by which $\text{EO}_{33}\text{SO}_{14}\text{EO}_{33}$ and $\text{EO}_{38}\text{SO}_{10}\text{EO}_{38}$ enhanced DOXO accumulation in the P-gp overexpressed cells, the P-gp ATPase activity was recorded. VER is a potent P-gp substrate that leads to ATP consumption and caused 2.68 ± 0.37 -fold increase in ATPase activity compared to the basal activity registered in the presence of orthovanadate, which is in agreement with previous results (45). This effect is the opposite of that recorded for Pluronic P85, which below 0.01% led to a decrease in ATPase activity to the half. As previously observed [19], the effect of Pluronic P85 on P-gp ATPase disappeared at 0.2%, indicating that only the unimers are able to inhibit the activity. Interestingly, $\text{EO}_{38}\text{SO}_{10}\text{EO}_{38}$ and, more remarkably, $\text{EO}_{33}\text{SO}_{14}\text{EO}_{33}$ behaved as Pluronic P85 (Table S3 in Supplementary Material). Namely they inhibited P-gp ATPase. The stronger inhibitory effect of $\text{EO}_{33}\text{SO}_{14}\text{EO}_{33}$, even greater than for Pluronic P85, could be related to its greater hydrophobicity and, thus, to an enhanced ability to alter the conformation of the efflux protein and the ATP-binding domains (19). In the case of $\text{EO}_{38}\text{SO}_{10}\text{EO}_{38}$, the inhibitory effect increased from 0.001% to 0.01% and then leveled off, which is also typical of an unimer concentration-dependent inhibitory effect (19).

Although the P-gp inhibitory effect has been found to be stronger at copolymer concentrations close to the cmc (19,20), we have not observed a detrimental effect on DOXO accumulation when the copolymers concentration raised from 0.001 to 0.2 wt.% (Table S3 in Supplementary Material), which in terms of successful pharmacotherapy, may be beneficial because of the greater ability of copolymers at 0.2 wt.% (due to the larger number of micelles available) to solubilize the drug inside the polymeric micelles and act as efficient drug carriers. At this latter concentration, $\text{EO}_{38}\text{SO}_{10}\text{EO}_{38}$ and $\text{EO}_{33}\text{SO}_{14}\text{EO}_{33}$ unimers in equilibrium with the micelles might be enough to inhibit the P-gp pump.

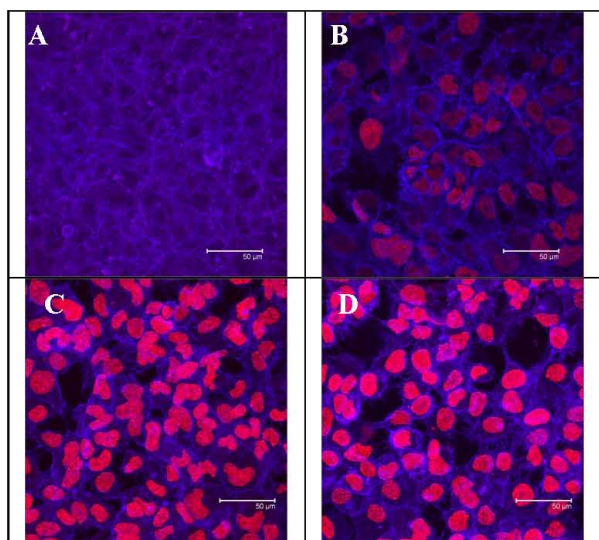


Figure 4: Confocal microscopy images of NCI-ADR-RES cells alone (A); in the presence of 50 μ M DOXO (B); pretreated with 100 μ M VER (C), and with 0.2 wt.% EO₃₃SO₁₄EO₃₃ (D) and then incubated with 50 μ M DOXO. Scale bar 50 μ m.

To evaluate the integrity of the NCI-ADR-RES monolayers and qualitatively assess the localization and intensity of DOXO inside cells, cells preincubated with 0.2 wt.% copolymer and, then, treated with DOXO solely solutions were observed under confocal microscopy (Figure 4). All the specimens showed the nuclear localization of DOXO (46). Cells exposed to VER or to the copolymers were more stained than the non-pretreated cells, confirming that DOXO efflux was inhibited to some extent. The relatively similar fluorescence intensity provided by the DOXO/VER and the DOXO/copolymer systems is in agreement with the quantitative analysis described above that showed no statistical differences in the accumulated DOXO between the systems.

2.4.4.6 Cellular uptake and in vitro cytotoxicity of DOXO-loaded polymeric micelles (P-gp evasion)

In order to avoid DOXO cardiotoxicity and to enhance its chemotherapeutic activity, it is crucial to deliver the drug and to sustain its release in the cytoplasm and right into the nucleus of cancerous cells. We tested the cellular uptake of DOXO-loaded polymeric micelles in the NCI-ADR-RES cell line at 37 °C and compared to that achieved with free DOXO solely solutions at 1 and 24 h after incubation (Figure 5 and Supplementary Material Figure S4). After exposure of the cells to free DOXO, drug accumulation was rapid but limited. DOXO fluorescence intensity after 24 h incubation in the presence of free drug was rather lower than after 1h. Free DOXO may cross the cell membrane by passive diffusion, a pathway that in MDR NCI-ADR-RES cells is affected by P-gp. The observations suggest that DOXO previously uptaken was extruded out of NCI-ADR-RES cells by the P-gp efflux pump. On the contrary, for the DOXO-containing polymeric micelles, drug accumulation increased as a function of time. Low

accumulation inside the cells at short incubation times (1 h, Figure S4) can be related to the relatively low release of DOXO from the micelles at such time (see Figure 2). Confocal images after 24 h of cell incubation in the presence of the drug-loaded polymeric formulations showed an important increase in the drug fluorescence staining inside the cells as a consequence of DOXO accumulation after micelle release. It has been previously shown that as a result of the self-quenching effect of DOXO in nanoparticles, fluorescence is only observed when DOXO is released (47). A more intense fluorescence is noted for larger drug concentrations entrapped in the polymeric micelle cores (see Figure 5). The spotty fluorescence pattern observed for the drug loaded in the polymeric formulations is typical of cytoplasmatic localization of the drug, in contrast to a more intense and continuous pattern observed for usual nuclear accumulation of free DOXO. This suggests that DOXO-loaded micelles might be taken up by an endocytosis-mediated mechanism, being initially located within the endosome vesicles, and enabling DOXO release in the cytosol in a sustained manner due to the endosome acidic environment. At the same time, micelle escape from endosomes and transport to cytoplasmatic organelles could contribute to the observed spotty fluorescence pattern (48). In contrast, free DOXO would be transported into cells via a passive diffusion mainly from the cytosol to the nucleus where would be avidly bound to the chromosomal DNA, generating the continuous fluorescence pattern (35).

Finally, the cytotoxicity of the DOXO-loaded polymeric micelles in NCI-ADR-RES and MCF-7 tumoral cell lines was evaluated applying the crystal violet method (Fig. 6 A and B). This procedure correlates well with others such as the MTT assay, which could not be used in this case because DOXO interferes in the formation of formazan crystals and make the assay unreliable (48). As a control, we have previously tested the potential cytotoxicity of the empty polymeric micelles of $\text{EO}_{33}\text{SO}_{14}\text{EO}_{33}$ and $\text{EO}_{38}\text{SO}_{10}\text{EO}_{38}$ in these cancerous cell lines. Both block copolymers were observed to be safe and non-toxic, with NCI-ADR-RES and MCF-7 viabilities larger than 95% after 24 h of incubation. The viability of NCI-ADR-RES cells scarcely decreased to ca. 87% after 48 h of incubation with $\text{EO}_{33}\text{SO}_{14}\text{EO}_{33}$ at the highest concentration tested (1.66 wt.%, see Figure S5 in Supplementary Material), in agreement with the results obtained with murine fibroblasts (Figure 3). MCF-7 cells resulted to be slightly more sensitive; $\text{EO}_{33}\text{SO}_{14}\text{EO}_{33}$ and $\text{EO}_{38}\text{SO}_{10}\text{EO}_{38}$ at 0.2 wt.% led to 21% and 17% inhibition of cell growth after 48 h of incubation (Figure 6B). Pluronic P85 placebo micelles (0.2 wt.%) resulted to be more cytotoxic and caused 37% and 77% inhibition of NCI-ADR-RES cell growth (Figure 6A) and 16% and 61% inhibition of MCF-7 cell growth after 24 h and 48 h of incubation, respectively (Figure 6B). Growth inhibition caused by Pluronic P85 itself is in agreement with previous reports and related to damage in cell membrane (49).

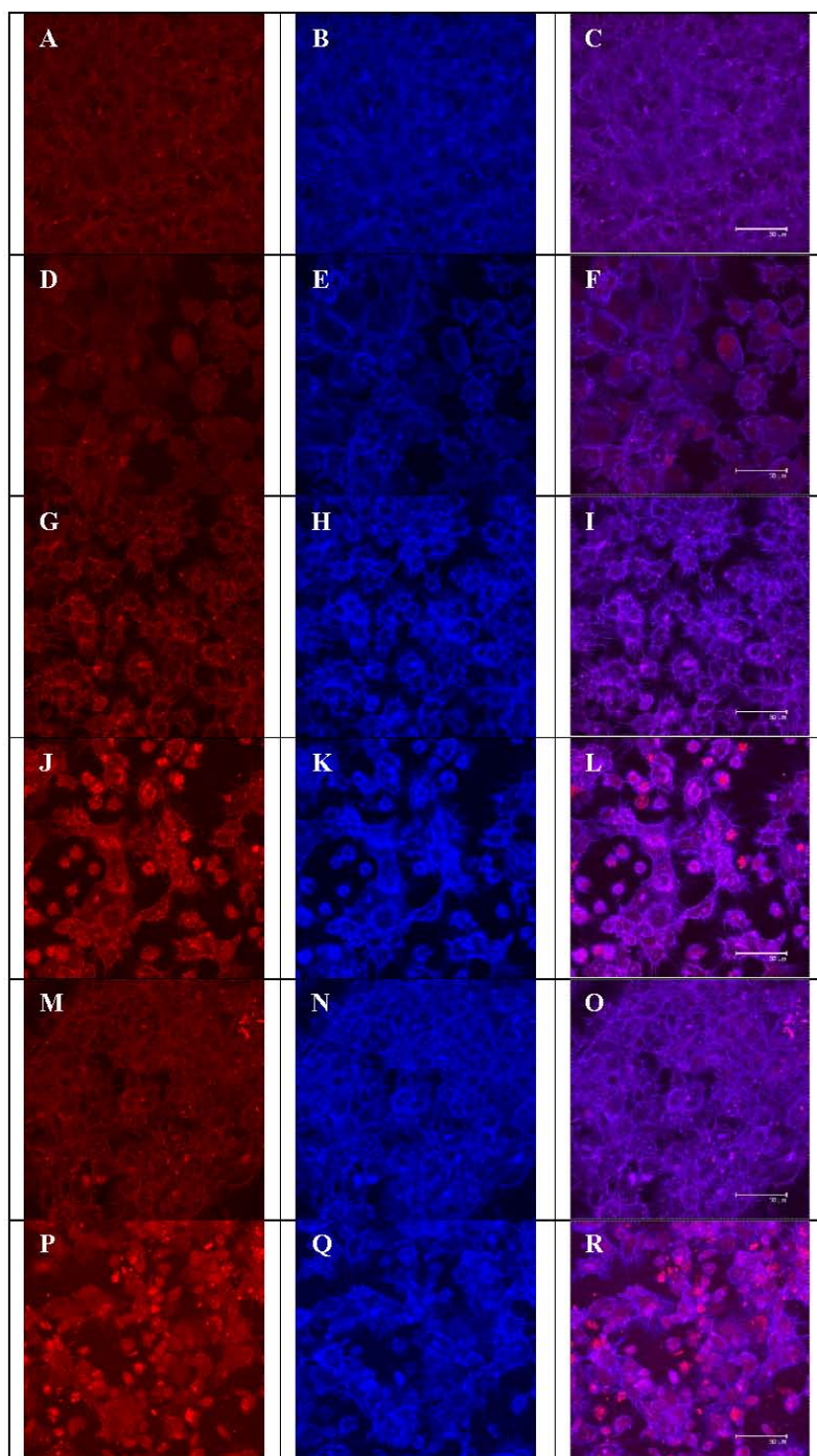


Figure 5: Confocal microscopy images recorded using a DOXO (left column) or a Bodipy® Phalloidin (middle column) filter, and superimposed images (right column) of NCI-ADR-RES cells after 24h of incubation in culture medium solely (A-C, control); with 50 μ M free DOXO (D-F); with 0.2 wt. % $\text{EO}_{33}\text{SO}_{14}\text{EO}_{33}$ micelles loaded with 10 μ M DOXO (G-I) or 50 μ M DOXO (J-L), and with 0.2 wt. % $\text{EO}_{38}\text{SO}_{10}\text{EO}_{38}$ micelles loaded with 10 μ M DOXO (M-O) or 50 μ M DOXO (P-R). Scale bar 50 μ m.

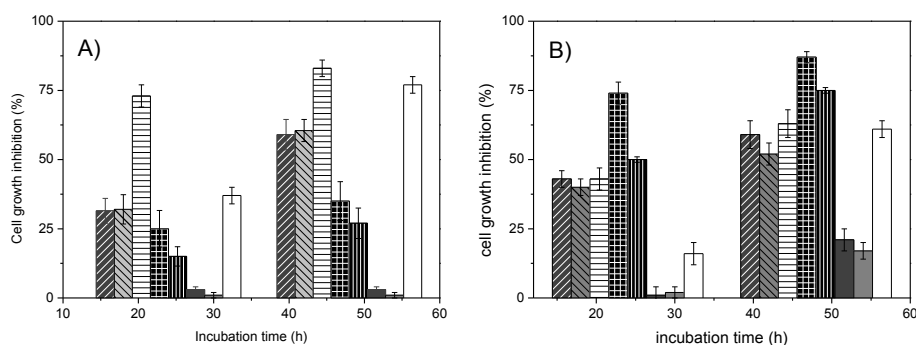


Figure 6: Growth inhibition of NCI-ADR-RES (A) and MCF-7 (B) cells exposed to polymeric micelles (0.2 wt.%) loaded with 50 μ M DOXO, or to 50 μ M and 100 μ M free DOXO solutions. From left to right, columns correspond to DOXO-loaded $\text{EO}_{33}\text{SO}_{14}\text{EO}_{33}$ micelles, DOXO-loaded $\text{EO}_{38}\text{SO}_{10}\text{EO}_{38}$ micelles, DOXO-loaded Pluronic P85 micelles, 100 μ M free DOXO, 50 μ M free DOXO, empty $\text{EO}_{33}\text{SO}_{14}\text{EO}_{33}$ micelles, empty $\text{EO}_{38}\text{SO}_{10}\text{EO}_{38}$ micelles, and empty Pluronic P85 micelles, respectively. Mean \pm SD (n = 3).

The enhancement in cell toxicity observed upon incubation with DOXO-loaded polymeric micelles can be ascribed to the cytotoxic effect of the loaded drug. In particular, the cytotoxic activity of the DOXO-loaded $\text{EO}_{33}\text{SO}_{14}\text{EO}_{33}$ and $\text{EO}_{38}\text{SO}_{10}\text{EO}_{38}$ micelles increased from 24 h to 48 h of incubation, which strongly supports the idea that both the sustained release and increased intracellular accumulation of DOXO leads to a more pronounced cell death. The growth inhibition of NCI-ADR-RES cells doubled from 24 h (ca. 30 % inhibition) to 48 h (ca. 60 % inhibition) (Figure 6A), which is compatible with an increased accumulation inside the cell and a subsequent sustained drug release from the micelles. The cytotoxicity of the drug-loaded polymeric micelles was also larger than that of free DOXO solutions in NCI-ADR-RES cells, even when the free drug concentration was greater than that encapsulated inside micelles (35). No significant differences in cell toxicity were observed between the two copolymers. The highest cytotoxicity recorded for DOXO-loaded Pluronic P85 micelles can be related to the concomitance of the drug internalization and the marked deleterious effect of this copolymer on NCI-ADR-RES cells (Figure 6A). As expected, MCF-7 cells resulted to be more sensitive to the treatment with DOXO, both free or encapsulated in the polymeric micelles (Figure 6B). The IC_{50} values of DOXO for both cell lines at 24 and 48 h are summarized in Table S4.

Provided that both $\text{EO}_{33}\text{SO}_{14}\text{EO}_{33}$ and $\text{EO}_{38}\text{SO}_{10}\text{EO}_{38}$ are highly cytocompatible, DOXO carried by the polymeric micelles would enter the cells most likely via internalization followed by entrapment of the micelles in endosomes/lysosomes. In this way, the drug may evade the P-gp pumps, favoring its cellular accumulation and, hence, increasing the cytotoxic activity when released from the polymeric micelles (37). The enhanced cytotoxicity of the drug-loaded micelles might be originated from both the endocytic intracellular transport (41), which increases the drug cellular uptake, and the contribution of the polystyrene oxide-based block copolymers to the sensitization of

cells, favoring DOXO-induced apoptotic cell death, as reported for Pluronic® and its derivatives (12,20,21,41,46).

2.4.5 Conclusions

The results obtained here with the present PEO-PSO block copolymers highlight the role of a judicious choice of the hydrophobic block and the relative block lengths to achieve a successful cytotoxic effect of the drug-loaded polymeric nanocarriers on cancer cells. Aqueous solutions of block copolymers $EO_{33}SO_{14}EO_{33}$ and $EO_{38}SO_{10}EO_{38}$ self-assemble at very low concentrations to form cytocompatible spherical micelles suitable for sterilizing filtration and administration by parenteral route. These polymeric micelles efficiently entrap DOXO and display a release profile with an initial burst phase at very short times followed by a more sustained rate. The observed pH-dependent release may prompt drug accumulation in tumoral tissues due to the acidic pH conditions in both cell membrane surroundings (caused by hypoxia) and in some intracellular compartments (i.e., lysosomes). The cytotoxic activity of the DOXO-loaded polymeric micelles is exclusively ascribed to the DOXO therapeutic action. Confocal microscopy images showed that DOXO progressively accumulates inside the MDR cells (evading efflux pumps), prolonging their residence inside and, consequently, enhancing cytotoxicity over that observed for free DOXO solutions. Moreover, $EO_{33}SO_{14}EO_{33}$ and $EO_{38}SO_{10}EO_{38}$ unimers have certain ability to inhibit P-gp efflux pump, as occurs for some Pluronic® and Tetronic® block copolymers. Hence, the role of the present copolymers evolve from plain “inert drug nanocarriers” to relevant “biological response inducers” as a consequence of complementation of the drug-cytotoxic activity with a moderate inhibition of the P-gp activity, which highlights the complexity of the cell response to the presence of the block copolymer micelles.

2.4.6 References

1. Farokhzad, O.C.; Langer, R. *Adv. Drug Deliv. Rev.*, **2006**, 58, 1456.
2. Lee, P.Y.; Wong, K.K.Y. *Curr. Drug Deliv.*, **2011**, 8, 245.
3. Heidel, J.; Davis, M. *Pharm. Res.*, **2011**, 28, 187.
4. Ming, S.; Huang, Y.; Han, L.; Qin, J.; Fang, X.; Wang, J.; Yang, V.C. *J. Controlled Release*, **2012**, 161, 884.
5. Markovsky, E.; Baabur-Cohen, H.; Eldar-Boock, A.; Omer, L.; Tiram, G.; Ferber, S. *J. Controlled Release*, **2012**, 161, 446.
6. Wiradharma, N.; Zhang, Y.; Venkataraman, S.; Hedrick, J.L.; Yang, Y.Y. *Nano Today*, **2009**, 4, 302.
7. Kabanov, A.V.; Alakhov, V.Y. *Crit. Rev. Ther. Drug Carrier Syst.*, **2002**, 19, 1.
8. Batrakova, E.V.; Kabanov, A.V. *J. Controlled Release*, **2008**, 130, 98.
9. Alvarez-Lorenzo, C.; Sosnik, A.; Concheiro, A. *Curr. Drug Targets*, **2011**, 12, 1112.

10. Yang, Z.; Crothers, M.; Ricardo, N.M.P.S.; Chaibundit, C.; Taboada, P.; Mosquera, V. *Langmuir*, **2003**, 19, 943.
11. Taboada, P.; Velasquez, G.; Barbosa, S.; Castelletto, V.; Nixon, S.K.; Yang, Z. *Langmuir*, **2005**, 21, 5263.
12. Booth, C.; Attwood, D.; Price, C. *Phys. Chem. Chem. Phys.*, **2006**, 8, 361.
13. Barbosa, S.; Cheema, M.A.; Taboada, P.; Mosquera, V. *J. Phys. Chem. B*, **2007**, 111, 10920.
14. Ribeiro, M.E.N.P.; Vieira, Í.G.P.; Cavalcante, I.M.; Ricardo, N.M.P.S.; Attwood, D.; Yeates, S.G. *Int. J. Pharm.*, **2009**, 378, 211.
15. Crothers, M.; Zhou, Z.; Ricardo, N.M.P.S.; Yang, Z.; Taboada, P.; Chaibundit, C. *Int. J. Pharm.*, **2005**, 293, 91.
16. Juárez, J.; Taboada, P.; Valdez, M.A.; Mosquera, V. *Langmuir* 24 (2008) 7107.
17. Crothers, M.; Ricardo, N.M.P.S.; Heatley, F; Nixon, S.K.; Attwood, D.; Booth, C. *Int. J. Pharm.*, **2008**, 358, 303.
18. Elsbahy, M.; Perron, M.E.; Bertrand, N.; Yu, G.E.; Leroux, J.C. *Biomacromolecules*, **2008**, 8, 2250.
19. Batrakova, E.V.; Li, S.; Li, Y.L.; Alakhov, V.Y.; Kabanov, A.V. *Pharm. Res.*, **2004**, 21, 2226.
20. Alvarez-Lorenzo, C., Rey-Rico, A.; Brea, J.; Loza, M.I.; Concheiro, A.; Sosnik, A. *Nanomedicine*, **2010**, 5, 1371.
21. Yamamoto, Y.; Nagasaki, Y.; Kato, Y.; Sugiyama, Y.; Kataoka, K. *J. Controlled Release*, **2001**, 77, 27.
22. Yalkowsky, S.H.; He, Y. *Handbook of aqueous solubility data*. 2003, Boca Raton: CRC Press.
23. Chiappetta, D.A.; Alvarez-Lorenzo, C.; Rey-Rico, A.; Taboada, P.; Concheiro, A.; Sosnik, A. *Eur. J. Pharm. Biopharm.*, **2010**, 76, 24.
24. Dong, X.; Mattingly, C.A.; Tseng, M.T.; Cho, M.J.; Liu, Y.; Adams, V.R. *Cancer Res.*, **2009**, 69, 3918.
25. Cambón, A.; Barbosa, S.; Rey-Rico, A.; Figueroa-Ochoa, E.; Soltero, J.F.A.; Yeates, S.G. *J. Colloid Interface Sci.* **2012**, 387, 275.
26. Yoo, H.S.; Park, T.G. *J. Control. Release*, **2001**, 70, 63.
27. Shuai, X.; Ai, H.; Nasongkla, N.; Kim, S.; Gao, J. *J. Controlled Release*, **2011**, 98, 415.
28. Diao, Y.Y.; Li, H.Y.; Fu, .Y.; Han, M.; Hu, Y.L.; Jian H.L. *Int. J. Nanomed.*, **2011**, 6, 1955.
29. Talelli, M.; Iman, M.; Varkouhi, A.K.; Rijcken, C.J.F., Schiffeler, R.M.; Etrych, T. *Biomaterials*, 2010, 31, 7797.
30. Diao, Y.Y.; Han, M.; Ding, P.T.; Chen, D.W.; Gao, J.Q. *Die Pharmazie - Int. J. Pharm. Sci.*, 2010, 65, 356.
31. Riess, G. *Progress Polym Sci.*, **2003**, 28, 1107.
32. Wei, Z.; Hao, J.; Yuan, S.; Li, Y.; Juan, W.; Sha, X. *Int. J. Pharm.*, 2009, 376, 176.

33. Lee, Y.; Park, S.Y.; Mok, H.; Park, T.G. *Bioconjug. Chem.*, **2007**, 19, 525.
34. Kim, J.; Lee, J.E.; Lee, S.H.; Yu, J.H.; Lee, J.H.; Park, T.G. *Adv. Mater.* **2008**, 20, 478.
35. Forrest, M.L.; Won, C.Y.; Malick, A.W.; Kwon, G.S. *J. Controlled Release*, **2006**, 103, 370.
36. Decker, T.; Lohmann-Matthes, M.L. *J. Immunol. Methods*, 115 (1988) 61.
37. Cavet, M.E.; Harrington, K.L.; Vandermeid, K.R.; Ward, K.W.; Zhang, J.Z. *Contact Lens Ant. Eye*, **2009**, 32,171.
38. Montesinos, R.; Béduneau, A.; Pellequer, Y.; Lampretch, A. *J. Controlled Release*, **2012**, 161, 50.
39. Wu, C.Y.; Benet, L.Z. *Pharm. Res.*, **2005**, 22, 11.
40. Zastre, J.A.; Jackson, J.K.; Wong, W.; Burt, H.M. *Mol. Pharm.*, 5 (2008) 643.
41. Werle, M. *Pharm. Res.*, **2008**, 25, 500.
42. Roschke, A.V.; Tonon, G.; Gehlhaus, K.S.; McTyre, N.; Bussey, K.J.; Labadidi, S. *Cancer Res.*, **2003**, 63, 8634.
43. Kars, M.D.; Iseri, O.D.; Gunduz, U.; Molnar, J. *Chemother.*, **2008**, 54, 194.
44. Limtrakul, P.; Chearwae, W.; Shukla, S.; Phisalpong, C.; Ambudkar, S.W. *Mol. Cell Biochem.*, **2007**, 296, 85.
45. Litman, T.; Zeuthen, T.; Skovsgaard, T. Stein. W.D. *Biochim. Biophys. Acta*, **1997**, 169, 1361.
46. Shen, S. C.; Bence, A.K.; Bailey, B.; Xue, X.; Erickson, P.A. *J. Pharmacol. Exp. Ther.* **2008**, 324, 95.
47. Li, Y.L.; Zhu, L.; Liu, Z.; Cheng, R.; Meng, F. Cui, J.H. *Angew. Chem. Int. Ed.*,**2009**, 48, 9914.
48. Savić, R.; Luo, L.; Eisenberg, A.; Maysinger, D. *Science*, **2003**, 300, 615.
49. Collier, A.C.; Pritsos, C.A. *Biochem. Pharmacol.*, **2003**, 66, 281.
50. Exner, A.A.; Krupka, T.M.; Scherrer, K.; Teets, J.M. *J. Controlled Release*, **2005**, 106, 188.

2.5 SUPPORTING INFORMATION FOR POLY (STYRENE OXIDE) - POLY(ETHYLENE OXIDE) BLOCK COPOLYMERS: FROM “CLASSICAL” CHEMOTHERAPEUTIC NANOCARRIERS TO ACTIVE CELL-RESPONSE INDUCERS

2.5.1 Materials and methods

Drug solubilisation: DOXO was added in excess to 0.2 wt% copolymer solutions. The systems were kept under magnetic stirring at 37 °C for 3–5 days and then were filtered (Millipore, 0.45 µm). The filtered solutions were diluted (1/1000) with methanol to disrupt the self-assembled structures, the amount of water after dilution being low enough to allow direct use of a calibration plot for methanol medium. The amounts of DOXO solubilised were determined spectrophotometrically at 480 nm (Cary 50 UV-Vis spectrophotometer, Agilent, Germany). Solutions of each copolymer at the same dilution were used as a blank. In order to confirm that solubilisation was predominantly in the core rather than in the EO-block corona, the apparent drug solubility in 5–30 wt% aqueous solutions of polyethylene glycol (M_n 6000 g mol⁻¹) was determined as previously reported (S1). The minimum solubilization observed indicate that only residual solubilisation occurs by incorporation in the corona.

Drug loaded, D.L., and entrapment efficiency, E.E., in the micelles were calculated as follows:

$$D.L.\% = \frac{\text{weight of the drug in micellar solution}}{\text{weight of polymer + drug}} \times 100\% \quad (1)$$

$$E.E.\% = \frac{\text{weight of the drug in micellar solution}}{\text{weight of feeding drug}} \times 100\% \quad (2)$$

The solubilisation capacity (S_{CP}) was estimated as the ratio between the amount of drug dissolved at 37 °C in 100 ml of copolymer solution and the amount dissolved in the same volume of water.

Physical stability of the drug-loaded micelles upon dilution: DLS measurements were made at a scattering angle $\theta = 90^\circ$ to the incident beam. Experiment duration was in the range 5-10 min, and each experiment was repeated at least twice. The correlation

functions from DLS runs were analyzed by the CONTIN method to obtain the intensity distributions of decay rates (I), from which the apparent diffusion coefficients ($D_{app} = I/q^2$, $q = (4\pi n_s/\lambda)\sin(\theta/2)$) were derived (being n_s the refractive index of solvent). Values of the apparent hydrodynamic radius ($r_{h,app}$) were calculated from the Stokes-Einstein equation

$$r_{h,app} = kT/(6\pi\eta D_{app}) \quad (3)$$

where k is the Boltzmann constant and η is the viscosity of water at temperature T .

Copolymer cytocompatibility evaluation. The cytocompatibility of the bare copolymer micelles was first assessed using BALB/3T3 clone A31 mouse embryonic fibroblast cells (CCL 163, ATCC), following a previously reported procedure (S2). Cells were trypsinated and cultured in 96-well plates ($2 \cdot 10^4$ cells/well). Autoclaved copolymer solutions in phosphate buffer pH 7.4 (final copolymer concentration 0.1, 0.5, 1.0 or 1.7%) were added and the cells incubated for 24 h. The medium was replaced by fresh one (200 μ L) containing MTT solution (20 μ L, 5 mg/mL) and the well plates were incubated for 4 h (37°C, 5% CO₂). Immediately after incubation, the supernatant was removed, formazan crystals were dissolved (0.1N HCl in anhydrous isopropanol) and the absorbance measured within 1 h using a microplate reader (BIORAD Model 680, USA) at 570 nm. Cells exposed to copolymer-free culture medium were used as negative control (100% viability). Cell viability was quantified as:

$$\% \text{ viability} = (\text{Abs}_{\text{sample}} / \text{Abs}_{\text{control}}) \times 100 \quad (4)$$

where $\text{Abs}_{\text{sample}}$ and $\text{Abs}_{\text{control}}$ represent the absorbances of the sample of cell culture in the presence and in the absence of copolymer, respectively. The assay was carried out in triplicate. Cell survival was also evaluated monitoring the release of lactate dehydrogenase (LDH) using the cytotoxicity detection Kit^{PLUS} (Roche, Spain). Triton X-100 (0.1%) and copolymer-free culture medium were used as positive control (total cell death) and blank, respectively. The viability (%) was determined from absorbance measurements at 490 nm according to the kit instructions.

Cellular uptake of DOXO after incubation with empty polymeric micelles (P-gp inhibition). DOXO accumulation in the absence and the presence of copolymer unimers and micelles was tested by using MDR NCI-ADR/RES cells and MCF-7 (American Type Culture Collection, MD, USA) seeded in a 24-wells plate (1.5×10^5 cells/well, 1000 μ L/well) in supplemented medium for 48 h following a previously reported method (S3). The medium was replaced by serum-free DMEM containing 4-(2-hydroxyethyl)-1-piperazineethanesulfonic acid (HEPES, 25 mM, pH=7.4). Polymer samples were added (20 μ L) and cells incubated at 37°C for 30 min. Polymer-free medium and VER solution (100 μ M) were used as blank and positive control, respectively. Then, 50 μ l of a DOXO

solution (100 μ M in water) was added and the samples incubated for 60 additional min. The medium was removed and the cells washed (PBS, 3 x 500 μ L) to eliminate DOXO and copolymer residues. Cells were lysed (1% Triton X-100, 300 μ L, 20 min), supernatant aliquots (200 μ L) transferred to opaque 96-well plates, and the fluorescence measured in a plate reader ($\lambda_{exc} = 485$ nm; $\lambda_{em} = 580$ nm; Tecan Ultra Evolution, Männedorf, Switzerland). The remaining 100 μ L were 10-fold diluted with PBS and protein content was measured using Bradford method. DOXO-free medium was used as blank. DOXO concentrations were calculated using a calibration curve (0.2 pmol-0.2 nmol, $R^2 = 0.997$). Determinations were carried out three separate times, each in triplicate. Data of DOXO concentration were normalized to the protein content in each well. DOXO accumulation factors were calculated as follows:

$$f_{DOXO} = AD_s/AD_0 \quad (5)$$

ADs and AD₀ being the accumulated DOXO for the sample and the basal AD obtained with a DOXO solution in absence of polymer or VER. Statistical significance was analyzed applying ANOVA (post hoc Dunnett's T3) with SPSS 15.1 software.

Additionally, confocal microscopy analysis was carried out by seeding the NCI-ADR/RES cells on coverslips in a 24-wells plate (1.5×10^5 cells/well, 1000 μ L/well) in RPMI 1640 medium with 2 mM L-glutamine, 10% FBS and 1% penicillin/streptomycin over sterile glass covers (from Invitrogen). After 48 hours the culture medium was replaced with RPMI 1640 containing HEPES 25 mM (pH 7.4). The cells were incubated at 37°C for 30 minutes with 50 μ L of VER 100 μ M or 0.2 wt.% polymeric dispersions. Then, DOXO (50 μ M, 50 μ L) was added and the cells incubated for another 60 minutes at 37°C. The formulations were removed and the cells were washed three times with phosphate saline buffer pH 7.4 (PBS, Sigma) and then fixed with paraformaldehyde 4% for 10 min, washed and stained with Bodipy® phalloidin (30 μ L/ml) in 0.2% Triton X-100 (permeabilizer). The cells were washed again with PBS pH 7.4 (3x10 min), mounted on glass slides using anti-fading solution (Bio-Rad laboratories, Hercules, CA, USA), and visualized at 20X and 63X using a **Confocal Spectral Microscope Leica TCS-SP2 (LEICA Microsystems Heidelberg GmbH, Mannheim, Germany)**; green channel for doxorubicin (λ_{exc} . 561nm) and red channel for Bodipy® Phalloidin (λ_{exc} . 633 nm).

Cellular uptake of calcein AM after incubation with the copolymers: NCI-ADR RES cells were seeded in black 96-well pretreated plates (1×10^5 cells/well) and cultured in supplemented medium for 48 h. The medium was replaced by serum-free RPMI 1640 containing 4-(2-hydroxyethyl)-1-piperazineethanesulfonic acid (HEPES, 25 mM, pH=7.4). Aliquots of copolymer solutions were added (20 μ L, 0.01 and 0.2 wt.% final concentrations) and the cells incubated at 37°C for 30 min. Then, 0.25 μ M calcein-AM was added and the cells incubated for other 30 min at 37°C. The medium was removed, the cells washed (PBS, 3 x 100 μ L) and the intracellular fluorescence of calcein measured

in a plate reader ($\lambda_{exc} = 485 \text{ nm}$; $\lambda_{em} = 535 \text{ nm}$) at 5 minutes intervals during 1 h in order to attain stable fluorescence lectures. Cells were lysed (1% Triton X-100, 100 μL) and the protein content was measured according to the Bradford method. The experiments were repeated four times. The calcein accumulation in the cells was expressed as fluorescence relative units (RFU) of calcein /mg of protein, as follows:

$$CA = C_t/C_0 \quad (6)$$

C_t and C_0 being the calcein accumulation in the presence and absence of the copolymer, respectively. Statistical significance was analyzed applying ANOVA (post hoc Dunnet's T3; SPSS 15.1 software).

In vitro cytotoxicity of drug loaded-polymeric micelles. Crystal violet assay: At the selected time points, the culture medium was removed and cells were fixed with glutaraldehyde (10 μL , 11%) for 15 min and, then, washed to eliminate glutaraldehyde residues. Cells were stained with 100 μL of crystal violet solution 0.1% in pH 6 buffer (orthophosphoric acid 200 mM, formic acid 200 mM, and 2-N-morpholine-ethanesulfonic acid 200 mM) at room temperature for 15 min, and then washed with distilled water and dried. Finally, cells were treated with 100 μL of 10% acetic acid at room temperature for 15 min under gentle stirring and the absorbance was measured in a plate reader ($\lambda = 595 \text{ nm}$; Tecan Ultra Evolution). Copolymer-free PBS was used as a control and showed 2-4% inhibition with respect to cells incubated in serum-containing medium. Experiments were carried out in triplicate. The growth inhibition was quantified as:

$$\%inhibition = 100 - (AO \cdot 100 / AT) \quad (7)$$

AO and AT being the absorbances of the sample and of the PBS control, respectively.

2.5.2 Modellization of release profiles

Drug release profiles from the micellar systems were fitted to the following Fickian diffusion model considering the micelles as perfect spheres (S4):

$$M_t/M_\infty = k_1 + k_2 \cdot t^{0.5} - k_3 \cdot t \quad (8)$$

where M_t and M_∞ represent the drug amount released at time t and that initially contained in the formulation, respectively, and k_1 , k_2 and k_3 are release rate coefficients. This model takes into account drug diffusion, conformational changes in the micellar structure during release and partial transfer of drug from one micelle to another. The model fitted well the release profiles (Table 4, $R^2 > 0.90$), unlike the simpler square-root model which could not explain the whole profiles. The coefficient associated to drug

diffusion, k_2 , became larger as the pH decreased from 7.4 to 5.5 for both copolymers, as expected for an enhanced out-diffusion process of the reprotonated DOXO under acidic conditions (Supplementary Material, Table S2).

2.5.3 Calcein accumulation studies

Calcein-AM tests were carried out to gain an insight into the mechanism of inhibition of P-gp pump (S5). Calcein-AM is a lipid soluble dye recognized as a substrate for both P-gp and MRP transporters (S6). Upon entering cells, endogenous esterases cleave calcein-AM to form the hydrophobic fluorescent calcein. ABC-transporters cause rapid efflux of calcein-AM, but they cannot expel calcein once formed inside the cells (S7). Although $\text{EO}_{33}\text{SO}_{14}\text{EO}_{33}$ and $\text{EO}_{38}\text{SO}_{10}\text{EO}_{38}$ enhanced DOXO accumulation in NCI-ADR RES cells, they did not increase the accumulation of calcein. At copolymer concentration of 0.01 wt.%, calcein accumulation was, respectively, 0.80 ± 0.16 and 0.92 ± 0.15 , and at 0.2 wt.% it was 0.89 ± 0.20 and 0.73 ± 0.10 -fold the basal level obtained for non-pretreated cells. This finding may be the result of several concomitant facts. One possibility is that, although MRP1 is scarcely found in NCI/ADR-RES cells (S8), the efficient inhibition of P-gp pump exerted by the copolymers may favor calcein efflux by MRP1 and MRP2, as observed by Evers and coworkers for Pluronic L61 (S9). Batrakova and Kabanov (S10) found that Pluronic P85 can inhibit P-gp drug efflux system, but cause an only partial inhibition on MRP activity. Tetronics have shown no inhibition of MRP1 in hepatocarcinoma cell lines (S11). Furthermore, it might occur that since the P-gp pump has several binding domains [S12], different substrates may interact with different sites of the protein and the same may happen with the inhibitors. For example, Pluronic F127 cannot block the binding of nelfinavir to the pump, while it effectively inhibits verapamil association (S13). This phenomenon makes the prediction of the inhibitory activity of a pump with respect to a specific substrate by a certain polymer very complex. On the other hand, the micellar encapsulation of calcein-AM could contribute to a lower accumulation (S14). The inherent property of the unimers to self-assemble as micelles could lead to a strong trapping of calcein-AM outside the cells. The high affinity of the calcein-AM for the lipophilic core provided by styrene oxide block could even prompt the self-assembling of more unimers into micelles, as previously observed for other copolymers and hydrophobic drugs (S15). Nevertheless, these aspects would require further elucidation.

Table S1: Critical micelle concentration, cmc , expansion factor, δ_t ; micellar molecular mass, M_w ; hydrodynamic radius, r_h ; association number, N_w ; and number of water molecules per EO group, n_{water} , of $EO_{33}SO_{14}EO_{33}$ and $EO_{38}SO_{10}EO_{38}$ at 37 °C.

Copolymer	cmc (wt%)	δ_t	M_w (mol g ⁻¹)	r_h (nm)	N_w	n_{water}
$EO_{33}SO_{14}EO_{33}$	$2.5 \cdot 10^{-3}$	4.7	$17.8 \cdot 10^4$	6.2	37	14
$EO_{38}SO_{10}EO_{38}$	$3.7 \cdot 10^{-3}$	3.5	$6.9 \cdot 10^4$	6.2	14	9

Table S2: Results of the fitting to equation 8 of the DOXO release profiles from $EO_{33}SO_{14}EO_{33}$ and $EO_{38}SO_{10}EO_{38}$ micellar solutions in pH 5.5 and 7.4 media without or with 10% FBS. The release rate coefficients are given as mean values, with standard deviations in parenthesis.

Copolymer	pH	FBS (%)	k_1	k_2	k_3	*F _{2,8d.f}	*P- value	R ²
$E_{33}SO_{14}EO_{33}$	5.5	0	5.28 (10.56)	27.48 (8.22)	-3.22 (1.38)	16.77	0.0114	0.8934
	7.4	0	0.06 (2.71)	11.24 (2.11)	-1.20 (0.35)	56.85	0.0012	0.9660
$E_{38}SO_{10}EO_{38}$	5.5	0	30.32 (3.68)	13.76 (2.86)	-1.28 (0.48)	65.29	0.0009	0.9703
	7.4	0	5.99 (3.38)	11.68 (2.63)	-1.39 (0.44)	28.59	0.0043	0.9346
$E_{33}SO_{14}EO_{33}$	5.5	10	11.08 (4.67)	17.28 (2.81)	-1.32 (0.31)	44.16	0.0000	0.9169
	7.4	10	2.10 (3.00)	12.46 (2.03)	-1.16 (0.25)	34.23	0.0001	0.8954
$E_{38}SO_{10}EO_{38}$	5.5	10	-1.67 (1.85)	21.22 (1.11)	-1.37 (0.12)	649.67	0.0000	0.9939
	7.4	10	-0.14 (2.00)	13.25 (1.35)	-1.13 (0.17)	112.34	0.0000	0.9656

* From ANOVA of the regression.

Table S3: DOXO accumulation factors (f_{DOXO}) attained after preincubation of drug-sensitive and drug-resistant cells for 30 min with the copolymers before adding DOXO to the medium (final drug concentration 50 μM), and P-gp ATPase activity recorded using the Pgp-Glo assay system. Mean values and, in parenthesis, standard deviations of three independent experiments. Cell preincubation with VER 100 mM led to 1.04-fold (1.05 nmolDOXO/mg protein) and 2.12-fold (6.8 nmolDOXO/mg protein) increase in DOXO accumulation in MCF-7 and NCI-ADR-RES cells, respectively. VER 12 mM resulted in 2.68-fold increase in ATPase activity. * $P < 0.05$; ** $P < 0.01$.

Parameter	EO ₃₃ SO ₁₄ EO ₃₃			EO ₃₈ SO ₁₀ EO ₃₈			Pluronic® P85		
	0.001%	0.01%	0.20%	0.001%	0.01%	0.20%	0.001%	0.01%	0.20%
f_{DOXO} in MCF-7 cells	1.52 (0.18)	1.18 (0.28)	1.09 (0.22)	1.13 (0.22)	1.06 (0.22)	1.02 (0.19)	1.16 (0.28)	1.07 (0.26)	1.03 (0.19)
f_{DOXO} in NCI-ADR-RES cells	1.56** (0.37)	1.44** (0.24)	1.58** (0.18)	1.54** (0.34)	1.47** (0.26)	1.34** (0.12)	1.96** (0.36)	2.18** (0.36)	2.23** (0.56)
P-gp ATPase activity	0.15** (0.20)	0.30** (0.13)	0.55 (0.20)	1.17 (0.26)	0.84 (0.25)	0.86 (0.19)	0.42* (0.28)	0.66 (0.22)	1.37 (0.22)

Table S4: IC₅₀ (μM) of DOXO. Mean values and, in parenthesis, standard error of the mean (n=3).

Cell line	24 h	48 h
MCF-7 cells	7.61 (0.70)	0.97 (0.13)
NCI-ADR-RES cells	20 (2)	31 (3)

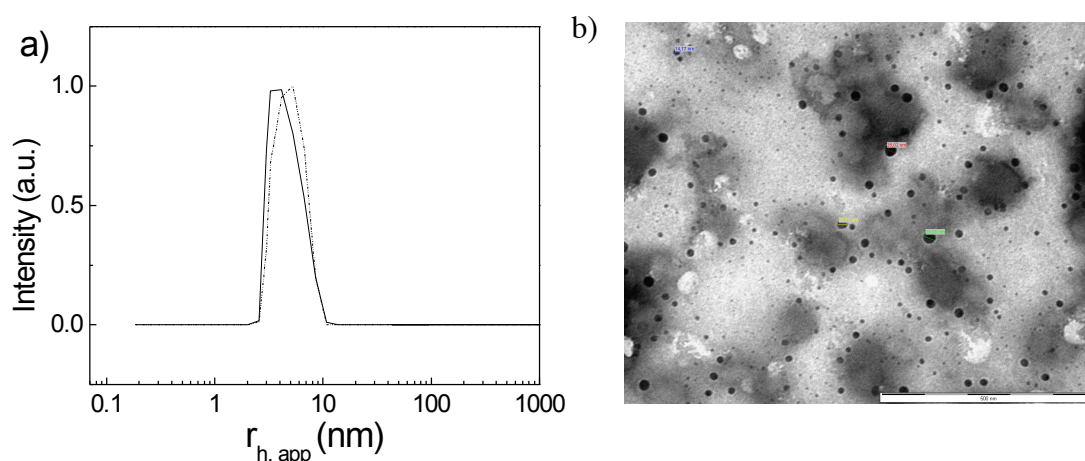


Figure S1: a) Intensity fraction size distributions of EO₃₃SO₁₄EO₃₃ (–) and EO₃₈SO₁₀EO₃₈(····) at a concentration of 90 g dm⁻³ and 37 °C; b) TEM image of EO₃₈SO₁₀EO₃₈ micelles .

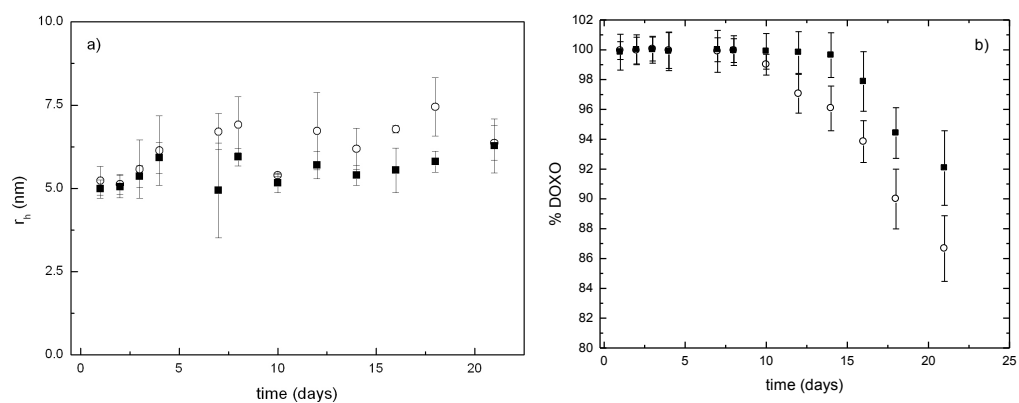


Figure S2: a) Temporal evolution of the size and b) of %DOXO remaining encapsulated of DOXO-loaded $\text{EO}_{33}\text{SO}_{14}\text{EO}_{33}$ (■) and $\text{EO}_{38}\text{SO}_{10}\text{EO}_{38}$ (○) micelles at pH 7.4 under strong dilution in buffer only medium.

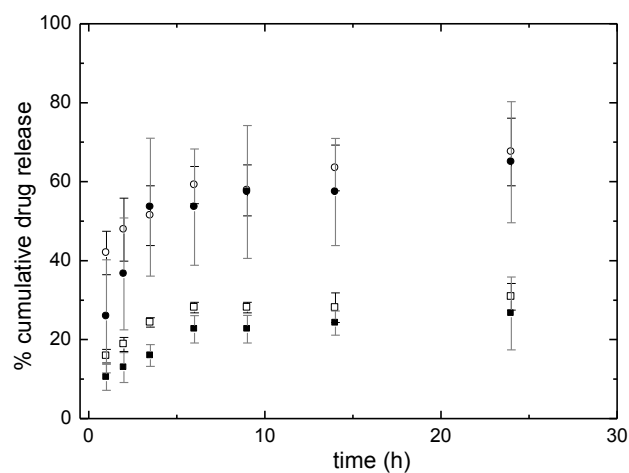


Figure S3: In vitro drug release profiles from DOXO-loaded copolymer micelles in buffer only solution at pH 7.4 (squares) and 5.5 (circles) for $\text{EO}_{33}\text{SO}_{14}\text{EO}_{33}$ (filled symbols) and $\text{EO}_{38}\text{SO}_{10}\text{EO}_{38}$ (open symbols).

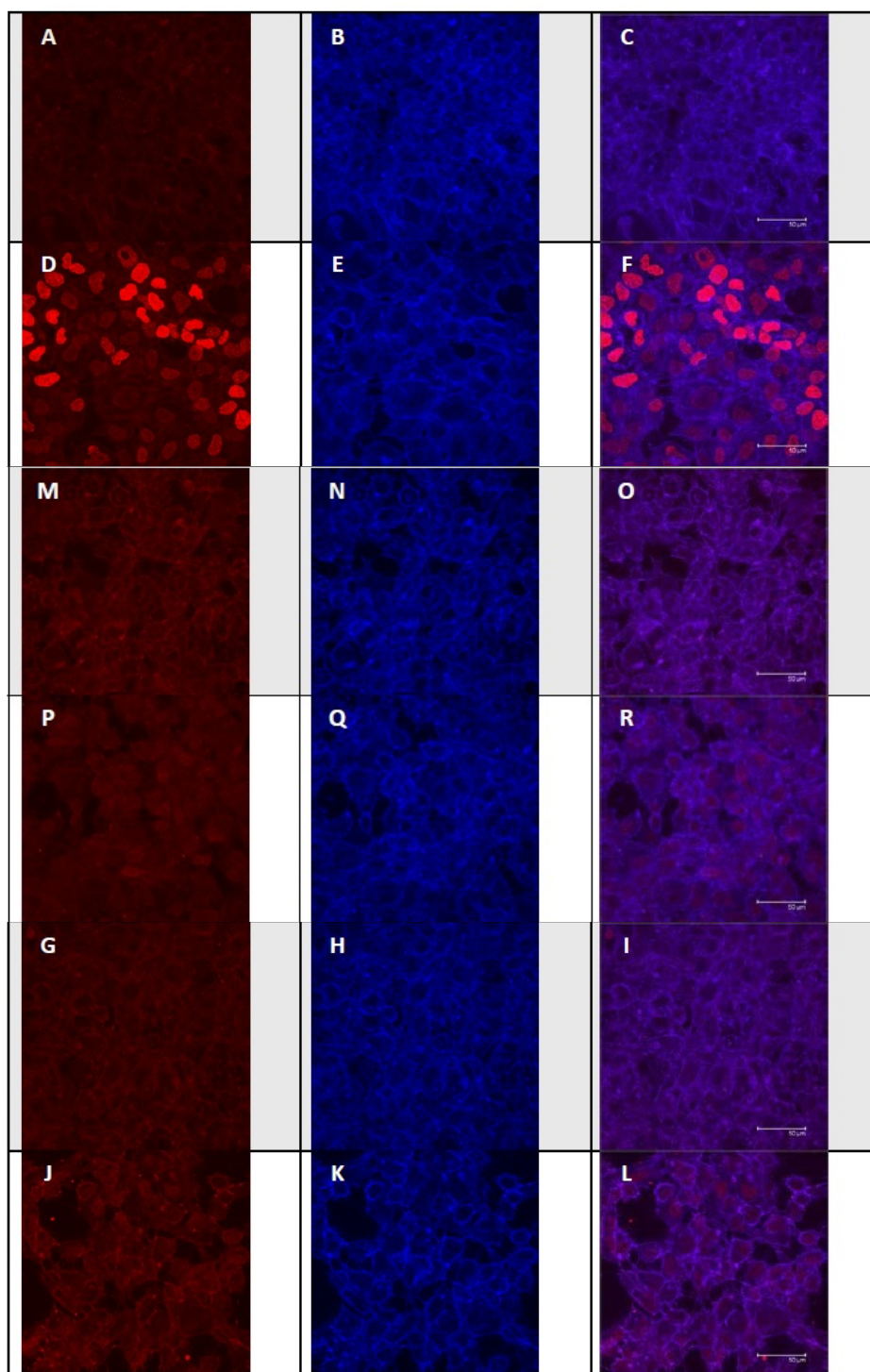


Figure S4: Confocal microscopy images with DOXO filter (left column), Bodipy® Phalloidin filter (middle column), and superimposed image (right column) for NCI-ADR-RES cells alone after 1h of incubation (A-C); with 50 μ M free DOXO (D-F); in the presence of 0.2 %wt. EO₃₃SO₁₄EO₃₃ micelles loading 10 μ M DOXO (G-I) and 50 μ M DOXO (J-L), and 0.2 %wt. EO₃₈SO₁₀EO₃₈ micelles loading 10 μ M DOXO (M-O) and 50 μ M DOXO (P-R). Scale bar 50 μ m.

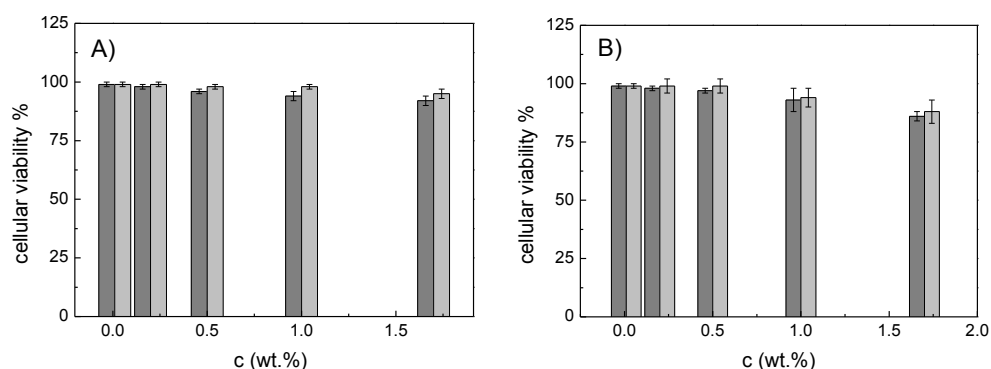


Figure S5: Growth inhibition of NCI-ADR-RES cells exposed to bare polymeric micelles at different concentrations of copolymers EO₃₃SO₁₄EO₃₃ (dark grey bars) and EO₃₈SO₁₀EO₃₈ (light grey bars) solutions at A) 24 h and B) 48 h.

2.5.4 References

- S1. Yalkowsky, S.H.; He, Y. Handbook of Aqueous Solubility Data.2003, Boca Raton: CRC Press.
- S2. Chiappetta, D.A.; Alvarez-Lorenzo, C.; Rey-Rico, A.; Taboada, P.; Concheiro, A.; Sosnik, A. Eur. J. Pharm. Biopharm., **2010**, 76, 24.
- S3 Alvarez-Lorenzo, C.; Rey-Rico, A.; Brea, J.; Loza, M.I.; Concheiro, A.; Sosnik, A. Nanomedicine, **2010**, 5, 1371.
- S4. Wang, H.; Xu, J.; Wang, J.; Chen, T.; Wang, Y.; Tan, Y.W. Angew. Chem. Int. Ed. **2010**, 49, 8426.
- S5. Dong, X.; Mattingly, C.A.; Tseng, M.T.; Cho, M.J.; Liu, Y.; Adams V.R. Cancer Res., **2009**, 69, 3918.
- S6. Limtrakul, P.; Chearwae, W.; Shukla, S.; Phisalpong, C.; Ambudkar, S.W. Mol. Cell Biochem., **2007**, 296, 85.
- S7. Eilers, M.; Roy, U.; Mondal, D. Exp. Biol. Med., **2008**, 233, 1149.
- S8. Zhang, S.; Yang, X.; Morris, M.E. Mol. Pharmacol., **2004**, 65, 1208.
- S9. Evers, R.; Kool, M.; Smith, A.J.; Van Deemter, L.; De Haas,M.; Borst, P. J. Cancer, **2000**, 83, 366.
- S10. Batrakova, E.V.; Kabanov, A.V. J. Controlled Release, **2008**, 130 (2008) 98.
- S11. Cuestas, M.A.L.; Sosnik, A.; Mathet, V.N.L. Mol. Pharm. **2011**, 8, 1152.
- S12. Garrigos, M.; Mir, L.M.; Orłowski, S. Eur. J. Biochem. **1997**, 244, 664.
- S13. Shaik, N.; Pan, G.; Elmquist, W.F. J. Pharm. Sci.**2008**, 97, 5421.
- S14. Hanke, U.; May, K.; Rozehnal, V.; Nagel, S.; Siegmund, W. Weitschies, W. Eur. J. Pharm. Biopharm., **2010**, 76, 260.

S15. Montesinos, R.; Béduneau, A.; Pellequer, Y.; Lampretch, A. J. Controlled Release,, 2012, 161, 50.

CHAPTER 3

$\text{BO}_n\text{EO}_m\text{BO}_n$ COPOLYMERS

AS NANOCARRIERS

OF HYDROPHOBIC DRUGS

3.1 AIM OF THE WORK

In the previous chapter two triblock copolymers were synthesized and tested as drug nanocarriers because their similar structure to Pluronics, one of the most deeply studied copolymers family up to day in nanopharmaceutics. ESE copolymers have a very hydrophobic central block that implies lower cmc values and, as a consequence, lower polymer concentrations needed to form micelles and encapsulate and release similar cargo amounts. In addition, the block lengths and E/S ratio of these copolymers were chosen to attain an optimal compromise between chain solubility, micelle formation ability, and core size that lead to an enhanced drug solubility, while ensuring renal clearance of unimers as required for non-biodegradable polymers (1-4).

In order to improve the properties related to micellar nanocarriers, specially micelle formation ability, we have analyzed the potential use of telechelic block copolymers generally used as associative thickeners as potential drug nanocarriers, new reverse triblock copolymers formed by an inner very long poly(ethylene oxide) (PEO) hydrophilic and two side poly(butylene oxide) (PBO) blocks were synthesized and tested, in which the poly(butylene oxide) (PBO) is less hydrophobic than PEO ones (in a ratio of 1:1.5 based on cmc value of structurally related linear block copolymers of the two families (see Figure 1) (5, 6). Nevertheless, by using reverse triblock copolymers having one central very long hydrophilic block (PEO) and two side hydrophobic blocks, an increase in hydrophobicity needed to improve the drug solubility is expected. Owing to have longer and less hydrophobic blocks, bigger nuclei are expected, which would also be related to an increase in drug solubility ability.

Five PBO-PEO-PBO copolymers were synthesised by sequential oxyanionic polymerization. To ensure aqueous solubility, they were provided with very long PEO central block. These polymers were designed with different PBO block lengths and PEO/PBO ratios with the aim to correlate the block composition and length with the observed physico-chemical properties in solution (7). Aggregation properties in aqueous solutions at low concentrations are the first focus point, provided that these copolymers could form unimolecular micelles as diblock EO-BO copolymers do (5). As well as EO-BO-EO copolymers, BO-EO-BO ones are expected to form spherical micelles in aqueous solution but with a very loosely corona (the so-called flower-like micelles) with an optimal size for intravenous injection of 10-30 nm (8). Micelles have a core-shell structure as expected, where the hydrophobic core might act as a drug reservoir for hydrophobic drugs and the PEO shell should contribute to extend blood circulation

times. [9, 10]. As a final goal, reverse triblock copolymers are expected to gel under low concentrations and/or temperature in order to create drug depots and achieve a prolonged sustained release, maintaining the therapeutic effect for weeks or months.

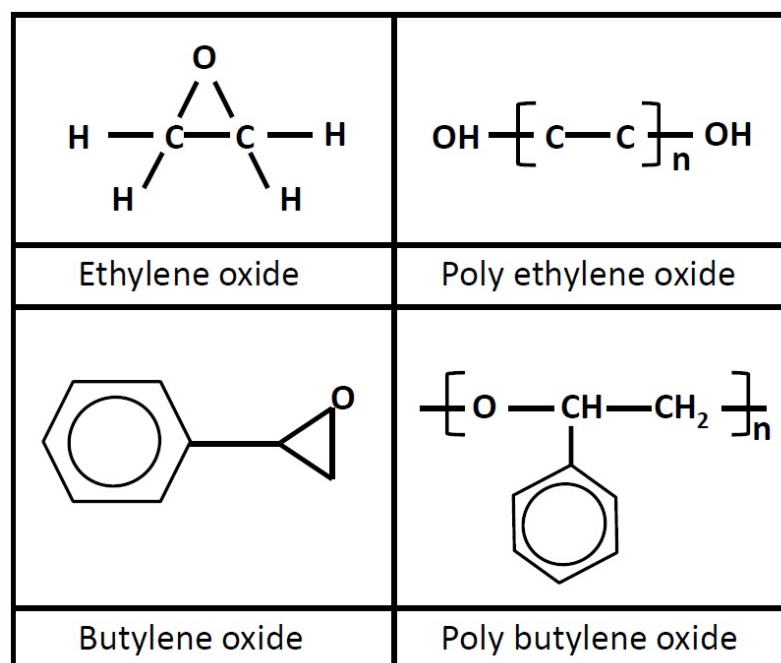


Figure 1. Constituent monomers of PBO-PEO-PBO block copolymers.

3.1.1 Aim of the work

In the present work, we report on the synthesis and characterization of the self-assembly properties of five new triblock PBO-PEO-PEO copolymers with lengthy PEO blocks (see Figure 1): $\text{BO}_8\text{EO}_{90}\text{BO}_8$, $\text{BO}_{12}\text{EO}_{227}\text{O}_{12}$, $\text{BO}_{14}\text{EO}_{378}\text{BO}_{14}$, $\text{BO}_{20}\text{EO}_{411}\text{O}_{20}$ and $\text{BO}_{21}\text{EO}_{385}\text{O}_{21}$ (where the subscripts denote the block lengths). To reveal the self-aggregation properties for these polymers in aqueous solution is the previous step to test the ability of this class of copolymers to encapsulate, protect, and ensure a sustained release of the loaded drug (doxorubicin), which are the main goals to achieve in this part of the work. Also, the cytotoxicity of empty and drug-loaded micelles was tested in order to verify the biocompatibility of the different types of micelles and to ensure their therapeutic activity.

3.1.2 Methodology

Physico-chemical characterization was performed by means of isothermal titration

calorimetry, UV-vis and fluorescence spectroscopy, light scattering, transmission electron microscopy (TEM), confocal microscopy and rheometry.

Briefly, five PBO-PEO-PBO triblock copolymers with lengthy inner hydrophilic blocks and relatively longer side hydrophobic blocks than those previously reported (11-13), have been designed and synthesized in order to obtain polymeric micelles at relatively low concentrations. The present block copolymers have been characterized to exactly determine their structural conformation, composition block length and purity (polydispersity index). A deep physico-chemical study on their aqueous solution properties in a broad copolymer concentration range was performed, from dilute solutions to gel structures. The micellization process was carefully analyzed in order to verify or neglect the existence of unimolecular micelles as an intermediate aggregation step between unimers and polymolecular micelles, previously observed in PEO-PBO diblock copolymers (14, 15). In addition, the spherical shape of polymolecular micelles was verified, as well as other micellar properties as the hydrophobic radius, molecular micellar weight and aggregation number, amongst others. Phase diagrams showing the clouding point and the gelation temperatures were performed in order to complete the polymer aggregation map from dilute aqueous solutions to physical gels (11-13, 16). To fulfill the study about the aggregation properties of PBO-PEO-PBO triblock copolymers, the gel region was deeply analyzed (10,17). Storage and loss modulus (G' and G'' , respectively), which can be ascribed to different internal forces of the polymeric network, were analysed under varying temperature and frequency conditions. To complete the rheological study, master curves were constructed to extend their profile to frequencies that are not achievable by the rheometer. These curves permit to extract a common rheological profile independent on the structure/composition of the corresponding polymer.

Efficiency entrapment tests were performed with the different copolymers in order to correlate the copolymer composition with their capabilities as drug reservoirs, in particular, of the chemotherapeutic drug doxorubicin. Colloidal stability and drug release experiments with the three most optimal drug/copolymer formulations into different buffer media were also performed. Despite some additional studies were previously performed in order to reveal the drug solubilisation ability of these copolymers (18,19), there are not studies regarding cytotoxicity, cytocompatibility, cellular uptake mechanisms. Here, the cytocompatibility of these block copolymers was tested against BALB/3T3 clone A31 mouse embryonic fibroblast cells (CCL 163, ATCC), which is highly sensitive to the presence of toxic species. Cytotoxicity and bioavailability of empty and drug-loaded micelles were also analyzed in an ovarian MDR NCI-ADR/RES cell line in order to achieve an optimal chemocytotoxic effect and to confirm their

potential use as effective and safe drug delivery systems. Finally, the capability of two of the present PBO-PEO-PBO copolymers as potential P-glycoprotein efflux pump inhibitors to enhance doxorubicin accumulation in the same ovarian MDR NCI-ADR/RES cell line was confirmed and compared to that observed for other block copolymers.

3.1.3 References

1. Yamamoto, Y.; Nagasaki, Y.; Kato, Y.; Sugiyama, Y.; Kataoka, K. J. Controlled Release, **2001**, 77, 27.
2. Crothers, M.; Zhou, Z.; Ricardo, Nagila M.P.S.; Yang, Z.; Taboada, P.; Chaibundit, C.; Attwood, D.; Booth, C. Int. J. Pharm. **2005**, 293, 91.
3. Taboada, P.; Velasquez, G.; Barbosa, S.; Castelletto, V.; Nixon, S. K.; Yang, Z.; Heatley, F.; Hamley, I.W.; Ashford, M.; Mosquera, V. Langmuir **2005**, 21, 5263.
4. Juárez, J.; Taboada, P.; Valdez, M.A.; Mosquera, V. Langmuir **2008**, 24, 7107.
5. Booth, C.; Attwood, D.; Price, C. Phys. Chem. Chem. Phys. **2006**, 8, 3612.
6. Attwood, D.; Booth, C.; Yeates, S.G.; Chaibundit, C.; Ricardo, N.M.P.S. Int. J. Pharm. **2007**, 345, 35.
7. Booth, C.; Attwood, D. Macromol. Rapid Commun. **2000**, 21, 501.
8. Heidel, J.; Davis, M. Pharm. Res. **2011**, 28, 187.
9. Branco, M.C.; Schneider, J.P. Acta Biomaterialia, **2009**, 5, 817.
10. Alexandridis, P.; Lindman, B. *Amphiphilic Block Copolymers. Self-Assembly and Applications*. 2000, Amsterdam: Elsevier.
11. Mistry, D.; Annable, T.; Yuan, X.-F.; Booth, C. Langmuir **2006**, 22, 2986.
12. Kellarakis, A.; Yuan, X.-F.; Mai, S.-M.; Yang, Y.-W.; Booth, C. Phys. Chem. Chem. Phys. **2003**, 5, 2628.
13. Zhou, Z.; Yang, Y.-W.; Booth, C.; Chu, B. Macromolecules **1996**, 29, 8357.
14. Ribeiro, M.E.N.P.; de Oliveira, S. A.; Ricardo, N.M.P.S.; Mai, S.-M.; Attwood, D.; Yeates, S.G.; Booth, C. Int. J. Pharm. **2008**, 362, 193.
15. Kellarakis, A. Havredaki, V.; Yu, G.-E.; Derici, L.; Booth, C. Macromolecules **1998**, 31, 944.
16. Liu, T.; Nace, V.M.; Chu, B. J. Phys. Chem. B **1997**, 101, 8074.
17. Booth, C.; Price, C. *Polymer Characterization*. Comprehensive Polymer Science. Vol. 1. 1989, Exeter: Pergamon Press.
18. Ribeiro, M.E.; Cavalcante, I. M.; Ricardo, N.M.P.S.; Mai, S.-M.; Attwood, D.; Yeates, S.G.; Booth, C. Int. J. Pharm. **2009**, 369, 196.
19. Elsabahy, M.; Perron, M.-E. Bertrand, N.; Yu, G.; Leroux, J.-C. Biomacromolecules **2007**, 8, 2250.

3.2 MICELLISATION OF TRIBLOCK COPOLYMERS OF ETHYLENE OXIDE AND 1,2-BUTYLENE OXIDE: EFFECT OF BO-BLOCK LENGTH

3.2.1 Abstract

We have used pyrene fluorescence spectroscopy and isothermal titration calorimetry (ITC) to investigate the effect of hydrophobic-block length on values of the critical micelle concentration (cmc) for aqueous solutions of triblock poly(butylene oxide)-poly(ethylene oxide)-poly(butylene oxide) block copolymers ($\text{BO}_n\text{EO}_m\text{BO}_n$, where m and n denote the respective block lengths) with hydrophobic block lengths in the range $n = 12$ -21. Combined with results from previous work on $\text{BO}_n\text{EO}_m\text{BO}_n$ copolymers with shorter BO blocks, plots of $\log_{10}(\text{cmc})$ (cmc in molar units and reduced to a common EO-block length) against total number of BO units ($n_t = n$ for diblock or $n_t = 2n$ for triblock copolymers) display transitions in the slopes of the two plots, which indicate changes in the micellisation equilibrium. These occur at values of n_t which can be assigned to the onset and completion of collapse of the hydrophobic BO blocks, an effect not previously observed for reverse triblock copolymers. The results are compared with related data for diblock EO_mBO_n copolymers.

3.2.2. Introduction

The properties of polymer surfactants combining hydrophilic poly(ethylene oxide) with various hydrophobic components have been reviewed in compilations edited by Nace (1) and by Alexandridis and Lindman (2), more recently by Booth *et al.* (3) Triblock copolymers which combine poly(oxyethylene) with poly(oxypropylene) are much in use, with important applications, for example, as emulsifiers (4), drug delivery systems (5), efflux pump inhibitors (6) and coating materials (7). To describe their repeat units we use the notation EO = oxyethylene, OCH_2CH_2 and PO = oxypropylene, $\text{OCH}_2\text{CH}(\text{CH}_3)$, with block copolymers of the two triblock architectures denoted $\text{EO}_m\text{PO}_n\text{EO}_m$ and $\text{PO}_m\text{EO}_n\text{PO}_m$, where the subscripts m and n denote number-average block lengths in repeat units. However, we note that the oxyanionic

polymerisation of propylene oxide is not straightforward, the problem being the transfer reaction originating from hydrogen abstraction rather than addition (8). For example, $EO_mPO_nEO_m$ copolymers often have a diblock component, detected as a pronounced shoulder on the high-elution-volume side of their gel permeation chromatography curves, and leading to variation in micellisation (9) and gelation (10) behaviour from batch to batch. As a consequence, effects of EO and PO block length on the association properties of these copolymers in aqueous solution are well understood qualitatively but less so quantitatively.

During the last few years, a series of more hydrophobic block copolymer counterparts with similar architecture but free from this complication has been examined. In particular, we have studied copolymers in which the PPO segment was replaced by a more hydrophobic one (e.g. poly(butylene oxide), poly(styrene oxide) or poly(phenylglycidyl ether)) in order to better elucidate the effects of block hydrophobicity on micellisation and micellar properties (3,11), with the aim of improving the rheological properties of micellar solutions and the solubilisation capacities of the micelles for poorly-water soluble drugs (12). Special attention has been paid to copolymers with 1,2-butylene oxide as the hydrophobic component. Transfer is not a problem in the laboratory polymerisation of 1,2-butylene oxide (13), but this monomer (as does propylene oxide) adds to the growing chain to give a secondary oxyanion, and slow initiation of EO chains at the secondary termination may lead to a broadened E-block-length distribution (14). However, this effect is eliminated if 1,2-butylene oxide blocks are polymerised last when forming EOBO diblock and BOEOBO triblock copolymers. Reverse BOEOBO triblock copolymers have potential for the control of rheological properties in aqueous systems, particularly associative thickeners (15). The effect originates from molecular association of the hydrophobic ends of the chains in dilute solution and, above the critical micelle concentration (cmc), from association of unimers into micelles in which the chains can either loop or extend. Bridging of extended chains between micelles, a dynamic process, leads to the formation of transient micelle clusters, and at high enough concentrations to the formation of transiently-linked networks.

The rheological effect depends on a balance between EO- and BO-block lengths. A lengthy EO-block length promotes bridging but at the expense of micellisation. Lengthening the B-block length restores micellisation, but a limit will be reached at which the longest hydrophobic blocks in the individual molecules will collapse to form a globule (16), i.e. the coiled unimers will form so-called unimolecular micelles. The

collapsed state involves a reduction in the number of contacts of the chain units of the core-forming block with solvent and, hence, a reduction in the hydrophobic effect which drives micellisation, the physics of which has been described in detail elsewhere (17).

An accurate knowledge of the conformational state of the dispersed copolymer in solution is desirable if the complexities of micellisation and micelle bridging in these associative systems is to be understood. The effect of hydrophobic-block collapse on the block-length dependence of the critical concentration for micellisation has been investigated recently for diblock EO_mBO_n copolymers covering a range of BO-block lengths from BO_7 to BO_{76} , with transitions in the results assigned to the onset and completion of unimolecular micelle formation (18). However, the possibility of related effects in the micellisation of $BO_nEO_mBO_n$ copolymers in dilute solution has not been investigated since the range of hydrophobicity has been much restricted for those copolymers, i.e. from BO_4 to BO_{12} , 8 to 24 BO units per molecule (3). In this paper, we describe the properties of BOEBO triblock copolymers with longer BO blocks, which provide a range of hydrophobicity more comparable with that of the diblocks. Specifically we present a direct comparison of the micellisation of triblock BOEBO copolymers with that of diblock EOBO copolymers over a wide range of hydrophobicity, with special emphasis on the effect of collapse of long BO blocks in molecular solution, and on the effect (if any) of splitting the total number of BO units between two blocks.

3.2.3 Experimental section

3.2.3.1 Materials

Five $BO_nEO_mBO_n$ copolymers with narrow chain length distributions were prepared and characterised using methods described previously (15,19) (see Table 1). Copolymer $BO_8EO_{90}BO_8$ was included to overlap with the range of copolymers studied previously and so provide direct validation of values of the cmc determined by different techniques.

Table 1. BO_nEO_mBO_n copolymers

Copolymer	10 ³ M _n (g mol ⁻¹)	M _w /M _n
BO ₈ EO ₉₀ BO ₈	0.51	1.07
BO ₁₂ EO ₂₂₇ BO ₁₂	11.7	1.05
BO ₁₄ EO ₃₇₈ BO ₁₄	18.6	1.12
BO ₂₀ EO ₄₁₁ BO ₂₀	21.0	1.08
BO ₂₁ EO ₃₈₅ BO ₂₁	20.0	1.10

Uncertainties in M_n determination are ca. ± 1%.

3.2.3.2 Methods

a. Fluorescence measurements

Values of the critical micelle concentration (cmc) were obtained from pyrene fluorescence measurements, as described by Lee *et al.* (20). Pyrene was obtained from Sigma-Aldrich Co. and used as received. Stock solutions were prepared by dissolving the copolymers in Milli-Q water and allowing 24 h for complete dissolution before diluting to desired concentrations within the range 1·50· 10³ mg dm⁻³. Pyrene dissolved in acetone was added to the copolymer solution and, after acetone evaporation, 24 h was allowed for equilibration. The final copolymer solution contained 3·10⁻⁷ mol dm⁻³ pyrene. A Cary Eclipse fluorescence spectrophotometer equipped with a temperature control Peltier device and a multi-cell sample holder (Varian Instruments Inc.) was used in the experiments, with solution temperatures kept at 25 ± 0.1 °C. The excitation wavelength (λ_{ex} = 335 nm) was the maximum intensity in the excitation spectrum. The fluorescence spectrum was the average of three scans and was corrected for scattering using an equivalent blank solution before determining the ratio I₁/I₃ of the first and third vibronic peaks. Reproducibility was better than 2 %.

b. Isothermal titration calorimetry measurements

Heats of demicellisation were measured using a VP-ITC titration microcalorimeter (MicroCal Inc., Northampton, MA, USA.) Small aliquots (5-10 ml) of stock solution of copolymers at concentrations well above the cmc were injected into a known volume of water (ca. 1 ml) held in the cell of the calorimeter, initially to produce a solution well below the cmc. Repeated additions of the stock solution gave the heat evolved (ΔH_i) as a function of copolymer concentration.

3.2.4 Results and discussion

3.2.4.1 Determination of critical micelle concentration

Figure 1a shows the dependence of the ratio I_1/I_3 from pyrene fluorescence intensity on copolymer concentration (logarithmic scale) for the block copolymer $\text{BO}_8\text{EO}_{90}\text{BO}_8$. As indicated, the value of the cmc at 25 °C was obtained as 0.33 g dm^{-3} from linear fitting of the two regions defined when the I_1/I_3 pyrene fluorescence intensity starts to decrease abruptly. As seen in Table 2, this value of the cmc fits well within the set of values determined using static light scattering in the Stonybrook and Manchester laboratories for copolymers $\text{BO}_4\text{EO}_{40}\text{BO}_4$ to $\text{BO}_{12}\text{EO}_{260}\text{BO}_{12}$. Figure 1b shows similar plots for copolymers $\text{BO}_{14}\text{EO}_{378}\text{BO}_{14}$ and $\text{BO}_{20}\text{EO}_{411}\text{BO}_{20}$, with the same construction used to obtain the values of the cmc listed in Table 2. The data points for the other two copolymers were treated in the same way but, for clarity, are omitted from Figure 1.

3.2.4.2 Influence of temperature on cmc

Figure 2 shows the limited effect of solution temperature (range 25 to 35 °C) on the concentration dependence of I_1/I_3 for copolymers $\text{BO}_{12}\text{EO}_{227}\text{BO}_{12}$ and $\text{BO}_{21}\text{EO}_{385}\text{BO}_{21}$. A similar insensitivity to temperature has been reported (3) for diblock and triblock copolymers with 15 or more BO units, with consequently low values of the van't Hoff enthalpy of micellisation, i.e.

$$\Delta_{\text{mic}}H = RT \, d \ln(\text{cmc})/d(1/T) \quad (1)$$

approaching zero.

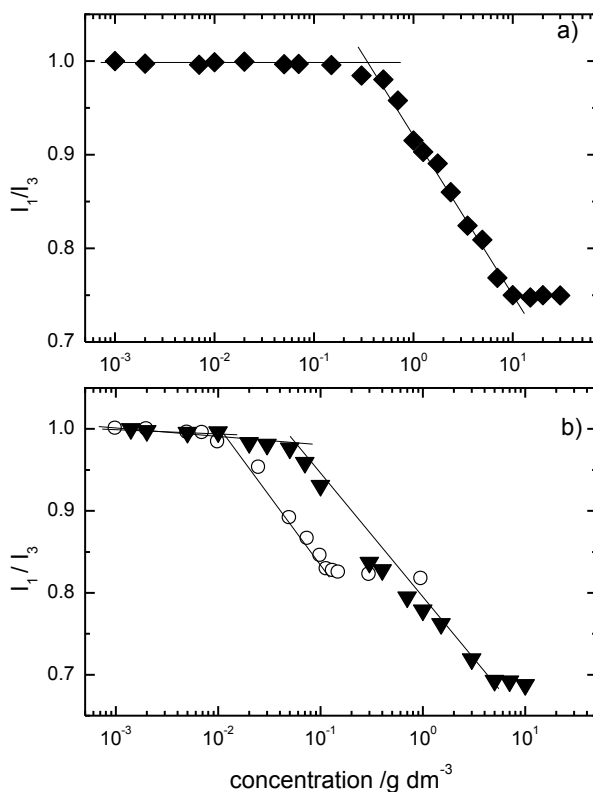


Figure 1: Normalised pyrene fluorescence intensities (I_1/I_3) for copolymers a) (◆) $\text{BO}_8\text{EO}_{90}\text{BO}_8$, b) (○) $\text{BO}_{20}\text{EO}_{411}\text{BO}_{20}$, and (▼) $\text{BO}_{14}\text{EO}_{378}\text{BO}_{14}$ in aqueous solution at 25 °C.

Isothermal titration calorimetry (ITC) was used to confirm this result. The ITC curve obtained for copolymer $\text{BO}_{12}\text{EO}_{227}\text{BO}_{12}$ at 20 °C is shown in Figure 3. The heat evolved (H_i) is plotted against the copolymer concentration. As discussed previously (25), at concentrations below the cmc the concentration dependence of H_i is determined by dilution of unimers, and that at high concentrations by dilution of micelles. The sharp increase in H_i as the concentration is increased from dilute to concentrated is the enthalpy of micellisation, $\Delta_{\text{mic}}H \approx 19 \text{ kJ mol}^{-1}$, very similar in value to the van't Hoff enthalpy reported for copolymer $\text{BO}_{12}\text{EO}_{260}\text{BO}_{12}$ in ref. 3. Very small values of $\Delta_{\text{mic}}H$ were recorded for the other four block copolymers.

Table 2. Values of the cmc for triblock copolymers $\text{BO}_n\text{EO}_m\text{BO}_n$ at $T = 25\text{ }^\circ\text{C}$.

Copolymer	$M_n / \text{g mol}^{-1}$	cmc / g dm^{-3}	Method ^b	Reference
$\text{BO}_4\text{EO}_{40}\text{BO}_4$	2340	120 ^a	SLS, ST	19
$\text{BO}_5\text{EO}_{39}\text{BO}_5$	2440	9.0 ^a	SLS	19
$\text{BO}_5\text{EO}_{91}\text{BO}_5$	4720	12.4	SLS	21
$\text{BO}_6\text{EO}_{46}\text{BO}_6$	2880	1.8	SLS	22
$\text{BO}_7\text{EO}_{40}\text{BO}_7$	2750	0.30 ^a	SLS	19
$\text{BO}_8\text{EO}_{90}\text{BO}_8$	5100	0.33	PF	this work
$\text{BO}_{10}\text{EO}_{271}\text{BO}_{10}$	13400	0.04	SLS	23
$\text{BO}_{12}\text{EO}_{260}\text{BO}_{12}$	13200	0.033	SLS	24
$\text{BO}_{12}\text{EO}_{227}\text{BO}_{12}$	11700	0.031	PF	this work
$\text{BO}_{14}\text{EO}_{378}\text{BO}_{14}$	18600	0.058	PF	this work
$\text{BO}_{20}\text{EO}_{411}\text{BO}_{20}$	21000	0.012	PF	this work
$\text{BO}_{21}\text{EO}_{385}\text{BO}_{21}$	20000	0.025	PF	this work

(a) Values interpolated or extrapolated from plots of $\log_{10}(\text{cmc})$ vs $1/T$.

(b) SLS - static light scattering; ST - surface tension; PF, pyrene fluorescence.

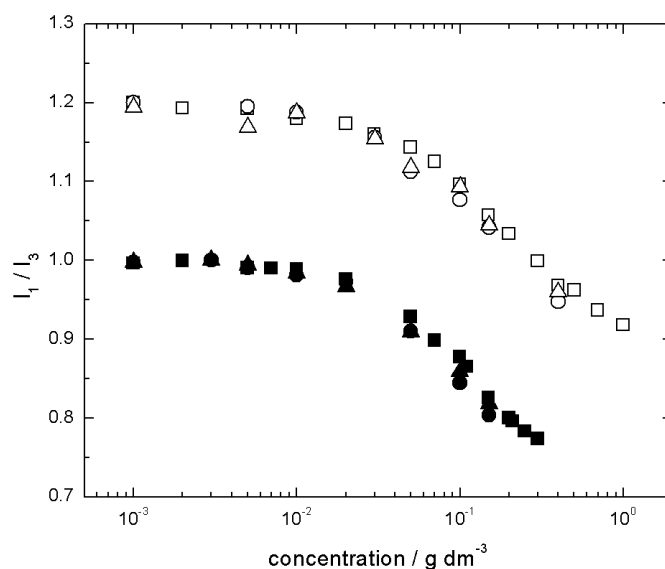


Figure 2: Normalized pyrene fluorescence intensities (I_1/I_3) for copolymers $\text{BO}_{12}\text{EO}_{227}\text{BO}_{12}$ (closed symbols) and $\text{BO}_{21}\text{EO}_{385}\text{BO}_{21}$ (open symbols) in aqueous solution at (\square) 25, (\circ) 30 and (Δ) 35 °C. For clarity data corresponding to copolymer $\text{BO}_{21}\text{EO}_{385}\text{BO}_{21}$ are shifted on the y-scale by -0.2.

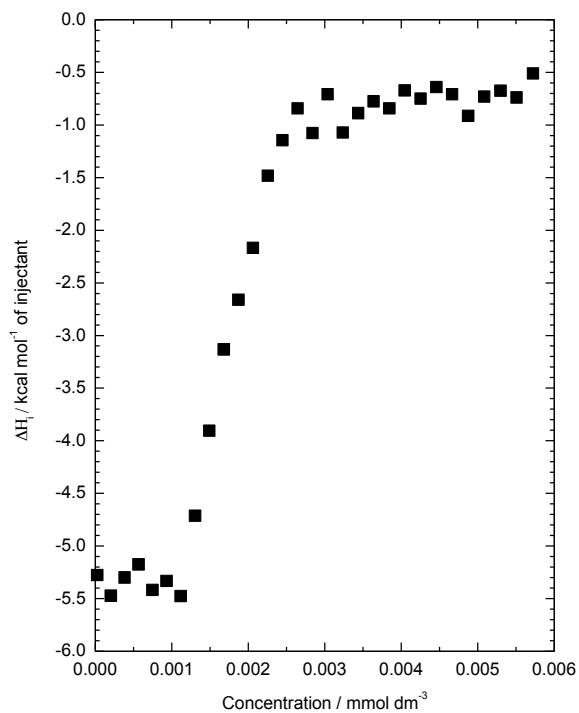


Figure 3: ITC curve obtained for copolymer $\text{BO}_{12}\text{EO}_{227}\text{BO}_{12}$ at 20 °C.

3.2.4.3 Correlation of cmc with hydrophobicity

The plot of $\log_{10}(\text{cmc})$ against number of BO units per molecule ($n_t = 2n$, Figure 4a) includes all the results in Table 2. Within the series values of the cmc are affected by variation in EO-block length. As described previously (3), we have used $\log_{10}(\text{cmc})/dn = 0.004$ (where n is the number of E units), an expression based on values of the cmc reported by Alexandridis *et al* (26), to adjust our results to a common number of EO units, $m = 100$, i.e. adjustments of $0.004(100-m)$. The data points in Figure 4a can be satisfactorily represented by lines showing two transitions in slope, at $n_t \approx 14$ and $n_t \approx 21$. These results can be compared with the corresponding plot published (18) for diblock EO_mBO_n copolymers which is reproduced in Figure 4b and shows transitions in slope at $n_t \approx 13$ and $n_t \approx 30$. Similar pairs of transitions have been noted (18) in related plots for diblock copolymers of ethylene oxide with DL-lactide or ϵ -caprolactone.

As discussed previously (3), the standard Gibbs energy of micellisation can be obtained without significant error from the critical micelle concentration (cmc) through

$$\Delta_{\text{mic}}G^{\circ} = -RT \ln K_c = RT \ln(\text{cmc}) \quad (2)$$

where the cmc is expressed in mol dm^{-3} , K_c is the unimer-micelle equilibrium constant, and the standard state is ideally dilute solution in which both unimers and micelles are of unit molarity. That is, $\log_{10}(\text{cmc})$ is directly related to the standard Gibbs energy of micellisation at a given temperature, and can be used as a convenient indicator of the position of equilibrium in the system. A change in the dependence of $\log_{10}(\text{cmc})$ on hydrophobic block length indicates a change in the micellisation equilibrium. Such a change will occur if the hydrophobic blocks of the dispersed copolymer molecules (unimers) start to collapse to a globule, much as discussed in a number of papers (16,17,27), and given the convenient name 'unimolecular micelle'.

The consequence of the collapse of the hydrophobic block is reduced contact of the chain units of the core-forming blocks with water and so a reduction in the hydrophobic effect which drives micellisation, as discussed in detail elsewhere (3). Because of the block-length distribution, the conversion of unimers to unimolecular micelles will increase gradually as the number of hydrophobic units is increased, and a second transition in the dependence of $\log_{10}(\text{cmc})$ on hydrophobic block length is seen (Figure 4) when effectively all dispersed molecules are in the form

of unimolecular micelles. This interpretation is confirmed by the negligible values of $\Delta_{\text{mic}}H$ observed by ITC for the copolymers with the longest B blocks, i.e. values consistent with a weak hydrophobic effect due to the collapsed state of the hydrophobic blocks both before and after dilution in the calorimeter cell.

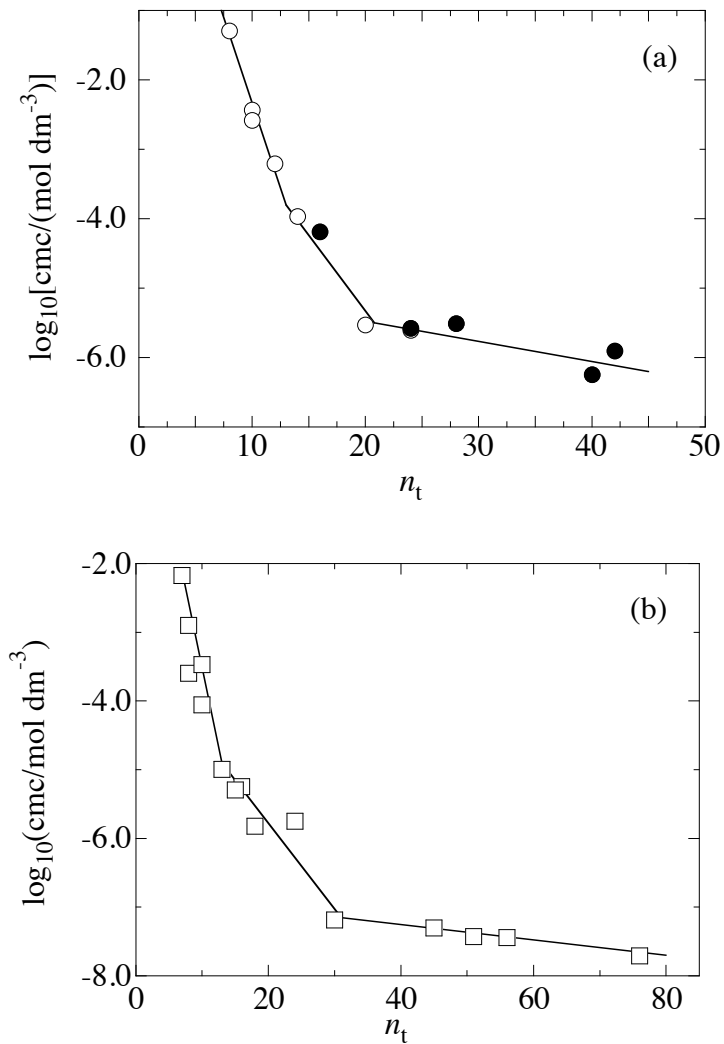


Figure 4: Variation of $\log_{10}(\text{cmc})$ expressed in mol dm^{-3} , with the number of BO units in the copolymers for a) (\bullet , present work; \circ , literature data) triblock $\text{BO}_n\text{EO}_m\text{BO}_n$; and b) (\square) diblock EO_mBO_n copolymers. Values of the cmc are adjusted to a common E-block length, $m = 100$. $T = 25$ °C. The lines are intended to guide the eye. n_t is equal to $2n$ (where n is the BO-block length) for triblock copolymers and equal to n for diblocks.

3.2.5 Conclusions

The collapse of the hydrophobic blocks of synthetic water-soluble block copolymers in solution has been well described for diblock copolymers. The nomenclature ‘unimolecular micelle’ is commonly used. Our results confirm that micellisation follows the same path in symmetrical triblock copolymers with hydrophobic end blocks, type BOEOBO. Moreover, comparison of our results for BOEOBO copolymers with previous results for diblock EOBO copolymers, as summarised in Figure 4, points for the first time to a close parallel between the two systems. That is, that the transition from solvated to collapsed hydrophobic blocks depends essentially on the overall composition of the block copolymers and not on their individual block lengths. Moreover we confirm for triblock copolymers, as previously for diblock copolymers, that collapsed hydrophobic blocks are an essential precursor to multimolecular micelles for copolymers with long hydrophobic blocks.

We believe that our study of coil collapse in solutions of BOEOBO copolymers has value in assessing the application of the related triblock copolymers associative thickeners in the controlled modification of rheological properties in aqueous systems. This useful property depends on the hydrophobic end blocks of the copolymers bridging between micelles to form transient networks which modify the rheology of the system. Collapse of long end blocks, with consequent reduction of the hydrophobic effect, will reduce the driving force for formation of intermicellar bridges. Our results provide a first indication of the need for further study to define and control this effect. Also, this collapsed state may also have an important influence for other colloidal applications of this kind of block copolymers, such as the use of BOEOBO reverse copolymers as adjuvants and/or enhancing solubilising entities of poorly soluble drugs at concentrations much lower than that usually required (28), and as potent biological response modifiers capable of sensitising multi-drug resistant (MDR) cancer cells and enhancers of drug transport across cellular barriers (29), in which polymeric monomers seems to play a crucial role (30).

3.2.6 References

1. *Nonionic Surfactants, Poly(oxyalkylene) Block Copolymers*, Surfactant Science Series, 1996. V. M. Nace, Ed.; Marcel Dekker, New York, Vol. 60.
2. *Amphiphilic Block Copolymers: Self assembly and Applications*, 2000. P. Alexandridis and B. Lindman, Eds; Elsevier Science; Amsterdam.

3. Booth, C.; Attwood, D.; Price, C. *Phys. Chem. Chem. Phys.* **2006**, *8*, 3612.
4. Holmberg, K. *Applications of Block Copolymers*. In *Amphiphilic Block Copolymers: Self assembly and Applications*, 2000. P. Alexandridis and B. Lindman, Eds; Elsevier Science; Amsterdam.
5. a) Malmsten, M. *Block copolymers in Pharmaceutics*. In *Amphiphilic Block Copolymers: Self assembly and Applications*, 2000. P. Alexandridis and B. Lindman, Eds; Elsevier Science; Amsterdam; b) Chiapetta, D.A; Sosnik, A. *Eur. J. Pharm. Biopharm.* **2007**, *66*, 303; c) Bakatrova, E. V.; Kabanov, A.V. *J. Controlled Release* **2008**, *130*, 98.
6. a) Kabanov, A.V.; Bakatrova, E.V.; Alakhov, V.Y. *Adv. Drug Deliv. Rev.* **2002**, *54*, 759; b) Werle, M.; *Pharm. Res.* **2008**, *25*, 500; c) Alvarez-Lorenzo, C.; Rey-Rico, A.; Brea, J.; Loza, M.I.; Concheiro, A.; Sosnik, A. *Nanomedicine* **2010**, *5*, 1371.
7. a) Qin, J.; Laurent, S.; Jo, Y.S.; Roch, A.; Mikhaylova, M.; Bhujwall, Z.M.; Muller, R.N.; Muhammed, M. *Adv. Mater.* **2007**, *19*, 1874; b) George, P.A.; Donose, B.C.; Cooper-White, J.J. *Biomaterials* **2009**, *30*, 2449.
8. See, for example, Yu, G.-E.; Masters, A.J.; Heatley, F.; Booth, C.; Blease, T.G. *Macromol. Chem. Phys.* **1994**, *195*, 1517.
9. See, for example, Yu, G.-E.; Altinok, H.; Nixon, S.K.; Booth, C.; Alexandridis, P.; Hatton, T.A. *Eur. Polym. J.* **1997**, *33*, 673.
10. Mortensen, K.; Batsberg, W.; Hvidt, S. *Macromolecules* **2008**, *41*, 1720.
11. a) Booth, C.; Attwood, D. *Macromol. Rapid Comm.* **2000**, *21*, 501; b) Taboada, P.; Velasquez, G.; Barbosa, S.; Castelletto, V.; Nixon, S.K.; Yang, Z.; Heatley, F.; Hamley, I.W.; Ashford, M.; Mosquera, V.; Attwood, D.; Booth, C. *Langmuir*, **2005**, *21*, 5263.; c) Barbosa, S.; Cheema, M.A.; Taboada, P.; Mosquera, V. *J. Phys. Chem. B* **2007**, *111*, 10920.
12. Crothers, M.; Zhou, Z.; Ricardo, N. M. P. S.; Yang, Z.; Taboada, P.; Chaibundit, C.; Attwood, D.; Booth, C. *Int. J. Pharm.*, **2005**, *293*, 91.
13. Heatley, F.; Yu, G.-E.; Sun, W.-B.; Pywell, E.J.; Mobbs, R.H.; Booth, C. *Eur. Polym. J.* **1990**, *26*, 583.
14. See, for example, (a) Nace, V.M.; Whitmarsh, R.H.; Edens, M.W. *J. Am. Oil Chem. Soc.* **1994**, *71*, 777. (b) Yu, G.-E.; Yang, Z.; Ameri, M.; Attwood, D.; Collett, J.H.; Price, C.; Booth, C. *J. Phys. Chem. B.* **1997**, *101*, 4394. (c) Yu, G.-E.; Li, H.; Price, C.; Booth, C. *Langmuir* **2002**, *18*, 7756.
15. Mistry, D.; Annable, T.; Yuan, X.-F.; Booth, C. *Langmuir* **2006**, *22*, 2986.

16. (a) Brown, R.A.; Masters, A.J.; Price, C.; Yuan, X.-F. in *Comprehensive Polymer Science*, Vol. 2, Polymer Properties, 1989. Booth, C.; Price C. Eds., Pergamon Press, Oxford, Ch. 6, pp. 185-186. (b) Tuzar, Z.; Kratochvil P. *Surf. Colloid Sci.* **1993**, 15, 1. (c) Chu, B. *Langmuir* **1995**, 11, 414.
17. Cooke, I.R.; Williams, D.R.M. *Macromolecules* **2003**, 36, 2149.
18. Ribeiro, M.N.E.P.; de Oliveira, S.A.; Ricardo, N.M.P.S.; Mai, S.-M.; Attwood, D.; Yeates, S.G.; Booth, C. *Int. J. Pharm.* **2008**, 362, 193.
19. Yang, Y.-W.; Yang, Z.; Zhou, Z.-K.; Attwood, D.; Booth, C. *Macromolecules* **1996**, 29, 670.
20. Lee, K.; Shin, C.-H.; Oh, I. *Arch. Pharm. Res.* **2003**, 26, 653.
21. Zhou, Z.; Chu, B.; Nace, V.M. *Langmuir* **1996**, 12, 5016.
22. Liu, T.; Zhou, Z.; Wu, C.; Schneider, D.K.; Chu, B.; Nace, V.M. *J. Phys. Chem. B.* **1997**, 101, 8808.
23. Liu, T.; Zhou, Z.; Wu, C.; Nace, V.M.; Chu, B. *J. Phys. Chem. B.* **1998**, 102, 2875.
24. Zhou, Z.; Yang, Y.-W.; Booth, C.; Chu, B. *Macromolecules* **1996**, 29, 8357.
25. (a) Taboada, P.; Mosquera, V.; Attwood, D.; Yang, Z.; Booth, C. *Phys. Chem. Chem. Phys.* **2003**, 5, 2625. (b) Taboada, P.; Velasquez, G.; Barbosa, S.; Yang, Z.; Nixon, S.K.; Zhou, K.; Heatley, F.; Ashford, M.; Mosquera, V.; Attwood, D.; Booth, C. *Langmuir*, **2006**, 22, 7465.
26. Alexandridis, P.; Holzwarth, J.F.; Hatton, T.A.; *Macromolecules* **1994**, 27, 2414.
27. Kelarakis, A.; Havredaki, V.; Rekas, C.J.; Booth, C. *Phys, Chem. Chem. Phys.* **2001**, 3, 5550.
28. Irache, J.M.; Salman, H.H.; Gomez, S.; Espuelas, S.; Gamazo, C. *Frontiers Bios.* **2010**, S2; 876.
29. Batrakova, E. V.; Kabanov, A.V. *J. Controlled Release* **2008**, 130, 98.
30. Cambón, A.; Rey-Rico; A.; Mistry, D.; Brea, J.; Loza, M.I.; Attwood, D.; Barbosa, S.; Alvarez-Lorenzo, C.; Concheiro, A.; Taboada, P.; Mosquera, V. *Int. J. Pharm.* **2013**, 445, 47.

3.3 COMPLEX SELF-ASSEMBLY OF REVERSE POLY(BUTYLENE OXIDE) - POLY(ETHYLENE OXIDE)-POLY(BUTYLENE OXIDE) TRIBLOCK COPOLYMERS WITH LONG HYDROPHOBIC AND EXTREMELY LENGTHY HYDROPHILIC BLOCKS

3.3.1 Abstract

Amphiphilic block copolymers have emerged during last years as a fascinating substrate material to develop micellar nanocontainers able to solubilize, protect, transport and release under external or internal stimuli different classes of cargos to diseased cells or tissues. However, this class of materials can also induce biologically relevant actions which complement the therapeutic activity of their cargo molecules through their mutual interactions with biological relevant entities (cellular membranes, proteins, organelles...), which, at the same time, are regulated by the nature, conformation and and state of the copolymeric chains. For this reason, in this paper we investigated the self-assembly process and physico-chemical properties of two reverse triblock poly(butylene oxide)-poly(ethylene oxide)-poly(butylene oxide) block copolymers, $BO_{14}EO_{378}BO_{14}$ and $BO_{21}EO_{385}BO_{21}$, which have been recently found to be very useful as drug delivery nanovehicles and biological response modifiers under certain conditions (A. Cambón *et al. Int. J. Pharm.* **2013**, *445*, 47-57) in order to obtain a clear picture of the solution behavior of this class or block copolymers and to understand their biological activity. These block copolymers are characterised by possessing long BO blocks and extremely lengthy central EO ones which provide them with a rich rheological behavior characterised by the formation of flower-like micelles with sizes ranging from 20 to 40 nm in aqueous solution and the presence of intermicellar bridging even at low copolymers concentrations as denoted by atomic force microscopy. Bridging is also clearly observed by analysing the rheological response of these block copolymers both storage and loss moduli upon changes on time, temperature and or concentration. Strikingly, the relatively wide Póisson distribution of copolymeric chains make the present copolymers to behave rather distinctly to conventional associative thickeners. The observed rich rheological behavior and their tunability make also these copolymers a promising materials to configure drug gelling depots.

3.3.2 Introduction

In the last two decades a great effort has been made through the development of a series of nanosized therapeutic products able to solubilize hydrophobic drugs, allow their sustained release, improve their pharmacokinetics and facilitate their access to the site of action (1-5) The properties of amphiphilic copolymers combining hydrophilic poly(ethylene oxide) units with different types of hydrophobic blocks have been found to show suitable characteristics for fulfill the former requirements, *i.e.* they can spontaneously self-assemble into nanoscopic core-shell micellar structures in which the core serve as reservoir for the hydrophobic cargo while the corona is in direct contact with the biological milieu providing “stealthness” to evade scavenging by the mononuclear phagocyte system, which results in larger circulation times and passive accumulation in solid tumors by the enhanced permeation and retention (EPR) effect.⁶ Copolymers which combine poly(oxyethylene) and poly(oxypropylene) (EO = oxyethylene, OCH_2CH_2 , and PO = oxypropylene, $\text{OCH}_2\text{CH}(\text{CH}_3)$) in a triblock structure, either direct, $\text{EO}_m\text{PO}_n\text{EO}_m$, or reverse, $\text{PO}_n\text{EO}_m\text{PO}_n$ (where the subscripts *m* and *n* denote number-average block lengths) have been the most extensively studied due to their commercial availability in a very broad range of compositions, a fair solubilization capacity and sustained release, a good biocompatibility of most varieties and approval of some varieties by regulatory agencies to be used in pharmaceutical formulations and medical devices (7-9). Nevertheless, $\text{EO}_m\text{PO}_n\text{EO}_m$ or $\text{PO}_n\text{EO}_m\text{PO}_n$ block copolymers possess several drawbacks. For example, the oxyanionic polymerization of propylene oxide is not straightforward, the problem lying in the transfer reaction originated from hydrogen abstraction rather than addition (10). For example, $\text{EO}_m\text{PO}_n\text{EO}_m$ copolymers often have a diblock component, detected as a pronounced shoulder on the high-elution-volume side of their gel permeation chromatographic curves, which leads to variation in micellisation (11-12) behavior from batch to batch. In addition, there exists an incomplete micellisation of the unimers which usually leads to self-assembled nanostructures with limited drug solubilisation ability and stability upon dilution in the bloodstream.

To circumvent these problems, during the last few years a series of more hydrophobic block copolymer counterparts with similar architecture but with the PO segment replaced by a more hydrophobic one such as poly(butylene oxide) (PBO), poly(styrene oxide) (PSO) or phenylglycidyl ether (PG) have been proposed with the aim of improving the solubilisation capacities, release profiles and the rheological properties of the polymeric micelles for poorly-water soluble drugs (13-19).

Special attention has been paid to copolymers with 1,2-butylene oxide (BO) as the hydrophobic monomer. Transfer is not a problem in the laboratory polymerisation of BO (20), but this monomer (as PO does) adds to the growing chain to give a secondary oxyanion; also, the slow initiation of EO chains at the secondary termination

may lead to a broadened EO-block-length distribution (21). However, this effect is eliminated if BO blocks are polymerised last when forming EO_mBO_m diblock and $BO_nEO_mBO_n$ triblock copolymers. Reverse $BO_nEO_mBO_n$ triblock copolymers have potential for the control of rheological properties in aqueous systems, particularly as associative thickeners thanks to the formation of transient micelle clusters or networks by bridging of extended chains between micelles as previously observed, for example, in copolymer $BO_{10}EO_{410}BO_{10}$ (22-24). The larger relative hydrophobicity of the BO block compared to PO (six-fold as estimated from the ratio of the logarithms of the molar critical micellar concentrations, *cmc*) (16) enables the formation of polymeric micelles at much lower copolymer concentrations and subsequent larger solubilised drug concentrations in the micelle core, providing excellent properties as drug delivery nanocarriers (25). In addition, these copolymers were demonstrated to be “biologically active” in the sense of, for example, enhancing drug toxicity to cancerous cells by inhibiting the P-glycoprotein P efflux pump mechanism (25). Nevertheless, a complete and detailed physico-chemical characterization of the former class copolymers is still lacking, which might help to obtain a better understanding of their behavior as biologically-response modifiers and to open up new potential applications as injectable drug gelling depots.

Hence, in this work we present a deep characterization of the self-assembly process and the physico-chemical properties of copolymers $BO_{14}EO_{378}BO_{14}$ and $BO_{21}EO_{385}BO_{21}$ by different techniques such as static and dynamic light scattering (SLS and DLS, respectively), transmission electron microscopy (TEM), atomic force microscopy (AFM), and rheometry. Both copolymers possess much longer BO blocks than previously analysed $BO_nEO_mBO_n$ copolymers. This enabled us to observe the effects of both the collapse of longer BO blocks in solution of reverse copolymeric structures and the splitting of BO units number between two blocks, especially in dilute solution since the range of hydrophobicity has been much restricted for these copolymers. i.e. from BO_4 to BO_{12} , 8 to 24 BO units per molecule (16).

3.3.3 Experimental section

3.3.3.1 Materials

Copolymers were prepared by oxyanionic polymerisation of dry 1,2-butylene oxide initiated by polyethylene glycol monomer of different molecular weights activated by mixing with KOH and heating while stirring under vacuum (70 °C, 0.1 mmHg, 100 h) to remove water. Vacuum line and ampoule techniques served to exclude moisture. Gel permeation chromatography (GPC) was used to characterise the distribution widths of the products as the ratio of mass-average to number-average molar mass, i.e. M_w/M_n by using a Waters GPC system equipped with a 1515 isocratic

pump and a 2410 refractive index detector (Waters, Milford, MA). Chloroform was used as eluent, and monodisperse PEO was employed as standard. ^{13}C NMR spectra recorded on a Bruker ARX400 spectrometer (Bruker, Milton, ON, Canada) in deuterated chloroform were used to obtain absolute values of block length and composition, and to verify block architecture. The general methods used have been described previously in detail (22,26). Table 1 summarises the molecular characteristics of the copolymers.

Table 1. Molecular characteristics of the copolymers.

Polymers	M_n (g/mol) ^a	M_w / M_n ^b	M_w (g/mol)	cmc (g/dm ³) ^c
BO ₁₄ EO ₃₇₈ BO ₁₄	18600	1.12	20830	0.058
BO ₂₁ EO ₃₈₅ BO ₂₁	20000	1.10	22000	0.025

^aEstimated by NMR; ^bEstimated by GPC; M_w calculated from M_n and M_w/M_n . Estimated uncertainty: M_n to $\pm 3\%$; M_w/M_n to ± 0.01 . ^cValues from Ref. (27).

3.3.3.2 Methods

a. Dynamic and static light scattering (DLS and SLS)

SLS intensities were measured by means of an ALV-5000F (ALV-GmbH, Germany) instrument with vertically polarized incident light ($\lambda = 488$ nm) supplied by a diode-pumped Nd:YAG solid-state laser (Coherent Inc., CA, USA) and operated at 2 W, and combined with an ALV SP-86 digital correlator with a sampling time of 25 ns to 100 ms (for DLS). Measurements were made at an angle $\theta = 90^\circ$ to the incident beam, as appropriate for particles smaller than the light wavelength. The intensity scale was calibrated against scattering from toluene. Solutions were filtered through Millipore Millex filters (Triton free, 0.22 μm porosity) directly into cleaned scattering cells and allowed to equilibrate at the requested temperature for 10 min before measurement. Each experiment was repeated at least three times. Sampling time was 5-10 min for each run in order to define an optimal correlation function. For DLS, the correlation functions were analyzed by the CONTIN method to obtain the intensity distributions of decay rates (Γ) (28). From the decay rate distributions the apparent diffusion coefficients ($D_{app} = \Gamma/q^2$, $q = (4\pi n_s/\lambda)\sin(\theta/2)$) were derived, being n_s the solvent refractive index. Values of the apparent hydrodynamic radius ($r_{h,app}$, radius of the hydrodynamically equivalent hard sphere corresponding to D_{app}) were calculated from the Stokes-Einstein equation

$$r_{h,app} = kT/(6\pi\eta D_{app}) \quad (1)$$

where k is the Boltzmann constant and η is the viscosity of water.

b. Transmission electron microscopy (TEM)

Micellar solutions of both copolymers were applied dropped over carbon-coated copper grids, blotted, washed, negatively stained with 2% (w/v) phosphotungstic acid, air-dried, and then examined with a Phillips CM-12 transmission electron microscope operating at an accelerating voltage of 120 kV.

c. Clouding

Copolymer solutions were prepared by weighting the required amount of each copolymer followed by the addition of the same volume of cold water (1 mL). Copolymer solutions were homogenized under stirring at low temperature before being stored at least for one day ($T \sim 4$ °C) to ensure complete dissolution. Clouding temperatures (T_{cl}) were determined by slowly heating (0.2 °C min^{-1}) the copolymer solutions from 0 to 90 °C by both visual inspection and detection of the transmitted light through solutions by means of a UV-Vis spectrophotometer equipped with a temperature control Peltier device and a multi-cell sample holder (Cary 100, Agilent, Germany). A plot of transmitted intensity versus temperature was obtained. The cloud point was determined as the midpoint of an abrupt decrease in the transmitted light intensity from a plot of transmitted intensity vs temperature, as previously described (24).

d. Rheometry

Solutions were prepared by weighting copolymer and deionized water into small tubes and subsequent mixing in the mobile state before being stored for a day or more at low temperature (ca. 5 °C). Rheological characterisation was carried out using a controlled stress AR2000 rheometer (TA instruments, DE, USA) with Peltier temperature control. Samples were investigated using cone-plate geometry (cone diameter 40 mm, angle 0.5°) and a solvent trap to maintain a water-saturated atmosphere around the sample cell to avoid evaporation. The temperature dependence of storage (G') and loss (G'') moduli was measured either by temperature scans at frequency $f = 1$ Hz and heating rates of 1 °C min^{-1} or via frequency scans at several temperatures (1-80°C). Experiments were carried out in oscillatory shear mode, with the strain amplitude (A) maintained at a low value ($A < 0.5$ %) by means of the autostress facility of the software. This ensured that measurements of G' and G'' were in the linear viscoelastic region. A dynamic time sweep test under $A = 0.5\%$ and $f = 1$ Hz was performed before each frequency scan at a fixed temperature to ensure that the sample truly reached the equilibrium state.

e. Atomic force microscopy (AFM)

AFM images of block copolymer solutions were performed on freshly cleaved mica substrates. The measurements were performed in a JEOL instrument (model JSPM 4210) in noncontact mode using nitride cantilevers NSC15 from MicroMasch, U.S.A. (typical working frequency and spring constant of 325 kHz and 40 N/m, respectively). The AFM samples were dried in air or under a nitrogen flow when required. Control samples (freshly cleaved mica and buffer solution) were also investigated to exclude possible artifacts. Topography and phase-shift data were collected in the trace and retrace direction of the raster, respectively. The offset point was adapted accordingly to the roughness of the sample. The scan size was usually 500 nm (aspect ratio, 1 x 1), with a sample line of 256 points and a step size of 1 μm . The scan rate was tuned proportionally to the area scanned and kept within the 0.35-2 Hz range. Each sample was imaged several times at different locations on the substrate to ensure reproducibility. Diameters and heights of copolymer aggregates were determined by sectional analysis taken from the average of several sections through the aggregates.

3.3.4 Results and discussion

3.3.4.1 Clouding

The clouding and phase behavior of $\text{BO}_n\text{EO}_m\text{BO}_n$ copolymers is not completely resolved yet due to the unavailability of a full range of block lengths. To fill this gap, clouding temperatures (T_{cl}) were firstly determined for solutions of copolymers $\text{BO}_{14}\text{EO}_{378}\text{BO}_{14}$ and $\text{BO}_{21}\text{EO}_{385}\text{BO}_{21}$ in the concentration range 0.1-10 wt.% by visual inspection and UV-Vis spectroscopy following the methodology of Zhou *et al* (24). A good agreement was observed between both methods. Figure 1 shows T_{cl} as a function of copolymer concentration. In the one-phase region, the *cmc* values were previously found to be below 0.1 mg/mL for both copolymers (27). Hence, the cloud point behavior can be represented the phase transition of a copolymer micellar solution which phase separates ca. 20 $^\circ\text{C}$ above T_{cl} . In general, copolymer $\text{BO}_{21}\text{EO}_{385}\text{BO}_{21}$ displayed lower T_{cl} than $\text{BO}_{14}\text{EO}_{378}\text{BO}_{14}$ as expected for its longer hydrophobic blocks. For $\text{BO}_{14}\text{EO}_{378}\text{BO}_{14}$, the cloud-point profile exhibited a shallow minimum at 50 mg/mL (at 60 $^\circ\text{C}$), whilst for $\text{BO}_{21}\text{EO}_{385}\text{BO}_{21}$ this minimum was observed at 30 mg/mL (at 51 $^\circ\text{C}$); for both copolymers T_{cl} starts again to increase at larger concentrations. High T_{cl} coincident with gel formation have been also observed in related systems, *i.e.* aqueous solutions of copolymers $\text{BO}_{12}\text{EO}_{114}\text{BO}_{12}$ and $\text{BO}_{12}\text{EO}_{227}\text{BO}_{12}$ (23,29,30). Liu *et al.*(31) have investigated the effect of EO and BO block lengths on T_{cl} of 1 wt. % solutions of $\text{BO}_n\text{EO}_m\text{BO}_n$ copolymers bearing short EO ($m < 40$) and BO ($n < 7$) blocks. These authors showed that T_{cl} decreased with increases in BO-block length at constant EO-block one, and it increased with an increase in EO-block length at constant BO-block one. The results reported here confirm that Liu's conclusions can be also applied to longer copolymers and higher concentrations, *i.e.* T_{cl} is lower the most hydrophobic the

copolymer is. However, in the present case the copolymers' behavior is largely influenced by their extremely long EO-blocks which makes T_{cl} to increase if compared to structurally related $\text{BO}_{12}\text{EO}_{114}\text{BO}_{12}$, $\text{BO}_{12}\text{EO}_{227}\text{BO}_{12}$ or $\text{BO}_{10}\text{EO}_{410}\text{BO}_{10}$ copolymers previously studied (22,32).

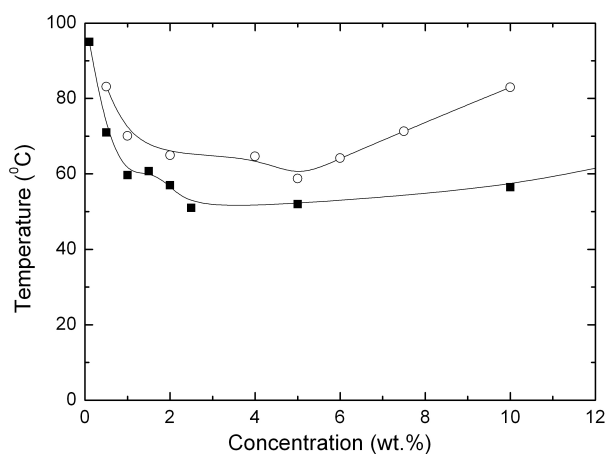


Figure 1. Clouding temperatures for copolymers $\text{BO}_{14}\text{EO}_{378}\text{BO}_{14}$ (○) and $\text{BO}_{21}\text{EO}_{385}\text{BO}_{21}$ (■) obtained by UV-vis spectroscopy. The lines were drawn to guide the eye.

3.3.4.2 Population size distributions

DLS measurements of $\text{BO}_{14}\text{EO}_{378}\text{BO}_{14}$ and $\text{BO}_{21}\text{EO}_{385}\text{BO}_{21}$ micellar solutions at different concentrations were carried out at 10 and 25 °C. Selected intensity fraction distributions of $\log r_{h,app}$ ($r_{h,app}$ being the apparent hydrodynamic radius) are illustrated in Figure 2a for copolymer $\text{BO}_{21}\text{EO}_{385}\text{BO}_{21}$ at 25 °C as an example. For $c < cmc$, the population distributions obtained show only a single peak attributed to singly dispersed copolymer chains ($r_{h,app} = 2\text{-}3$ nm) (Figure 2a, red line). It is conceivable that under these conditions the present copolymers can arrange the unimers in the form of unimolecular micelles in order to prevent the contact of BO blocks with water thanks to the flexibility of the central, very long EO block. The low micellization enthalpy values previously derived from isothermal titration calorimetry (ITC) would confirm the tightly packing of BO blocks in the unimer state so that their hydrophobic interaction with water would be really small (27). At $c > cmc$, several peaks are observed in the intensity-fraction population distributions which can correspond to unimers ($r_{h,app} = 2\text{-}3$ nm), flower-like micelles ($r_{h,app} = \text{ca. } 8\text{ to } 20$ nm) and micelle clusters formed by micellar bridging ($r_{h,app} = 40\text{-}60$ nm) (Figure 2a, black line). Owing to the special chain architecture of $\text{BO}_n\text{EO}_m\text{BO}_n$ -type block copolymers, the formation of flower-like micelles would involve bending of EO blocks while keeping the two terminal BO blocks in the same micellar core (an entropy-loss process). Another possibility might be the two BO blocks in one polymer chain would reside in two adjacent micelles and the EO block would be used as a bridge. This kind of crosslinking among the micelles can

finally promote an open network structure (the so-called micellar clusters), reflected in the DLS population distributions (Figure 2a, blue line). Peaks corresponding to unimers and micelles were single narrow peaks, while those belonging to micellar clusters were broader. As the concentration increased, the latter peak became more intense denoting larger cluster sizes. Population distributions also slightly shifted to smaller sizes as the temperature decreases (not shown). This was as expected provided that water becomes a better solvent for micelles as the temperature is lowered and, hence, micellar bridging (and hence clustering) is reduced. On the other hand, the shape of micelles was nearly spherical as observed by TEM and AFM, with their diameters (ca. 27 ± 4 and 32 ± 5 nm for $\text{BO}_{14}\text{EO}_{378}\text{BO}_{14}$ and $\text{BO}_{21}\text{EO}_{385}\text{BO}_{21}$ as calculated from TEM, respectively) in fair agreement with those obtained from DLS data despite the usual dehydration of the copolymer corona and subsequent shrinking of the copolymer structure upon solvent evaporation during sample preparation (see Figure 3a). From AFM images the protrusion of the EO corona can be also observed showing a slightly less spherical micellar shape than in TEM images (Figure 3b).

From plots of $1/r_{h,app}$ against copolymer concentration the micellar hydrodynamic radii (r_h) was obtained as the intercept of each curve at $c = 0$ (see Figure 2b and Table 2). $1/r_{h,app}$ is proportional to the apparent diffusion coefficient, D_{app} , but without the influence of temperature and solution viscosity. The negative slopes of these plots pointed to negative values of the second virial (A_2) coefficient; this indicates that micelles interact attractively by bridging (33), as confirmed by the protrusions observed from some micelles to others denoting intermicellar bridging in AFM images (Figure 3c); van der Waals attraction and polymer depletion should not play significant roles in the present dilute micellar systems (24,26).

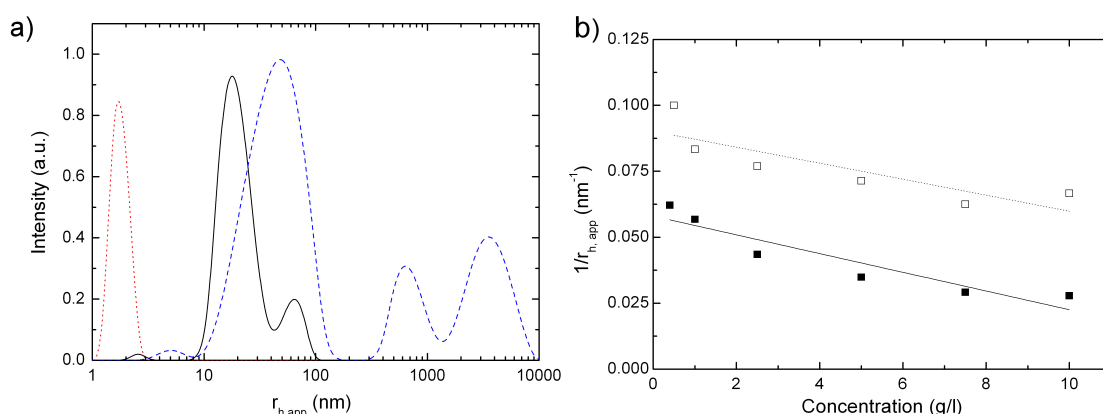


Figure 2. a) Intensity-weighted population distributions obtained by DLS for copolymer $\text{BO}_{21}\text{EO}_{385}\text{BO}_{21}$ in solution at 25°C (red, black and blue lines correspond to 0.4, 2.5 and 10 mg/mL solutions, respectively); b) Reciprocal apparent hydrodynamic radius, $1/r_{h,app}$, against concentration for copolymer $\text{BO}_{21}\text{EO}_{385}\text{BO}_{21}$ at 10°C (\square) and 25°C (\blacksquare).

Both the BO and EO block lengths will affect intermicellar interactions: Longer BO-end blocks should imply that intermicellar interaction can become stronger, while long central EO blocks can make the BO blocks to be extended into the solution more easily (34). Comparison of the present data with those previously reported for shorter $\text{BO}_m\text{EO}_n\text{BO}_m$ copolymers suggested that $\text{BO}_{14}\text{EO}_{378}\text{BO}_{14}$ and $\text{BO}_{21}\text{EO}_{385}\text{BO}_{21}$ displayed a stronger intermicellar attraction as would correspond to reverse copolymers with relatively long BO blocks and extremely lengthy EO ones.

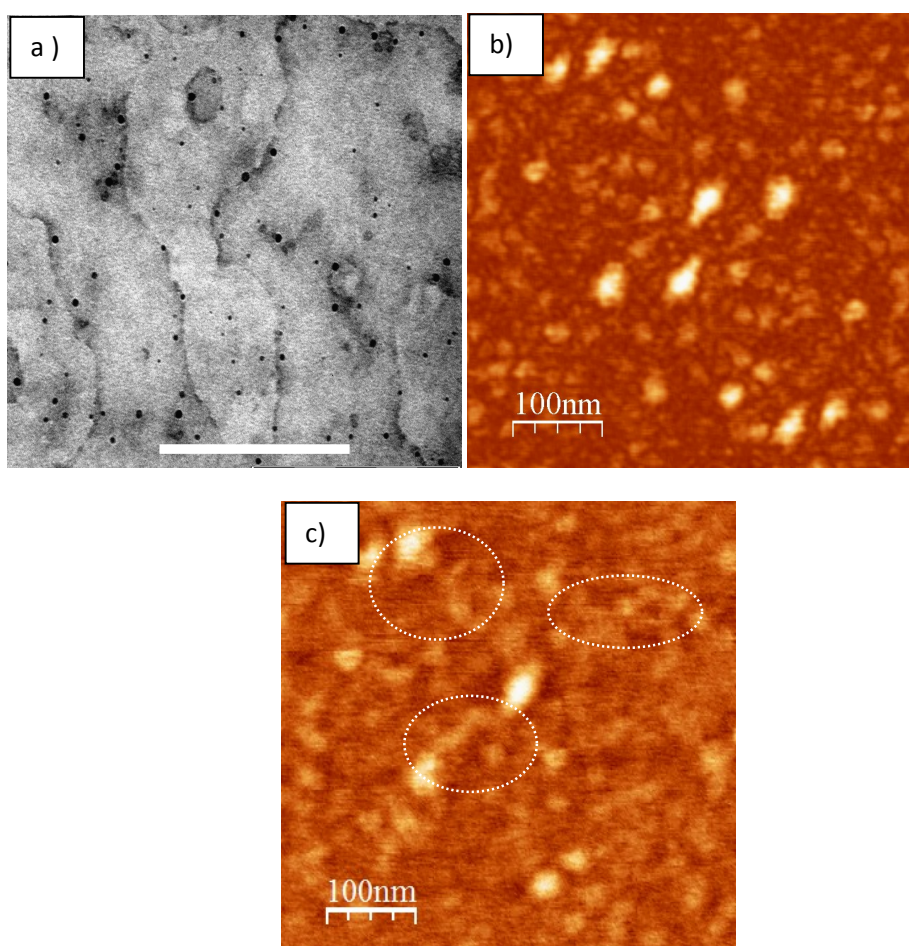


Figure 3. a) TEM image of micelles formed by copolymer $\text{BO}_{21}\text{EO}_{385}\text{BO}_{21}$ (scale bar 500 nm); b) AFM image of $\text{BO}_{21}\text{EO}_{385}\text{BO}_{21}$ micelles with a protruded corona; c) AFM image showing interchain bridges between copolymer micelles.

3.3.4.3 Micellar properties

Since the hydrodynamic radii of the present polymeric micelles (Table 2) are small compared to the light wavelength, intraparticle interference can be neglected. Clustering at higher copolymer concentrations changes this picture, but here we focused on the behavior in the dilute regime. Debye plots, *i.e.* plots based on

$$\frac{K^*c}{I-I_s} = \frac{1}{M_w^m} + 2A_2c + \dots \quad (2)$$

where I is the light scattering intensity from solution relative to that from toluene, I_s is the corresponding quantity for the solvent, c is the concentration (in g dm^{-3}), M_w^m is the mass-average molar mass of the solute, A_2 the second virial coefficient, and K^* the appropriate optical constant for $\text{BO}_{14}\text{EO}_{378}\text{BO}_{14}$ and $\text{BO}_{21}\text{EO}_{385}\text{BO}_{21}$ at 10 and 25 °C, are shown in Figure 4. K^* includes the specific refractive index increment (dn/dc), whose insensitiveness to composition in $\text{BO}_n\text{EO}_m\text{BO}_n$ systems is already known ($dn/dc = 0.135 \text{ cm}^3/\text{g}$) (26). Although at low concentrations the present copolymers should tend to loop in isolated micelles there is a finite probability of bridging because the system is in dynamic equilibrium as corroborated previously by AFM images, which implies an attractive intermicellar interaction. In particular, the upturns in the Debye plots at low concentrations would be caused by both the micelle-molecule equilibrium, *i.e.* the dissociation of micelles at concentrations approaching the *cmc*, and the existence of attractive interactions due to bridging even at such low concentrations ($c < 5 \text{ mg/mL}$). At larger concentrations repulsive interactions (effectively a hard-sphere interaction) are increasingly dominant giving rise to large positive slopes in the Debye plots. However, in the present case attractive interactions due to intermicellar bridging also play an important role counter-balancing the effect of repulsive interactions, as denoted by the small observed positive slopes of Debye plots (see Figure 4) in the concentration range analysed. Bridging is also observed to increase by rising the solution temperature. Water becomes a better solvent at low temperatures and a more-solvated EO-block corona involves a larger excluded volume of one micelle to another, as observed from steeper slopes at high copolymer concentrations at 10 °C.

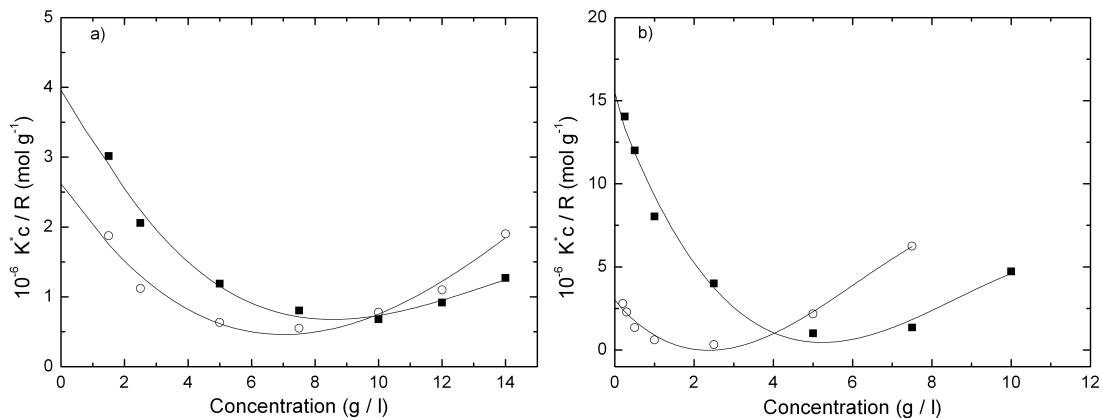


Figure 4. Debye plots for $\text{BO}_{14}\text{EO}_{378}\text{BO}_{14}$ (○) and $\text{BO}_{21}\text{EO}_{385}\text{BO}_{21}$ (■) copolymers at a) 10 °C and b) 25 °C.

Values of M_w^m were obtained by linear extrapolation of experimental data at $c < 5 \text{ mg/mL}$ and calculated from $N_w = M_w^m/M_w$ (Table 2). Association numbers for copolymer $\text{BO}_{21}\text{EO}_{385}\text{BO}_{21}$ were larger than those of $\text{BO}_{14}\text{EO}_{378}\text{BO}_{14}$ as corresponds to a

copolymer with a larger hydrophobic core and stronger intermicellar interactions. Also, N_w values for these copolymers slightly increased as temperature rose provided that water becomes a poorer solvent for the polyoxyethylene blocks (13). The present N_w values were also larger than those previously obtained for $\text{BO}_{10}\text{EO}_{410}\text{BO}_{10}$ copolymer as corresponds to copolymers with longer BO blocks, and similar as those of $\text{BO}_{10}\text{EO}_{271}\text{BO}_{10}$ or $\text{BO}_{12}\text{EO}_{260}\text{BO}_{12}$, (24,34) with much shorter EO blocks. In the latter cases, the increment of N_w due to the presence of longer BO blocks in the present copolymers was counter-balanced by the N_w reduction expected by their longer EO blocks, as observed for other pol(oxyalkylene)s copolymers (16).

Table 2: Micellar parameters of copolymers $\text{BO}_{14}\text{EO}_{378}\text{BO}_{14}$ and $\text{BO}_{21}\text{EO}_{385}\text{BO}_{21}$.^a

<i>Copolymer</i>	<i>T (°C)</i>	$10^5 M_w$ (g/mol)	r_h (nm)	N_w
$\text{BO}_{14}\text{EO}_{378}\text{BO}_{14}$	10	2.5	8.4	13
	25	3.4	18.5	18
$\text{BO}_{21}\text{EO}_{385}\text{BO}_{21}$	10	1.7	11.1	8
	25	1.8	20.4	9

^aEstimated uncertainty in M_w and r_h : $\pm 5\%$.

3.3.4.4 Rheological behavior

a. Tube inversion

Tube inversion was used to obtain a preliminary definition of the mobile-immobile regions of the phase diagrams. For copolymer $\text{BO}_{14}\text{EO}_{378}\text{BO}_{14}$ a mobile viscous fluid is present up to a concentration of 5 wt.% whilst an immobile gel is formed above (Figure 5a). The gel phase progressively converts into a very viscous fluid, resembling a high temperature boundary, in the range 40 to 90 °C depending on concentration: the higher the concentration the larger the boundary temperatures was. In the case of copolymer $\text{BO}_{21}\text{EO}_{385}\text{BO}_{21}$, a relatively mobile fluid is observed at concentrations below 4 wt.% and 15 °C. From such temperature and above the formation of a more viscous fluid took place, possibly as a consequence of micellar bridging (Figure 5b). Above 4 wt.%, a transparent immobile gel is observed. Nevertheless, it is worth mentioning that the characterisation of solutions containing these two triblock copolymers above ca. 3 wt.% by the tube-inversion method was complicated by the relatively important viscosity of the fluids, no doubt a result of micellar bridging, which made accurate detection of fluid/gel boundaries by this method difficult. Whereas fluid/gel boundaries in solutions of EO_mBO_n and $\text{EO}_m\text{BO}_n\text{EO}_m$ diblock copolymers can be readily detected to ± 1 °C, those in the present system could only be detected to ± 4 °C. Hence, to ensure the boundaries of the phase diagrams, rheometry measurements were also performed.

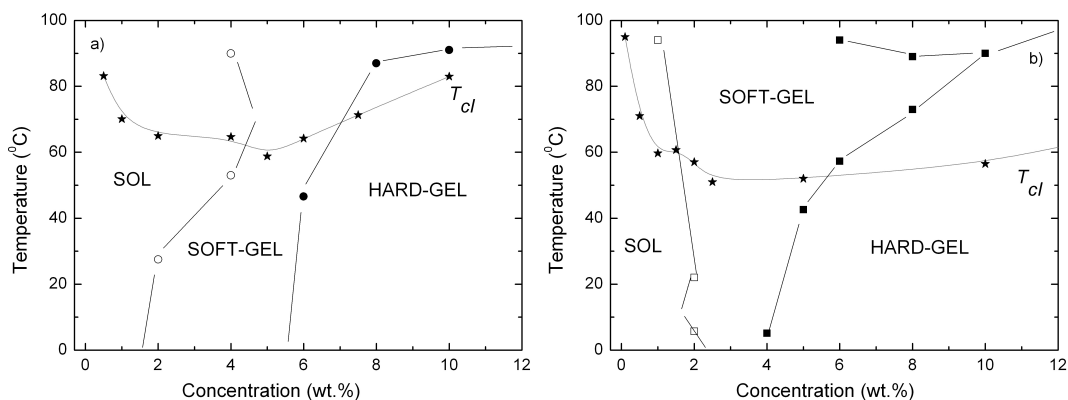


Figure 5. Phase diagrams delined using tube inversion and rheometry data from temperature scans. a) corresponds to $\text{BO}_{14}\text{EO}_{378}\text{BO}_{14}$, and b) to $\text{BO}_{21}\text{EO}_{385}\text{BO}_{21}$. (○) corresponds to the sol-soft gel transition, (■) denotes the soft gel-hard gel one and (★) the clouding temperature. Lines were drawn to guide the eye.

b. Concentration and temperature dependence

Temperature scans of $\log(G')$ at $f = 1$ Hz for copolymers $\text{BO}_{14}\text{EO}_{378}\text{BO}_{14}$ and $\text{BO}_{21}\text{EO}_{385}\text{BO}_{21}$ in the range 1-90 °C were performed. A view of the dependence of G' on concentration and temperature is provided by the examples shown in Figure 6. At 1wt.%, copolymer samples are unstructured fluids (sols, with $G' < 10$ Pa and $G'' > G'$). In the concentration range from 1 to 4 wt.% copolymer $\text{BO}_{14}\text{EO}_{378}\text{BO}_{14}$ was a viscous complex fluid at low and room temperatures characterized by $10 < G' < 1000$ Pa and $G' > G''$ (i.e. a soft gel adopting Hvidt's et al. notation) (35), and it became a sol at higher temperatures (45, and 53 °C at 2 and 4 wt.%, respectively). The observed decrease in G' at high temperatures and, thus, the transition from a viscous fluid to a sol can be associated with a worsening solvent environment compressing the EO-block corona. At 5 wt.% the copolymer was a viscous fluid in the whole temperature range, while it became an immobile gel at larger concentrations (arbitrarily defined by $G' > G''$ and $G' > 1000$ Pa at $f = 1$ Hz). In particular, the copolymer was an immobile gel in the temperature range 5 to ca. 50 °C at 6 wt.% and in the whole temperature range at 8 and 10 wt.%. At these concentrations, packing becomes the dominant contribution and the temperature dependence of G' resembled that found for non-bridging micellar solutions but, presumably, modified by bridging.

Since copolymer $\text{BO}_{21}\text{EO}_{385}\text{BO}_{21}$ has longer hydrophobic blocks than $\text{BO}_{14}\text{EO}_{378}\text{BO}_{14}$ and, thus, a lower *cmc* value its gelification is expected to take place at lower concentrations. As observed from Figure 6b, $\text{BO}_{21}\text{EO}_{385}\text{BO}_{21}$ was a viscous fluid above 6 °C at 2 wt.%, whereas at 3 and 4 wt.% remained in such a state in the whole temperature range. At 5 and 6 wt.% this copolymer became an immobile gel below ca. 44 and 60 °C, respectively, and a viscous fluid above such temperatures. Finally, above 8 wt.% the copolymer formed an immobile gel in the whole temperature range.

All the above data allowed a more exact definition of the phase diagram, as shown in Figure 5. In addition, more information could be extracted from rheology plots. At comparable concentrations, maximum values of $G'(T)$, G'_{max} , were larger for solutions of $\text{BO}_{21}\text{EO}_{385}\text{BO}_{21}$ than for $\text{BO}_{14}\text{EO}_{378}\text{BO}_{14}$ (Figure 6c). This is consistent with a stronger intermicellar bridging of the copolymer bearing longer BO blocks and the formation of micelles with a more-swollen EO-block corona, so high exclusion volumes would favor packing at high polymer concentrations. In fact, for both copolymers G' values increased markedly with concentration, with a predominant elastic behavior ($G' > G''$) in most of the temperature and concentration ranges analyzed.

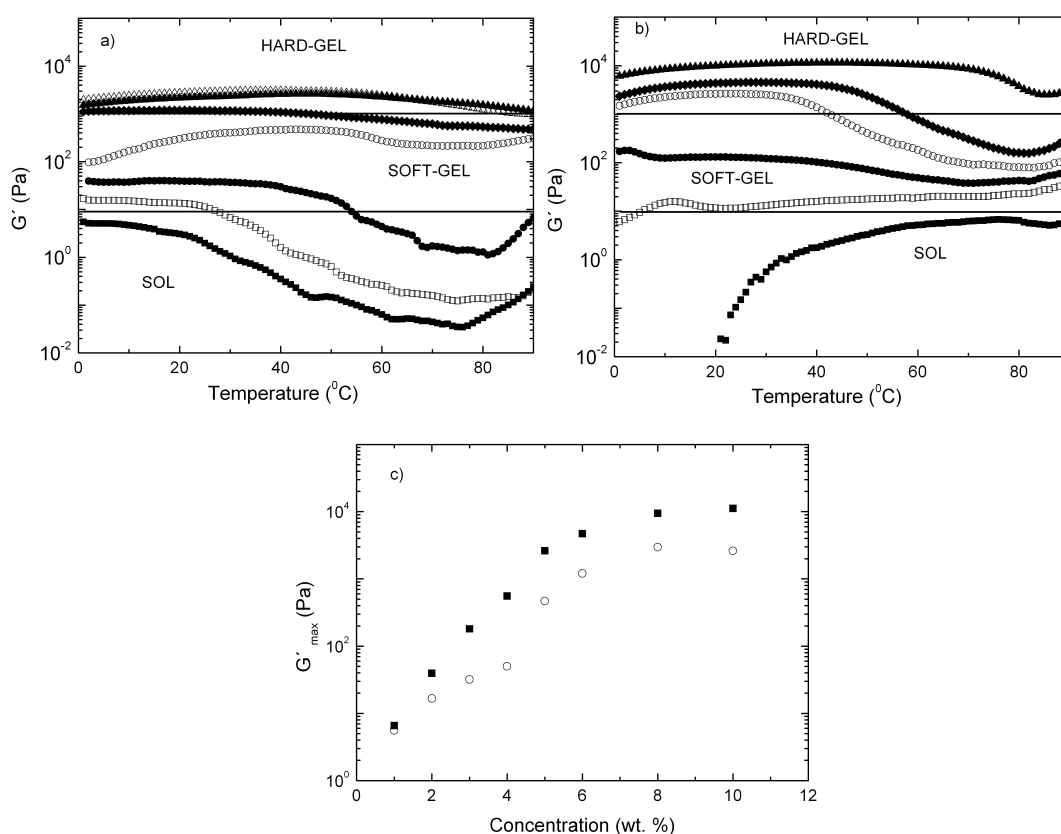


Figure 6. Temperature scans in the range 1-90 °C of $\log(G')$ at $f = 1$ Hz for copolymers a) $\text{BO}_{14}\text{EO}_{378}\text{BO}_{14}$ and b) $\text{BO}_{21}\text{EO}_{385}\text{BO}_{21}$. The concentrations analysed for copolymer $\text{BO}_{14}\text{EO}_{378}\text{BO}_{14}$ were (■) 1, (□) 2, (●) 4, (○) 5, (◆) 6, (▲) 8, and (△) 10 wt.%, whilst (■) 1, (□) 2, (●) 3, (○) 5, (◆) 6, and (▲) 10 wt.% for $\text{BO}_{21}\text{EO}_{385}\text{BO}_{21}$. c) Plots of G'_{max} against concentration for copolymers (○) $\text{BO}_{14}\text{EO}_{378}\text{BO}_{14}$ and (■) $\text{BO}_{21}\text{EO}_{385}\text{BO}_{21}$.

In general, at concentrations above ca. 5-6 wt.% G' is observed to increase in the temperature range from 5 to ca. 50-60 °C (depending on copolymer concentration) to subsequently decrease at higher temperatures, promoting a transition from an immobile gel to a complex viscous fluid. Structural studies by SAXS and SANS of aqueous solutions of block copolymers have shown that just outside the gel phase the fluid contains small micellar domains with the same structure as the gel phase (36); hence, the viscous fluid after the gel phase can be characterized as a defective cubic

structure, as previously observed for related EO_mBO_n and $\text{EO}_m\text{BO}_n\text{EO}_m$ copolymers (37).

As discussed elsewhere (37) for aqueous micellar gels of copoly(oxyalkylene)s of different block architectures, the onset of gelation and the associated increase in G' with T at low temperatures is associated with an increase in the extent of micellisation and, in the present case, with the extent of bridging. The observed decrease in G' at high temperatures for both copolymers can be associated with a worsening solvent environment compressing the EO-block corona and, thereby, with a decrease in the effective micellar volume fraction. The observation of peaks in G'' at the high- T boundaries of the immobile gels provides another indication of these effects (30).

c. Steady shear

The measurement of the yield stress (σ_y) provides a second measure of the resistance to motion under shear stress. The shear stress required to cause immobility in the tube inversion test has been previously shown to be 30-40 Pa (38). Yield stresses were measured in particular to confirm the concentration regions at which a viscous fluid is present, that is, the point at which the shear rate departed measurably from zero. Examples are shown in Figure 7a, *i.e.* $\sigma_y \sim 20$ Pa for a 3 wt.% solution at 20 °C but $\sigma_y \sim 0$ Pa for the same solution at $T = 50$ °C for copolymer $\text{BO}_{14}\text{EO}_{378}\text{BO}_{14}$. At higher concentrations the yield stress was high at all temperatures *i.e.* $\sigma_y \sim 350$ Pa for a 10 wt.% solution at 20 °C. There is also evidence in Figure 7a of shear thinning attributed to disruption of the structure under shear flow. The effect of steady shear was also investigated for a 6 wt.% solution at 30 °C, which was subjected to a steady shear stress of 500 Pa (well above the yield stress) for 45 s prior to immediate determination of modulus under the usual conditions. Then, the steady shear was immediately reapplied for subsequent periods and the determination of modulus repeated until accumulating 225 s of shear overall (Figure 7b). It was observed that moduli measured at $f = 1$ Hz decreased with this treatment. Resting the solution after the experiment for ca. 90 min resulted in only a small change in modulus, but resting overnight restored the modulus to, essentially, the initial G value. The 6 wt.% gel at 30 °C is near to its fluid-gel transition temperature (see Figure 5), and this may allow extensive disruption of structure and lead to slow recovery, which may well be an effect of the bridged network, as also observed in some related systems (23). This behavior is in contrast to diblock EO_mBO_n and triblock $\text{EO}_m\text{BO}_n\text{EO}_m$ copolymers, which have shown similar reductions in G' after application of large-amplitude oscillatory shears, but rapid recovery (< 1 min) of the modulus at rest.

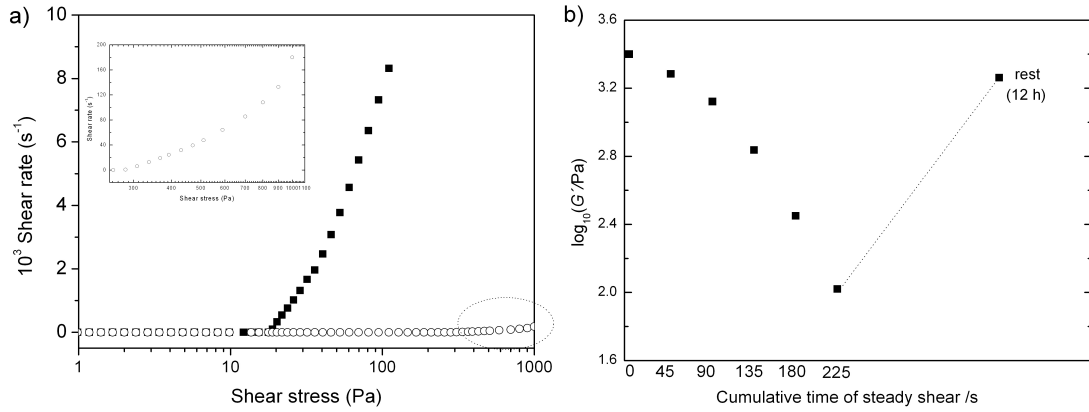


Figure 7: a) Yield stresses under continuous shear for 3 and 10 wt.% solutions of copolymer BO₁₄EO₃₇₈BO₁₄ at 20°C. The inset shows the yield of the 10 wt.% solution in greater detail. b) Dynamic moduli measurement at 1 Hz and 0.5% strain amplitude after time under steady shear and after rest for a 10 wt.% solution of copolymer BO₁₄EO₃₇₈BO₁₄.

d. Frequency scans

Effects of changes in the extent of micellar bridging and packing are apparent in the different mechanical responses to the applied frequency. Hence, the frequency dependence of the moduli was determined for solutions of copolymers BO₁₄EO₃₇₈BO₁₄ and BO₂₁EO₃₈₅BO₂₁ in the concentration range 1-10 wt.%. Examples are shown in Figure 8. For example, 1 wt.% solutions of copolymers BO₁₄EO₃₇₈BO₁₄ and BO₂₁EO₃₈₅BO₂₁ possessed typically values of G'' exceeding those of G' over most accessible frequency range except at high frequencies, where a moduli crossover occurs from which a relaxation time $t = 0.90$ and 0.55 s, respectively, could be determined (Figure 8a-b). The behavior can be approximated to that of a Maxwell element:

$$\begin{aligned} G' &= (G_{\infty} \tau^2 \omega^2) / (1 + \tau^2 \omega^2) \\ G'' &= (G_{\infty} \tau \omega) / (1 + \tau^2 \omega^2) \end{aligned} \quad (3)$$

where G_{∞} is the plateau value of G' at high frequency, τ is the relaxation time, and $\omega = 2\pi f$ (f = frequency in Hz). At all temperatures investigated, the slopes of the best straight lines through the data points were near to values of 2 ($\log G'$) and 1 ($\log G''$) which are expected when $\omega\tau \ll 1$, *i.e.* typical of a Newtonian fluid.

At copolymer concentrations between 2-4 wt. % at $T = 10$ °C, the scans obtained for both copolymers showed a more complex rheology with values of $G' < 1$ kPa. For example, a modulus crossover could be observed at low frequencies for BO₂₁EO₃₈₅BO₂₁ at 2 and 3 wt.% corresponding to a Maxwell fluid showing, at most, localized cubic order (37). This effect must be a consequence of the attraction of micelles at temperatures at which water is a poor solvent for micelles, and favored by micellar bridging too (Figure 8c). As the copolymer concentration was further

increased G' became progressively insensitive to frequency and consistently greater than G'' for both copolymers (see Figure 8c-d). In particular, for copolymer concentrations ranging from 4 to 6 wt.% an immobile gel with relatively high G' values (> 1 kPa) existed typically below 50-60 °C depending on copolymer type and concentration. Above such temperature threshold, a viscous fluid was observed (Figure 8d). This type of viscous fluid at temperatures and concentrations relatively near the gel boundary can be assigned as defective versions of cubic packed gels as mentioned previously; they are characterized by a constant value of G' , the shallow minimum in G'' , and both moduli do not show a crossover point in the measured frequency range as observed in Figure 8d. Nevertheless, the G' values for the viscous fluid are much lower compared to those of a pure gel phase, which well exceeded 1 kPa and possessed the characteristic features of immobile gels constituted by cubic packing of spherical micelles completely independent on temperature and frequency (39). The plateau behavior of G' and the minimum in G'' have been also observed for colloidal hard spheres near the glass-fluid transition (40), and is also characteristic of the cubic phase in block copolymer melts.⁴¹ The frequency-independent regime took place at lower concentrations for copolymer $\text{BO}_{21}\text{EO}_{385}\text{BO}_{21}$ than for $\text{BO}_{14}\text{EO}_{378}\text{BO}_{14}$ due to its larger hydrophobicity, which favored both micellization and micellar bridging due to the longer BO blocks.

Plots of G' and G'' vs. frequency presented in Figure 8 then show a wide variety of viscoelastic characteristics from purely viscous to highly elastic. This behavior confirms the formation of a dynamic network which becomes more robust as the concentration is increased, as also observed for other $\text{BO}_m\text{EO}_n\text{BO}_m$ copolymers as $\text{BO}_{12}\text{EO}_{114}\text{BO}_{12}$ (23), $\text{BO}_{10}\text{EO}_{227}\text{BO}_{10}$ (32) and $\text{BO}_{10}\text{EO}_{227}\text{BO}_{10}$ (29). Apart from the direct visual observations of certain chain crosslinking between micelles by AFM, the emergence of slow relaxation processes as the concentration increased in the dilute regime (< 4 wt.%) also corroborates the existence of this dynamic network. The contribution of micelle packing as effective hard spheres in the gel phase to the rheological response became predominant at larger concentrations for which G' became frequency-independent. Nevertheless, the effect of bridging was still observed, notably upon the slow relaxation after shearing when compared to the fast relaxation of micellar solutions of non-bridging spherical micelles. Also, $\text{BO}_{14}\text{EO}_{378}\text{BO}_{14}$ and $\text{BO}_{21}\text{EO}_{385}\text{BO}_{21}$ copolymers did not behave as classical colloidal suspensions interacting through weak short-range attractive forces, in which G' is frequency-independent and increases with concentration, and G'' is concentration-independent and increases linearly with frequency. These facts allow to scale the moduli against frequency to give smooth master curves (42) (see below).

Hence, $\text{BO}_{14}\text{EO}_{378}\text{BO}_{14}$ and $\text{BO}_{21}\text{EO}_{385}\text{BO}_{21}$ denote a more complex rheology as observed from frequency scans, which also impeded to fit their behavior to that of a Maxwell fluid. Strikingly, this behavior was rather different to that observed for other

structurally very related copolymer, $\text{BO}_{10}\text{EO}_{410}\text{BO}_{10}$. For this copolymer typical values of G'' exceed those of G' over a similar accessible frequency range, as also observed for other classical associative thickeners such as $\text{C}_n\text{UEO}_m\text{UC}_n$ and $\text{C}_n\text{EO}_m\text{C}_n$ polymers (C = methylene unit, and U = urethane linkage via an isophoronediiisocyanate residue) (43), whose lengthy EO and C blocks can be modelled by a single Maxwell element. Despite the similar EO length and larger BO blocks compared with $\text{BO}_{10}\text{EO}_{410}\text{BO}_{10}$, the larger polydispersities of $\text{BO}_{14}\text{EO}_{378}\text{BO}_{14}$ and $\text{BO}_{21}\text{EO}_{385}\text{BO}_{21}$ can broaden the Poisson distribution of BO block-lengths (assuming ideal polymerization) (44). The larger distribution of hydrophobic-block lengths implies a wider temperature range for micellization, with the full associative thickening effect being developed only when the extent of micellization and, consequently, the extent of bridging, is high, that is, the present copolymers effectively behave as having lower effective BO block lengths having a behavior closer to $\text{BO}_{12}\text{EO}_{114}\text{BO}_{12}$, $\text{BO}_{10}\text{EO}_{227}\text{BO}_{10}$ or $\text{BO}_{10}\text{EO}_{227}\text{BO}_{10}$ copolymers.

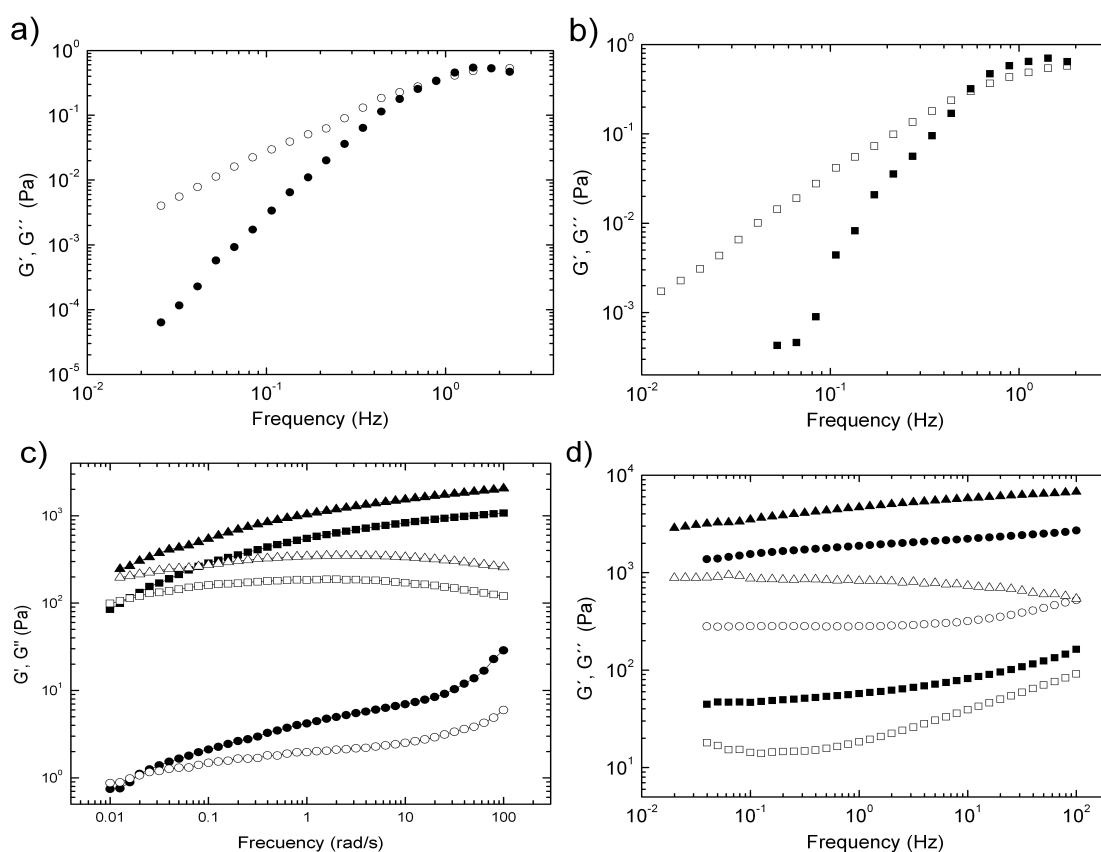


Figure 8: Frequency scans for a) $\text{BO}_{14}\text{EO}_{378}\text{BO}_{14}$ and b) $\text{BO}_{21}\text{EO}_{385}\text{BO}_{21}$ at 1 wt.% and 10 °C. c) $\text{BO}_{21}\text{EO}_{385}\text{BO}_{21}$ copolymer at 2 (circles), 3 (squares) and 4 wt.% (triangles) at 20 °C; and d) $\text{BO}_{14}\text{EO}_{378}\text{BO}_{14}$ copolymer at 6 wt.% and 20 (circles) and 60 °C (squares) and 10 wt.% (triangles) at 20 °C. Filled symbols denoted G' whilst open ones denoted G'' .

e. Scaling of rheological response

To additionally evaluate the mechanical response of copolymers $\text{BO}_{14}\text{EO}_{378}\text{BO}_{14}$ and $\text{BO}_{21}\text{EO}_{385}\text{BO}_{21}$ the construction of a master curve through the time-temperature superposition of the measured moduli was performed in order to facilitate the comparison of the frequency response at different temperatures. The moduli and the frequencies for each data set were independently scaled by factors a_T and b_T respectively to obtain a superposition of G' and G'' . The temperature dependence of the moduli was explored for 6 and 10 wt.% solutions in the range of 5-70 °C as examples, *i.e.* corresponding to the immobile gel phase for copolymers $\text{BO}_{14}\text{EO}_{378}\text{BO}_{14}$ and $\text{BO}_{21}\text{EO}_{385}\text{BO}_{21}$ (Figure 9). The data suggested that there were no changes in the nature of the dynamic mechanical response in the gel phase as a function of temperature in the range 10-50 °C. As commented previously, the independence of G' with frequency and the minimum in G'' in the gel phase region were, in part, the result of the formation of a cubic mesophase similar as that observed in hard sphere suspensions under shear near the fluid-glass transition. However, the shrinkage of the micellar corona at relatively high temperatures can lead to defects in micellar packing and the bridged network, which might well change the scaling of the viscoelastic behavior with frequency within the hard gel phase.

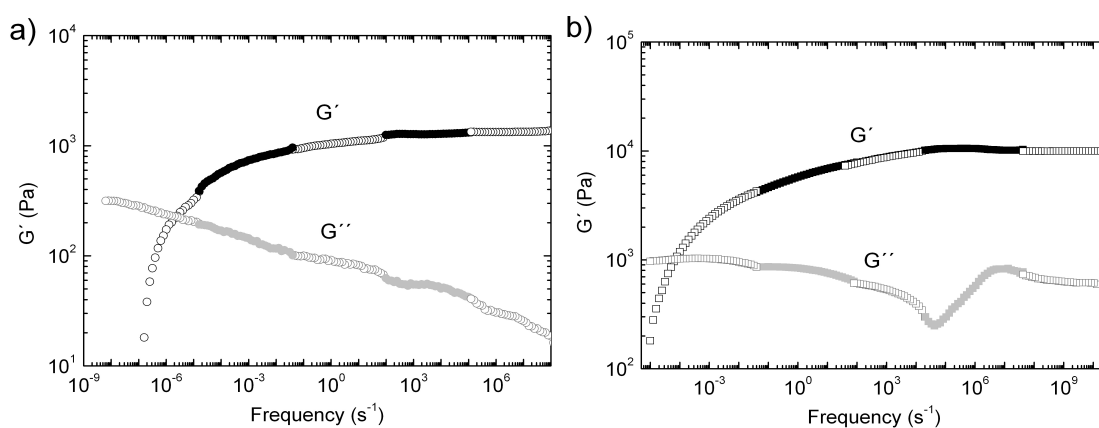


Figure 9: Master curve plots obtained for a) $\text{BO}_{14}\text{EO}_{378}\text{BO}_{14}$ copolymer at 6 wt.%, and b) $\text{BO}_{21}\text{EO}_{385}\text{BO}_{21}$ copolymer at 10 wt.% (reference temperature, $T_0 = 30^\circ\text{C}$).

The Arrhenius plot of $-\log(a_T)$ against $1/T$ (Figure 10a), which has a slope equivalent to a plot of $\log(\text{relaxation rate})$ against $1/T$, gave mean activation energy values, E , of -17 kJ and -50 kJ mol^{-1} for copolymers $\text{BO}_{14}\text{EO}_{378}\text{BO}_{14}$ and $\text{BO}_{21}\text{EO}_{385}\text{BO}_{21}$, respectively, as an average value over all components of the copolymer solutions. The lower (more negative) E value for $\text{BO}_{21}\text{EO}_{385}\text{BO}_{21}$ is in agreement with harder gels resulting from a more hydrophobic copolymer. The plot of $1/b_T$ against T shown in Figure 10b indicates an increase in the high-frequency storage modulus with temperature in the interval 10 to 50 °C for the 5 wt.% solution, with the dependence of G' on T being much greater than that predicted by the kinetic theory of network

elasticity for a fully formed network; conversely, at 10 wt.% the behavior is the opposite, in agreement with the shrinkage of the cubic mesoscopic structure of packed micelles.

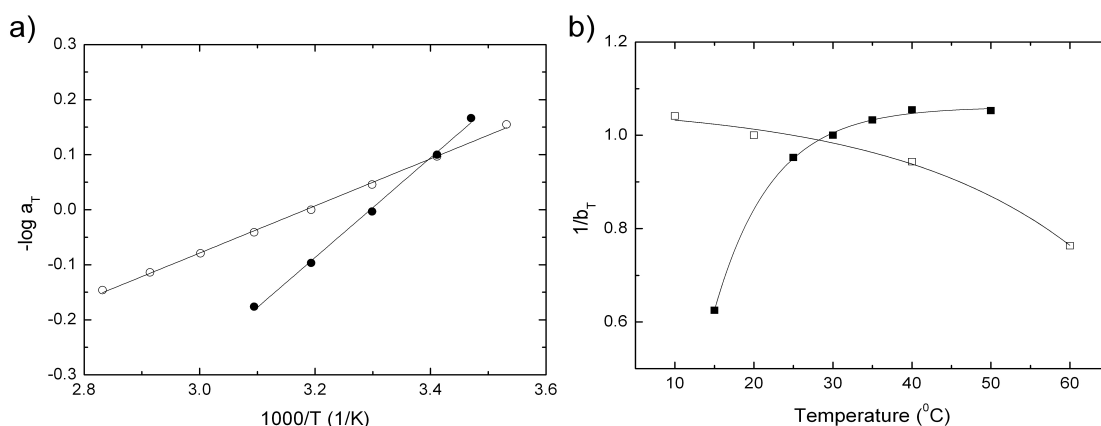


Figure 10: a) Arrhenius plot for scaling parameter a_T for copolymer $\text{BO}_{14}\text{EO}_{378}\text{BO}_{14}$ at 6 (○) and 10 (●) wt.%. b) Temperature dependence of $1/b_T$ for copolymer $\text{BO}_{21}\text{EO}_{385}\text{BO}_{21}$ at 5 (■) and 10 (□) wt.% solutions.

The negative values of the activation energy for the relaxation process found for solutions of the present copolymers were similar to those previously found for copolymer $\text{BO}_{10}\text{EO}_{410}\text{BO}_{10}$, and are in great contrast to positive values ($E = +30$ to $+70$ kJ mol^{-1}) measured for solutions of other associative thickeners such as $\text{C}_n\text{UEO}_m\text{UC}_n$ and $\text{C}_n\text{EO}_m\text{C}_n$ copolymers (43,45,46), that is, the relaxation times for $\text{BO}_{14}\text{EO}_{378}\text{BO}_{14}$ and $\text{BO}_{21}\text{EO}_{385}\text{BO}_{21}$ solutions increased with increasing temperature, whereas those for $\text{C}_n\text{UEO}_m\text{UC}_n$ and $\text{C}_n\text{EO}_m\text{C}_n$ solutions decreased with increasing temperatures. Hence, for the present copolymers the activation energy might involve both the disengagement of chain ends from micelles (a positive contribution) and micellization (a negative one) in contrast to alkyl-ended copolymer solutions, where only disengagement is important provided that their extent of micellization is low over the temperature range of interest. For both $\text{BO}_{14}\text{EO}_{378}\text{BO}_{14}$ and $\text{BO}_{21}\text{EO}_{385}\text{BO}_{21}$ copolymers micellization is the dominant process, and increases as temperature does. The increase of the high-frequency G' modulus with increasing T is consistent with this explanation. For solutions of classical associative thickeners copolymers $\text{C}_n\text{UE}_m\text{UC}_n$ and $\text{C}_n\text{E}_m\text{C}_n$, the high frequency storage modulus is either weakly sensitive to temperature (C_{16}U or C_{20}) (43,45,47) or falls with increasing temperature (C_{12}U or C_{16}) (46). The fall has been ascribed to an increased tendency as temperature is increased for the copolymers to loop in a single micelle rather than to bridge between micelles. Hence, at first sight, it could be thought that there is a contradiction between our assumptions that $\text{BO}_{14}\text{EO}_{378}\text{BO}_{14}$ and $\text{BO}_{21}\text{EO}_{385}\text{BO}_{21}$ copolymers are fully micellized at room temperature in dilute solution (0.1-1 wt %) but not in a concentrated solution (> 4 wt.%). However, it is known (48) that the micelle-unimer equilibrium changes dramatically when the concentration of copolymer is increased (*i.e.* when the H-bonded structure of water

and, hence, the hydrophobic effect that drives micellization is greatly reduced) (49). The effect of mass action is opposed by this reduction in the hydrophobic effect, and in a gel solution, the shorter BO blocks are less likely to enter micelles than in an 1 wt. % solution, which is favored by the broader Poisson BO block distributions.

3.3.5 Conclusions

In summary, in this work the self-assembly and physical properties of reverse triblock copolymers $\text{BO}_{14}\text{EO}_{378}\text{BO}_{14}$ and $\text{BO}_{21}\text{EO}_{385}\text{BO}_{21}$ have analysed in detail. These block copolymers form swollen flower-like micelles 20 to 40 nm in size as observed from DLS images, which can even be interconnected to certain extent in the very dilute regime as denoted by DLS and AFM data, creating certain hydrophobic domains which might enhance their interaction with cellular membranes (and subsequent internalization) and help to explain their induced cellular responses. As a result of their long BO blocks and extremely lengthy EO ones, these two copolymer exhibited a very rich phase behavior. This could be modulated from an unstructured fluid to a viscoelastic one to a fully developed gel by changing the solution temperature, concentration, and/or by the application of an external stress. In this way, the presence of bridging could be confirmed by observing, for example, the slow the relaxation of the gel network under the application of an external stress. Also, their complex rheology was observed from frequency scans, with a wide variety of viscoelastic characteristics from purely viscous to highly elastic. This behavior confirms the formation of a dynamic network which becomes more robust as the concentration is increased, which impeded to fit their behavior to that of Maxwell fluids. The larger distribution of hydrophobic-block lengths implies a wider temperature range for micellization, with the full associative thickening effect being developed only when the extent of micellization and, consequently, the extent of bridging, is high, that is, the present copolymers can effectively behave as having lower effective BO block lengths. The negative values of the activation energy for the relaxation process derived from master curves might involve both the disengagement of chain ends from micelles (a positive contribution) and micellization (a negative one), with evident predomiannce of the latter. This tunable complex rheological behavior makes these block copolymers very interesting candidates to configure gelling depots for implantation.

3.3.6 References

1. Farokhzad, O.C.; Langer, R. *Adv. Drug Deliv. Rev.*, **2006**, 58, 1456.
2. Cho, K.; Wang, X.; Nie, S.; Chen, Z.; Shin, D. M. *Clin. Cancer Res.*, **2008**, 14, 1310.
3. Arias, J.L. *Mini-Rev. Med. Chem.*, **2011**, 11, 1.

4. Lee, P.Y; Wong, K. K. Y. *Curr. Drug Deliv.* **2011**, 8, 245.
5. Heidel, J.; Davis, M. *Pharm. Res.*, **2011**, 28, 187.
6. Chu, B. *Langmuir*, **1995**, 11, 414.
7. Kabanov, A.V.; Alakhov, V. Y. *Crit. Rev. Ther. Drug Carrier Syst.*, **2002**, 19, 1.
8. Batrakova, E.V.; Kabanov, A. V. *J. Controlled Release*, **2008**, 130, 98.
9. Alvarez-Lorenzo, C., Sosnik, A.; Concheiro, A. *Curr. Drug Targets*, **2011**, 12, 1112.
10. Yu, G.-E.; Masters, A. J.; heatley, F.; Booth, C.; Blease, T. G. *Macromol. Chem. Phys.*, **1994**, 195, 1517.
11. Yu, G.-E.; Altinok, H.; Nixon, S. K.; Booth, C.; Alexandridis, P.; Hatton, T. A. *Eur. Polym. J.*, **1997**, 33, 673.
12. Mortensen, K.; Batsberg, W.; Hvidt, S. *Macromolecules*, **2008**, 41, 1720-1727.
13. Booth, C.; Attwood, D. *Macromol. Rapid Commun.*, **2000**, 21, 501-527.
14. Taboada, P.; Velasquez, G.; Barbosa, S.; Castelletto, V.; Nixon, S. K.; Yang, Z.; heatley, F.; Hamley, I. W.; Ashford, M.; Mosquera, V.; Attwood, D.; Booth, C. *Langmuir*, **2005**, 21, 5263-5271.
15. Taboada, P.; Velasquez, G., Barbosa, S.; Yang, Z.; Nixon, S. K.; Zhou, Z.; Heatley, F.; Ashford, M.; Mosquera, V.; Attwood, D.; Booth, C. *Langmuir*, **2006**, 22, 7465-7470.
16. Booth, C.; Attwood, D.; Price, C. *Phys. Chem. Chem. Phys.* **2006**, 8, 3612-3622.
17. Barbosa, S.; Cheema, M. A.; Taboada, P.; Mosquera, V. *J. Phys. Chem. B*, **2007**, 111, 10920.
18. Crothers, M.; Zhou, Z.; Ricardo, N. M. P. S.; Yang, Z.; Taboada, P.; Chaibundit, C.; Attwood, D.; Booth, C. *Int. J. Pharm.*, **2005**, 293, 91.
19. Ribeiro, M.E.N.P.; de Oliverira, S. M.; Ricardo, N. M. P. S.; Mai, S.-M.; attwood, D.; Yeates, S. G.; Booth, C. *Int. J. Pharm.*, **2008**, 362, 193.
20. Heatley, F.; Yu, G.-e.; Sun, W.-B.; ywell, J.; Mobbs, R. H.; Booth, C. *Eur. Polym. J.*, **1990**, 26, 583.
21. Yu, G.-e.; Yang, Z.; Ameri, M.; Attwood, D.; Collett, J. H.; Price, C.; Booth, C. *J. Phys. Chem. B*, **1997**, 101, 4394.
22. Mistry, D.; Annable, T.; Yuan, X.-F.; Booth, C. *Langmuir*, **2006**, 22, 2986.
23. Kelarakis, A.; Yuan, X.-F.; Mai, S.-M.; Yang, Y.-W.; Cooth, C. *Phys. Chem. Chem. Phys.*, **2003**, 5, 2628.
24. Zhou, Z.; Yang, Y.-W.; Booth, C.; Chu, B. *Macromolecules*, **1996**, 29, 8357.
25. Cambón, A.; Rey-Rico, A.; Mistry, D.; Brea, J.; Loza, M. I.; Attwood, D.; Barbosa, S.; Alvarez-Lorenzo, C.; Concheiro, A.; Taboada, P.; Mosquera, V. *Int. J. Pharm.*, **2013**, 445, 47.
26. Yang, Y.-W.; Yang, Z.; Zhou, Z.-K.; Attwood, D.; Booth, C. *Macromolecules*, **1996**, 29, 670.
27. Cambón, A.; Alatorre-Meda, M.; Juárez, J.; Topete, A.; Mistry, D.; Attwood, D.; Barbosa, S.; Taboada, P.; Mosquera, V. *J. Colloid Interface Sci.*, **2011**, 361, 154.

28. Provencher, S. W. *Die Makromol. Chemie*, **1979**, 180, 201.
29. Kellarakis, A.; Ming, X.-T.; Yuan, X.-F.; Booth, C. *Langmuir*, **2004**, 20, 2036.
30. Castelletto, V.; Hamley, I. W.; Yuan, X.-F.; Kellarakis, A.; Booth, C. *Soft Matter*, **2005**, 1, 138.
31. Liu, T.; Nace, V. M.; Chu, B. J. *Phys. Chem. B*, **1997**, 101, 8074.
32. Kellarakis, A.; Havredaki, V.; Yuan, X.-F.; Chaibundit, C.; Booth, C. *Macromol. Chem. Phys.*, **2006**, 207, 903.
33. Cambón, A.; Barbosa, S.; rey-rico, A.; Figueroa-Ochoa, E. B.; Soltero, J. F. A.; Yeates, S. G.; Alvarez-Lorenzo, C.; Concheiro, A.; Taboada, P.; Mosquera, V. J. *Colloid Interface Sci.*, **2012**, 387, 275.
34. Liu, T.; Zhou, Z.; Wu, C.; Nace, V. M.; Chu, B. J. *Phys. Chem. B*, **1998**, 102, 2875.
35. Hvidt, S.; Joergensen, E. B.; Brown, W.; Schillen, K. J. *Phys. Chem.*, **1994**, 98, 12320.
36. Prud'homme, R. K.; Wu, G.; Schneider, D. K. *Langmuir*, **1996**, 12, 4651.
37. Hamley, I. W.; Mai, S.-M.; Ryan, A. J.; Fairclough, P. A.; Booth, C. *Phys. Chem. Chem. Phys.*, **2001**, 3, 2972.
38. Li, H.; Yu, G.-E.; Price, C.; Booth, C. *Macromolecules*, **1997**, 30, 1347.
39. Juárez, J.; Taboada, P.; Valdez, M. A.; Mosquera, V. *Langmuir*, **2008**, 24, 7107.
40. Mason, T. G.; Weitz, D. A. *Phys. Rev. Lett.*, **1995**, 75, 2770.
41. Zhao, J.; Majumdar, B.; schulz, M. F.; Bates, F. S. *Macromolecules*, **1996**, 29, 1204.
42. Trappe, V.; Weitz, D. A. *Phys. Rev. Lett.*, **2000**, 85, 449.
43. Annable, T.; Buscall, R.; Ettelaie, R. *Colloids Surfaces A*, **1996**, 112, 97.
44. Flory, P.J. *Principles of Polymer Chemistry*. 1953, Cornell University Press, Ithaca.
45. Alexandridis, P.; Lindman, B. *Amphiphilic Block Copolymers. Self-Assembly and Applications*. 2000, Elsevier, Amsterdam.
46. Mistry, D. Ph.D. Thesis, University of Manchester, Manchester, UK. 2000.
47. Annable, T.; Buscall, R.; Ettelaie, R.; Whittlestone, D. J. *Rheol.*, **1993**, 37, 695.
48. Nixon, S.K.; Hvidt, S.; Booth, C. *J. Colloid Interface Sci.*, **2004**, 280, 219.
49. Tanford, C. *The Hydrophobic Effect*. 1980, Wiley, New York.

3.4 SOLUTION BEHAVIOR OF REVERSE TRIBLOCK REVERSE POLY(BUTYLENE OXIDE)-POLY (ETHYLENE OXIDE) - POLY(BUTYLENE OXIDE) COPOLYMERS WITH LENGTHY HYDROPHILIC BLOCKS.

3.4.1 Abstract

Triblock polyethylene oxide-polybutylene oxide-based block copolymers overcome some of the drawbacks of commercially available Pluronic block copolymers as the avoidance of transfer reaction in the polymerization reaction of propylene oxide. In addition, the larger hydrophobicity of butylene oxide (BO) in comparison to propylene oxide (PO) makes butylene oxide bearing-copolymers to micellize at much lower concentrations, behavior which can be exploited to use this class of copolymer as efficient nanocarriers of poorly aqueous soluble drugs. In particular, several reverse triblock poly(butylene oxide)-poly(ethylene oxide)-poly(butylene oxide) block copolymers have been recently found to be very useful as drug delivery nanovehicles and biological response modifiers (A. Cambón et al. *Int. J. Pharm.* 2013, 445, 47-57). Their interactions with biological relevant entities (cellular membranes, proteins, organelles...) and biological performance should be regulated by the nature, conformation and state of the copolymeric chains. For this reason, in this work we investigated the self-assembly process and physico-chemical properties of two of these reverse triblock poly(butylene oxide)-poly(ethylene oxide)-poly(butylene oxide) block copolymers, $\text{BO}_8\text{EO}_{90}\text{BO}_8$ and $\text{BO}_{20}\text{EO}_{411}\text{BO}_{20}$ in order to obtain a clear picture of their solution behavior and to correlate it with their biological performance. As a consequence of their structure and long EO blocks (specially $\text{BO}_{20}\text{EO}_{411}\text{BO}_{20}$) these copolymers possess a rich rheological behavior characterized by the formation of flower-like micelles with sizes ranging from ca. 10 to 30 nm in aqueous solution and the presence of intermicellar bridging even at low copolymers concentrations as denoted by atomic force microscopy and rheology specially for $\text{BO}_{20}\text{EO}_{411}\text{BO}_{20}$ as a result of their more lengthy BO and EO blocks; conversely, $\text{BO}_8\text{EO}_{90}\text{BO}_8$ displays a behaviour more similar to that observed for diblock EO_mBO_m and direct triblock $\text{EO}_m\text{BO}_n\text{EO}_n$ copolymers, with single non-associated micelles at low concentrations and a flow behaviour typical of mesoscopic ordered cubic structures. Nevertheless, the presence of micellar clusters due to bridging is also observed but to much lower extents. Strikingly, the relatively wide Poisson distribution of copolymeric chains

make the present copolymers to behave also rather distinctly to conventional associative thickeners.

3.4.2 Introduction

Hydrophobically end-capped poly(oxyethylene oxide)s have applications in paint coatings, personal care products and in the oil industry because of their ability to dramatically modify rheological properties (1-4). The industrially important type are the HEUR (hydrophobically ethoxylated urethane) associating polymers, which comprise lengthy poly(oxyethylene) chains end-capped via urethane links by alkyl chains. Corresponding poly(oxyethylene) dialkyl ethers and esters have been also used (5-6). Their desirable properties originate from molecular association of the hydrophobic ends of the chains in dilute solution and, above a critical micelle concentration (cmc), from the association of molecules into micelles in which the chains can either loop or extend (7). The bridging of chains between micelles, a dynamic process, leads to the formation of transient micelle clusters and networks.

Conventional triblock copolymers with hydrophobic end blocks, in particular triblock poly(oxyalkylene)s, offer a different synthetic route with the potential for interesting differences in properties and potential applications, as reported for $PO_nEO_mPO_n$ (8-9), $BO_nEO_mBO_n$ (10-13) and $SO_nEO_mSO_n$ (14-15), where EO, PO, BO and SO denote ethylene oxide, propylene oxide, butylene oxide and styrene oxide blocks, respectively. Amongst them, $PO_nEO_mPO_n$ copolymers have been the most extensively studied due to their commercial availability in a range of compositions. However, these copolymers present several drawbacks as, for example, their inherent polydispersity after oxyanionic polymerization as a consequence of the transfer reaction from hydrogen abstraction during the polymerization of the PO blocks (16), which results in an important diblock component in the synthesized material. This gives rise to variations in their physico-chemical properties from batch to batch which can preclude their use in different applications where an accurate reproducibility of the physico-chemical properties is required such as, for example, in drug delivery since these copolymers are amphiphilic and are able to self-assemble into nanoscopic core-shell micelles. The micellar core may serve as a reservoir for hydrophobic cargos while the corona provides stability and stealthiness into the aqueous biological medium.

An alternative to $PO_nEO_mPO_n$ copolymers are $BO_nEO_mBO_n$ ones provided that transfer is not a problem in the laboratory polymerization of butylene oxide and, hence, the chain distributions are much narrower. In addition, the larger relative hydrophobicity of BO blocks compared to PO (six-fold as estimated from the ratio of the logarithms of the cmcs) (17) allows the formation of polymeric micelles and of transient micelle clusters and/or networks by bridging of extended chains between micelles (13,18) at much lower concentrations than $PO_nEO_mPO_n$ do. This may enable their use as nanocarriers to solubilize much higher concentrations of poorly aqueous

soluble drugs in a reproducible manner (19) in the form of injectable solutions, oral suspensions and/or sub-dermal gelling depots (19-21) provided that these copolymers have been proved to be biocompatible (22). However, a detailed and complete characterization of the physico-chemical properties of this class of copolymers is still lacking: A deep knowledge about the correlations between copolymer structure and reflected properties must be key to explain, for example, the biological activity of some of these copolymers, for example, as enhancers of drug toxicity to cancerous cells by inhibiting the P-glycoprotein P efflux pump mechanism (19), which seems to be regulated by the nature, conformation and and state of the copolymeric chains

Hence, in this work we analyze the physico-chemical behavior in aqueous solution of two $\text{BO}_n\text{EO}_m\text{BO}_n$ block copolymers: $\text{BO}_8\text{EO}_{90}\text{BO}_8$ and $\text{BO}_{20}\text{EO}_{411}\text{BO}_{20}$, which largely differ in the hydrophilic block length. This should result in large differences in the micellization process, intermicellar interactions and, thus, solution behavior. In particular, as a result of its long BO blocks and extremely lengthy EO ones copolymer $\text{BO}_{20}\text{EO}_{411}\text{BO}_{20}$ clearly shows the formation of micellar clusters formed by micellar bridging as observed from dynamic light scattering (DLS), atomic force microscopy (AFM), and rheometry. Due to their shorter EO and BO blocks, copolymer $\text{BO}_8\text{EO}_{90}\text{BO}_8$ behaves more similarly to a solution of interacting micelles which pack in a mesoscopic structure (a gel) at large concentrations, although some extent of bridging could be also detected. The differences in the copolymer structures allows us then to observe the effects of both the collapse of longer BO blocks in solution of reverse copolymeric structures and the splitting of BO units number between two blocks, especially in dilute solution since the range of hydrophobicity has been much restricted for these copolymers *i.e.* from BO_4 to BO_{12} , 8 to 24 BO units per molecule (17).

3.4.3 Experimental Section

3.4.3.1 Materials

Triblock copolymers were prepared by oxyanionic polymerisation as previously reported.¹⁰ Briefly, dry 1,2-butylene oxide was initiated by polyethylene glycol monomer of different molecular weights activated by mixing with KOH and heating while stirring under vacuum (70 °C, 0.1 mmHg, 100 h) to remove water. Vacuum line and ampoule techniques served to exclude moisture. Gel permeation chromatography (GPC) was used to characterize the distribution widths of the products as the ratio of mass-average to number-average molar mass, *i.e.* M_w/M_n by using a Waters GPC system equipped with a 1515 isocratic pump and a 2410 refractive index detector (Waters, Milford, MA). Chloroform was used as eluent, and monodisperse PEO was employed as standard. ¹³C NMR spectra recorded on a Bruker ARX400 spectrometer (Bruker, Milton, ON, Canada) in deuterated chloroform were used to obtain absolute values of block length and composition, and to verify block architecture. Table 1

summarises the molecular characteristics of the copolymers.

Table 1. Molecular characteristics of the copolymers

Polymers	M_n (g/mol) ^a	M_w/M_n ^b	M_w (g/mol)	cmc (g/dm ³) ^c
BO ₈ EO ₉₀ BO ₈	5100	1.07	5457	0.33
BO ₂₀ EO ₄₁₁ BO ₂₀	21000	1.08	22680	0.01

^aEstimated by NMR; ^bEstimated by GPC; M_w calculated from M_n and M_w/M_n . Estimated uncertainty: M_n to $\pm 3\%$; M_w/M_n to ± 0.01 . ^cValues from Ref. 10.

3.4.3.2 Methods

a. Dynamic and static light scattering (DLS and SLS)

SLS intensities were measured by means of an ALV-5000F (ALV-GmbH, Germany) instrument with vertically polarized incident light ($\lambda = 488$ nm) supplied by a diode-pumped Nd:YAG solid-state laser (Coherent Inc., CA, USA) and operated at 2 W, and combined with an ALV SP-86 digital correlator with a sampling time of 25 ns to 100 ms (for DLS). Measurements were made at an angle $\theta = 90^\circ$ to the incident beam, as appropriate for particles smaller than the light wavelength. The intensity scale was calibrated against scattering from toluene. Solutions were filtered through Millipore Millex filters (Triton free, 0.22 μ m porosity) directly into cleaned scattering cells and allowed to equilibrate at the requested temperature for 10 min before measurement. Each experiment was repeated at least three times. Sampling time was 5-10 min for each run in order to define an optimal correlation function.

To obtain the micellar molecular weights and aggregation number, Debye plots *i.e.* plots based on

$$\frac{K^*c}{I-I_s} = \frac{1}{M_w^m} + 2A_2c + \dots \quad (1)$$

where I is the light scattering intensity from solution relative to that from toluene, I_s is the corresponding quantity for the solvent, c is the concentration (in g dm⁻³), M_w^m is the mass-average molar mass of the solute, A_2 the second virial coefficient, and K^* the appropriate optical constant, were used. K^* includes the specific refractive index increment (dn/dc), whose insensitiveness to composition in BO_{*n*}EO_{*m*}BO_{*n*} systems is already known ($dn/dc = 0.135$ cm³/g).²³

For DLS, the correlation functions were analyzed by the CONTIN method to obtain the intensity distributions of decay rates (Γ).²⁴ From the decay rate distributions the apparent diffusion coefficients ($D_{app} = \Gamma/q^2$, $q = (4\pi n_s/\lambda)\sin(\theta/2)$) were derived, being n_s the solvent refractive index. Values of the apparent hydrodynamic radius ($r_{h,app}$,

radius of the hydrodynamically equivalent hard sphere corresponding to D_{app}) were calculated from the Stokes-Einstein equation

$$r_{h,app} = kT / (6\pi\eta D_{app}) \quad (2)$$

where k is the Boltzmann constant and η is the viscosity of water.

b. Transmission electron microscopy (TEM)

Micellar solutions of both copolymers were applied dropped over carbon-coated copper grids, blotted, washed, negatively stained with 2% (w/v) phosphotungstic acid, air-dried, and then examined with a Phillips CM-12 transmission electron microscope operating at an accelerating voltage of 120 kV.

c. Clouding

Copolymer solutions were prepared by weighting the requested amount of each copolymer followed by the addition of the same volume of cold water (1 mL). Copolymer solutions were homogenized under stirring at low temperature before being stored at least for one day ($T \sim 4$ °C) to ensure complete dissolution. Clouding temperatures (T_{cl}) were determined by slowly heating (0.2 °C min^{-1}) the copolymer solutions from 0 to 90 °C by both visual inspection and detection of the transmitted light through solutions by means of a Cary Eclipse UV-Vis spectrophotometer equipped with a temperature control Peltier device and a multi-cell sample holder (Cary 100, Agilent, Germany). As a result, a plot of transmitted intensity versus temperature was obtained. The cloud point was determined as the midpoint of an abrupt decrease in the transmitted light intensity from a plot of transmitted intensity vs temperature, as previously described (18).

d. Rheology

Solutions were prepared by weighting powder copolymer and deionized water into small tubes and subsequent mixing in the mobile state before being stored for at least one day at low temperature (ca. 4 °C). Rheological characterisation was carried out using a controlled stress AR2000 rheometer (TA instruments, DE, USA) with Peltier temperature control. Samples were investigated using cone-plate geometry and a solvent trap to maintain a water-saturated atmosphere around the sample cell to avoid evaporation. The temperature dependence of storage (G') and loss (G'') moduli was measured either by temperature scans (1-90°C) at frequency $f = 1$ Hz and heating rates of 1 °C min^{-1} or via frequency scans at several temperatures. Experiments were carried out in oscillatory shear mode, with the strain amplitude (A) maintained at a low value ($A < 0.5$ %) by means of the autostress facility of the software. This ensured that

measurements of G' and G'' were in the linear viscoelastic region. A dynamic time sweep test under $A = 0.5\%$ and $f = 1$ Hz was performed before each frequency scan at a fixed temperature to ensure that the sample truly reached the equilibrium state.

e. Atomic force microscopy (AFM)

AFM images of block copolymer solutions were performed on freshly cleaved mica substrates. The measurements were performed in a JEOL instrument (model JSPM 4210) in noncontact mode using nitride cantilevers NSC15 from MicroMasch, U.S.A. (typical working frequency and spring constant of 325 kHz and 40 N/m, respectively). The AFM samples were dried in air or under a nitrogen flow when required. Control samples (freshly cleaved mica and buffer solution) were also investigated to exclude possible artifacts. Topography and phase-shift data were collected in the trace and retrace direction of the raster, respectively. The offset point was adapted accordingly to the roughness of the sample. The scan size was usually 500 nm (aspect ratio, 1 x 1), with a sample line of 256 points and a step size of 1 μm . The scan rate was tuned proportionally to the area scanned and kept within the 0.35-2 Hz range. Each sample was imaged several times at different locations on the substrate to ensure reproducibility. Diameters and heights of copolymer aggregates were determined by sectional analysis taken from the average of several sections through the aggregates.

3.4.4 Results and Discussion

3.4.4.1 Clouding

Clouding temperatures (T_{cl}) were firstly determined for solutions of copolymers $\text{BO}_8\text{EO}_{90}\text{BO}_8$ and $\text{BO}_{20}\text{EO}_{411}\text{BO}_{20}$ in the concentration range 0.1-10 wt.% by visual inspection and UV-Vis spectroscopy following the methodology of Zhou *et al* (18). For $\text{BO}_8\text{EO}_{90}\text{BO}_8$ the cloud-point profile exhibited a shallow minimum at 0.75 wt.% (at 43 $^\circ\text{C}$), whilst for $\text{BO}_{20}\text{EO}_{411}\text{BO}_{20}$ this minimum was observed at 1.5 wt.% (at 41 $^\circ\text{C}$) (Figure 1). For both copolymers T_{cl} starts again to increase at larger concentrations from their respective minima. In general, copolymer $\text{BO}_8\text{EO}_{90}\text{BO}_8$ displayed lower T_{cl} than $\text{BO}_{20}\text{EO}_{411}\text{BO}_{20}$ as a consequence of their lower EO/BO ratio: Regardless copolymer $\text{BO}_{20}\text{EO}_{411}\text{BO}_{20}$ possesses much longer BO blocks which should largely decrease T_{cl} , the extremely long hydrophilic EO block counterbalances this effect and favors an important enhancement of T_{cl} (25), in agreement with previous observations (11,26). This behavior is further supported when comparing, for example, copolymer $\text{BO}_8\text{EO}_{90}\text{BO}_8$ with the structurally related $\text{BO}_7\text{EO}_{40}\text{BO}_7$: By doubling the EO block length while keeping almost constant the BO one results in a great increase of T_{cl} from 35 $^\circ\text{C}$ to 75 $^\circ\text{C}$ at a copolymer concentration of 10 wt.% (18). In addition, an increase in the BO block length while keeping constant the EO one leads to an important decrease in

T_{cl} , for example, from 53 to 41.5 °C at 2 wt.% when comparing, for example, copolymers $\text{BO}_{10}\text{EO}_{410}\text{BO}_{20}$ and $\text{BO}_{20}\text{EO}_{411}\text{BO}_{20}$, or from 66 to 57°C for copolymers $\text{BO}_{14}\text{EO}_{378}\text{BO}_{14}$ and $\text{BO}_{21}\text{EO}_{385}\text{BO}_{21}$, respectively (27). However, it is worth mentioning that for concentrations above 3.5 wt.% the more efficient packing of $\text{BO}_{20}\text{EO}_{411}\text{BO}_{20}$ micelles and their subsequent packing and ordering in solution (gel formation) leads to a sharper T_{cl} increase above those values corresponding to copolymer $\text{BO}_{10}\text{EO}_{410}\text{BO}_{20}$ (Figure 1a). High T_{cl} coincident with gel formation have been also observed in related systems, *i.e.* aqueous solutions of copolymers $\text{BO}_{12}\text{EO}_{114}\text{BO}_{12}$ and $\text{BO}_{12}\text{EO}_{227}\text{BO}_{12}$ (12,13,28).

Provided that the *cmc* values of the present copolymers were previously found to be below 0.35 mg/mL (11), the cloud point behavior would represent the phase transition of a copolymer micellar solution which phase separates at a temperature well above the T_{cl} . On the other hand, plotting T_{cl} values against EO/BO ratio at fixed copolymer concentration (1 wt.%) an empirical correlation for $\text{BO}_n\text{EO}_m\text{BO}_n$ copolymers with short (≤ 10) and long (≥ 10) BO blocks could be observed (Figure 1b). The lowest values of T_{cl} are directly dependent on copolymer hydrophobicity, that is, T_{cl} at the minimum decreases as the EO/BO ratio does (Table S1).

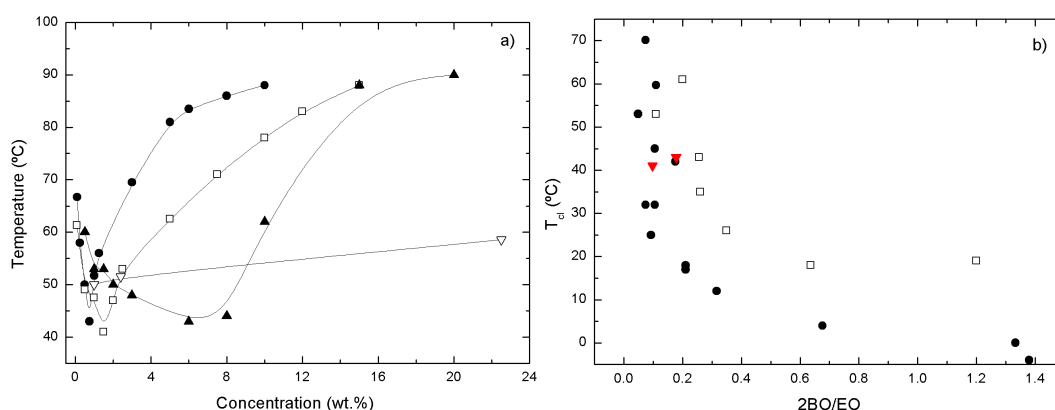


Figure 1. a) Clouding temperatures for $\text{BO}_n\text{EO}_m\text{BO}_n$ triblock copolymers as a function of concentration: (●) $\text{BO}_8\text{EO}_{90}\text{BO}_8$ and (□) $\text{BO}_{20}\text{EO}_{411}\text{BO}_{20}$. For comparison, structurally-related copolymers (▽) $\text{BO}_5\text{EO}_{91}\text{BO}_5$ and (▲) $\text{BO}_{10}\text{EO}_{410}\text{BO}_{10}$ (11) are also shown. b) Minimum clouding temperatures copolymers as a function of BO/EO block length ratio for $\text{BO}_n\text{EO}_m\text{BO}_n$ triblock with (□) $\text{BO} < 10$ and (●) $\text{BO} > 10$. The present $\text{BO}_8\text{EO}_{90}\text{BO}_8$ and $\text{BO}_{20}\text{EO}_{411}\text{BO}_{20}$ copolymers are shown in red.

3.4.4.2 Population size distributions

DLS measurements of micellar solutions of copolymers $\text{BO}_8\text{EO}_{90}\text{BO}_8$ and $\text{BO}_{20}\text{EO}_{411}\text{BO}_{20}$ at different concentrations were carried out at 10 and 25 °C. Selected intensity fraction distributions of $\log r_{h,app}$ ($r_{h,app}$ being the apparent hydrodynamic

radius, *e.g.* the radius of gyration of the hydrodynamically equivalent hard sphere) are illustrated in Figure 2a for copolymer $\text{BO}_8\text{EO}_{90}\text{BO}_8$ at 25 °C as an example. At the lowest concentration analysed (0.1 wt. %), the population distribution showed a single peak attributed to flower-like micelles ($r_{h,app} \sim 13$ nm). At larger concentrations (0.25 wt.%), two peaks were observed in the intensity-fraction population distributions, which can correspond to micelles and micelle clusters formed by micellar bridging ($r_{h,app} = 140$ nm), respectively. Further increases in copolymer concentration leads to an enhancement of the light scattered by flower-like micelles and to a certain reduction (in intensity) in the population distribution of the micellar clusters, which shifts to larger sizes and becomes broader (ca. 200 nm). This behaviour can be probably a consequence, on one hand, of a better packing of BO blocks inside micelles as the copolymer concentration increases and, on the other, to an extension of bridging resulting in associated larger micellar clusters.

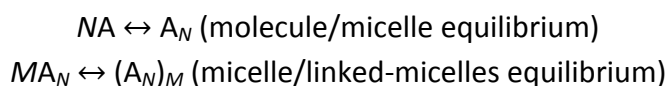
Owing to the special chain architecture of $\text{BO}_n\text{EO}_m\text{BO}_n$ -type block copolymers, the formation of flower-like micelles involves the bending of the hydrophilic EO blocks while keeping the two-end BO blocks in the same micellar core, which is an entropically-loss process. Another possibility is that the two BO blocks in one polymer chain can reside in two adjacent micelles while the EO block is used as a bridge. This kind of cross-linking among the micelles can finally promote an open network structure (the so-called micellar clusters), which is reflected in the DLS population distributions.

Copolymer $\text{BO}_{20}\text{EO}_{411}\text{BO}_{20}$ possessed a similar behavior as $\text{BO}_8\text{EO}_{90}\text{BO}_8$ except that sizes of micelles and micellar clusters become larger due to the lengthy EO blocks of this copolymer. At this respect, it is worth mentioning that micellar cluster sizes for this copolymer reaches ca. 900 nm, and even a third much larger population at ca. 3000-4000 nm can be observed probably being a result of the formation of insoluble aggregated material as a consequence of cluster aggregation (Figure 2a). For both $\text{BO}_8\text{EO}_{90}\text{BO}_8$ and $\text{BO}_{20}\text{EO}_{411}\text{BO}_{20}$ the micellar shape was nearly spherical as observed by TEM and AFM, with their diameters (ca. 22 ± 4 and 32 ± 5 nm for $\text{BO}_8\text{EO}_{90}\text{BO}_8$ and $\text{BO}_{20}\text{EO}_{411}\text{BO}_{20}$ as calculated from TEM, respectively), in fair agreement with those obtained from DLS in spite of the usual dehydration of the copolymer corona and subsequent shrinking of the copolymer structure upon solvent evaporation during sample preparation (Figure 2b). From AFM images a deformation of the EO corona can be observed as a result of bridging and subsequent formation of micellar clusters (Figure 2c).

Intensity-average values of $1/r_{h,app}$ were calculated for micelles by integrating over the micelles peak in the intensity distributions of decay rate. Since the dissymmetry ratio was found to be near unity, the values obtained were essentially z-

averages. Micellar hydrodynamic radii (r_h) were obtained as the intercept of each curve at $c = 0$ (Figure 2e and Table 3) from plots of $1/r_{h,app}$ against copolymer concentration. $1/r_{h,app}$ is proportional to the apparent diffusion coefficient, D_{app} , but without the influence of temperature and solution viscosity. It can be observed that the average values of $r_{h,app}$ increased as concentration did, *i.e.* the apparent diffusion coefficient ($D_{app} = kT / 6\pi\eta r_{h,app}$) decreased (Figure 2d). Also, micellar sizes become smaller as the temperature decreases. This was as expected provided that water becomes a better solvent for micelles as the temperature is lowered and, hence, micellar bridging (and hence clustering) was reduced.

The negative slopes of plots in Figure 2d and, hence, the negative second virial coefficients (A_2) derived as reported previously (Table 3, see SI for additional details) (29) implies a substantial attractive contribution to their intermicellar interaction, resulting in small excluded volumes for the micelles of $BO_nEO_mBO_n$ copolymers, especially for $BO_8EO_{90}BO_8$ due to its shorter EO corona which, in turn, results in small values of A_2 . This is consistent with the micelles having a fraction of their BO blocks extended into the solvent and available for interaction, either with BO blocks protruding from a second micelle or by entering the core of a second micelle, as confirmed visually (Figure 2c-d), and considering that Van der Waals attraction and polymer depletion forces would not play significant roles in the present relatively dilute micellar systems (18,23). In either case, the effect results in transient micellar linking, which implies a second equilibrium in the system:



Both BO and EO block lengths will affect these interactions: Longer BO-end blocks imply that the intermicellar interaction can become stronger, while central EO blocks can make the BO blocks to be more or less extended into the solution (30). The smaller (more negative) A_2 values for copolymer $BO_{20}EO_{411}BO_{20}$ compared to those of $BO_8EO_{90}BO_8$ might be a consequence of the longer BO and EO blocks of the former copolymer which favoured direct contacts between micelles even at very low concentrations. Also, A_2 coefficients increases (become less negative) as temperature raises as a consequence of water becoming a worst solvent for micelles which would make EO coronas to be less hydrated and shrunk and decreasing the extent of bridging, in agreement with static light scattering data (see below).

In summary, the present data would support the view that for molecules of this type limited open molecular association accompanies closed association to micelles. This means (in a simplified model) that several components are in equilibrium: molecules, micelles, and micellar associates (linked micelles).

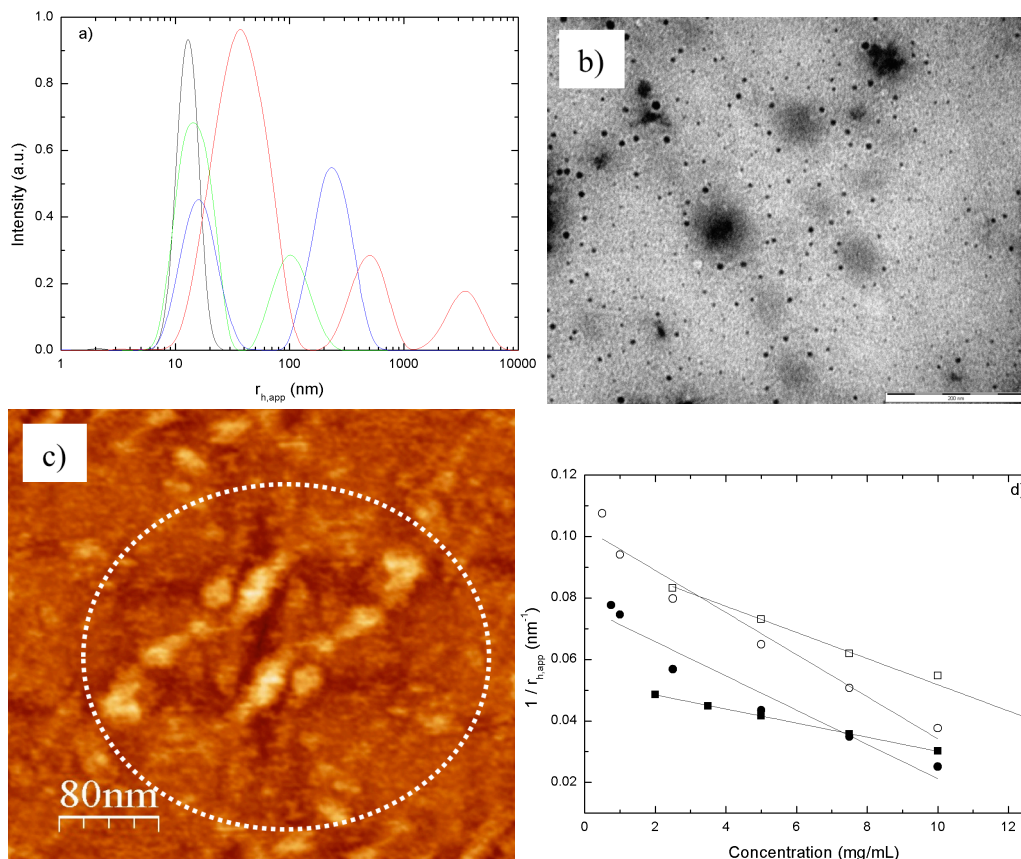


Figure 2. a) Intensity-weighted population distributions obtained by DLS for copolymer $\text{BO}_8\text{EO}_{90}\text{BO}_8$ in solution at 25°C (black, green and blue lines correspond to 1, 5 and 10 mg/mL solutions, respectively) and copolymer $\text{BO}_{20}\text{EO}_{411}\text{BO}_{20}$ (10 mg/mL, red line). b) TEM image of $\text{BO}_{20}\text{EO}_{411}\text{BO}_{20}$ micelles at a concentration of 0.5 wt.% (scale bar 200 nm). c) AFM image of $\text{BO}_{20}\text{EO}_{411}\text{BO}_{20}$ copolymer showing interchain bridges between micelles. d) Reciprocal apparent hydrodynamic radius, $1/r_{h,app}$, against concentration for copolymers $\text{BO}_8\text{EO}_{90}\text{BO}_8$ (●,○) and $\text{BO}_{20}\text{EO}_{411}\text{BO}_{20}$ (■,□) in solution at 10°C at 10 °C (open symbols) and 25 °C (filled symbols).

3.4.4.3 Micellar properties

Since the hydrodynamic radii of the present micelles (listed in Table 3) are small compared to the light wavelength, intraparticle interference can be neglected. Clustering at higher concentrations changes this picture, but we here focused on the behaviour in the dilute micellar regime. Debye plots for copolymers $\text{BO}_8\text{EO}_{90}\text{BO}_8$ and $\text{BO}_{20}\text{EO}_{411}\text{BO}_{20}$ at 10 and 25 °C are shown in Figure 3. These plots indicate associates of higher molar mass at 25 °C compared with 10 °C for both copolymers, as expected for water to be a poorer solvent at the highest temperature. The overall scattering behavior of $\text{BO}_8\text{EO}_{90}\text{BO}_8$ and $\text{BO}_{20}\text{EO}_{411}\text{BO}_{20}$ copolymer solutions is consistent with a closed association process into micelles, but the slopes and curvatures of the Debye

plots at the highest concentrations (specially for copolymer $\text{BO}_{20}\text{EO}_{411}\text{BO}_{20}$) are much changed compared with those for EO_nBO_n or $\text{EO}_n\text{BO}_m\text{EO}_n$ copolymers. Although at low concentrations the present copolymers, and especially $\text{BO}_8\text{EO}_{90}\text{BO}_8$, tend to loop in isolated micelles there is a finite probability of bridging because the system is in dynamic equilibrium, which implies an attractive intermicellar interaction. Hence, the minima and low positive slopes seen in Figure 3b for $\text{BO}_{20}\text{EO}_{411}\text{BO}_{20}$ results from the competition between repulsive and attractive interactions between the micelles, which are less important for copolymer $\text{BO}_8\text{EO}_{90}\text{BO}_8$ at 25 °C, in agreement with our interpretation of the DLS results in the former section. The repulsive interaction, effectively a hard-sphere interaction, clearly dominates at the largest concentrations where higher virial coefficients are required to describe the slope of the Debye plots. The effect of the attractive interaction between micelles, which derives from bridging, is seen at lower concentrations where A_2 dominates, and represented by the upturns in the plots for copolymer $\text{BO}_{20}\text{EO}_{411}\text{BO}_{20}$. In this case, such upturns cannot be ascribed to the micelle-molecule equilibrium, *i.e.* the dissociation of micelles at concentrations approaching the critical micelle concentration, provided that the concentration range analyzed is well-above the copolymers *cmcs*.

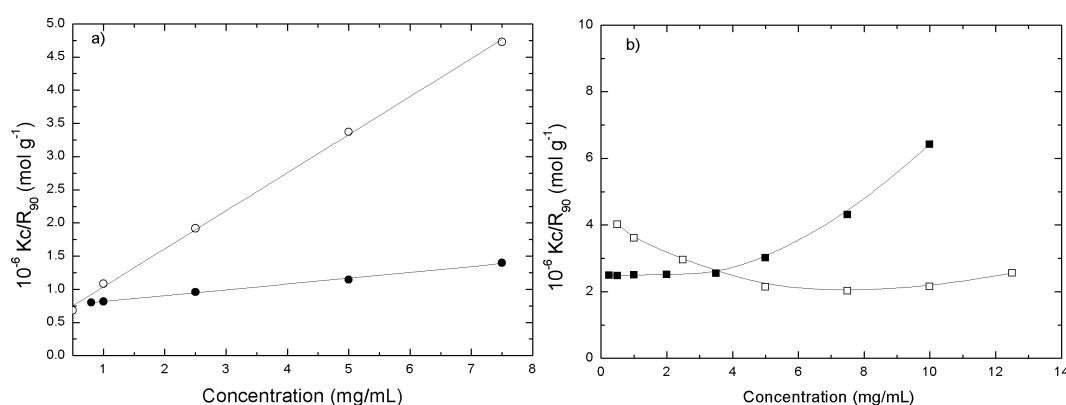


Figure 3. Debye plots for a) $\text{BO}_8\text{EO}_{90}\text{BO}_8$ and b) $\text{BO}_{20}\text{EO}_{411}\text{BO}_{20}$ copolymers at 10 °C (open symbols) and 25 °C (filled symbols).

Values of M_w^m were obtained by simply applying the Debye equation for copolymer $\text{BO}_8\text{EO}_{90}\text{BO}_8$ and by linear extrapolation of experimental data at $c < 5$ mg/mL and by for $\text{BO}_{20}\text{EO}_{411}\text{BO}_{20}$, respectively, and calculated from $N_w = M_w^m/M_w$ (Table 2). The almost ideal behavior of the $\text{BO}_8\text{EO}_{90}\text{BO}_8$ system at low concentration is attributed to counter-balanced attractive and repulsive interactions of micelles in the dilute solution range and the polymer ability to pack in single micelles at low concentrations due to its much shorter blocks, as commented previously (see Figure 2a).

Association numbers for copolymer $\text{BO}_8\text{EO}_{90}\text{BO}_8$ were larger than those of $\text{BO}_{20}\text{EO}_{411}\text{BO}_{20}$ as corresponds to a copolymer with a lower EO/BO ratio and much shorter EO block length: The increment of N_w due to the presence of longer BO blocks

for copolymer BO₂₀EO₄₁₁BO₂₀ was counter-balanced by the N_w decrease expected by their longer EO blocks, as observed for other poly(oxyalkylene)s copolymers (16). Also, N_w values for these copolymers slightly increased as temperature rose provided that water becomes a poorer solvent for the polyoxyethylene blocks, as previously mentioned (17). Association numbers of copolymer BO₂₀EO₄₁₁BO₂₀ are similar to those obtained for the structurally related copolymer BO₁₀EO₄₁₀BO₁₀ despite its larger BO block length, and are lower than those of other BO_mEO_nBO_m with lengthy EO blocks such as BO₁₄EO₃₇₈BO₁₄ ($N_w = 18$),²⁹ BO₁₂EO₂₇₀BO₁₂ ($N_w = 28$) (30) and BO₁₂EO₂₆₀BO₁₂ ($N_w = 29$) (18). In this regard, it is worth mentioning that BO_mEO_nBO_m copolymers possessing EO < 300 units exhibit an increase in N_w as their hydrophobic block length increases as observed for BO₅EO₉₁BO₅, BO₆EO₄₆BO₆ (30), BO₇EO₄₀BO₇ (18), BO₁₀EO₂₇₁BO₁₀ and BO₁₂EO₂₇₀BO₁₂ (30), for example. Conversely, BO_mEO_nBO_m copolymers with EO > 300 units decrease their N_w values as the BO block length increases as, for example, from 18 to 9 for BO₁₄EO₃₇₈BO₁₄ and BO₂₁EO₃₈₅BO₂₁, or from 8 to 7 for BO₁₀EO₄₁₀BO₁₀ and BO₂₀EO₄₁₁BO₂₀, respectively. This trend is a consequence of steric restrictions of the lengthy EO corona to efficiently pack more hydrophobic chains inside the micellar core nuclei (17).

Table 2. Micellar data obtained from DLS experiments at 10 and 25°C for copolymers BO₈EO₉₀BO₈ and BO₂₀EO₄₁₁BO₂₀.

polymer	T (°C)	$10^5 M_w$ (g/mol)	r_h (nm)	N_w	$10^{-4} A_2$ (mol·cm ³ ·g ⁻²)
BO ₈ EO ₉₀ BO ₈	10	1.4	9.7	25	-8.3
	25	2.1	13.0	38	-19.7
BO ₂₀ EO ₄₁₁ BO ₂₀	10	2.4	10.6	11	-10.7
	25	3.8	18.9	17	-60.2

On the other hand, Figure 4a shows the dependence of N_w on BO-block length for different BO_mEO_nBO_m reported so far (17). Values of N_w were adjusted for differences in n (the EO block length) using the scaling exponent $N_w \sim (n')^{1.07}$, where n' ($n' = n - n_{crit}$, $n_{crit} = 4$ is the effective hydrophobic block length, that is, the minimum hydrophobic block length in reverse BO_mEO_nBO_m for micellization) is the effective hydrophobic block length. The line through the data points of $\log(N_w/n'^{1.07})$ against $\log(m)$ has a slope of -0.84. Attwood *et al.* previously obtained an exponent of -0.63 (17), whilst Föster *et al.* derived an exponent of -0.71 for short C_nEO_m copolymers with $n = 8-16$ and $m = 4-23$ (31). The difference may arise from introducing in Figure 4a BO_mEO_nBO_m copolymers with extremely lengthy EO blocks (EO > 375 units) and long BO blocks (BO > 14) which possess relatively low aggregation numbers due to their very long chains. On the other hand, Figure 4b effectively verified that data points plotted as $\log(N_w/m^{0.84})$ against $\log(n')$ do indeed fit satisfactorily to a straight line of slope 1.0 with evident correspondence with scaling exponents of N_w as a function of

the EO block length (ca. 1.07) derived from diblock and non-bridging triblock copolymers.

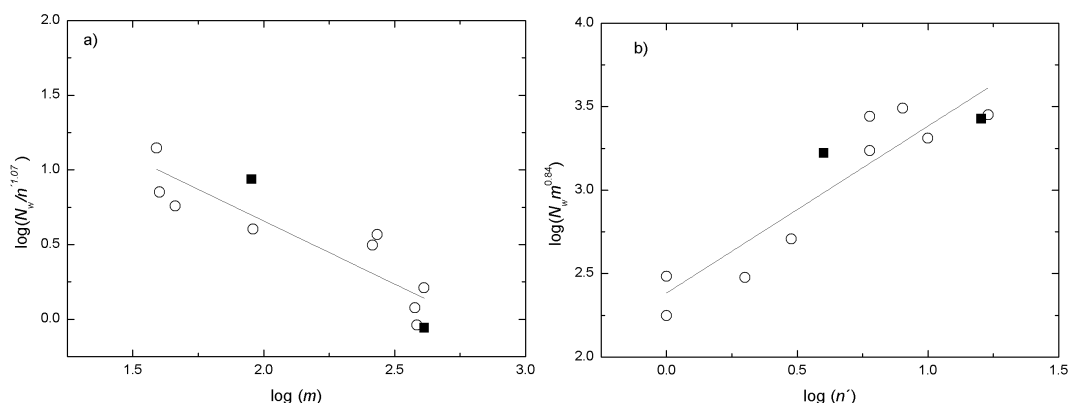


Figure 4. a) Dependence of association number on a) EO-block length, m , and b) effective hydrophobic block length, n' . Association numbers are corrected for variation in hydrophobic and hydrophilic block lengths, respectively. (■) denote the copolymers studied in the present work.

3.4.4.4 Rheological behaviour

a. Tube inversion

Tube inversion was used to obtain a preliminary definition of the mobile-immobile regions of the phase diagram of each copolymer. For both polymers the mobile region (sol) transforms progressively into a viscous fluid and, then, to a gel as the concentration increases. For $\text{BO}_8\text{EO}_{90}\text{BO}_8$ a mobile viscous fluid was present up to a concentration of 6 wt.% whilst an immobile gel was formed above (Figure 5). The gel phase progressively converts into a very viscous fluid, resembling a high temperature boundary, in the temperature range 40 to 70 °C depending on concentration: the higher the concentration the larger the boundary temperature was. In the case of copolymer $\text{BO}_{20}\text{EO}_{411}\text{BO}_{20}$, a mobile more or less viscous fluid is present up to 8 wt.%, whilst an immobile transparent gel is formed above such value within a determined temperature range, which is broader as the copolymer concentration increases. At 12 wt.%, the gel phase of the present copolymer is present along the whole temperature range analyzed. Comparison of phase transitions of $\text{BO}_n\text{EO}_m\text{BO}_n$ copolymers with lengthy EO blocks ($\text{EO} > 350$ units) showed that the transition point from sole to soft gel largely depends on the EO block length at temperatures below room temperature, whilst the change from soft-gel to hard gel is dominated by the BO/EO ratio, that is, the most hydrophobic the copolymer is, the gel phase appears at lower concentrations and temperatures (29).

To perfectly define the boundaries of the phase diagrams and to further characterize the flow behaviour of semi-dilute and concentrated copolymer solution, rheometry measurements were also performed.

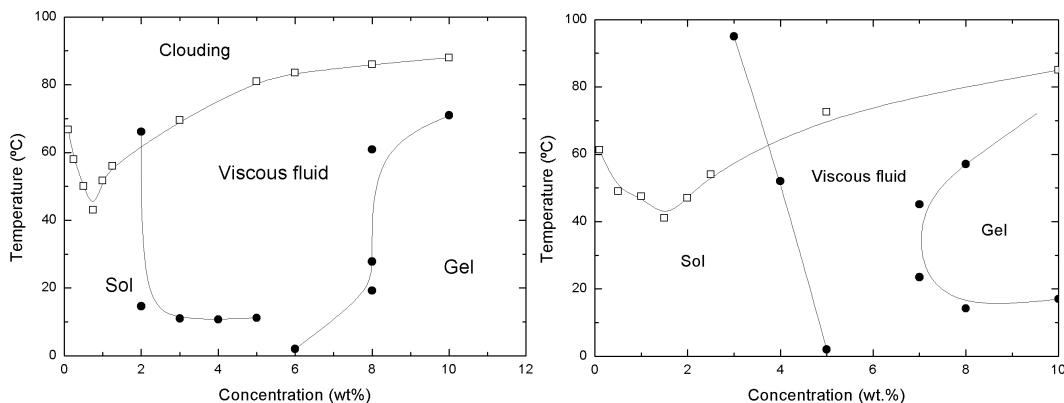


Figure 5. Phase diagrams delined using tube inversion and rheometry data from temperature scans. a) corresponds to $\text{BO}_8\text{EO}_{90}\text{BO}_8$, and b) to $\text{BO}_{20}\text{EO}_{411}\text{BO}_{20}$. (\square) denote clouding boundaries obtained UV-Vis, whereas (\bullet) are experimental points measured by rheometry. Lines were drawn to guide the eye.

b. Concentration and temperature dependence of storage and loss moduli

Oscillatory tests were performed in order to determine the linear viscoelastic region in which oscillatory shear measurements need to be performed ensuring, at the same time, that the system is frequency-dependent (see Figure S2).

The G'' values were consistently smaller than the G' ones for both copolymers (not shown). A linear region in which the G' value was almost independent of strain was observed. In addition, for both copolymers G' and G'' increases as copolymer concentration does being G' larger for $\text{BO}_8\text{EO}_{90}\text{BO}_8$ than for $\text{BO}_{20}\text{EO}_{411}\text{BO}_{20}$; however, it is observed that while for $\text{BO}_8\text{EO}_{90}\text{BO}_8$ the linear viscoelastic region becomes wider as the concentration increases, for copolymer $\text{BO}_{20}\text{EO}_{411}\text{BO}_{20}$ the opposite behaviour is found. This different behaviour results from differences in packing and flow behaviour, that is, much longer EO and BO blocks facilitates bridging.

Once determined the linear viscoelastic region, temperature scans in the range 1-90 °C of $\log(G')$ at $f = 1$ Hz for copolymers $\text{BO}_8\text{EO}_{90}\text{BO}_8$ and $\text{BO}_{20}\text{EO}_{411}\text{BO}_{20}$ were performed. The dependence of G' on concentration and temperature is provided by the examples shown in Figure 6. At 1 wt.%, copolymer samples are unstructured fluids (sols, with $G' < 10$ Pa and $G'' > G'$). At 2 wt.% copolymer $\text{BO}_8\text{EO}_{90}\text{BO}_8$ was a viscous complex fluid characterized by $10 < G' < 1000$ Pa and $G' > G''$ (*i.e.* a soft gel adopting Hvidt's *et al.* notation) (32), in the temperature range 16 to 63°C, and it became a sol below and above such temperature interval (Figure 6a). In particular, the observed decrease in G' at high temperatures and, thus, the transition from a viscous fluid to a

sol can be associated with a worsening solvent environment compressing the EO-block corona. In the concentration range from 3 to 5 wt.%, this copolymer was a viscous fluid in the whole temperature range analyzed above 5 °C. At 6 wt.% copolymer $\text{BO}_8\text{EO}_{90}\text{BO}_8$ became a gel concentrations (arbitrarily defined by $G' > G''$ and $G' > 1000$ Pa at $f = 1$ Hz, a hard gel adopting Hvidt's et al. notation) between the temperature range 5-20 °C and then a viscous fluid. This gel region expands within a broader temperature range as the copolymer concentration increases: from 0 to 27°C, at 8 wt.% and until 70 °C at 10 wt.%, becoming then a soft gel. Hence, despite their reverse structure, copolymer $\text{BO}_8\text{EO}_{90}\text{BO}_8$ displayed a behaviour similar to diblock EO_nBO_m and triblock $\text{EO}_n\text{BO}_m\text{EO}_n$ copolymers, in which micellar packing determines the moduli behaviour as the polymer concentration increases.

Despite possessing longer hydrophobic and hydrophilic blocks, the larger EO/BO ratio and the existence of bridging which may difficult effective cubic packing makes copolymer $\text{BO}_{20}\text{EO}_{411}\text{BO}_{20}$ to remain in a sol state up to a concentration of 3 wt.% (Figure 6b). At 4 wt.% it already became a viscous fluid between ca. 30 and 50°C and 5 and 6 wt.% in the whole temperature range. At 7 and 8 wt.% this copolymer is a gel between 24-45°C and 14-57°C, respectively and a viscous fluid in the remaining temperature interval. At 10 wt.%, the copolymer is a gel above 20 °C and in the whole temperature range at 12 wt.%. All the above data allowed a more exact definition of the phase diagram, as shown in Figure 5. On the other hand, maximum values of $G'(T)$, G'_{max} of copolymer $\text{BO}_{20}\text{EO}_{411}\text{BO}_{20}$ are similar to those of structurally related copolymers with EO blocks ~400 units such as $\text{BO}_{21}\text{EO}_{385}\text{BO}_{21}$ and $\text{BO}_{14}\text{EO}_{378}\text{BO}_{14}$; in addition, copolymer $\text{BO}_8\text{EO}_{90}\text{BO}_8$ possesses G'_{max} values larger than the latter copolymers despite having much lower BO and EO units as a consequence of a better cubic packing of micelles with shorter solvated EO coronas. Despite the observed differences, both $\text{BO}_8\text{EO}_{90}\text{BO}_8$ and $\text{BO}_{20}\text{EO}_{411}\text{BO}_{20}$ copolymers G' values increased markedly with concentration, with a predominant elastic behavior ($G' > G''$) in most of the temperature and concentration ranges analyzed, as occurred for other reverse $\text{BO}_n\text{EO}_m\text{BO}_n$ copolymers with lengthy EO blocks (Figure S2).

On the other hand, as discussed elsewhere (33) for aqueous micellar gels of copoly(oxyalkylene)s of different block architectures, the onset of gelation and the associated increase in G' with T at low temperatures for copolymer $\text{BO}_{20}\text{EO}_{411}\text{BO}_{20}$ is associated with an increase in the extent of micellization and, in the present case, with the extent of bridging. This is in contrast with the behavior observed for $\text{BO}_8\text{EO}_{90}\text{BO}_8$ whose G' values in the gel region (at 10 wt.%) are fairly constant until relatively high temperatures (> 70 °C) at which then decrease. This observed decrease in G' at high temperatures can be associated with a worsening solvent environment compressing the EO-block corona and, thereby, with a decrease in the effective micellar volume fraction. This viscous fluid after the immobile gel phase has been shown to be

composed by small micellar domains with the same structure as the gel phase as observed by SAXS and SANS (34); hence, it can be characterized as a defective cubic structure, as previously observed for related EO_mBO_n and $EO_mBO_nEO_m$ copolymers (33).

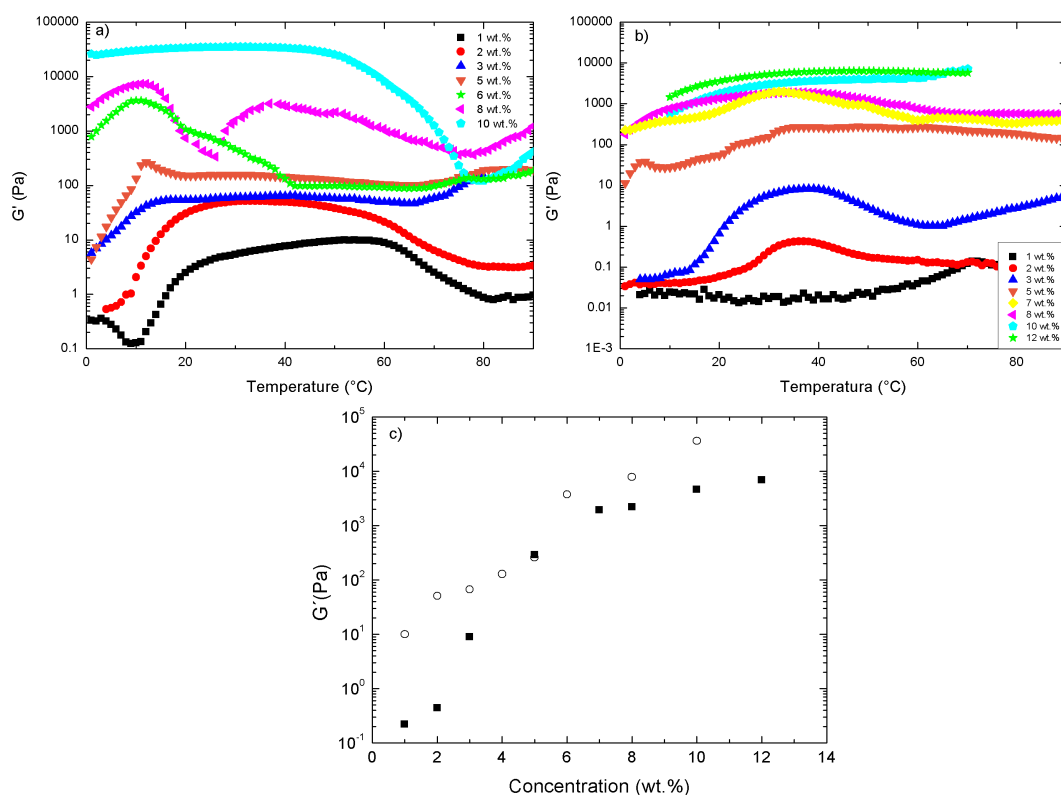


Figure 6. Temperature scans in the range 1-90 $^{\circ}C$ of G' at $f = 1$ Hz for copolymers a) $BO_8EO_{90}BO_8$ and b) $BO_{20}EO_{411}BO_{20}$ at different concentrations. c) Plots of G'_{max} against concentration for copolymers (O) $BO_8EO_{90}BO_8$ and (■) $BO_{20}EO_{411}BO_{20}$.

c. Frequency scans

Effects of changes in the extent of micellar bridging and packing are apparent in the different mechanical responses of the system to the applied frequency. Hence, the frequency dependence of the modulus was determined for solutions of copolymers $BO_8EO_{90}BO_8$ and $BO_{20}EO_{411}BO_{20}$ in the concentration range 1-10 wt.%. For example, Figure 8a shows an 1 wt.% solution for copolymers $BO_8EO_{90}BO_8$ and $BO_{20}EO_{411}BO_{20}$ at 10 $^{\circ}C$, with values of G' exceeding those of G'' over most accessible frequency range, except at high frequencies, where a moduli crossover occurs from which a relaxation time $t = 0.90$ and 0.35 s, respectively, could be determined. The behavior can be approximated to that of a Maxwell element:

$$\begin{aligned} G' &= (G_{\infty}\tau^2\omega^2)/(1 + \tau^2\omega^2) \\ G'' &= (G_{\infty}\tau\omega)/(1 + \tau^2\omega^2) \end{aligned} \quad (3)$$

where G_{∞} is the plateau value of G' at high frequency, τ is the relaxation time, and $\omega = 2\pi f$ (f = frequency in Hz). At all temperatures investigated, the slopes of the best straight lines through the data points were near to values of 2 ($\log G'$) and 1 ($\log G''$) which are expected when $\omega\tau \ll 1$, *i.e.* typical of a Newtonian fluid.

For copolymer $\text{BO}_{20}\text{EO}_{411}\text{BO}_{20}$ G'' is consistently larger than G' in the whole frequency range analysed in the concentration range 2-4 wt.% at temperatures below 50 °C except at very frequencies ($f > 10$ Hz) where a moduli crossover takes place. At larger temperatures, the moduli crossover can be observed at much lower frequencies corresponding to a Maxwell fluid showing, at most, localized cubic order (Figure 8b) (33). This effect must be a consequence of the attraction of micelles at temperatures at which water is a poor solvent for micelles, and favored by micellar bridging too. A similar behavior can be observed at larger copolymer $\text{BO}_{20}\text{EO}_{411}\text{BO}_{20}$ concentrations (5-7 wt.%) and for copolymer for copolymer $\text{BO}_8\text{EO}_{90}\text{BO}_8$ in the concentration range 2-5 wt.% but only at temperatures below room temperature (Figure 8c). Then, as the concentration is further increase for both copolymers (> 8 wt.% and 6 wt.% for $\text{BO}_{20}\text{EO}_{411}\text{BO}_{20}$ and $\text{BO}_8\text{EO}_{90}\text{BO}_8$, respectively) an immobile gel with relatively high G' values (> 1 kPa) existed typically below 70 °C depending on copolymer type and concentration, as commented previously. Above such temperature threshold, a viscous fluid was observed (Figure 8d). This type of viscous fluid at temperatures and concentrations relatively near the gel boundary can be assigned as defective versions of cubic packed gels as mentioned previously; they are characterized by a constant value of G' , the shallow minimum in G'' , and both moduli do not show a crossover point in the measured frequency range as observed in Figure 8d. Nevertheless, the G' values for the viscous fluid are much lower compared to those of a pure gel phase, which well exceeded 1 kPa and possessed the characteristic features of immobile gels constituted by cubic packing of spherical micelles completely independent on temperature and frequency (35). The plateau behavior of G' and the minimum in G'' have been also observed for colloidal hard spheres near the glass-fluid transition (36), and is also characteristic of the cubic phase in block copolymer melts (37). The frequency-independent regime took place at lower concentrations for copolymer $\text{BO}_8\text{EO}_{90}\text{BO}_8$ than for $\text{BO}_{20}\text{EO}_{411}\text{BO}_{20}$ due to its larger BO/EO ratio, which favored micellization.

Plots of G' and G'' vs frequency presented in Figure 8 show a wide variety of characteristics from purely viscous to highly elastic fluids. The observed behaviours seems to confirm the formation of a dynamic network for both copolymers, but specially for $\text{BO}_{20}\text{EO}_{411}\text{BO}_{20}$, which becomes more and more robust as the concentration is increased, as observed for other $\text{BO}_m\text{EO}_n\text{BO}_m$ copolymers with very lengthy EO blocks as $\text{BO}_{12}\text{EO}_{114}\text{BO}_{12}$ (13), $\text{BO}_{10}\text{EO}_{227}\text{BO}_{10}$ (26), $\text{BO}_{12}\text{EO}_{227}\text{BO}_{12}$ (28), $\text{BO}_{10}\text{EO}_{410}\text{BO}_{10}$ (11), $\text{BO}_{21}\text{EO}_{385}\text{BO}_{21}$ and $\text{BO}_{14}\text{EO}_{378}\text{BO}_{14}$ (27). The existence of slow

relaxation processes as the copolymer concentration increases also seems to corroborate this point. For $\text{BO}_8\text{EO}_{90}\text{BO}_8$ micelle packing as effective hard spheres in the gel phase becomes the predominant response at much lower concentrations than for copolymer $\text{BO}_{20}\text{EO}_{411}\text{BO}_{20}$ which agrees with that previously mentioned.

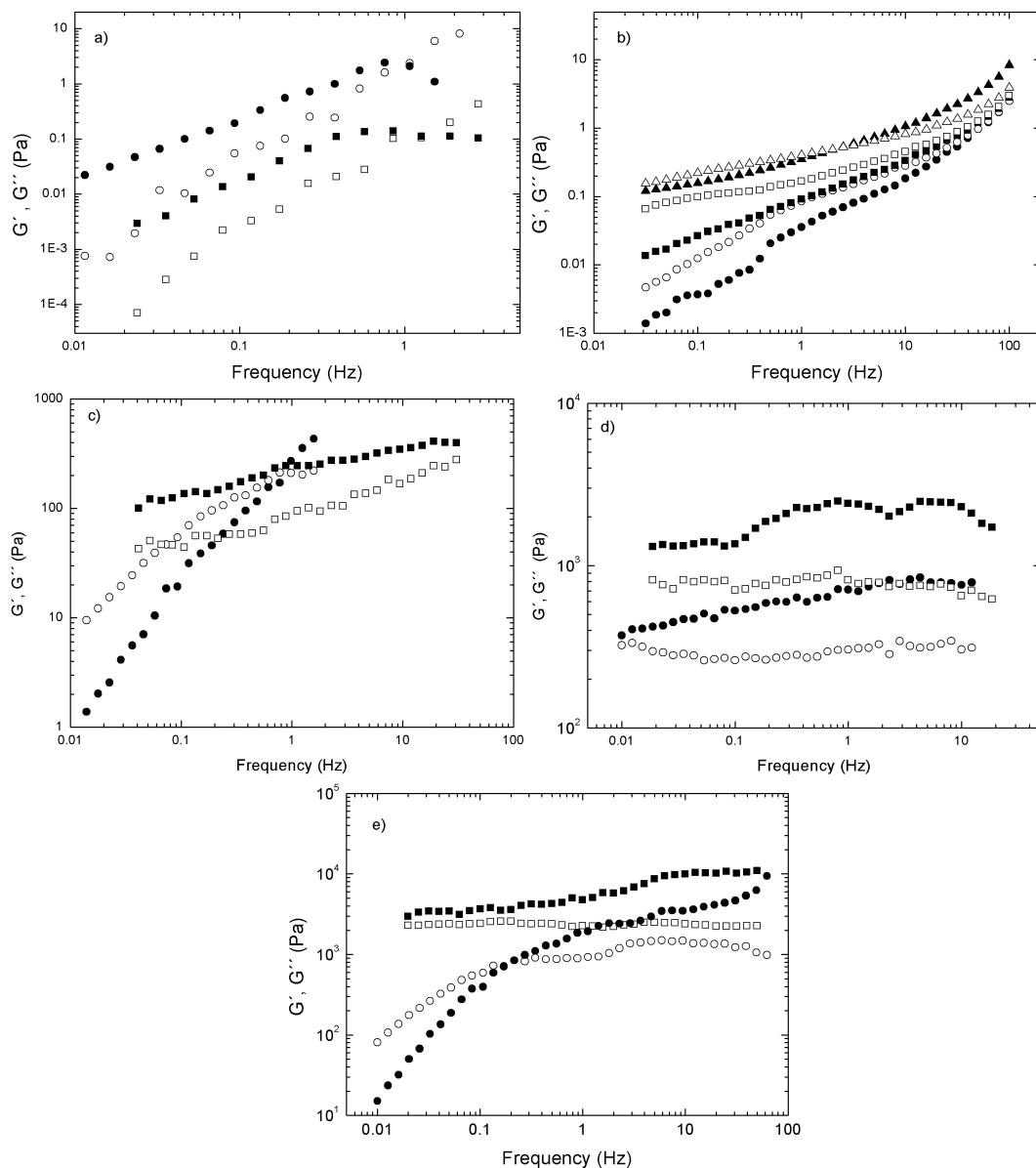


Figure 8. Frequency scans for the present copolymers at different concentrations and temperatures: a) $\text{BO}_8\text{EO}_{90}\text{BO}_8$ (\bullet, \circ) and $\text{BO}_{20}\text{EO}_{411}\text{BO}_{20}$ (\blacksquare, \square) at 2 wt.% and 10 °C; b) $\text{BO}_{20}\text{EO}_{411}\text{BO}_{20}$ copolymer at 3 wt. % and (\bullet, \circ) 10 °C, (\blacksquare, \square) 20 °C, and ($\blacktriangle, \triangle$) 60 °C; c) $\text{BO}_8\text{EO}_{90}\text{BO}_8$ copolymer at 5 wt. % and (\bullet, \circ) 10 °C and (\blacksquare, \square) 40 °C; d) $\text{BO}_8\text{EO}_{90}\text{BO}_8$ copolymer at 8 wt.% and (\bullet, \circ) 30 °C and (\blacksquare, \square) 50 °C; $\text{BO}_{20}\text{EO}_{411}\text{BO}_{20}$ copolymer at 12 wt. % at (\bullet, \circ) 10 °C and (\blacksquare, \square) 40 °C. Closed symbols denote G' whilst open ones correspond to G'' .

On the other hand, copolymer $\text{BO}_{20}\text{EO}_{411}\text{BO}_{20}$ showed rather different behavior

to that observed for other structurally related copolymer, $\text{BO}_{10}\text{EO}_{410}\text{BO}_{10}$. For this copolymer typical values of G'' exceed those of G' over a similar accessible frequency range, as also observed for other classical associative thickeners (38). Despite the similar EO length and larger BO blocks compared with $\text{BO}_{10}\text{EO}_{410}\text{BO}_{10}$, the larger polydispersity of $\text{BO}_{20}\text{EO}_{411}\text{BO}_{20}$ (as also occurred for copolymers $\text{BO}_{14}\text{EO}_{378}\text{BO}_{14}$ and $\text{BO}_{21}\text{EO}_{385}\text{BO}_{21}$) can broaden the Poisson distribution of BO block-lengths (assuming ideal polymerization) (39), which involves a wider temperature range for micellization. Hence, this copolymer effectively behaves as having lower effective BO block lengths with a behavior more related to that observed to $\text{BO}_{12}\text{EO}_{114}\text{BO}_{12}$, $\text{BO}_{10}\text{EO}_{227}\text{BO}_{10}$ or $\text{BO}_{10}\text{EO}_{227}\text{BO}_{10}$ copolymers.

Also, both $\text{BO}_8\text{EO}_{90}\text{BO}_8$ and $\text{BO}_{20}\text{EO}_{411}\text{BO}_{20}$ do not behave as classical colloidal suspensions interacting through weak short-range attractive forces, that is, G' being frequency-independent and increasing with concentration, and G'' being concentration-independent and increasing linearly with frequency. All these facts allow to scale the moduli against frequency to give smooth master curves (40), which allows to gain access to sample's behaviour under frequencies that are not accessible using common instrumentation (see below).

d. Scaling of rheological response

The construction of a master curve through the time-temperature superposition of the measured moduli was performed in order to facilitate comparison of the frequency response at different temperatures of copolymers $\text{BO}_8\text{EO}_{90}\text{BO}_8$ and $\text{BO}_{20}\text{EO}_{411}\text{BO}_{20}$. The moduli and the frequencies for each data set were independently scaled by factors a_T and b_T respectively to obtain a superposition of G' and G'' . The temperature dependence of the moduli was explored for the copolymers in the gel region. Figure 9a and Figure S3 show the superposition achieved at 8 wt. % and 12 wt. % for copolymers $\text{BO}_8\text{EO}_{90}\text{BO}_8$ and $\text{BO}_{20}\text{EO}_{411}\text{BO}_{20}$, respectively. The data suggest that there are no changes in the nature of the dynamic mechanical response in the gel phase as a function of temperature in the range 10-50 °C. As already discussed, higher temperatures worsen the solvent environment and progressively compress the micellar corona. The shrinkage of the micellar corona will lead to defects in micellar packing and the bridged network, which may well change the scaling of the viscoelastic behaviour with frequency within the hard gel phase.

The Arrhenius plot of $-\log(a_T)$ against $1/T$ (Figure 9b and Figure S4), which has a slope equivalent to a plot of $\log(\text{relaxation rate})$ against $1/T$, gave activation energy values (the energy related to the relaxation mechanism in crosslinking or bonding processes) through the application of the Williams-Landel-Ferry equation (41)

$$\log a_T = -C_1(T-T_r)/(C_2 + (T-T_r)) \quad (4)$$

where T is the temperature, T_r is the reference temperature to construct the compliance master curve, and C_1 and C_2 are empirical constants to fit the values of the superposition. Therefore, the activation energy, E_a , can be derived as

$$E_a = 2.303 R C_1 C_2 T^2 / (C_2 + T - T_r)^2 \quad (5)$$

Activation energies of $E_a = -11$ and -41 kJ/mol were obtained for copolymers $\text{BO}_8\text{EO}_{90}\text{BO}_8$ and $\text{BO}_{20}\text{EO}_{411}\text{BO}_{20}$, respectively, as an average value over all components of the copolymer solutions. The negative values imply that the relaxation time increases as temperature rises, which is in agreement with the progressive hardening of the gel in the temperature range analyzed (11). As can be seen in Figure 9b, the obtained slope for copolymer $\text{BO}_{20}\text{EO}_{411}\text{BO}_{20}$ (and hence, activation energies) is rather to other $\text{BO}_n\text{EO}_m\text{BO}_n$ copolymers having EO block lengths > 350 units, as for example, $\text{BO}_{10}\text{EO}_{410}\text{BO}_{10}$ ($E_a = -40$ kJ/mol) or $\text{BO}_{21}\text{EO}_{385}\text{BO}_{21}$ ($E_a = -50$ kJ/mol) (11,27). In fact, there is a slight increase in the slope net value obtained for the BEB block copolymers as the BO/EO ratio increases.

Also, the negative activation energy values indicate that both the disengagement of chain ends from micelles (a positive contribution) and micellization (a negative one) can contribute in contrast to alkyl-ended copolymer solutions, where only disengagement is important provided that their extent of micellization is low over the temperature range of interest and, hence, positive activation energies are obtained (42,43). This behaviour is confirmed when analyzing the dependence of storage modulus with temperature by plotting $1/b_T$ against T (see Figure 9c). Copolymer $\text{BO}_8\text{EO}_{90}\text{BO}_8$ at 8 wt. % exhibits an important decrease of $1/b_T$ (or storage modulus) with temperature. This decrease is much greater in the low temperature range in agreement with the progressive shrinkage of the cubic mesoscopic structure of packed micelles and the increased tendency as temperature is increased for the copolymers to loop in a single micelle rather than to bridge between micelles (43). Conversely, for copolymer $\text{BO}_{20}\text{EO}_{411}\text{BO}_{20}$ a slight increase of $1/b_T$ against T can be observed, which points to an increase in the high-frequency storage modulus in the temperature interval analyzed compatible with an increase in the extent of micellization and, then, of bridging. This temperature dependence is greater than that predicted by the kinetic theory of elasticity for a fully formed network.

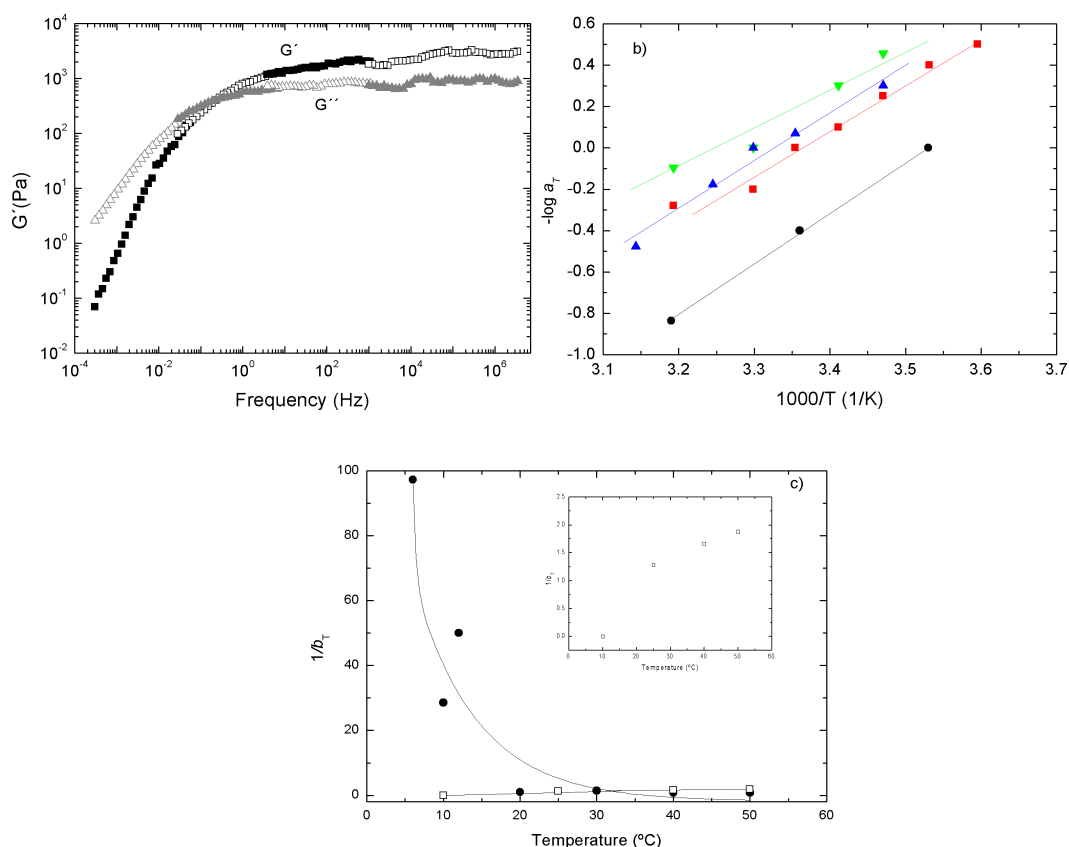


Figure 9. a) Master curve plots obtained for copolymer $\text{BO}_8\text{EO}_{90}\text{BO}_8$ at 8 wt.% (reference temperature $T_r = 10^\circ\text{C}$). b) Arrhenius plot for copolymer (●) $\text{BO}_{20}\text{EO}_{411}\text{BO}_{20}$, (■) $\text{BO}_{10}\text{EO}_{410}\text{BO}_{10}$, (▲) $\text{BO}_{21}\text{EO}_{385}\text{BO}_{21}$, and (▼) $\text{BO}_{14}\text{EO}_{378}\text{BO}_{14}$. Concentration for $\text{BO}_{20}\text{EO}_{411}\text{BO}_{20}$, $\text{BO}_{21}\text{EO}_{385}\text{BO}_{21}$, and $\text{BO}_{14}\text{EO}_{378}\text{BO}_{14}$ is 12 wt. % whilst for $\text{BO}_{10}\text{EO}_{410}\text{BO}_{10}$ is 15 wt.%. c) Temperature dependence of $1/b_T$ for copolymers (●) $\text{BO}_8\text{EO}_{90}\text{BO}_8$ and (□) $\text{BO}_{20}\text{EO}_{411}\text{BO}_{20}$ (see also inset) at 8 and 12 wt.%, respectively.

3.4.5 Conclusions

In summary, the present $\text{BO}_8\text{EO}_{90}\text{BO}_8$ and $\text{BO}_{20}\text{EO}_{411}\text{BO}_{20}$ copolymers form swollen flower-like micelles with sizes ranging from ca. 13 to 30 nm. Copolymer $\text{BO}_8\text{EO}_{90}\text{BO}_8$ can form individual micelles in very dilute solutions whilst $\text{BO}_{20}\text{EO}_{411}\text{BO}_{20}$ already display a secondary population at sizes ca. 200-300, which represents interconnected micelles by bridging as confirmed by AFM images. At slightly larger concentrations, these micellar clusters are already observed for both copolymers and even for $\text{BO}_{20}\text{EO}_{411}\text{BO}_{20}$ a third population with sizes ca. 3000-4000 nm is detected which would correspond to the aggregation of several micellar bridged clusters. As a result of their long BO blocks and extremely lengthy EO ones, these two copolymers exhibited a very rich phase behaviour. This could be modulated from an unstructured fluid to a viscoelastic one to a fully developed gel by changing the solution

temperature and concentration. In particular, bridging could be observed by the appearance of slow relaxation modes at relatively low polymer concentrations as denoted from the frequency scans, specially for copolymer $\text{BO}_{20}\text{EO}_{411}\text{BO}_{20}$ thanks to their lengthy EO blocks and longer BO ones, which favoured a much larger exclusion volume and intermicellar attraction while reaching a less efficient packing of micelles. As the concentration increases the dynamic network becomes more robust as the concentration, which impeded to fit their behavior to that of Maxwell fluid. At this respect and confirming this view, copolymer $\text{BO}_8\text{EO}_{90}\text{BO}_8$ displays a more classical behaviour of packed mesoscopic cubic structures in the gel phase at much lower concentrations than $\text{BO}_{20}\text{EO}_{411}\text{BO}_{20}$. The negative values of the activation energy for the relaxation processes derived from master curves might involve both the disengagement of chain ends from micelles (a positive contribution) and micellization (a negative one), with evident predominance of the latter.

3.4.6 References

1. *Polymer as Rheology Modifiers*. ACS Symp. Ser. Schulz, D. N. and Glass, J. E. Eds. American Chemical Society, Washington DC, 1991, vol. 462.
2. *Water -soluble Polymers: Beauty with Performance*. Glass, E. E. Ed. American Chemical Society, Washington DC, 1986, vol. 213.
3. Winnik, M. A.; Yekta, A. *Curr. Opin. Colloid Interface Sci.* **1997**, 2, 424.
4. Francois, S.; Maitre, S.; Rawiso, M.; Sarazin, D.; Beinert, G. Isel, F. *Colloids Surfaces A*, **1996**, 112, 251.
5. Beuadoin, E.; Borisov, O. V.; Lapp, A.; Francois, J. *Macromol. Symp.* **2002**, 189, 89.
6. Mistry, D.; Annable, T.; Booth, C. *ACS Abstr.* **1999**, 218, 41.
7. Annable, T.; Buscall, R.; Ettelaie, R.; Whittlestone, D. J. *Rheol.* **1993**, 37, 695.
8. Mortensen, K.; Brown, W.; Jørgensen, E. *Macromolecules* **1994**, 27, 5654.
9. Altinok, H.; Yu, G.-E.; Nixon, S. K.; Gorry, P. A.; Attwood, D.; Booth, C. *Langmuir* **1997**, 13, 5837.
10. Cambón, A.; Alatorre-Meda, M.; Juárez, J.; Topete, A.; Mistry, D.; Attwood, D.; Barbosa, S.; Taboada, P.; Mosquera, V. J. *Colloid Interface Sci.* **2011**, 361, 154.
11. Mistry, D.; Annable, T.; Yuan, X.-F.; Booth, C. *Langmuir* **2006**, 22, 2986.
12. Castelletto, V.; Hamley, I. W.; Yuan, X.-F.; Kelarakis, A.; Booth, C. *Soft Matter* **2005**, 1, 138.
13. Kelarakis, A.; Yuan, X.-F.; Mai, S.-M.; Yang, Y.-W.; Booth, C. *Phys. Chem. Chem. Phys.* **2003**, 5, 2628.
14. Mai, S.-M.; Ludhera, S.; Heatley, F.; Attwood, D.; Booth, C. *J. Chem. Soc., Faraday Trans.* **1998**, 94, 567.
15. Ricardo, N. M. P. S.; Honorato, S. B.; Yang, Z.; Castelletto, V.; Hamley, I. W.; Yuan, X.-F.; Attwood, D.; Booth, C. *Langmuir* **2004**, 20, 4272.

16. Yu, G.-E.; Masters, A. J.; Heatley, F.; Booth, C.; Blease, T. G. *Macromol. Chem. Phys.* **1994**, 195, 1517.
17. Booth, C.; Attwood, D.; Price, C. *Phys. Chem. Chem. Phys.* **2006**, 8, 3612.
18. Zhou, Z.; Yang, Y.-W.; Booth, C.; Chu, B. *Macromolecules* **1996**, 29, 8357.
19. Cambón, A.; Rey-Rico, A.; Mistry, D.; Brea, J.; Loza, M. I.; Attwood, D.; Barbosa, S.; Alvarez-Lorenzo, C.; Concheiro, A.; Taboada, P.; Mosquera, V. *Int. J. Pharm.* **2013**, 445, 47.
20. Ribeiro, M. E. N. P.; Cavalcante, I. M.; Ricardo, N. M. P. S.; Mai, S.-M.; Attwood, D.; Yeates, S. G.; Booth, C. *Int. J. Pharm.* **2009**, 369, 196.
21. Attwood, D.; Booth, C.; Yeates, S. G.; Chaibundit, C.; Ricardo, N. M. P. S. *Int. J. Pharm.* **2007**, 345, 35.
22. Cambón, A.; Brea, J.; Loza, M. I.; Alvarez-Lorenzo, C.; Concheiro, C.; Barbosa, S.; Taboada, P.; Mosquera, V. *Mol. Pharm.* **2013**, 10, 3232.
23. Yang, Y.-W.; Yang, Z.; Zhou, Z.-K.; Attwood, D.; Booth, C. *Macromolecules* **1996**, 29, 670.
24. Provencher, S.W. *Die Makromol. Chem.* **1979**, 180, 201.
25. Liu, T.; Nace, V. M.; Chu, B. J. *Phys. Chem. B* **1997**, 101, 8074.
26. Kelarakis, A.; Havredaki, V.; Yuan, X.-F.; Chaibundit, C.; Booth, C. *Macromol. Chem. Phys.* **2006**, 207, 903.
27. Cambón, A.; Figueroa-Ochoa, E.; Juárez, J.; Villar-Alvarez, Pardo, A.; Barbosa, S.; Soltero, J. F. A.; Taboada, P.; Mosquera, V. J. *Phys. Chem. B* in press.
28. Kelarakis, A.; Ming, X.-T.; Yuan, X.-F.; Booth, C. *Langmuir* **2004**, 20, 2036.
29. Cambón, A.; Barbosa, S.; Rey-Rico, A.; Figueroa-Ochoa, E. B.; Soltero, J. F. A.; Yeates, S. G.; Alvarez-Lorenzo, C.; Concheiro, A.; Taboada, P.; Mosquera, V. J. *Colloid Interface Sci.* **2012**, 387, 275.
30. Liu, T.; Zhou, Z.; Wu, C.; Nace, V. M.; Chu, B. J. *Phys. Chem. B* **1998**, 102, 2875.
31. Förster, S.; Zisenis, M.; Wenz, E.; Antonietti, M. J. *Chem. Phys.* **1996**, 104, 9956.
32. Hvidt, S.; Joergensen, E. B.; Brown, W.; Schillen, K. J. *Phys. Chem.* **1994**, 98, 12320.
33. Hamley, I. W.; Mai, S.-M.; Ryan, A. J.; Fairclough, P. A.; Booth, C. *Phys. Chem. Chem. Phys.* **2001**, 3, 2972.
34. Prud'homme, R. K.; Wu, G.; Schneider, D. K. *Langmuir* **1996**, 12, 4651.
35. Juárez, J.; Taboada, P.; Valdez, M. A.; Mosquera, V. *Langmuir* **2008**, 24, 7107.
36. Mason, T. G.; Weitz, D. A. *Phys. Rev. Lett.* **1995**, 75, 2770.
37. Zhao, J.; Majumdar, B.; Schulz, M. F.; Bates, F. S. *Macromolecules* **1996**, 29, 1204.
38. Annable, T.; Buscall, R.; Ettelaie, R. *Colloids Surfaces A* **1996**, 112, 97.
39. Flory, P.J. *Principles of Polymer Chemistry*. Cornell University Press, Ithaca, 1953.
40. Trappe, V.; Weitz, D. A. *Phys. Rev. Lett.* **2000**, 85, 449.
41. Ferry, J. D. *Viscoelastic Properties of Polymers*, Wiley, London, 1980.

42. Alexandridis, P.; Lindman, B. *Amphiphilic Block Copolymers. Self-Assembly and Applications*. Elsevier, Amsterdam, 2000.
43. Mistry, D. Ph.D. Thesis, University of Manchester, Manchester, UK. 2000.

3.5 SUPPORTING INFORMATION FOR SOLUTION BEHAVIOR OF REVERSE TRIBLOCK REVERSE POLY(BUTYLENE OXIDE)-POLY(ETHYLENE OXIDE) - POLY(BUTYLENE OXIDE) COPOLYMERS WITH LENGTHY HYDROPHILIC BLOCKS.

Table S1. Lowest clouding temperatures for some $BO_nEO_mBO_n$ triblock copolymers.

<i>Copolymer</i>	$T_{cl, min}$ ($^{\circ}C$)	<i>Copolymer</i>	$T_{cl, min}$ ($^{\circ}C$)	<i>Copolymer</i>	$T_{cl, min}$ ($^{\circ}C$)
$BO_{23}EO_{68}BO_{23}$	4.0	$BO_{12}EO_{260}BO_{12}$	25.0	$BO_{20}EO_{411}BO_{20}$	41.5
$BO_{12}EO_{76}BO_{12}$	12.0	$BO_{10}EO_{271}BO_{10}$	32.0	$BO_{10}EO_{410}BO_{10}$	53.0
$BO_5EO_{91}BO_5$	53.0	$BO_{12}EO_{227}BO_{12}$	32.0	$BO_{21}EO_{385}BO_{21}$	50.2
$BO_8EO_{90}BO_8$	43.0	$BO_{10}EO_{227}BO_{10}$	45.0	$BO_{14}EO_{378}BO_{14}$	59.7

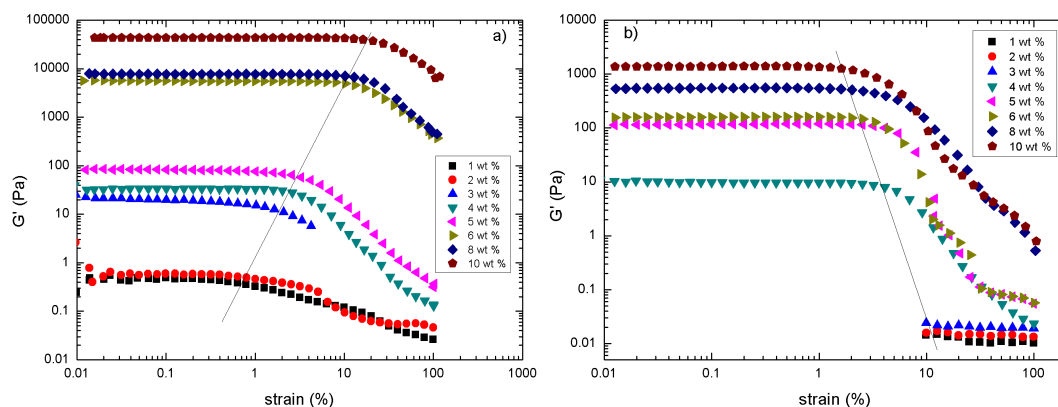


Figure S1. Strain sweep tests for copolymers a) $BO_8EO_{90}BO_8$ and b) $BO_{20}EO_{411}BO_{20}$ at different concentrations. The straight line points to the beginning of the non-linear region.

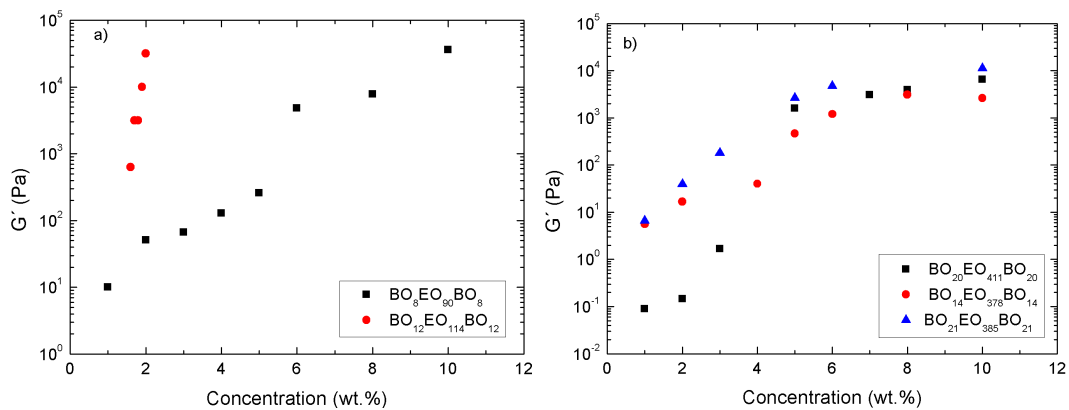


Figure S2. Plots of G'_{max} against concentration for copolymers a) (■) $\text{BO}_{12}\text{EO}_{114}\text{BO}_{12}$ and (●) $\text{BO}_8\text{EO}_{90}\text{BO}_8$; b) (■) $\text{BO}_{20}\text{EO}_{411}\text{BO}_{20}$, (●) $\text{BO}_{14}\text{EO}_{378}\text{BO}_{14}$, and (▲) $\text{BO}_{21}\text{EO}_{385}\text{BO}_{21}$.

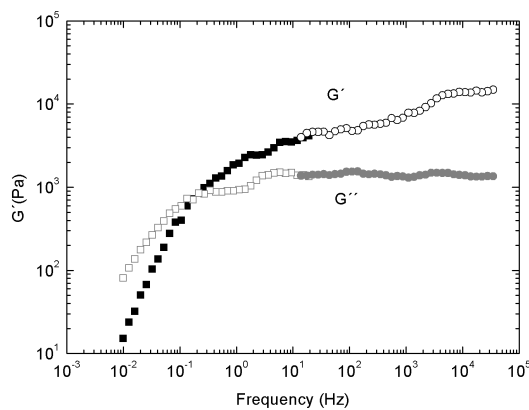


Figure S3. Master curve plots obtained for copolymer $\text{BO}_{20}\text{EO}_{411}\text{BO}_{20}$ at 12 wt.% (reference temperature $T_r = 10^\circ\text{C}$).

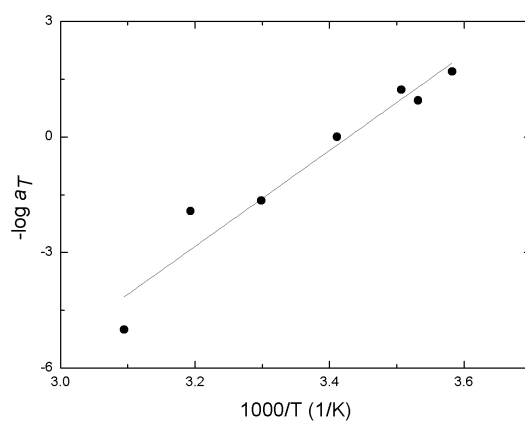


Figure S4. Arrhenius plot for scaling parameter a_T for copolymer $\text{BO}_8\text{EO}_{90}\text{BO}_8$ at 8 wt.%.

3.6 DOXORUBICIN-LOADED MICELLES OF REVERSE POLY (BUTYLENE OXIDE) – POLY (ETHYLENE OXIDE)- POLY(BUTYLENE OXIDE) BLOCK COPOLYMERS AS EFFICIENT “ACTIVE” CHEMOTHERAPEUTIC AGENTS

3.6.1 Abstract

Five reverse poly(butylene oxide)-poly(ethylene oxide)-poly(butylene oxide) block copolymers, $BO_nEO_mBO_n$, with BO ranging from 8 to 21 units and EO from 90 to 411 were synthesized and evaluated as efficient chemotherapeutic drug delivery nanocarriers and inhibitors of the P-glycoprotein (P-gp) efflux pump in a multidrug resistant (MDR) cell line. The copolymers were obtained by reverse polymerization of poly(butylene oxide), which avoids transfer reaction and widening of the EO block distribution, commonly found in commercial poly(ethylene oxide)-poly(propylene oxide) block copolymers (poloxamers). $BO_nEO_mBO_n$ copolymers formed spherical micelles of 10-40 nm diameter at lower concentrations (one order of magnitude) than those of equivalent poloxamers. The influence of copolymer block lengths and BO/EO ratios on the solubilisation capacity and protective environment for doxorubicin (DOXO) was investigated. Micelles showed drug loading capacity ranging from ca. 0.04 to 1.5%, more than 150 times the aqueous solubility of DOXO, and protected the cargo from hydrolysis for more than a month due to their greater colloidal stability in solution. Drug release profiles at various pHs, and the cytocompatibility and cytotoxicity of the DOXO-loaded micelles were assessed *in vitro*. DOXO loaded in the polymeric micelles accumulated more slowly inside the cells than free DOXO due to its sustained release. All copolymers were found to be cytocompatible, with viability extents larger than 95%. In addition, the cytotoxicity of DOXO-loaded micelles was higher than that observed for free drug solutions in a MDR ovarian NCI-ADR-RES cell line which overexpressed P-gp. The inhibition of the P-gp efflux pump by some $BO_nEO_mBO_n$ copolymers, similar to that measured for the common P-gp inhibitor verapamil, favoured the retention of DOXO inside the cell increasing its cytotoxic activity. Therefore, poly(butylene oxide)-poly(ethylene oxide) block copolymers offer interesting features as cell response modifiers to complement their role as efficient nanocarriers for cancer chemotherapy.

3.6.2 Introduction

Treatment of a wide range of diseases including viral, bacterial and fungi infections, hypercholesterolemia, and different types of cancers involves the administration of poorly water soluble hydrophobic drugs. In the last two decades a great effort has been made through the development of a series of nanosize therapeutic products able to solubilize drugs, allow their sustained release, improve their pharmacokinetics and facilitate their access to the site of action (1-5). Among the diverse nanoparticulate systems suitable for encapsulating and delivering drugs, polymeric micelles play a relevant role (6-9). In aqueous media, amphiphilic block copolymers can spontaneously self-assemble into nanoscopic core-shell micellar structures of various morphologies (e.g. spheres, small rods, and worm-like) (10), in which the hydrophobic blocks form the micelle core and the hydrophilic segments constitute the corona (10- 13). The core serves as a reservoir for the hydrophobic cargo, while the corona is in direct contact with the biological milieu providing “stealthness” to evade scavenging by the mononuclear phagocyte system, resulting in larger circulation times and passive accumulation in solid tumors (14). Encapsulation of the drug in the micellar structures enables the regulation of the pharmacokinetics and biodistribution of the incorporated drug (15). The most widely studied amphiphilic copolymers are those composed of poly(ethylene oxide) (PEO) and poly(propylene oxide) (PPO) blocks, particularly, the linear and bifunctional poloxamers (Pluronics[®]) and the X-shaped poloxamines (Tetronics[®]). Their popularity is based on their commercial availability in a very broad range of compositions, a fair solubilization capacity and sustained drug delivery, good biocompatibility of most varieties, inhibition of different efflux transporters overexpressed in multidrug resistant (MDR) cells, and approval of some varieties by regulatory agencies (i.e. FDA and EMA) to be used in pharmaceutical formulations and medical devices (16-18). Nevertheless, PEO–PPO block copolymers show several drawbacks as, for example, the variation in their micellization behavior from batch to batch (19), or an incomplete micellization of the unimers which usually leads to self-assembled nanostructures with limited drug solubilisation ability and stability upon dilution in the bloodstream.

To circumvent these problems, during the last few years a series of more hydrophobic block copolymer counterparts with similar architecture but with the PPO segment replaced by a more hydrophobic one, such as poly(butylene oxide) (PBO), poly(styrene oxide) (PSO) or phenylglycidyl ether (PG), have been proposed (20- 27). In this regard, special attention has been paid to copolymers with 1,2-butylene oxide (BO) as the hydrophobic block. Transfer reaction is not a problem in the laboratory polymerization of BO (28); nonetheless, this monomer (as propylene oxide does) adds to the growing chain to give a secondary oxyanion, and a slow initiation of EO chains at the secondary termination may lead to a broadened EO block length distribution (29-

31). This effect can be suppressed if BO blocks are polymerized last when forming BO_nEO_m diblock and $\text{BO}_n\text{EO}_m\text{BO}_n$ triblock copolymers. Also, the larger relative hydrophobicity of the BO block compared to PPO (six-fold as estimated from the ratio of the logarithms of the molar critical micellar concentrations, cmc) (22) enables the formation of polymeric micelles at much lower polymer concentrations, with the subsequent savings on cost of materials and the reduction of possible toxic side effects associated with polymeric chains inside the body. Also, the enhanced hydrophobicity of the micellar core should allow a more efficient solubilisation capacity for this class of copolymers. Despite $\text{BO}_n\text{EO}_m\text{BO}_n$ triblock copolymers have been previously studied as potential associative thickeners for the control of rheological properties in aqueous systems through the formation of transient micelle clusters or networks by bridging of extended chains between micelles (32), to the best of our knowledge there exist no reports on the potential use of this type of copolymers as drug delivery nanocarriers.

Hence, in this work we assess the ability of five $\text{BO}_n\text{EO}_m\text{BO}_n$ triblock copolymers ($\text{BO}_8\text{EO}_{90}\text{BO}_8$, $\text{BO}_{12}\text{EO}_{227}\text{BO}_{12}$, $\text{BO}_{14}\text{EO}_{378}\text{BO}_{14}$, $\text{BO}_{20}\text{EO}_{411}\text{BO}_{20}$ and $\text{BO}_{21}\text{EO}_{385}\text{BO}_{21}$) to dissolve and chemically protect the antitumoral drug doxorubicin (DOXO), evaluating the colloidal stability of the drug-loaded polymer micelles, their drug release profile, the safety of the polymeric nanocarrier, and their *in vitro* efficacy as an antitumoral formulation. The block lengths and the EO/BO ratios were selected in order to analyze the effect of copolymer composition on the chain solubility, micelle formation ability, and core size. The interplay between micellar bridging (promoted by very long EO blocks) and full micellization (promoted by lengthening of the BO blocks) (33) should allow identification of the optimal copolymer structures for achieving an enhancement of drug solubilization and sustained release, while ensuring renal clearance of unimers as required for non-biodegradable polymers (11,16,17). In addition, the ability of this type of polymer as a potential inhibitor of P-gp efflux pump was investigated for the first time. DOXO accumulation in an *in vitro* model of multi-drug resistant (MDR) cell line (an ovarian tumor cell line, NCI-ADR-RES) with high expression of P-gp was evaluated and compared with that achieved using other block copolymers such as Pluronic[®] and Tetronic[®] which have demonstrated an important inhibitory activity and a subsequent enhancement of the bioavailability of P-gp substrates in different tissues and organs (17,34). The micellar systems based on EO/BO block copolymers are observed to improve DOXO encapsulation and chemotherapeutic activity by combining sustained drug release and inhibition of the P-gp efflux pump.

3.6.3 Experimental section

3.6.3.1 Materials

Five $\text{BO}_n\text{EO}_m\text{BO}_n$ copolymers with narrow chain length distributions ($\text{BO}_8\text{EO}_{90}\text{BO}_8$, $\text{BO}_{12}\text{EO}_{227}\text{BO}_{12}$, $\text{BO}_{14}\text{EO}_{378}\text{BO}_{14}$, $\text{BO}_{20}\text{EO}_{411}\text{BO}_{20}$ and $\text{BO}_{21}\text{EO}_{385}\text{BO}_{21}$) were prepared and characterized as previously described (32,35). Weight-average (M_w) to number-average (M_n) molecular weight ratios were determined at 25°C using a gel permeation chromatography (GPC) system equipped with a 1515 isocratic pump and a 2410 refractive index detector (Waters, Milford, MA). Chloroform was used as eluent, and monodisperse PEO was employed as a standard. M_n values were estimated from ^1H NMR spectra recorded on a Bruker ARX400 spectrometer (Bruker, Milton, ON, Canada) in deuterated chloroform. The critical micelle concentration (cmc) in aqueous solution was estimated from pyrene fluorescence measurements as previously reported (33). Table 1 summarizes the molecular characteristics of the copolymers.

Table 1. Molecular weight and critical micelle concentration (cmc) of the copolymers.

<i>Copolymers</i>	M_n^* (g/mol)	M_w/M_n^{**}	M_w (g/mol)
$\text{BO}_8\text{EO}_{90}\text{BO}_8$	5100	1.07	5460
$\text{BO}_{12}\text{EO}_{227}\text{BO}_{12}$	11700	1.05	12285
$\text{BO}_{14}\text{EO}_{378}\text{BO}_{14}$	18600	1.12	20832
$\text{BO}_{20}\text{EO}_{411}\text{BO}_{20}$	21000	1.08	22680
$\text{BO}_{21}\text{EO}_{385}\text{BO}_{21}$	20000	1.10	22000

*Estimated by NMR; **Estimated by GPC; M_w calculated from M_n and M_w/M_n . Estimated uncertainty: M_n to $\pm 3\%$; M_w/M_n to ± 0.01 .

3.6.3.2 Methods

a. Copolymer cytocompatibility evaluation

The cytocompatibility of the block copolymers at 0.1, 0.5, 1.0 or 1.7% was tested against BALB/3T3 clone A31 mouse embryonic fibroblast cells (CCL 163, ATCC), which were maintained in GIBCO™ Dulbecco's Modified Eagle's medium (DMEM; Invitrogen Corp, Carlsbad, CA) supplemented with 10% fetal bovine serum (FBS) and gentamicin (52 $\mu\text{g}/\text{mL}$) at 37°C in 5% CO_2 humidified atmosphere. Copolymer solutions in phosphate buffer pH 7.4 were added to cells cultured in 96-well plates ($2 \cdot 10^4$ cells/well) and incubated for 24 h. Cells exposed to copolymer-free culture medium were used as negative control. The medium was replaced by fresh medium (200 μL) containing MTT solution (20 μL , 5 mg/mL) and the well plates were incubated for 4 h (37°C, 5% CO_2) as stated in the MTT kit (Sigma-Aldrich). After incubation and removal of the supernatant,

formazan crystals were dissolved (0.1N HCl in anhydrous isopropanol) and the absorbance measured within 1 h using a microplate reader (BIORAD Model 680, USA) at 570 nm. Cell viability was quantified as

$$\% \text{ viability} = (\text{Abs}_{\text{sample}} / \text{Abs}_{\text{control}}) \times 100 \quad (1)$$

where $\text{Abs}_{\text{sample}}$ and $\text{Abs}_{\text{control}}$ represent the absorbance of the sample of cell culture in the presence and in the absence of copolymer, respectively. The assays were carried out in triplicate. Cell survival was also evaluated monitoring the release of lactate dehydrogenase (LDH) using the cytotoxicity detection Kit^{PLUS} (Roche, Spain). Triton X-100 (0.1%) and copolymer-free culture medium were used as positive control (total cell death) and blank, respectively. The viability (%) was determined from absorbance measurements at 490 nm according to the kit instructions.

b. Drug solubilisation

Doxorubicin hydrochloride (DOXO·HCl) was acquired from Sigma-Aldrich. DOXO base (36) was obtained by means of aqueous precipitation of DOXO·HCl aqueous solution (1 mg/mL) by adding triethylamine (three moles per drug mol) and methylene chloride. The system was kept under vigorous stirring for 1 h. The organic phase was then removed and evaporated in order to recover DOXO base. Hereinafter, DOXO refers to DOXO base. Solubilization of DOXO (intrinsic solubility in water ca. 0.5 mg dm⁻³) (37) in micellar copolymer solutions was tested in triplicate following the procedure of Elsabahy et al. with minor modifications (38). Briefly, the desired amount of DOXO dissolved in dichloromethane (100 μM) was added to the weighed solid copolymer. The organic solution was stirred and the solvent evaporated until dryness. Then, distilled water was added to the dried sample and left under stirring overnight (copolymer concentrations ranging from 0.025 to 1.7 wt. %). The solution was centrifuged at 3000 rpm for 30 min, and the supernatant filtered (Millipore Millex filters, 0.45 μm pore size) to remove non-solubilized drug. The filtered solutions were diluted (1/1000) with methanol to disrupt the self-assembled structures, and the amount of solubilized DOXO was determined spectrophotometrically at 480 nm (Cary 50 UV-Vis spectrophotometer, Agilent, Germany). Solutions of each copolymer at the same dilution conditions were used as blanks.

Drug loading, D.L., entrapment efficiency, E.E., and the solubilisation capacity per gram of copolymer in solution, S_{CP} (namely, the amount of drug dissolved at 37 °C in 100 mL of copolymer solution in excess of that dissolved in an equivalent volume of water) were calculated as follows:

$$D.L.\% = \frac{\text{weight of the drug in micellar solution}}{\text{weight of polymer} + \text{drug}} \times 100\% \quad (2)$$

$$E.E.\% = \frac{\text{weight of the drug in micellar solution}}{\text{weight of feeding drug}} \times 100\% \quad (3)$$

$$S_{CP} = \frac{\text{weight of the drug in micellar solution (mg)}}{\text{weight of polymer (g)}} \quad (4)$$

c. Physical stability of the drug-loaded micelles upon dilution

The physical stability of the drug-loaded micelles was assessed by dilution of the samples (1/50) in cell culture medium supplemented with 10% fetal bovine serum (FBS) at 37 °C under slow stirring, and the drug concentration monitored over time by UV spectrophotometry, as described above. The experiments were performed in triplicate. Simultaneously, aliquots were taken, filtered (Triton free Millipore Millex, 0.22 μm porosity) into scattering cells and allowed to equilibrate at 37°C for 30 min before recording changes in the size of drug-loaded micelles by DLS using an ALV-5000F (ALV-GmbH, Germany) instrument with vertically polarized incident light ($\lambda = 488$ nm) supplied by a diode-pumped Nd:YAG solid-state laser (Coherent Inc., CA, USA) operated at 2 W, and combined with an ALV SP-86 digital correlator (sampling time of 25 ns to 100 ms; scattering angle $\theta = 90^\circ$). Experiment duration was in the range 5-10 min, and each measurement was repeated at least twice. The correlation functions from DLS runs were analyzed by the CONTIN method to obtain the intensity distributions of decay rates (I), the apparent diffusion coefficients, and then the apparent hydrodynamic radius ($r_{h,app}$) applying the Stokes-Einstein equation (13,26).

d. In vitro DOXO release

Cell culture media supplemented with 10% FBS at pH 7.4 and 5.5 (a small volume of 1M HCl was added to reach the acidic pH) were used to prepare DOXO-loaded micelles (with 0.2 wt. % copolymer) and also as the release medium. Aliquots (4 mL) of the DOXO-loaded micellar systems were placed into dialysis tubes (SpectraPore®, MWCO 3500) and the release medium (100 mL) was kept at 37°C under stirring and replaced every 6 h in order to maintain sink conditions. Samples of the release medium (20 μL) were taken at given time intervals and the drug concentration was spectrophotometrically monitored at 480 nm after dilution in methanol. Assays were carried out in triplicate.

Drug release profiles from the micellar systems were fitted to the square-root kinetics (39)

$$M_t/M_\infty = k \cdot t^{0.5} \quad (5)$$

and to the Fickian diffusion model considering the micelles as perfect spheres (40)

$$M_t/M_\infty = k_1 + k_2 \cdot t^{0.5} - k_3 \cdot t \quad (6)$$

where M_t and M_∞ represent the drug amount released at time t and that initially contained in the formulation, respectively, and k , k_1 , k_2 and k_3 are release rate coefficients, respectively.

e. Cellular uptake of DOXO after incubation with empty polymeric micelles (P-gp inhibition)

NCI-ADR/RES cells (American Type Culture Collection, MD, USA) were seeded in a 24-well plate (1.5×10^5 cells/well, 1000 μ L/well) in supplemented medium for 48 h, and the medium was then replaced by serum-free DMEM containing 4-(2-hydroxyethyl)-1-piperazineethanesulfonic acid (HEPES, 25 mM, pH=7.4). Copolymer solutions, verapamil (100 μ M, from Sigma Aldrich) solution (positive control) or copolymer-free medium (blank) (20 μ L) were added and cells incubated at 37°C for 30 min. DOXO HCl solution (50 μ L, 100 mM in water) was then added and the samples incubated for 60 additional minutes. The medium was removed and the cells washed (PBS, 3 x 500 μ L) to eliminate DOXO and copolymer residues (34). Cells were lysed (1% Triton X-100, 300 μ L, 20 min) and the fluorescence of aliquots of supernatant (200 μ L) placed in opaque 96-well plates was measured in a plate reader ($\lambda_{exc} = 485$ nm; $\lambda_{em} = 580$ nm; Tecan Ultra Evolution). The remaining 100 μ L were diluted 10-fold with PBS, and the protein content was measured applying the Bradford method. DOX-free medium was used as blank. The experiments were repeated three separate times, each in triplicate. DOXO concentration values were normalized to the protein content in each well. DOXO accumulation factors (f_{DOXO}) were calculated as follows:

$$f_{DOXO} = AD_s/AD_0 \quad (7)$$

AD_s and AD_0 being the amounts of DOXO accumulated in the cells in the presence of copolymer or verapamil, and in the blank, respectively. Statistical analysis was carried out applying ANOVA (post hoc Dunnet's T3) with SPSS 15.1 software.

Additionally, confocal microscopy analysis was carried out to visualize DOXO accumulation inside the cells. NCI-ADR/RES cells (American Type Culture Collection, MD, USA) were seeded in a 24-well plate (1.5×10^5 cells/well, 1000 μ L/well) in RPMI 1640 medium with 2 mM L-glutamine, 10% FBS and 1% penicillin/streptomycin over sterile glass covers (from Invitrogen). After 48 hours the culture medium was replaced with RPMI 1640 containing HEPES 25 mM (pH 7.4). Then, the cells were incubated at 37°C for 30 minutes with 50 μ L of verapamil (100 μ M) or copolymer (0.2 wt. %) solutions. DOXO HCl (50 μ M, 50 μ L) was added and the cells incubated for another 60 minutes at 37°C. The formulations were removed and the cells were washed three times with phosphate

saline buffer pH 7.4 (PBS, Sigma), fixed with paraformaldehyde 4% for 10 min, washed and stained with Bodipy® phalloidin (30 µL/mL) in 0.2% Triton X-100 (permeabilizer). The cells were washed again with PBS pH 7.4 (3x10 min), mounted on glass slides using anti-fading solution (Bio-Rad laboratories, Hercules, CA, USA), and visualized at 20X and 63X using a Confocal Spectral Microscope Leica TCS-SP2 (LEICA Microsystems Heidelberg GmbH, Mannheim, Germany); green channel for doxorubicin (λ_{exc} . 561nm) and red channel for Bodipy® Phalloidin (λ_{exc} . 633 nm).

f. Cellular uptake of DOXO-loaded polymeric micelles (P-gp evasion)

NCI-ADR/RES cells were seeded as explained above over sterile glass covers. After 48 h, culture medium was replaced with RPMI 1640 with HEPES 25 mM (pH 7.4) and the cells were incubated with DOXO-loaded micelles for 1 and 24 h at 37°C. DOXO formulations were removed and the cells were washed and stained as described above. Cells incubated with DOXO·HCl solution (50 µM) in PBS pH 7.4 were used as a control.

g. In vitro cytotoxicity of drug loaded-polymeric micelles

Human NCI-ADR/RES cells were seeded onto 96-well plate (1.5×10^5 cells/mL, 100 µL/well, RPMI 1640 medium with 10% FBS, 2mM L-glutamine and 1% penicillin/streptomycin). After 24 h at 37°C, 5% CO₂, DOXO-loaded micellar solutions in PBS pH 7.4, or DOXO·HCl solutions (50 and 100 µM final concentrations) in PBS pH 7.4 were added. Cytotoxicity was evaluated in triplicate at 24 and 48 h applying the crystal violet method, as previously described (33). The growth inhibition was quantified as:

$$\%inhibition = 100 - (AO \cdot 100 / AT) \quad (8)$$

AO and AT being the absorbance of samples from cells in contact with the DOXO formulations and the PBS control, respectively. The results were analyzed by means of t-student's test (SPSS 15.1 software).

3.6.4 Results and discussion

Five BO_nEO_mBO_n copolymers that cover a wide range of molecular weights and cmc values were chosen for the study. These copolymers form spherical micelles ranging from 17 to 35 nm in diameter and association numbers between 20 and 43 (see Table S1) (20,41). At high concentration (> 2-8 wt. % depending on copolymer type and solution temperature) micellar bridging appears (42, 43).

3.6.4.1 Cytocompatibility of $\text{BO}_n\text{EO}_m\text{BO}_n$ copolymers

As a first step to elucidate the potential interest of the $\text{BO}_n\text{EO}_m\text{BO}_n$ polymeric micelles as drug carriers, their cytocompatibility was evaluated on a murine fibroblast cell line (BALB/3T3 clone A31), which is highly sensitive to the presence of toxic species. The LDH assay, which measures membrane permeability (42), revealed viability extents between 89.8% and 100% for the highest copolymer concentrations tested (1.5 wt. %, well above the cmc of all copolymers) after 24 h of incubation (see Figure 1A). Complete cytocompatibility was found for lower copolymer concentrations (data not shown). In order to prevent false positives arising from a possible delayed LDH release from cells after induction of cell apoptosis or necrosis and, hence, to additionally confirm the previous results, the activity of the mitochondrial dehydrogenase enzyme was studied by means of the MTT assay. Viabilities close to 100% were found for all copolymers at 1.5 wt. % except for $\text{BO}_8\text{EO}_{90}\text{BO}_8$, for which a 73% was observed (see Figure 1B). When decreasing concentration, cell viability progressively increased up to ca. 99 % (0.01 wt. % copolymer). Thus in the concentration range evaluated, the copolymers can be considered cytocompatible (44) and even exhibit larger viabilities than some commercially available Pluronic® and Tetronic® copolymers previously assayed in a similar cell line (34,45).

3.6.4.2 Solubilization capacity

Further studies were carried out with $\text{BO}_{12}\text{EO}_{227}\text{BO}_{12}$, $\text{BO}_{14}\text{EO}_{378}\text{BO}_{14}$ and $\text{BO}_{21}\text{EO}_{385}\text{BO}_{21}$, since these first two copolymers have similar BO length and different EO length, while in the second and the third one the EO block is comparable but the BO length is different. $\text{BO}_8\text{EO}_{90}\text{BO}_8$ was discarded because of its high cmc and relatively lower cytocompatibility, while $\text{BO}_{20}\text{EO}_{411}\text{BO}_{20}$ is quite similar to $\text{BO}_{21}\text{EO}_{385}\text{BO}_{21}$.

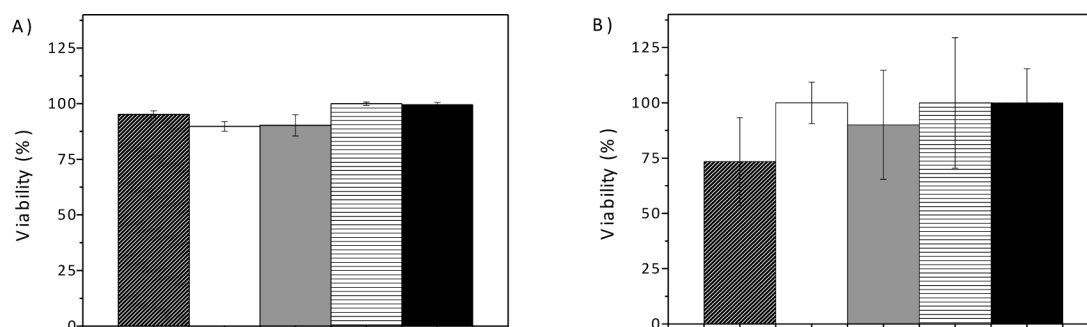


Figure 1: Viability of BALB/3T3 fibroblasts exposed to 1.5 wt.% micellar solutions of copolymers $\text{BO}_8\text{EO}_{90}\text{BO}_8$, $\text{BO}_{12}\text{EO}_{227}\text{BO}_{12}$, $\text{BO}_{14}\text{EO}_{378}\text{BO}_{14}$, $\text{BO}_{20}\text{EO}_{411}\text{BO}_{20}$ and $\text{BO}_{21}\text{EO}_{385}\text{BO}_{21}$ (from left to right) measured by means of LDH (A) and MTT (B) assays.

Encapsulation experiments were carried out using the anticancer drug DOXO. This drug accumulates inside the cell nucleus where it intercalates into DNA and interacts with topoisomerase II to cause DNA cleavage and cytotoxicity (46). However, DOXO binding to cell membranes ultimately results in the production of active oxygen species attacking the myocytes, which is the main cause of severe DOXO cardiotoxicity (47,48). Therefore, encapsulation in polymeric micelles is expected to improve the efficiency and safety of the treatment.

Table 2: Doxorubicin loading, D.L., entrapment efficiency, E.E., and solubility per gram of copolymer, S_{CP} , of the copolymers.

<i>Copolymers</i>	<i>DOXO/copolymer</i> (w/w %)	<i>D.L.^a</i> (wt.%)	<i>E.E.^a</i> (wt.%)	<i>S_{CP}^b</i> (mg/g)
BO ₁₂ EO ₂₂₇ BO ₁₂	0.4	0.10	26.6	0.96
	1.1	0.44	41.0	4.45
	2.5	1.51	62.7	15.48
	5.5	1.20	23.3	12.63
BO ₁₄ EO ₃₇₈ BO ₁₄	0.4	0.04	11.4	0.41
	1.1	0.36	34.1	3.68
	2.5	0.84	35.8	8.89
	5.5	1.46	27.4	15.47
BO ₂₁ EO ₃₈₅ BO ₂₁	0.4	0.11	31.2	1.12
	1.1	0.39	36.2	3.93
	2.5	1.56	59.6	14.92
	5.5	1.35	26.2	14.20

^a Estimated uncertainty $\pm 0.2\%$; ^b $\pm 1 \text{ mg g}^{-1}$

The apparent solubility of DOXO was tested adding an excess of drug (100 μM DOXO HCl) to solid copolymer to reach final concentrations ranging from 0.025 to 1.5 wt. % in aqueous solution, namely at least 10 times higher than the respective cmc ensuring complete micellization (22). Systems prepared with different DOXO/copolymer weight ratio showed that the entrapment efficiency (E.E.) exhibits a maximum at the [DOXO]/[copolymer] ratio equal to 2.5, from which it apparently decreases as a consequence of the saturation of the inner micellar core (Table 2). E.E. reached values of ca. 63%, 36% and 60% for BO₁₂EO₂₂₇BO₁₂, BO₁₄EO₃₇₈BO₁₄ and BO₂₁EO₃₈₅BO₂₁, respectively. Maximum values of drug loading (D.L.) of ca. 1.5% were observed for the three block copolymers. These quantities are somewhat larger than those previously obtained for PEO-PPO-based block copolymers such as Pluronic[®] (49), Tetronic[®] (50) or PEO-poly[N-(2-hydroxypropyl) methacrylamide-lactate copolymers (40), but slightly lower than maximum E.E. values found for PEO-based block copolymers with more hydrophobic blocks such as poly(styrene oxide) (23), poly(lactic-co-glycolic acid) (51) or

poly(caprolactone) (52). The solubility of DOXO per gram of copolymer (S_{CP}) was concentration-dependent, reaching values of up to ca. 15.5 mg g⁻¹. Thus, BO₁₂EO₂₂₇BO₁₂, BO₁₄EO₃₇₈BO₁₄ and BO₂₁EO₃₈₅BO₂₁ encapsulate DOXO very efficiently enhancing the apparent solubility up to 15 mg/L, i.e., more than 30 times the aqueous solubility of free DOXO.

3.6.4.3 Size and stability of the DOXO-loaded polymeric micelles.

Micellar sizes ranged from ca. 15 to 45 nm depending on the copolymer with narrow and monodisperse intensity distribution functions (Figure 2). No differences between non-loaded and DOXO-loaded systems were observed. The loaded micelles could be readily freeze-dried and their initial size distribution was recovered upon reconstitution in aqueous solution. The micellar sizes also remained stable upon extensive incubation in cell culture medium, which points to the great stability of the present polymeric micelles and the capability of the PEO stealth layer to avoid protein binding and subsequent micelle aggregation (see Figure 2).

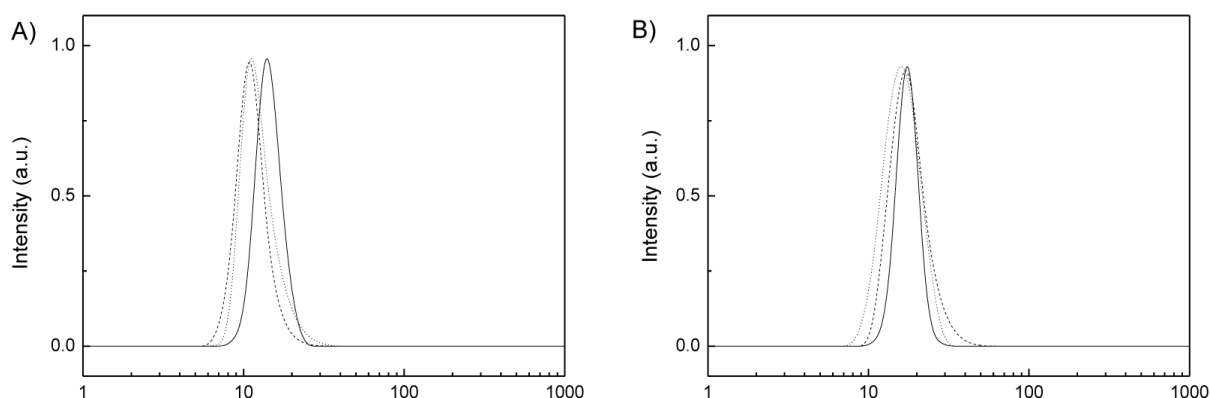


Figure 2: Intensity fraction size distribution of (–) free micelles, (···) DOXO-loaded micelles and (---) DOXO-loaded micelles upon freeze-drying for the triblock copolymers A) BO₁₂EO₂₂₇BO₁₂ and B) BO₂₁EO₃₈₅BO₂₁ in cell culture medium supplemented with 10% FBS.

The physical stability of drug-loaded micelles was tested upon high dilution (1/50) with cell culture medium containing 10% FBS, mimicking *in vivo* administration. Both changes in micellar size and free drug concentration in solution were monitored over time (final copolymer concentrations were well below the cmc). Polymeric micelles remained stable upon extensive incubation, at least for 20 days, in the protein rich medium (Figure 3). DOXO solubility remained above 80% of the initial value for all the three tested copolymers (Figure 3B). Nevertheless, BO₂₁EO₃₈₅BO₂₁ micelles displayed the largest resistance to disintegration, which is in agreement with its larger hydrophobic core that favors drug affinity. DOXO retention values were larger than those observed for other structurally related PEO-based copolymers (38,40,45) and

similar to those observed for more hydrophobic copolymers such as PSO-PEO-based block copolymers (53).

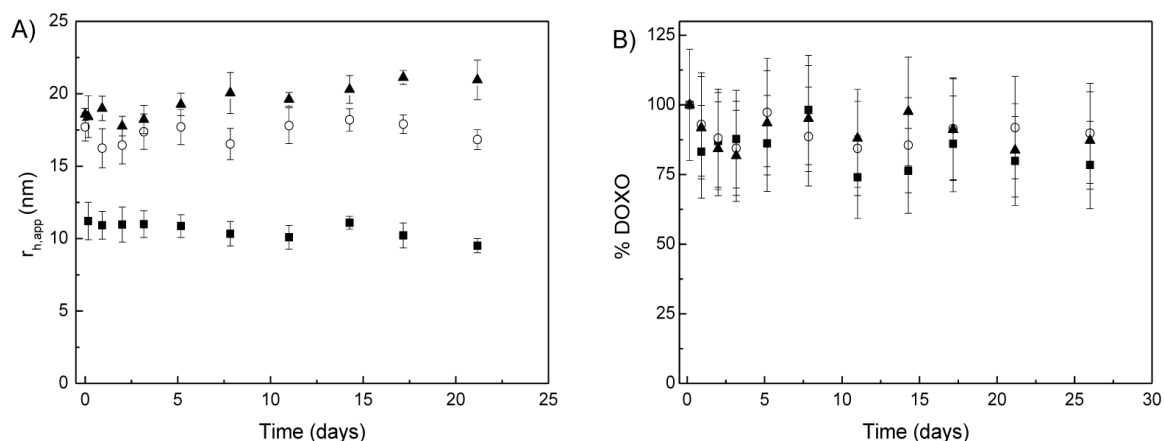


Figure 3: A) Temporal evolution of the size of polymeric micelles in cell culture medium in the presence of 10% FBS, and B) % DOXO in solution of diluted drug-loaded polymeric micelles over time at 37 °C (BO₁₂EO₂₂₇BO₁₂, ■; BO₁₄EO₃₇₈BO₁₄, □; and BO₂₁EO₃₈₅BO₂₁, ▲).

3.6.4.4 In vitro release

The release of DOXO from the micellar systems (0.2 wt. % copolymer) was tested using a dialysis tube (membrane cutoff 3500 Da) that ensured that no micellar diffusion occurred. Release profiles in FBS medium at both neutral (pH 7.4) and acidic (pH 5.5) conditions showed an initial burst followed by a sustained release pattern (Figure 4), with a similar pattern for all the block copolymers. As occurred for the stability micellar tests, no significant differences in the release profiles were observed when serum is not present in the micellar medium (figure not shown). The release was slower at pH 7.4, with ca. 40, 41 and 35 % DOXO released from BO₁₂EO₂₂₇BO₁₂, BO₁₄EO₃₇₈BO₁₄ and BO₂₁EO₃₈₅BO₂₁ micelles in the first 5 h, respectively; meanwhile, at pH 5.5 the amount of released drug was 49, 52 and 50%, respectively. After 30 h of incubation, copolymer BO₁₄EO₃₇₈BO₁₄ reached a cumulative DOXO released of ca. 84%, in contrast to the 70 and 78 % of BO₁₂EO₂₂₇BO₁₂ and BO₂₁EO₃₈₅BO₂₁, respectively, at pH 5.5 (65, 60 and 55% at pH 7.4, respectively). The faster release at pH 5.5 is consistent with the reprotonation of the amine group of DOXO, which leads to an increase in its hydrophilicity and, consequently, in a lower affinity for the hydrophobic micellar cores (54). This pH-dependent release profile may contribute to a more specific release of DOXO in the acidic environment of the tumor tissues once the BO_nEO_mBO_n micelles passively accumulate into them (55,56). Both free DOXO and DOXO-loaded micelles could be taken up by tumor cells through nonspecific endocytosis. The micelles would locate preferentially at the acidic endosome compartments, where the low pH might trigger DOXO release for the subsequent diffusion in the cytosol. Uptake of the loaded micelles could overcome the multidrug resistance (MDR) effect, due to efflux pumps, which is

often observed for free DOXO. The effect of the copolymers on the efflux is discussed in the following sections.

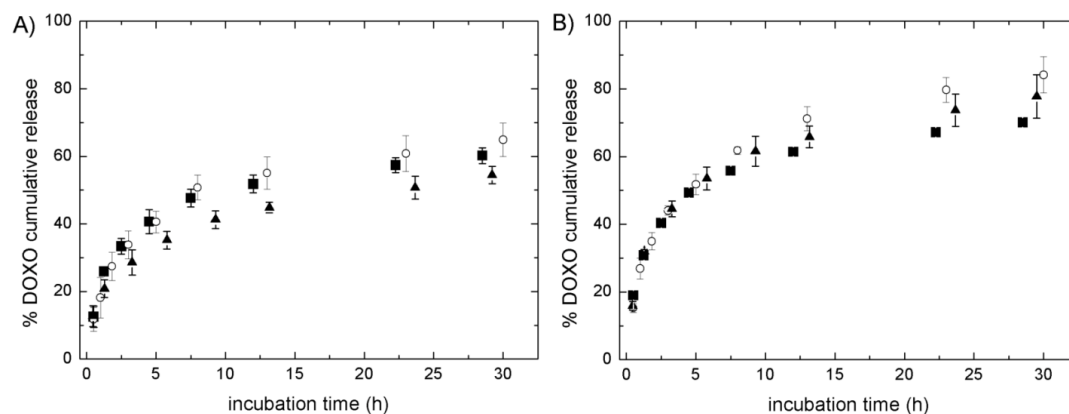


Figure 4: In vitro drug release profiles from DOXO-loaded copolymer micelles at pH A) 7.4 and B) 5.5 in cell culture medium with 10% FBS for triblock copolymers BO₁₂EO₂₂₇BO₁₂ (■), BO₁₄EO₃₇₈BO₁₄ (○) and BO₂₁EO₃₈₅BO₂₁ (▲).

The Fickian diffusion model fitted well the whole release profile (Table S2, correlation coefficient $R^2 > 0.90$). This model takes into account drug diffusion, conformational changes in the micellar structure during release and partial transfer of drug from one micelle to another. The constant associated to drug diffusion (k_2) became larger at pH 5.5 than at pH 7.4 and was similar (within uncertainty) for the three copolymers investigated.

3.6.4.5 Intracellular DOXO accumulation by inhibition of P-gp efflux pump.

The therapeutic effects of many chemotherapeutic agents are restricted by the multiple drug resistance mechanisms (MDR), including over-expression in cancer cells of efflux transporters belonging to the ATP-binding cassette proteins superfamily (57-59). P-gp is a membrane protein particularly involved in the removal of drugs (including the cytotoxic agents such as DOXO) from inside the cells, preventing intracellular accumulation (60). For example, P-gp is overexpressed in 40% of breast cancer tumors, these being up to three times less likely to respond to chemotherapy than those not expressing P-gp (61). In consequence, several methods have been applied to suppress such effect either by modifying the sensitization of the tumoral cells, or by changing the activity of the P-gp protein (62). It has been previously shown that other block copolymers, such as Pluronic® (17,18), Tetronic® (34,), or PEO-PCL (62,63), have an inhibitory effect on this efflux pump which is particularly relevant at concentrations at which the unimers are the predominant species and for copolymers with intermediate hydrophobic block lengths (34,64). The P-gp inhibitory performance of the BO_nEO_mBO_n triblock copolymers was tested at 0.2 wt. % (concentration used in solubilisation and

drug release experiments) in the ovarian tumor cell line NCI-ADR-RES, which is an adequate *in vitro* model of MDR cells with a relatively high expression of P-gp (65). Although the inhibitory effect could be larger for concentrations below cmc, the experiments were carried at 0.2 wt. % to mimic the situation in which the copolymers act as micellar carriers able to host DOXO and to carry it to the tumor site. Thus, from the point of view of the inhibition of the P-gp pump, this is not the most favourable condition. Intracellular accumulation of DOXO HCl favoured by the previous incubation of the cells with the unloaded copolymers was compared to that achieved when cells were pretreated with verapamil, a P-gp inhibitor used as reference (63). As expected, verapamil 100 μ M enhanced 2.00-fold DOXO accumulation compared to non-pretreated cells. BO₁₂EO₂₂₇BO₁₂, BO₁₄EO₃₇₈BO₁₄ and BO₂₁EO₃₈₅BO₂₁ increased DOXO accumulation by 1.52, 1.50 and 1.24-fold, respectively; these values being statistically higher ($P < 0.01$, ANOVA test, post-hoc T3 Dunnet) than those achieved without preincubation. The inhibitory capacity of the P-gp efflux pump is in the range recorded for other PPO-PEO and PSO-PEO copolymers considered as P-gp inhibitors of intermediate efficiency (23,33).

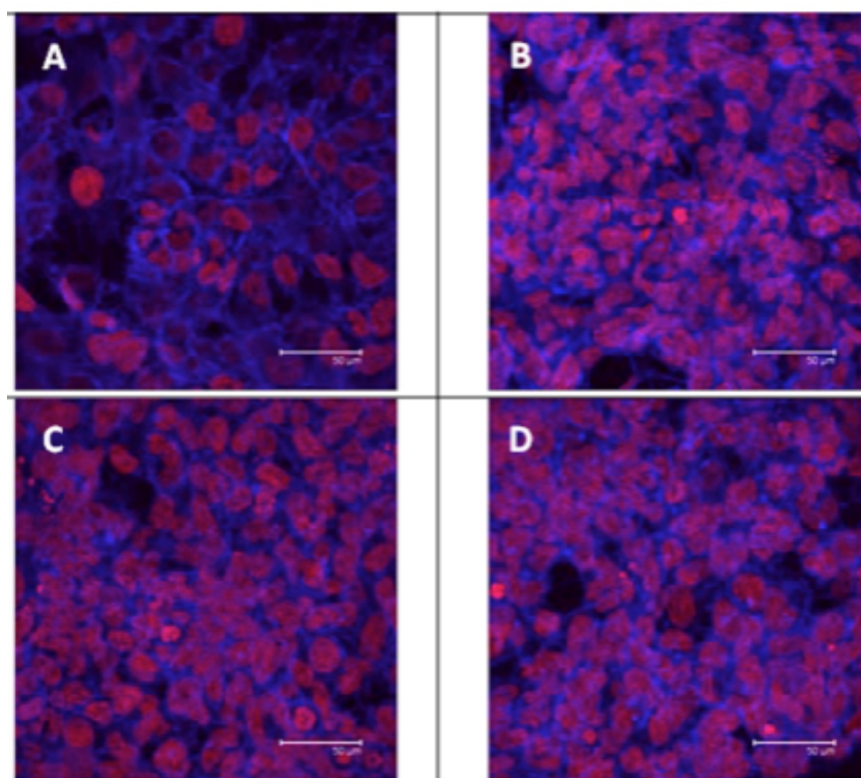
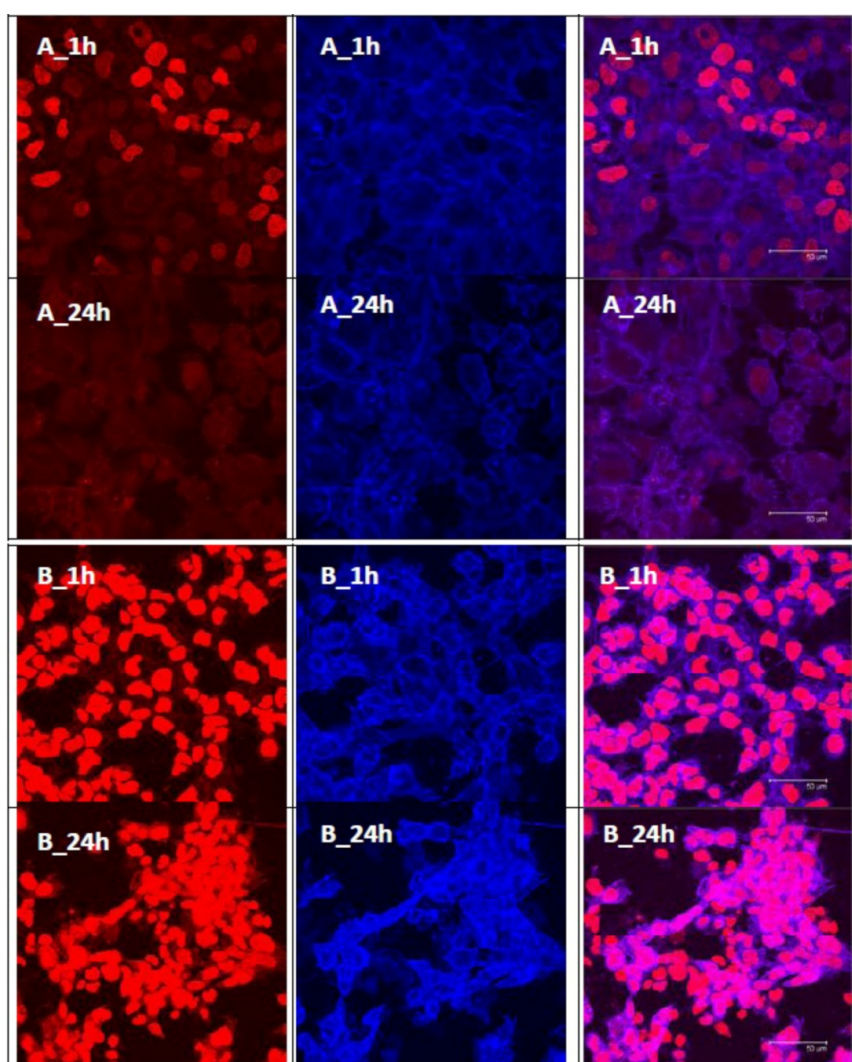


Figure 5: Confocal microscopy images of NCI-ADR-RES cells (A) incubated in the presence of free 50 μ M DOXO; (B) pretreated with 100 μ M verapamil and then incubated with 50 μ M DOXO; (C) pretreated with 0.2 wt.% BO₁₂EO₂₂₇BO₁₂ and then incubated with 50 μ M DOXO; (D) and pretreated with 0.2 wt.% BO₁₄EO₃₇₈BO₁₄ and then incubated with 50 μ M DOXO.

The integrity of the NCI-ADR-RES monolayers and the localization of DOXO inside cells was examined under confocal microscopy for cells preincubated with 0.2 wt. % $\text{BO}_{12}\text{EO}_{227}\text{BO}_{12}$ and $\text{BO}_{14}\text{EO}_{378}\text{BO}_{14}$ (those with the largest DOXO accumulation values), and then treated with DOXO HCl only solutions (Figure 5). Pretreatment with the copolymers or verapamil resulted in more fluorescence due to DOXO accumulation in both the cytoplasm and the nucleus of the cells.

3.6.4.6 Cellular uptake of DOXO-loaded polymeric micelles (P-gp evasion)

In a subsequent experiment, MDR NCI-ADR-RES ovarian cells were not pretreated with the non-loaded copolymers but directly incubated with DOXO-loaded micelles at 37 °C for 1 or 24 h (Figure 6). Cell exposure to free DOXO HCl, caused rapid but limited drug accumulation. In fact, the fluorescence intensity was lower after 24 h incubation than after the first hour (Figure 6A), which is consistent with a fast drug passive diffusion through the cell membrane followed by its efflux by the P-gp pump.



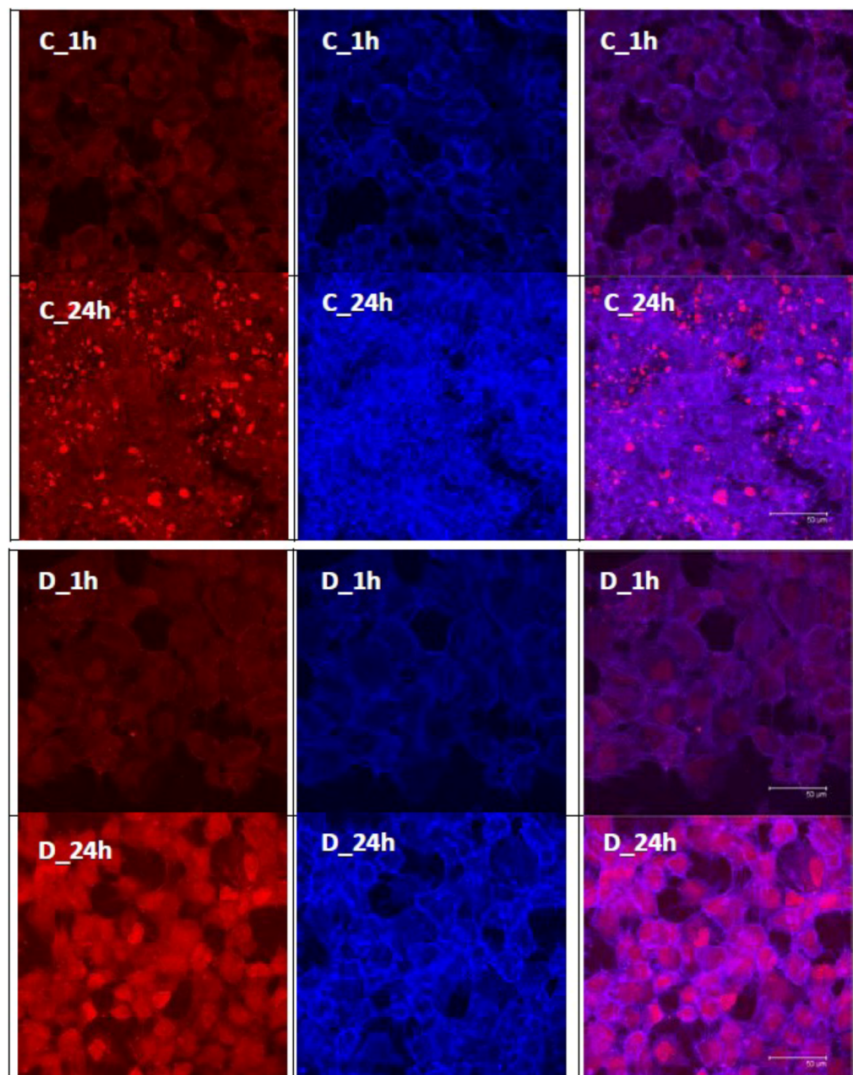


Figure 6: Confocal microscopy images recorded using a DOXO (left column) or a Bodipy® Phalloidin (middle column) filter, and superimposed images (right column) of NCI-ADR-RES cells incubated in culture medium (A) with 50 μM free DOXO; (B) with 100 μM of verapamil and 100 μM DOXO; (C) with 0.2 wt.% $\text{BO}_{12}\text{EO}_{227}\text{BO}_{12}$ micelles loaded with 100 μM DOXO; (D) and with 0.2 wt.% $\text{BO}_{14}\text{EO}_{378}\text{BO}_{14}$ micelles loaded with 100 μM DOXO after 1 and 24 hours, as indicated in the images. Scale is 50 μm .

Verapamil improved initial internalization of DOXO HCl by the cells (Figure 6B), but after 24 h of incubation the amount of DOXO inside the cells drastically decreased. In contrast, DOXO-loaded micelles increased drug accumulation with time. The initial lower accumulation may be caused by the slow release of DOXO from the micelles (see Figure 4). The self-quenching effect of DOXO inside the micelles makes fluorescence observable only when DOXO is released (59). After 24 h of incubation, DOXO fluorescence inside the cells was particularly intense, indicating that large drug amounts had been released from the micellar cores and remained inside the cells (see for

example Figure 6D after 24 h of incubation). These findings support the hypothesis of a sustained drug release inside the cells. Some differences in the fluorescence pattern after 24 h of incubation were observed among the three copolymers tested. In the case of $\text{BO}_{12}\text{EO}_{227}\text{BO}_{12}$, a spotty fluorescence pattern was seen, which is typical of cytoplasmic drug localization (52). The escape of micelles from endosomes and their transport to cytoplasmic organelles could be responsible for this fluorescence pattern (66). In contrast, a more intense and continuous fluorescent pattern in the nucleus was noted for $\text{BO}_{14}\text{EO}_{378}\text{BO}_{14}$, which might arise from the larger amount of DOXO released from $\text{BO}_{14}\text{EO}_{378}\text{BO}_{14}$ micelles at acidic pH, which would contribute to an enhanced DOXO accumulation in the cytoplasm and subsequent higher transfer to the nuclear region. Also, the existence of subtle differences in the internalization mechanisms of the loaded copolymer micelles due to differences in the physico-chemical properties of their copolymer chains could be possible and is currently under study. Preliminary experiments suggest that the cell uptake of DOXO-loaded $\text{BO}_n\text{EO}_m\text{BO}_n$ micelles would take place by an endocytosis-mediated mechanism, micelles being initially located within endosome vesicles enabling DOXO release in the cytosol in a sustained manner due to the endosome acidic environment, so bypassing the MDR barrier.

The cytotoxicity of the DOXO-loaded $\text{BO}_n\text{EO}_m\text{BO}_n$ micelles in the NCI-ADR-RES tumoral cell line at different polymer concentrations was evaluated by means of the crystal violet method. A MTT assay could not be used because DOXO interferes with the formation of formazan crystals (66,67). Empty polymeric micelles (controls) tested at different concentrations were observed to be safe and non-toxic, with cell viabilities larger than 95 % even after 48 h of incubation (Figure 7A). Thus, NCI-ADR-RES tumoral cells viability in the presence of unloaded polymeric micelles agrees with the results obtained with murine fibroblasts, despite the differences in the *in vitro* assays used and in the sensitivity of the two cell lines (53). In contrast, DOXO-loaded polymeric micelles exhibited a marked cell toxicity, which can thus be ascribed exclusively to the cytotoxic effect of the drug. The cytotoxicity of the DOXO-loaded polymeric micelles increased with time (Figure 7B), which strongly supports the protection and progressive release of DOXO exerted by the polymeric micelles, and its subsequent intracellular accumulation leading to enhanced cell death. In this regard, growth inhibition caused by 0.2 wt. % polymeric micelles loaded with 50 μM DOXO increased from 36, 43 and 21% at 24 h to 54, 66, and 48% at 48 h of incubation for $\text{BO}_{12}\text{EO}_{227}\text{BO}_{12}$, $\text{BO}_{14}\text{EO}_{378}\text{BO}_{14}$ and $\text{BO}_{21}\text{EO}_{385}\text{BO}_{21}$, respectively. This is compatible with an increased micelle accumulation inside the cell and a subsequent sustained drug release from the micelles (Figure 7B). DOXO-loaded $\text{BO}_{14}\text{EO}_{378}\text{BO}_{14}$ micelles were the most cytotoxic, in agreement with the continuous fluorescence DOXO pattern observed under confocal microscopy. Also, growth cell inhibition was dependent on the concentration of DOXO-loaded polymeric micelles; i.e., the cytotoxicity increased with increase of concentration of DOXO released from the micelles (Figure 7C). A similar trend was previously observed, for example, for DOXO-

loaded MPEG-b-PCL micelles (PCL, poly(caprolactone)) at 10 μM applied to human MCF-7 breast cancer cells (52). DOXO encapsulated in dextran-*b*-poly(DL-lactide-*co*-glycolide) micelles also displayed concentration-dependent cell viabilities, which ranged from 20 to 100% for DOXO concentrations between 50 and 0.01 $\mu\text{g/mL}$ in a DOXO-resistant HuCC-T1 cell line (61).

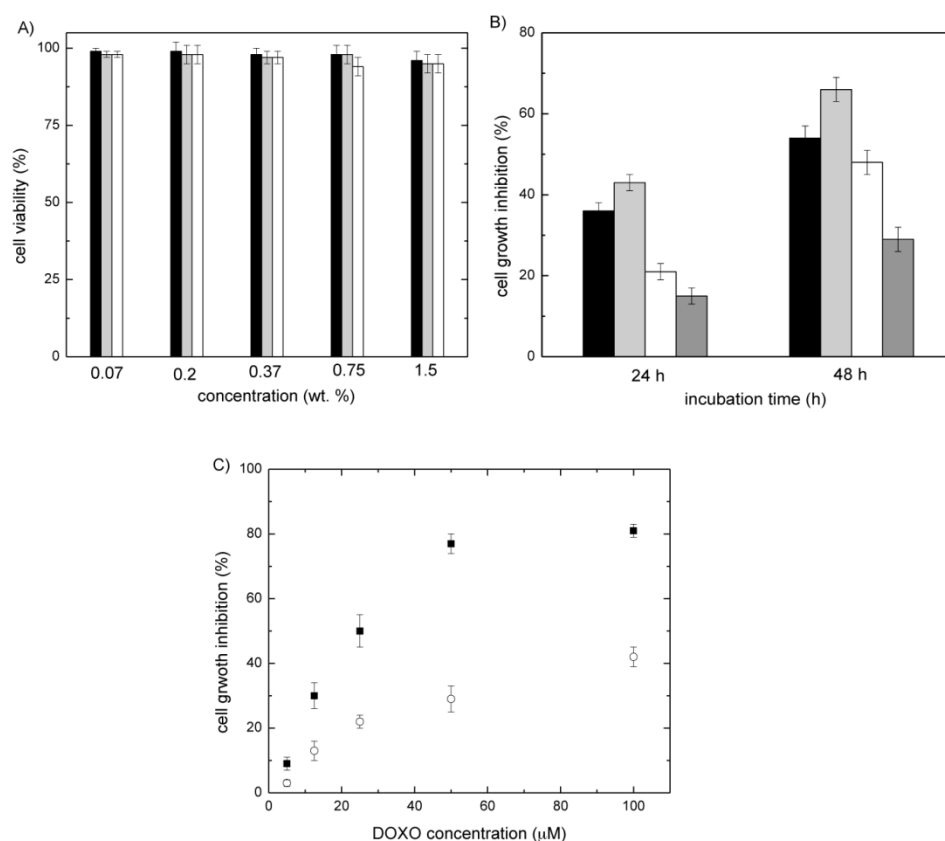


Figure 7: Growth inhibition of NCI-ADR-RES cells exposed to (A) different concentrations of empty polymeric micelles of BO₁₂EO₂₂₇BO₁₂ (black), BO₁₄E₃₇₈B₁₄ (grey) and BO₂₁EO₃₈₅BO₂₁ (white) after 48 h of incubation; (B) 0.2 wt.% micelles of copolymers BO₁₂EO₂₂₇BO₁₂ (black), BO₁₄E₃₇₈B₁₄ (light grey) and BO₂₁EO₃₈₅BO₂₁ (white) loaded with 50 μM DOXO, or in the presence of a 50 μM free DOXO solution (dark grey) after 24 and 48 h of incubation; (C) to different free DOXO concentrations in solution (○), or encapsulated in micelles of the copolymer BO₁₄E₃₇₈B₁₄ after 48 h of incubation. In (C) experiments were performed by dilution of a polymeric micelles stock solution of 1.5 wt% loaded with 100 μM DOXO. Mean \pm SD (n = 3).

Importantly, the cytotoxicity of the drug-loaded polymeric micelles was larger than that of free DOXO HCl solutions, even for higher free drug concentrations than those encapsulated inside micelles. Provided that BO_nEO_mBO_n copolymers are cytocompatible, it is expected that DOXO carried by polymeric micelles enters into the cells most likely via internalization followed by entrapment in endosomes/lysosomes. In this way, the drug may evade the P-gp pumps favouring its cellular accumulation and,

hence, increasing the cytotoxic activity when released from the polymeric micelles (68,69). Thus, the enhanced cytotoxicity of the drug-loaded micelles may be a result of the concomitant roles of the copolymers as P-gp inhibitors and P-gp evaders.

3.6.5 Conclusions

Reverse triblock poly(butylene oxide)-poly(ethylene oxide) block copolymers represent a new family of polymers able to be used as effective drug delivery systems overcoming several of the drawbacks of commercially available Pluronic® and Tetronic® copolymers currently used in clinical trials, such as relatively high polymeric chain polydispersity upon synthesis, poor-to-moderate drug solubilization capacity or micelle instability under high dilution. Aqueous solutions of $BO_nEO_mBO_n$ self-assemble at low concentrations to form cytocompatible spherical micelles of size ranging between ca. 10 to 40 nm in diameter depending on block length, which are suitable for filtration by sterilization and administration by the parenteral route. These polymeric micelles entrap the hydrophobic antitumoral DOXO with efficiencies up to ca. 63%, and display a release profile with an initial burst release at short times followed by a more sustained release phase. The enhanced release rate for DOXO due to drug protonation under acidic conditions should prompt drug release in tumoral tissues in both the environment of cell membranes (caused by hypoxia) and in some intracellular compartments (i.e., lysosomes). The cytotoxic activity of the DOXO-loaded polymeric micelles on an ovarian MDR NCI-ADR-RES cell line is exclusively ascribed to the DOXO therapeutic action in the light of the excellent cytocompatibility observed for all the copolymers (> ca. 95%). Confocal microscopy images showed that DOXO solubilized in micelles progressively accumulates inside the cells, resulting in a more prolonged residence and, consequently, in a much larger cytotoxicity than that observed for free DOXO. This enhanced cytotoxicity is also supported by the observed inhibition of the P-gp efflux pump mechanism of the MDR cell line by some of the copolymers. The extent of inhibition was found to be similar to that of verapamil or several Pluronic® and Tetronic® block copolymers previously studied. Hence, the role of the block copolymers evolves from simple “inert drug nanocarriers” to “active cell response inducers” as a consequence of complementation of the drug-cytotoxic activity with a moderate inhibition of the P-glycoprotein activity favouring drug accumulation inside MDR cells.

3.6.6 References

1. Arias, J.L. Mini-Rev. Med. Chem., **2011**, 11, 1.
2. Cho, K., Wang, X., Nie, S., Chen, Z., Shin, D.M. Clin. Cancer Res., **2008**, 14, 1310.
3. Farokhzad, O.C., Langer, R. Adv. Drug Deliv. Rev., **2006**, 58, 1456.
4. Heidel, J.; Davis, M. Pharm. Res., **2011**, 28, 187.
5. Lee, P.Y., Wong, K.K.Y. Curr. Drug Deliv., **2011**, 8, 245.

6. Fox, M.E., Szoka, F.C., Fréchet, J.M.J. *Acc. Chem. Res.*, **2009**, 42, 1141.
7. Gao, W., Chan, J.M., Farokhzad, O.C. *Mol. Pharm.*, **2010**, 7, 1913.
8. Oerlemans, C., Bult, W., Bos, M., Storm, G., Nijsen, J., Hennink, W. *Pharm. Res.*, **2010**, 27, 2569.
9. Wiradharma, N., Zhang, Y., Venkataraman, S., Hedrick, J.L., Yang, Y.Y. *Nano Today*, **2009**, 4, 302.
10. Battaglia, G., Ryan, A.J. *J. Am. Chem. Soc.*, **2005**, 127, 8757.
11. Castelletto, V., Hamley, I.W. *Polym. Adv. Technol.*, **2006**, 17, 137.
12. Ganguly, R., Aswal, V.K., Hassan, P.A. *J. Colloid Interface Sci.*, **2007**, 315, 693.
13. Juárez, J., Taboada, P., Valdez, M.A., Mosquera, V. *Langmuir*, **2008**, 24, 7107.
14. Chu, B., 1995. *Langmuir*, **1995**, 11, 414.
15. Hamaguchi, T., Matsumura, Y., Suzuki, M., Shimizu, K., Goda, R., Nakamura, I., Nakatomi, I., Yokoyama, M., Kataoka, K., Kakizoe, T. *Br. J. Cancer*, **2005**, 92, 1240.
16. Alvarez-Lorenzo, C., Sosnik, A., Concheiro, A. *Curr. Drug Targets*, **2011**, 12, 1112.
17. Batrakova, E.V., Kabanov, A.V. *J. Controlled Release*, **2008**, 130, 98.
18. Kabanov, A.V., Batrakova, E.V., Alakhov, V.Y. *Adv. Drug Deliv. Rev.*, **2002**, 54, 759.
19. Yu, G.-e., Yang, Z., Ameri, M., Attwood, D., Collett, J.H., Price, C., Booth, C. *J. Phys. Chem. B*, **1997**, 101, 4394.
20. Barbosa, S., Cheema, M.A., Taboada, P., Mosquera, V. *J. Phys. Chem. B*, **2011**, 111, 10920.
21. Booth, C., Attwood, D. *Macromol. Rapid Commun.*, **2000**, 21, 501.
22. Booth, C., Attwood, D., Price, C. *Phys. Chem. Chem. Phys.*, **2006**, 8, 3612.
23. Crothers, M., Zhou, Z., Ricardo, N.M.P.S., Yang, Z., Taboada, P., Chaibundit, C., Attwood, D., Booth, C. *Int. J. Pharm.*, **2005**, 293, 91.
24. Chiappetta, D.A., Sosnik, A. *Eur. J. Pharm. Biopharm.*, **2007**, 66, 303.
25. Ribeiro, M.E.N.P., de Oliveira, S.A., Ricardo, N.M.P.S., Mai, S.-M., Attwood, D., Yeates, S.G., Booth, C. *International Journal of Pharmaceutics*, **2008**, 362, 193.
26. Taboada, P., Velasquez, G., Barbosa, S., Castelletto, V., Nixon, S.K., Yang, Z., Heatley, F., Hamley, I.W., Ashford, M., Mosquera, V., Attwood, D., Booth, C. *Langmuir*, **2005**, 21, 5263.
27. Taboada, P., Velasquez, G., Barbosa, S., Yang, Z., Nixon, S.K., Zhou, Z., Heatley, F., Ashford, M., Mosquera, V., Attwood, D., Booth, C. *Langmuir*, **2006**, 22, 7465.
28. Heatley, F., Yu, G.-E., Sun, W.-B., Pywell, E.J., Mobbs, R.H., Booth, C. *Eur. Polym. J.*, **1990**, 26, 583.
29. Nace, V., Whitmarsh, R., Edens, M. *J. Am. Oil Chem. Soc.*, **1994**, 71, 777.
30. Yu, G.-E., Li, H., Price, C., Booth, C. *Langmuir*, **2002**, 18, 7756.
31. Yu, G.-E., Altinok, H., Nixon, S.K., Booth, C., Alexandridis, P., Hatton, T.A. *Eur. Polym. J.*, **1997**, 33, 673.
32. Mistry, D., Annable, T., Yuan, X.-F., Booth, C. *Langmuir*, **2006**, 22, 2986.

33. Cambón, A., Alatorre-Meda, M., Juárez, J., Topete, A., Mistry, D., Attwood, D., Barbosa, S., Taboada, P., Mosquera, V. J. *Colloid Interface Sci.*, **2011** 361, 154.
34. Alvarez-Lorenzo, C., Rey-Rico, A., Brea, J., Loza, M.I., Concheiro, A., Sosnik, A. *Nanomedicine* **2010**, 5, 1371.
35. Yang, Y.-W., Yang, Z., Zhou, Z.-K., Attwood, D., Booth, C. *Macromolecules*, **1996**, 29, 670.
36. Kim, J., Lee, J.E., Lee, S.H., Yu, J.H., Lee, J.H., Park, T.G., Hyeon, T. *Adv. Mater.*, **2008**, 20, 478.
37. Yalkowsky, S.H., He, Y. *Handbook of Aqueous Solubility Data*. 2003, CRC Press, Boca Raton, FL.
38. Elsabahy, M., Perron, M.E., Bertrand, N., Yu, G.E., Leroux, J.C. *Biomacromolecules*, **2007**, 8, 2250.
39. Wang, H., Xu, J., Wang, J., Chen, T., Wang, Y., Tan, Y.W., Su, H., Chan, K.L., Chen, H. *Angew. Chem. Int. Ed.*, **2010**, 49, 8426.
40. Wei, Z., Hao, J., Yuan, S., Li, Y., Juan, W., Sha, X., Fang, X. *Int. J. Pharm.*, **2009**, 376, 176.
41. Yamamoto, Y., Nagasaki, Y., Kato, Y., Sugiyama, Y., Kataoka, K. *J. Controlled Release*, **2001**, 77, 27.
42. Decker, T., Lohmann-Matthes, M.-L. *J. Immunol. Methods* **1988**, 115, 61.
43. Liu, T., Schuch, H., Gerst, M., Chu, B. *Macromolecules*, **1999**, 32, 6031.
44. Cavet, M.E., Harrington, K.L., VanDerMeid, K.R., Ward, K.W., Zhang, J.-Z. *Contact Lens Anter. Eye*, **2009**, 32, 171.
45. Chiappetta, D.A., Alvarez-Lorenzo, C., Rey-Rico, A., Taboada, P., Concheiro, A., Sosnik, A. *Eur. J. Pharm. Biopharm.*, **2010**, 76, 24.
46. Zunino, F., Capranico, G. *Anticancer Drug Design*, **1990**, 5, 307.
47. Berthiaume, J.M., Wallace, K.B. *Cell. Biol. Toxicol.*, **2007**, 23, 15.
48. Mohan, P., Rapoport, N. *Mol. Pharm.*, **2010**, 7, 1959.
49. Oliveira, C.P., Vasconcellos, L.C.G., Ribeiro, M.E.N.P., Ricardo, N.M.P.S., Souza, T.V.d.P., Costa, F.d.M.L.L., Chaibundit, C., Yeates, S.G., Attwood, D. *Int. J. Pharm.*, **2011**, 409, 206.
50. Alvarez-Lorenzo, C., Gonzalez-Lopez, J., Fernandez-Tarrio, M., Sandez-Macho, I., Concheiro, A. *Eur. J. Pharm. Biopharm.*, **2007**, 66, 244.
51. Diao, Y.Y., Li, H.Y., Fu, Y.H., Han, M., Hu, Y.L., Jiang, H.L., Tsutsumi, Y., Wei, Q.C., Chen, D.W., Gao, J.Q. *Int. J. Nanomed.*, **2011**, 6, 1955.
52. Shuai, X., Ai, H., Nasongkla, N., Kim, S., Gao, J. *J. Controlled Release*, **2004**, 98, 415.
53. Cambón, A., Barbosa, S., Rey-Rico, A., Figueroa-Ochoa, E.B., Soltero, J.F.A., Yeates, S.G., Alvarez-Lorenzo, C., Concheiro, A., Taboada, P., Mosquera, V. J. *Colloid Interface Sci.*, **2012**, 387, 275.
54. Forrest, M.L., Won, C.-Y., Malick, A.W., Kwon, G.S. *J. Controlled Release*, **2006**, 110, 370.

55. Peppas, N.A., Sahlin, J.J. *Int. J. Pharm.*, **1989**, 57, 169.
56. Lee, Y., Park, S.Y., Mok, H., Park, T.G. *Bioconj. Chem.*, **2007**, 19, 525.
57. Kabanov, A.V., Alakhov, V.Y. *Crit. Rev. Ther. Drug Carrier Syst.*, **2002**, 19, 1.
58. Raviv, Y., Pollard, H.B., Bruggemann, E.P., Pastan, I., Gottesman, M.M. *J. Biol. Chem.*, **1990**, 265, 3975.
59. Rees, D.C., Johnson, E., Lewinson, O. *Nat. Rev. Mol. Cell Biol.*, **2009**, 10, 218.
60. Wu, C.Y., Benet, L.Z., 2005. *Pharm. Res.*, **2005**, 22, 11.
61. Trock, B.J., Leonessa, F., Clarke, R. *J. Natl. Cancer Inst.*, **1997**, 89, 917.
62. Zastre, J.A., Jackson, J.K., Wong, W., Burt, H.M. *Mol. Pharm.*, **2008**, 5, 643.
63. Perez-Tomas, R. *Curr. Med. Chem.*, **2006**, 13, 1859.
64. Batrakova, E., Lee, S., Li, S., Venne, A., Alakhov, V., Kabanov, A. *Pharm. Res.*, **1999**, 16, 1373.
65. Roschke, A.V., Tonon, G., Gehlhaus, K.S., McTyre, N., Bussey, K.J., Lababidi, S., Scudiero, D.A., Weinstein, J.N., Kirsch, I.R. *Cancer Res.*, **2003**, 63, 8634.
66. Collier, A.C., Pritsos, C.A. *Biochem. Pharmacol.*, **2003**, 66, 281.
67. Chiba, K., Kawakami, K., Tohyama, K. *Toxicol. in Vitro*, **1998**, 12, 251.
68. Diao, Y.-Y., Han, M., Ding, P.-T., Chen, D.-W., Gao, J.-Q. *Int. J. Pharm. Sci.*, **2010**, 65, 356.
69. Jeong, Y.I., Kim do, H., Chung, C.W., Yoo, J.J., Choi, K.H., Kim, C.H., Ha, S.H., Kang, D.H. *Int. J. Nanomed.*, **2011**, 6, 1415.

3.7 SUPPORTING INFORMATION FOR DOXORUBICIN-LOADED MICELLES OF REVERSE POLY (BUTYLENE OXIDE) – POLY (ETHYLENE OXIDE)- POLY(BUTYLENE OXIDE) BLOCK COPOLYMERS AS EFFICIENT “ACTIVE” CHEMOTHERAPEUTIC AGENTS

Table S1: Critical micelle concentration, cmc , expansion factor, δ_t ; micellar molecular mass, $M_{w,micelle}$; hydrodynamic radius, r_h ; association number, N_w ; and number of water molecules per EO group, n_{water} , at 37 °C.

Copolymer	cmc (wt.%)	δ_t	$M_{w,micelle}$ 10^4 mol g^{-1}	r_h (nm)	N_w	n_{water}
BO ₈ EO ₉₀ BO ₈	0.0330	5.3	10.4	8.5	20	12
BO ₁₂ EO ₂₂₇ BO ₁₂	0.0031	4.2	25.0	13.3	21	8
BO ₁₄ EO ₃₇₈ BO ₁₄	0.0058	5.0	42.0	16.6	23	10
BO ₂₀ EO ₄₁₁ BO ₂₀	0.0012	5.5	89.6	17.3	43	11
BO ₂₁ EO ₃₈₅ BO ₂₁	0.0025	7.9	57.8	17.2	29	18

Table S2: Results of the fitting to Eq. 6 of the DOXO release profiles from BO₁₂EO₂₂₇BO₁₂, BO₁₄EO₃₇₈BO₁₄, and BO₂₁EO₃₈₅BO₂₁ micellar solutions in pH 5.5 and 7.4 media with 10% FBS. The release rate coefficients are given as mean values, with standard deviations in parenthesis.

<i>Copolymer</i>	<i>pH</i>	<i>k</i> ₁	<i>k</i> ₂	<i>k</i> ₃	<i>*F</i> _{2,5d.f}	<i>*P</i> - <i>value</i>	<i>R</i> ²
BO ₁₂ EO ₂₂₇ BO ₁₂	5.5	-0.301 (1.73)	33.58 (3.14)	-4.272 (0.76)	96.31	0.0001	0.975
	7.4	2.554 (3.34)	23.87 (4.78)	-2.915 (1.73)	25.13	0.0025	0.909
BO ₁₄ EO ₃₇₈ BO ₁₄	5.5	-3.337 (0.98)	32.33 (1.24)	-3.199 (0.24)	359.88	0.0000	0.992
	7.4	-4.644 (2.78)	27.57 (4.34)	-3.305 (0.58)	114.32	0.0000	0.974
BO ₂₁ EO ₃₈₅ BO ₂₁	5.5	-4.020 (2.45)	35.91 (2.55)	-4.429 (0.71)	109.80	0.0003	0.982
	7.4	3.815 (3.02)	21.27 (5.23)	-2.643 (0.91)	30.52	0.0016	0.924

From ANOVA of the regression.

CHAPTER 4

LINEAR COPOLYMERS

4.1 AIM OF THE WORK

As mentioned before, one of the areas of greater impact in biomedical therapeutics is the development of new biocompatible polymer systems to construct drug delivery systems (1,2). Amphiphilic polymeric micelles greatly improve the solubilization and sustained release of hydrophobic drugs and provide a protective environment for the cargo molecules in aqueous media, which favours lower drug administration doses, reduces adverse side effects, increases blood circulation times and passive targeting to specific cells (3,4). These capabilities strongly depend on the structure and composition of the polymeric chains. Composition and block length have been shown to play an important role in the modification of cellular responses such as drug internalization processes or transduction pathways when polymeric unimer/micelles are in close contact to cells (5-7).

In this work, we chose a broad spectrum of linear block copolymers with diblock and triblock architectures (monomers composition is shown in Figure 1) to study the role copolymer structure and composition play on cell viability and cellular response upon interaction with polymeric micelles. More than 30 structurally-related copolymers containing different hydrophobic blocks and PEO as the common hydrophilic unit have been analysed regarding their cytocompatibility and their potential as “active” cell response modifiers by testing their influence on the P-gP efflux pump mechanism in a multi-drug resistance cell line.

4.1.1 Aim of the work

To gain an insight into the cytocompatibility and performance as efflux pump inhibitors of more than 30 block copolymer micelles which have been previously shown as highly efficient drug solubilizing agents.

4.1.2 Methodology

Characterization and properties determination was performed by fluorescence spectroscopy, UV-vis spectroscopy and confocal microscopy.

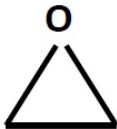
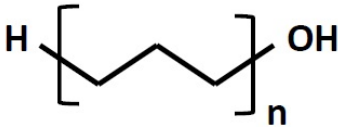
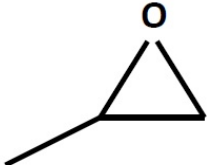
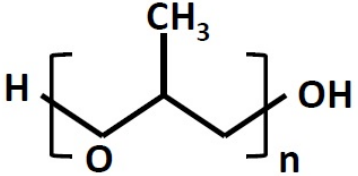

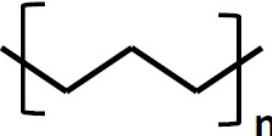
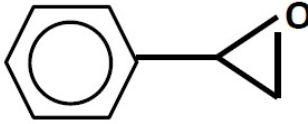
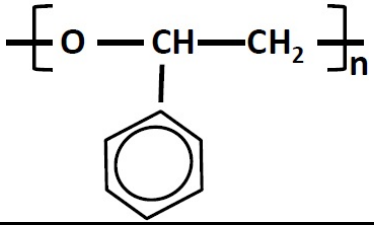
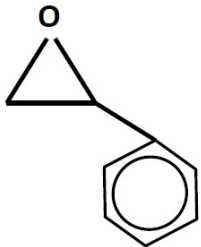
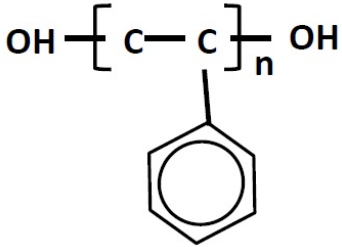
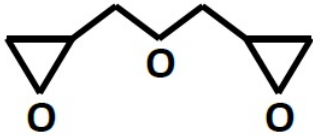
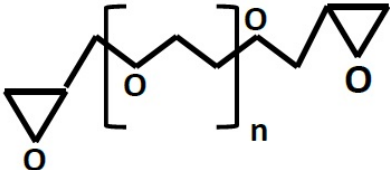
	
Ethylene oxide	Poly ethylene oxide
	
Propylene oxide	Poly propylene oxide
	
Methylene	Poly methylene
	
Butylene oxide	Poly butylenes oxide
	
Styrene oxide	Poly styrene oxide
	
Glycidyl ether	Poly glycidyl ether

Figure 1. Constituent monomers of the analyzed block copolymers.

Amphiphilic diblock and triblock copolymers have been synthesised in a broad range of block compositions and lengths, but most of the performed studies are related

to their structural characterization and aggregation properties, and their potential capability as drug delivery systems. However, their capabilities as potential biological response modifiers and cell-response inducers has not been extensively studied yet, which can provide additional advantages for more efficient drug therapeutic activity. Hence, in this work 30 non-commercial diblock and triblock copolymers with a common PEO hydrophilic block and different hydrophobic blocks were chosen. In this way, we try to establish a relationship between copolymer behavior and performance and block copolymer structure and hydrophobicity. The different hydrophobic blocks chosen are: propylene oxide (PO), methylene (C), butylene oxide (BO), styrene oxide (SO) and glycidyl ether (G) (see Figure1). The relative hydrophobicity of these blocks was estimated to be 1:5:6:12:15 for PO:C:BO:SO:G (3,8). The micellization process and aggregation properties of most of these polymers were already previously studied (8-13), so here we focus on the influence of block copolymer micelles on cellular response by analyzing their cytocompatibility and the capability of these polymeric micelles to inhibit the P-gP efflux mechanisms in a MDR cell line. First, cytotoxicity assays revealed the biocompatibility of a great part of the analyzed copolymer in a murine fibroblast (BALB/3T3 clone A31 mouse embryonic fibroblast cells CCL 163, ATCC) cell line and, for some selected copolymers, a murine neural stem cell line (C17.2) isolated from mouse-cerebellum. Then, doxorubicin accumulation in the absence and the presence of copolymer unimers and micelles was analyzed by using an MDR NCI-ADR/RES cell line in order to test their ability as efflux pump inhibitors. Conversely, only some few possess the ability to inhibit the P-glycoprotein efflux pump, promoting an enhanced drug accumulation inside cancer cells (14,15).

4.1.3 References

1. Tarcha, P.J., *Polymers for Controlled Drug Delivery*. 1991, Boca Raton: CRC Press.
2. Uchegbu, I.F.S.A.G., *Polymers in Drug Delivery*. 2006, Boca Raton, FL: CRC/Taylor & Francis.
3. Attwood, D.; Booth, C.; Yeates, S.G.; Chaibundit, C.; Ricardo, N.M.P.S. *Int. J. Pharm.* **2007**, 345, 35.
4. Elsabahy, M.; Perron, M.-E.; Bertrand, N.; Yu, G.; Leroux, J.-C. *Biomacromolecules*, **2007**, 8, 2250.
5. Alvarez-Lorenzo, C.; Sosnik, A.; Concheiro, A. *Curr. Drug Targets* **2011**, 12, 1112.
6. Batrakova, E.; Lee, S.; Li, S.; Venne, A.; Alakhov, V.; Kabanov, A. *Pharm. Res.* **1999**, 16, 1373.
7. Batrakova, E.V.; Li, S.; Alakhov, V.Y.; Miller, D.W.; Kabanov, A.V. *J. Pharmacol. Exp. Ther.* **2003**, 304, 845.
8. Booth, C.; Attwood, D.; Price, C. *Phys. Chem. Chem. Phys.* **2006**, 8, 3612.
9. Booth, C.; Attwood, D. *Macromol. Rapid Commun.* **2000**, 21, 501.
10. Taboada, P.; Velasquez, G.; Barbosa, S.; Castelletto, V.; Nixon, S.K.; Yang, Z.; Heatley, F.; Hamley, I.W.; Ashford, M.; Mosquera, V. *Langmuir* **2005**, 21, 5263.

11. Taboada, P.; Velasquez, G. Barbosa, S.; Yang, Z.; Nixon, S. K.; Zhou, Z.; Heatley, F.; Ashford, M.; Mosquera, V.; Attwood, D. *Langmuir* **2006**, 22, 7465.
12. Barbosa, S.; Cheema, M.A.; Taboada, P.; Mosquera, V. *J. Phys. Chem. B*, **2007**, 111, 10920.
13. Juárez, J.; Taboada, P.; Valdez, M.A.; Mosquera, V. *Langmuir* **2008**, 24, 7107.
14. Trock, B.J.; Leonessa, F.; Clarke, R. *J. Natl. Cancer Inst.* **1997**, 89, 917.
15. Alvarez-Lorenzo, C.; Carmen; Rey-Rico, A.; Brea, J.; Loza, M.I.; Concheiro, A.; Sosnik, A. *Nanomedicine*, **2010**, 5, 1371.

4.2 CYTOCOMPATIBILITY AND P-GLYCOPROTEIN INHIBITION OF BLOCK COPOLYMERS: STRUCTURE–ACTIVITY RELATIONSHIP

4.2.1 Abstract

Amphiphilic polymeric micelles greatly improves the solubilization and sustained release of hydrophobic drugs and provides a protective environment for the cargo molecules in aqueous media, which favors lower drug administration doses, reduced adverse side effects, increases in blood circulation times and passive targeting to specific cells. These capabilities depend, amongst other variables, of the structure and composition of the polymer chains. Composition and, in particular, block length, have been shown to play an important role in the modification of cellular responses such as drug internalization processes or transduction pathways when polymeric unimer/micelles are in close contact with cells. Here we present a detailed study about the role copolymer structure and composition play on cell viability and cellular response of several cell lines. To do that, more than 30 structurally-related copolymers with diblock and triblock architectures containing different hydrophobic blocks and poly(ethylene oxide) as the common hydrophilic unit have been analysed in order to test their cytocompatibility and their potential as “active” cell response modifiers by testing their influence on the P-gp efflux pump efflux mechanism responsible of multidrug resistance in cancerous cells. The present data indicated an empirical threshold for cell viability data at a copolymer EO/PO_{effective} value above ca. 1.5 for copolymers with triblock structure, whereas no empirical rule could be observed for diblocks. On the other hand, some of the tested copolymers were observed to act as efficient inhibitors of the P-gp efflux pump mechanism promoting an enhanced DOXO accumulation inside MDR NCI-ADR-RES cells, in some cases through the alteration of the P-gp ATPase activity.

4.2.2. Introduction

Effective chemotherapy in cancer and infectious diseases relies on the attainment of sufficient high intracellular drug concentrations. Polymer-based nanotechnology has become one of the most attractive and fast growing set of tools for advanced delivery (1). Materials that are currently being examined include liposomes,

polymeric micelles, polymersomes, nanogels, dendrimers and other nanosized materials which take advantage of their nanoscale dimensions to enhance cargo loading, to improve cargo pharmacokinetics and biodistribution, and to reduce drug toxicity (2,3). Amphiphilic block copolymers are particularly interesting due to their ability to self-assemble in aqueous solution as hydrophobic core-hydrophilic shell structures known as polymeric micelles. These structures allow the encapsulation and controlled release of hydrophobic drugs and enable escape from mononuclear phagocyte system or reticuloendothelial system (RES) uptake, which favours longer blood circulation times and drives the micelles to specific cells by enhanced permeability and retention effect (EPR) and eventually by active targeting (4, 5).

Moreover, recent investigations have pointed out that selected block copolymers can drastically modify specific cellular responses (6-8) as, for example, by altering the genomic responses to drugs (9) or by affecting the intracellular signal transduction pathways as apoptosis (10,11) In this regard, the well-known solubilizers and in situ gelling agents of the poly(ethylene oxide)–poly(propylene oxide)-based block copolymer (PEO-PPO) family as the linear poloxamers (Pluronic[®]) and the X-shaped poloxamines (Tetronic[®]) (12,13), have been shown to be potent biological response modifiers capable of sensitizing multidrug resistant (MDR) cells and enhancing drug transport across cellular barriers, such as polarized intestinal epithelial, Caco-2, and brain endothelium cells (14,15). The sensitization of MDR cells by Pluronic[®] and Tetronic[®] appears to be related to the inhibition of drug efflux systems, particularly, P-glycoprotein (P-gP) (14), which actively pumps the drugs out of the cells and, thus, reduces their intracellular effects. In the case of antitumor drugs, the inhibition of the efflux can increase the cytotoxicity of drugs and, thus, the therapeutic effect by 2 to 3 orders of magnitude. The mechanism involves the interaction of the block copolymer molecules with cell membranes, decreasing the membrane microviscosity which alters the pump conformation and ATP binding, and generating a pronounced depletion of ATP intracellular levels and the subsequent perturbation of different metabolic pathways (16,17). The combination of these effects causes a shutdown of the drug efflux systems, increasing the drug incorporation into cells and, as a result, leading to an effective sensitization of MDR cells. Therefore, the combination of suitable physico-chemical properties to encapsulate, protect and transport drugs together with an active role as cell response modifiers which enhances chemotherapeutic activity have led to the selection of some Pluronic formulations for clinical development. For example, SP1049C (Supratek Pharma Inc., Montreal, Canada), a doxorubicin (DOXO)-loaded mixed micellar system composed of the hydrophobic Pluronic L61 and the hydrophilic Pluronic F127, has successfully undergone phase I and II clinical trials and recently entered phase III studies. This formulation could successfully treat patients with advanced resistant solid tumors, and has been granted orphan drug designation by the FDA for the treatment of esophageal and gastric cancer (18).

A drawback for the successful application of PEO–PPO block copolymers in the clinical area is their incomplete micellization and the low physical stability of micelles upon dilution in the bloodstream. To overcome these pitfalls, Attwood and Booth's group in collaboration with us have developed during the last years new linear block copolymers in which the PPO segment was replaced by a more hydrophobic one, such as poly(butylene oxide) (PBO), poly(styrene oxide) (PSO) or phenylglycidyl ether (PG), amongst others (19-24). The relative hydrophobicity of the different hydrophobic blocks was estimated to be 1:4:5:6:10:12:12:15 for PO:L:C:BO:VL:CL:SO:G, where PO refers to propylene oxide, L refers to lactide, C to methylene, BO to butylene oxide, VL to valerolactone, CL to caprolactone, SO to styrene oxide, and G to glycidyl ether, respectively (22,25). These copolymers have lower critical micellar concentration (cmc) and an improved micellar stability and solubilization ability compared to Pluronic[®] and Tetronic[®] (26-28). To move forward towards the use of these types of block copolymers as components of clinically-valuable drug nanocarriers, a detailed evaluation of their biocompatibility and a complete analysis of the cellular responses they can induce are required (29).

In this context, the aim of the present work was to gain an insight into the cytocompatibility and the performance as efflux pump inhibitors of more than 30 block copolymers synthesized by us, which have been previously showed as highly efficient drug solubilizing agents (see Table 1 for molecular characteristics of the copolymers). These copolymers possess a similar architecture to that of Pluronic[®] linear block copolymers, but different hydrophobic blocks and block lengths. In that way, it would be possible to analyse the effect of such variables on the efficiency of the block copolymers as biological response modifiers. The cytocompatibility of the block copolymers was tested on a murine fibroblast (BALB/3T3 clone A31 mouse embryonic fibroblast cells -CCL 163, ATCC) cell line, whilst cytotoxicity of selected copolymers was also evaluated in a murine neural stem cell line (C17.2) isolated from mouse-cerebellum. The inhibition of the P-gp efflux pump was also evaluated and compared to that previously observed for several Pluronic[®] and Tetronic[®] copolymers. P-gp can transport a wide range of structurally and functionally unrelated cytotoxic drugs out of tumor cells and, if over-expressed, the tumor is less likely to respond to chemotherapy (30). This point was evaluated by recording the *in vitro* accumulation of DOXO in a MDR ovarian tumor cell line, NCI-ADR-RES, with a high expression of P-gp.

4.2.3 Experimental section

4.2.3.1 Materials

Copolymers with narrow chain length distributions were previously prepared and characterized as described in literature (see Table 1). Only copolymers C₁₂EO₄₅₅,

C₁₆EO₄₅₅ and C₂₀EO₄₅₅ were specifically synthesized and characterised in our laboratories to enable comparison with structurally related triblock copolymers of similar block lengths. The synthesis was performed as described elsewhere (31). Conversions to alkyl ethers were >99% and chain-length distributions were narrow ($M_w/M_n < 1.07$ by gel permeation chromatography using a Waters GPC system equipped with a 1515 isocratic pump and a 2410 refractive index detector (Waters, Milford, MA). ¹³C NMR spectra recorded on a Bruker ARX400 spectrometer (Bruker, Milton, ON, Canada) in deuterated chloroform were used to obtain absolute values of block length and composition, and to verify block architecture.

On the other hand, verapamil (VER), and doxorubicin hydrochloride (DOXO·HCl) were obtained from Sigma-Aldrich. Other reagents were of analytical grade. Milli-Q water was used for solution preparation.

4.2.3.2 Methods

a. Copolymer cytocompatibility evaluation

The cytocompatibility of the bare copolymer micelles was assessed using BALB/3T3 clone A31 mouse embryonic fibroblast (CCL 163, ATCC) and C17.2 murine neural stem cell line from mouse-cerebellum immortalised by avian melocytomatosis viral-related oncogene transfection, following a previously reported procedure (32). Cells were trypsinated and cultured in 96-well plates ($2 \cdot 10^4$ cells/well). Autoclaved copolymer solutions in phosphate buffer pH 7.4 (final copolymer concentration 0.1, 0.5, 1.0 or 1.5 wt.%) were added and the cells incubated for 24 h. The medium was replaced by fresh one (200 μ L) containing MTT solution (20 μ L, 5 mg/mL) and the well plates were incubated for 4 h (37°C, 5% CO₂). Immediately after incubation, the supernatant was removed, formazan crystals were dissolved (0.1N HCl in anhydrous isopropanol) and the absorbance measured within 1 h using a microplate reader (BIORAD Model 680, USA) at 570 nm. Cells exposed to copolymer-free culture medium were used as negative control (100% viability). Cell viability was quantified as:

$$\% \text{ viability} = (\text{Abs}_{\text{sample}} / \text{Abs}_{\text{control}}) \times 100 \quad (1)$$

where $\text{Abs}_{\text{sample}}$ and $\text{Abs}_{\text{control}}$ represent the absorbances of the sample of cell culture in the presence and in the absence of copolymer, respectively. The assay was carried out in triplicate. Cell survival was also evaluated monitoring the release of lactate dehydrogenase (LDH) using the cytotoxicity detection Kit^{PLUS} (Roche, Spain). Triton X-100 (0.1%) and copolymer-free culture medium were used as positive control (total cell death) and blank, respectively. The viability (%) was determined from absorbance measurements at 490 nm according to the kit instructions.

b. Cellular uptake of DOXO after incubation with empty polymeric micelles (P-gp inhibition)

DOXO accumulation in the absence and the presence of copolymer unimers and micelles was tested by using MDR NCI-ADR/RES cells (American Type Culture Collection, MD, USA) seeded in a 24-wells plate (1.5×10^5 cells/well, 500 μ L/well) in supplemented medium for 48 h following a previously reported method (33). The medium was replaced by serum-free RPMI-1640 medium containing 4-(2-hydroxyethyl)-1-piperazineethanesulfonic acid (HEPES, 25 mM, pH=7.4). Polymer samples were added (50 μ L) and cells incubated at 37°C for 30 min. Polymer-free medium and VER solution (100 μ M) were used as blank and positive control, respectively. Then, 50 μ L of a DOXO solution (100 μ M in water) was added and the samples incubated for 60 additional min. The medium was removed and the cells washed (PBS, 3 x 500 μ L) to eliminate DOXO and copolymer residues. Cells were lysed (1% Triton X-100, 300 μ L, 20 min), supernatant aliquots (200 μ L) transferred to opaque 96-well plates, and the fluorescence measured in a plate reader ($\lambda_{exc} = 485$ nm; $\lambda_{em} = 580$ nm; Tecan Ultra Evolution, Männedorf, Switzerland). DOXO-free medium was used as blank. DOXO concentrations were calculated using a calibration curve (0.2 pmol-0.2 nmol, $R^2 = 0.997$). The remaining 100 μ L were 10-fold diluted with water and protein content was measured using Bradford method. Determinations were carried out three separate times, each in triplicate. Data of DOXO concentration were normalized to the protein content in each well. DOXO accumulation factors were calculated as follows:

$$f_{DOXO} = AD_s/AD_0 \quad (2)$$

AD_s and AD_0 being the accumulated DOXO for the sample and the basal AD obtained with a DOXO solution in absence of polymer or VER. Statistical significance was analyzed applying ANOVA (post hoc Dunnett's T3) with SPSS 15.1 software.

Additionally, confocal microscopy analysis was carried out by seeding the NCI-ADR/RES cells on coverslips in a 24-wells plate (1.5×10^5 cells/well, 500 μ L/well) in RPMI 1640 medium with 2 mM L-glutamine, 10% FBS and 1% penicillin/streptomycin over sterile glass covers (from Sigma Aldrich). After 48 hours the culture medium was replaced with RPMI 1640 containing HEPES 25 mM (pH 7.4). The cells were incubated at 37°C for 30 minutes with 50 μ L of VER 100 μ M or 0.2 wt. % polymeric dispersions. Then, DOXO (50 μ M, 50 μ L) was added and the cells incubated for another 60 minutes at 37°C. The formulations were removed and the cells were washed three times with phosphate saline buffer pH 7.4 (PBS) and then fixed with paraformaldehyde 4% for 10 min, washed and stained with Bodipy[®] phalloidin (30 μ L/ml) in 0.2% Triton X-100 (permeabilizer). The cells were washed again with PBS pH 7.4 (3x10 min), mounted on glass slides using anti-fading solution (Bio-Rad laboratories, Hercules, CA, USA), and visualized at 20X and 63X

using a Confocal Spectral Microscope Leica TCS-SP2 (LEICA Microsystems Heidelberg GmbH, Mannheim, Germany); green channel for doxorubicin ($\lambda_{\text{exc.}}$ 561nm) and red channel for Bodipy® Phalloidin ($\lambda_{\text{exc.}}$ 633 nm).

c. *P-gp ATPase assay*

The effect of the copolymers at 0.2 wt% on the ATPase activity of P-gp was measured using P-gp-Glo™ Assay System with P-glycoprotein (V3601, Promega Biotech Ibérica, SL, Madrid, Spain) following the manufacturer's protocol. Na_3VO_4 and VER (12 μM) were used as controls of inhibition and stimulation of ATPase activity, respectively. Briefly, the tested substances were placed in 96 well plates containing 25 μg of P-gp containing membranes and incubated for 5 min at 37°C. Then, MgATP (5 mM) was added to the wells, which were incubated again at 37°C for 90 min. Then, the reaction was stopped and the remaining unmetabolized ATP was detected as a luciferase-generated luminescent signal (Tecan Ultra Evolution, Tecan, Switzerland).

4.2.4 Results and discussion

4.2.4.1 Cytocompatibility of the block copolymers

Cytocompatibility was evaluated by means of the LDH and MTT assays at copolymers concentration of 1.5 wt. %, well above their respective cmc values, thus, being a concentration useful for having micelles suitable for hosting of drug molecules. The selected murine fibroblast cell line (BALB/3T3 clone A31 mouse embryonic fibroblast cells) is highly sensitive to the presence of toxic species (43). The LDH assay reports if this cytosolic enzyme was released to the culture medium due to an enhanced membrane permeability, indicating cell damage or lysis (44). By contrast, the MTT assay measures the reduction of yellow 3-(4,5-dimethylthiazol-2-yl)-2,5-diphenyl tetrazolium bromide by mitochondrial succinate dehydrogenase enzyme to produce an insoluble, colored (dark purple) formazan product (only present in metabolically active cells).

Regarding triblock copolymers, our findings remarked the excellent cytocompatibility of all of those bearing BO and C blocks in their structure, with viabilities above 90%, as derived from both MTT and LDH assays (Figure 1). By contrast, copolymers possessing G units were found to be cytotoxic by MTT assay, with viabilities lower than 30%. A similar behavior was observed for copolymers containing SO units in their backbone, especially those with largest EO/SO ratios. Only $\text{EO}_{10}\text{SO}_{10}\text{EO}_{10}$ showed a good cytocompatibility, with a viability of ca. 100%.

Table 1: Molecular characteristics of the block copolymers

Copolymers	M_n^* (g/mol)	M_w / M_n^{**}	M_w (g/mol)	cmc (g/dm ³)
EO ₃₈ G ₁₂ EO ₃₈	5200	1.02	5300	< 0.01 ²⁰
EO ₆₂ G ₈ EO ₆₂	6700	1.03	6900	0.09 ²⁰
G ₅ EO ₅₇	3730	1.08	4030	0.065 ²¹
EO ₇₆ SO ₅ EO ₇₆	7350	1.06	7790	> 0.2 ³⁴
EO ₆₉ SO ₈ EO ₆₉	7030	1.05	7380	0.14 ²³
EO ₁₁₂ SO ₉ EO ₁₁₂	11000	1.08	11900	0.14 ³⁴
EO ₁₀ SO ₁₀ EO ₁₀	1980	1.06	2130	0.012 ²⁴
EO ₆₅ SO ₁₁ EO ₆₅	7040	1.05	7390	0.12 ³⁴
EO ₆₉ SO ₁₅ EO ₆₉	7700	1.04	8100	0.026 ³⁴
EO ₁₃₇ SO ₁₈ EO ₁₃₇	14200	1.06	15100	0.015 ²⁴
SO ₁₀ EO ₁₃₅	7140	1.04	7430	0.023 ²³
SO ₁₇ EO ₆₅	4940	1.04	5140	< 0.01 ³⁵
BO ₈ EO ₉₀ BO ₈	5100	1.07	5460	0.330 ³⁶
BO ₁₂ EO ₂₂₇ BO ₁₂	11700	1.05	12285	0.031 ³⁶
BO ₁₄ EO ₃₇₈ BO ₁₄	18600	1.12	20830	0.058 ³⁶
BO ₂₀ EO ₄₁₁ BO ₂₀	21000	1.08	22680	0.012 ³⁶
BO ₂₁ EO ₃₈₅ BO ₂₁	20000	1.10	22000	0.025 ³⁶
EO ₄₀ BO ₁₀	2480	1.04	2580	5 ³⁷
BO ₂₀ EO ₅₁₀	23900	1.06	25300	< 1 ³⁸
BO ₂₀ EO ₆₁₀	28300	1.06	30800	< 1 ³⁸
BO ₂₀ EO ₇₁₀	36300	1.12	40650	< 138
EO ₅₇ PO ₄₆ EO ₅₇	7680	1.07	8200	20 ³⁹

PO ₉₄ EO ₃₁₆	19350	1.07	20700	0.25 ⁴⁰
C ₁₂ EO ₄₅₅ C ₁₂	20380	1.09	22215	--- ⁴¹
C ₁₅ EO ₂₂₇ C ₁₅	10420	1.10	11460	--- ⁴²
C ₁₆ EO ₄₅₅ C ₁₆	20490	1.09	22340	--- ⁴¹
C ₂₀ EO ₄₅₅ C ₂₀	20610	1.10	22670	--- ⁴²
C ₁₂ EO ₄₅₅	20210	1.07	21625	---- ^a
C ₁₆ EO ₄₅₅	20270	1.07	21690	---- ^a
C ₂₁ EO ₄₅₅	20340	1.07	21760	---- ^a

^a This work

Nevertheless, a discrepancy is noted when comparing viability data derived from MTT and LDH tests. From the LDH assay, EO_mSO_nEO_m (where *m* and *n* denote the block lengths) copolymers were observed to be non-toxic, except EO₆₅SO₁₁EO₆₅ (cell growth inhibition ca. 37%), with viabilities ranging from 60% for EO₁₁₂SO₉EO₁₁₂ to 83% for EO₆₇SO₁₅EO₆₇. The same discrepancy was also observed for EO₅₇PO₄₆EO₅₇, a copolymer rather similar in composition to commercial Pluronic® F87 which has been found toxic to cells by MTT assay, as other several copolymers belonging to this family when evaluated at high concentrations as done in the present work (33,45-47). The observed differences from MTT and LDH assays may arise from the different markers employed to test copolymer cytocompatibility. Namely, the copolymer may be toxic to cells by altering their metabolic pathway soon after administration (recorded by MTT assay) without inducing an immediate response over cell membrane/structure integrity (tested through the LDH assay), which might take place at longer times (48). These facts stressed the relevance of performing both enzymatic activity (LDH) and proliferation (MTT) tests to elucidate the complete cytocompatibility of a given compound.

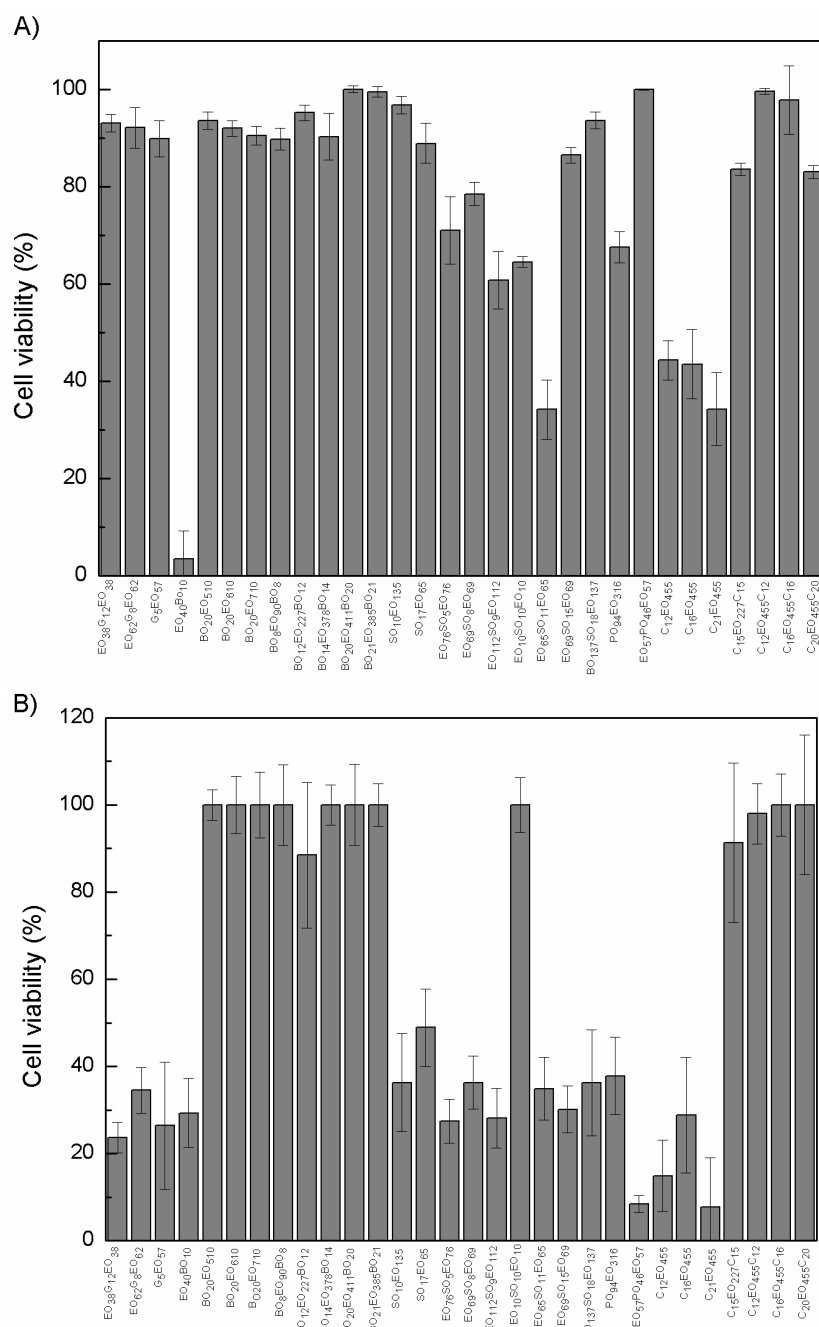


Figure 1: Cell viabilities of block copolymers at 1.5 wt. % in cell culture medium derived by A) LDH and B) MTT assays.

Cell viability of some diblock (G_nEO_m and SO_nEO_m) and triblock ($EO_mG_nEO_m$ and $EO_mSO_nEO_m$) copolymers was also assayed through the MTT assay in a murine neural stem cell line (C17.2, isolated from mouse-cerebellum immortalised by avian melocytomatosis viral-related oncogene transfection) (49) in order to consider possible variations due to cell sensitivity (see Figure S1). The observed cell viabilities for these copolymers were in agreement with those found in the murine fibroblast cell line, corroborating their inherent cell toxicity at the tested concentration. The cytotoxicity of some copolymers of these two families was also evaluated at lower concentrations. Cell

mortality was found to linearly decrease when the copolymer was diluted up to 0.1 wt. % (Figure S2). Nevertheless, EO₃₈G₁₂EO₃₈ was found to be still quite cytotoxic at such a low concentration, pointing out at its chemical composition as the responsible for the marked deleterious effect.

On the other hand, most of copolymers with a diblock structure were cytotoxic as indicated by the MTT assay, except those bearing hydrophobic BO blocks and long hydrophilic EO units, with cell viability values of ca. 100%. As occurred for their triblock counterparts, G-based and some SO-based diblock copolymers were cytocompatible in the light of LDH assay data (viabilities ranging from 85 to 95% were found, for example, for copolymers G₅EO₅₇, EO₆₅SO₁₇ and EO₁₃₅SO₁₀), but toxic when considering the MTT data. Also, their toxicity was additionally corroborated when performing a MTT assay in the C17.2 neural stem cell line (Figure S1). It was observed that diblock PO-based EO₁₄₄PO₁₀₅ and PO₉₄EO₃₁₆ polymers and diblock copolymers containing aliphatic methylene hydrophobic units were also non-cytocompatible at 1.5 wt. %, with survival rates after 24 h below 25 % by both LDH and MTT assays in strong contrast to their triblock counterparts, previously found to be fully non-toxic to cells.

From the data shown above, it seems that those block copolymers bearing the most hydrophobic units (G and SO) are toxic to cells, whereas those with low to intermediate hydrophobic ones (C and BO blocks) display a good cytocompatibility. Provided that the tested copolymers possess different hydrophobic units in their structure and a wide range of block lengths, for comparison purposes we expressed the chemical formulas of the analysed copolymers in terms of a “common” hydrophobic unit, in this case PO_{effective} units. To do that, the units of the hydrophobic block were multiplied by the relative hydrophobicity of the hydrophobic block, according to the empirical scale based on critical micelle concentrations shown in the introduction section. In this way, it is possible to carry out a homogeneous comparison between all the different copolymers and to check the influence of polymer hydrophobicity (in terms of the EO/hydrophobic unit block ratio) in cell viability (Table S1). For triblock copolymers, the effective length of the inner middle block (usually hydrophobic except for reverse PBO-based copolymers) was taken as half of the absolute value due to looping and subsequent formation of two junctions at the core/fringe boundary upon micellization compared to just one for a similar diblock counterpart. This procedure also allows us to establish a qualitative direct comparison of the obtained data with those previously reported for commercial Pluronic® and Tetronic® copolymers.

A preliminary analysis of the structure-cell toxicity relationship at a standardised concentration for all copolymers, 1.5 wt. %, can be found in Figure 2. For triblock copolymers, a boundary for cytotoxicity could be traced from MTT viability data at an EO/PO_{effective} value of ca. 1.5. Copolymers below such threshold are cytotoxic whereas

those above appear as cytocompatible. This threshold is also fulfilled by different Pluronic® and Tetronic® copolymers (32,33) Nevertheless, there exist some exceptions for this empiric rule: For example, copolymers EO₇₆SO₅EO₇₆, EO₁₁₂SO₉EO₁₁₂ and EO₅₇PO₄₆EO₅₇ are found to be toxic to cells despite having an EO/PO_{effective} ratio above the threshold value, whilst copolymer EO₁₀SO₁₀EO₁₀, with an EO/PO_{effective} value of 0.16, is completely non-toxic (Figure 1). By contrast, such threshold value delimiting cytocompatibility was not able to be defined for diblock copolymers, all essentially cytotoxic; only PBO-based block copolymers bearing long EO blocks (from ca. 500 to 700 units, EO/PPO_{effective} values ranging from 4.2 to 5.8) were non-toxic to cells at such elevated polymer concentration (1.5 wt. %) probably due to the stealthness provided by the long PEO shell around their hydrophobic inner core. Even those diblock copolymers bearing PO units in their molecular structure appear not cytocompatible. We hypothesize that the inherent cytotoxicity observed from MTT data for most of the diblock copolymers might be originated by the fact that these copolymers usually possess lower EO/PO_{effective} ratios than their triblock counterparts. Previous studies have indicated that copolymer hydrophobicity (denoted by either the hydrophobic block length and/or the hydrophilic-to-hydrophobic molar ratio) is the critical parameter that rules the interaction of block copolymers, such as Pluronic®, with model cell membranes as phospholipid bilayers (50,51). Copolymers with short hydrophobic PPO segments and radius of gyration smaller than the hydrophobic tails of the lipid bilayer probably intercalate in the cellular membrane (52) while those bearing longer hydrophobic blocks probably span the bilayer. Hence, copolymer hydrophobicity would favour a greater affinity of the copolymer chains for cellular membrane structures. In addition, the larger hydrophobicity of the diblock copolymers compared to their triblock counterparts involves lower cmc values, i.e. at the same polymer concentration (1.5 wt.%) there would exist a much larger number of micelles formed by diblock copolymers which can interact with the cell membrane and, subsequently, able to be internalized. The excess of polymeric micelles in contact with the cell membrane or even inside the cell can contribute to the observed enhanced cell mortality by interfering on the cell metabolism and/or altering their structural integrity, as denoted by the cytotoxicity tests (14,15). However, additional studies are required to exactly decipher the mechanisms involved in such elevated cell toxicity.

4.2.4.2 Block copolymers as inhibitors of the P-gp efflux pump

The therapeutic effects of many chemotherapeutic agents are restricted by the presence of cell multiple drug resistances (MDR). One well studied mechanism of MDR involves the over-expression in cancer cells of efflux transporters belonging to the ATP-binding cassette proteins superfamily, such as the ABC-transporter family P-gp, which transport chemotherapeutic agents out of the cells and prevent their intracellular accumulation (14,53). In this framework, the investigation of block copolymers that self-

assemble in the form of polymeric micelles in aqueous medium and are able to act as “active elements”, *i.e.* not only as passive drug nanocarriers but also as effective cell response modifiers, is of great interest (15,33).

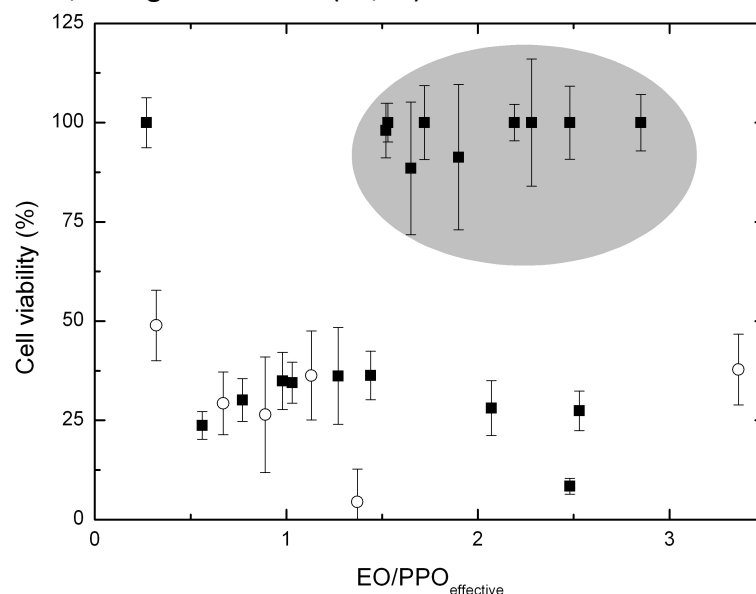


Figure 2: Relationship between cell viability (derived from MTT assay) and copolymer structure expressed through the EO/PPO_{effective} ratio for our diblock (○) and triblock (■) copolymers at a concentration of 1.5 wt.%.

In this line, the P-gp inhibitory performance of the previously tested copolymers was evaluated by measuring the intracellular accumulation of the chemotherapeutic agent DOXO (an exclusive substrate of P-gp) in an ovarian tumor cell line NCI-ADR-RES, which is an adequate *in vitro* model of MDR cells with a relatively high expression of P-gp (54). Since this quantitative analysis is carried out on a protein content basis, copolymers displaying moderate cytotoxicity could lead to some overestimation of the inhibitory activity due to the reduced protein content upon cell death. In order to avoid cytotoxicity induced by the copolymers, their concentration was fixed at 0.2 wt. % and the time of preincubation of the cells with the copolymers was set to 30 min. Then, DOXO was added and its accumulation inside the micelles was measured after 60 min of its administration. Thus, the total time that the cells were in contact with the copolymers was 90 min, for which low cytotoxicity due to the copolymers was detected (data not shown). Hence, the protein content was rather similar for all tested copolymers (Figure S3) allowing an effective comparison. Moreover, the use of a diluted polymer solution enables a better elucidation of the role of the copolymer unimers and minimizes drug sequestration inside the polymeric micelles. The inhibitory performance of the copolymers was assessed and compared with that of verapamil (VER), which is a well-characterized selective P-gp inhibitor (55).

Compared to the accumulation levels achieved when a DOXO solely solution was applied to cells, cells pre-incubated with VER 100 μ M showed a 2.00-fold increased

accumulation, f_{DOXO} . P-gp inhibitory capacities of the selected copolymers are shown in Figure 3. For comparison purposes, some Pluronic® and Tetronic® polymers were also tested under the same conditions. Copolymers $\text{BO}_{12}\text{EO}_{227}\text{BO}_{12}$, $\text{BO}_{14}\text{EO}_{378}\text{BO}_{14}$, $\text{BO}_{21}\text{EO}_{385}\text{BO}_{21}$, $\text{C}_{16}\text{EO}_{455}\text{C}_{16}$, $\text{BO}_{20}\text{EO}_{510}$ $\text{BO}_{20}\text{EO}_{610}$ and $\text{EO}_{57}\text{PO}_{46}\text{EO}_{57}$ improved DOXO accumulation compared to drug solely solution levels ($P < 0.01$, ANOVA, post-hoc T3 Dunnet) (56). The obtained values were similar to those measured in the present study for some PPO-based block copolymers such as Pluronic P85 (1.57), or Tetronic T904 (1.27), or for Pluronic F68, F127, L43 and P123, Tetronic T1307, met-T908, met-1107 and T304, or poly(styrene oxide)-poly(ethylene oxide) block copolymers $\text{EO}_{33}\text{SO}_{14}\text{EO}_{33}$ and $\text{EO}_{38}\text{SO}_{10}\text{EO}_{38}$ previously obtained (29,33). Special attention deserves the accumulation achieved by copolymer $\text{C}_{16}\text{EO}_{455}\text{C}_{16}$, 2.66-fold larger than that free DOXO, and even larger than that achieved after pre-incubation with verapamil. Although the P-gp inhibitory effect has been found to be stronger at copolymer concentrations close to the cmc (33,57), we have here observed successful DOXO accumulation for some of the copolymers at a concentration of 0.2 wt.% at which most of them are fully micellised (Table 1). In terms of successful pharmacotherapy, this may be beneficial because of the greater ability of copolymers (due to the larger number of micelles available) to solubilize the drug inside the polymeric micelles and act as efficient drug carriers.

The tested copolymers do not directly comply with the structural requirements previously stated by Batrakova *et al.* to attain maximal inhibition with Pluronic® copolymers (14), that is, copolymers bearing intermediate-lengthy PO blocks (30-60 units) and with relatively low HLB values. In our case, the tested block copolymers would possess on the basis of “effective” PO units, in general, much longer hydrophobic blocks than those considered optimal Pluronic® and Tetronic® polymers (Table S1), and hence, their $\text{EO}/\text{PO}_{\text{effective}}$ molar ratio (thus their HLB) would be also relatively low, being out of the expected window for P-gp inhibitory capacity. On the other hand, other copolymers as $\text{EO}_{67}\text{SO}_{15}\text{EO}_{67}$ or $\text{EO}_{62}\text{G}_8\text{EO}_{62}$ strikingly induced significant decreases in DOXO accumulation, with values of 0.60 and 0.53 respectively. This leads us to think that these copolymers probably enhance the P-gp efflux mechanism.

To gain further insight into the mechanism by which this set of copolymers enhance DOXO accumulation in the P-gp overexpressed cells, the P-gp ATPase activity was evaluated. VER is a potent P-gp substrate that leads to ATP consumption and caused 3.04 ± 0.12 -fold increase in ATPase activity compared to the basal activity registered in the presence of ortovanadate, which is in agreement with previous results (58). Acting as a substrate, VER impedes the expulsion of other drugs from cells by the P-gp pump mechanism resulting in their known inhibitory effect of P-gp-mediated efflux.

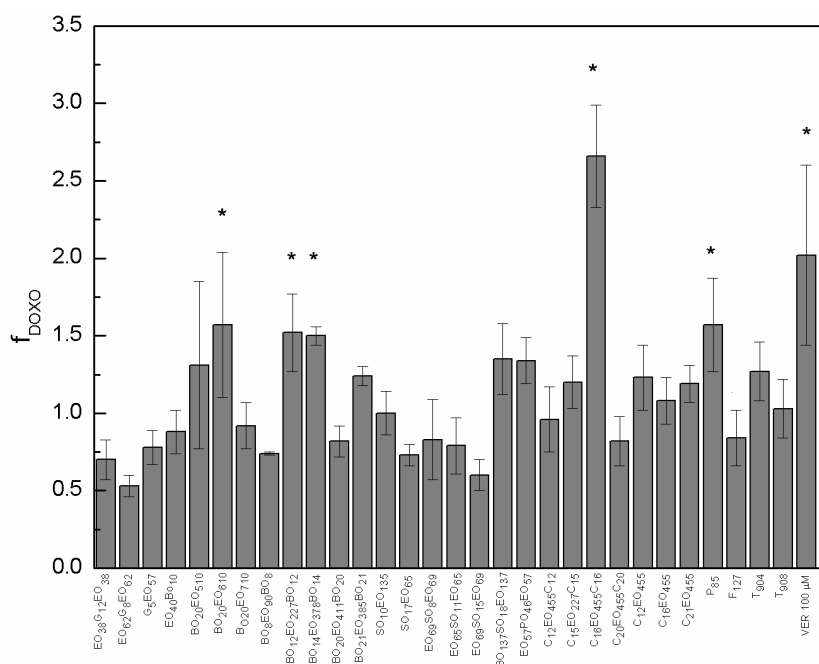


Figure 3: Doxorubicin accumulation, f_{DOXO} , in the presence of different copolymers at a concentration of 0.2 wt. %. 100 μM VER was used as a control. All the samples contained 100 μM DOXO ($n = 3$). For comparison purposes, Pluronic® P85 and F127, and Tetriconic® T904 and T908 are also included. *Statistically significant increase ($p < 0.05$) of DOXO accumulated amount when compared with DOXO/VER.

Statistically significant increases in ATPase activity have been also observed for copolymers BO₁₂EO₂₂₇BO₁₂, EO₅₇PO₄₆EO₅₇, and C₂₁EO₄₅₅. Although for the latter two copolymers no significant accumulation of DOXO inside cells was observed, for copolymer BO₁₂EO₂₂₇BO₁₂ an enhanced DOXO retention in cells was noted, which suggests that this copolymer might act as a P-gp substrate in a similar fashion as VER does. This effect is the opposite of that recorded for copolymers EO₁₃₇SO₁₈EO₁₃₇, EO₄₀BO₁₀, C₁₅EO₂₂₇C₁₅, C₁₆EO₄₅₅C₁₆ and EO₆₂G₈EO₆₂ which led to a decrease in ATPase activity to the half, or even less in some cases (Figure 4). Nevertheless, from the five copolymers which inhibit ATPase, only C₁₆EO₄₅₅C₁₆ promoted a 2.66-fold enhanced DOXO accumulation in the cells, i.e., even larger than that of VER. A similar behaviour was also previously observed, for example, for copolymer Pluronic P85, which also decreased ATPase activity to the half at a concentration of 0.01 wt. % and enhanced DOXO accumulation in cells, which suggests a possible shared pathway by both copolymers. However, at larger concentrations as that of the present study (0.2 wt. %) the inhibition ability of P85 completely disappeared, indicating that only the unimers are able to inhibit the ATPase activity. Provided that all of the five previous copolymers are much more hydrophobic than Pluronic P85, at 0.2 wt. % they can be considered to be almost completely micellised. Therefore, the ATPase inhibitory effect may result from a combination of the effect of polymer unimers in equilibrium with micelles in

solution together with the ability of these copolymers to alter the conformation of the efflux protein and the ATP-binding domains due to their greater hydrophobicity (57), as also observed for some poly(ethylene oxide)-poly(styrene oxide) block copolymers (29).

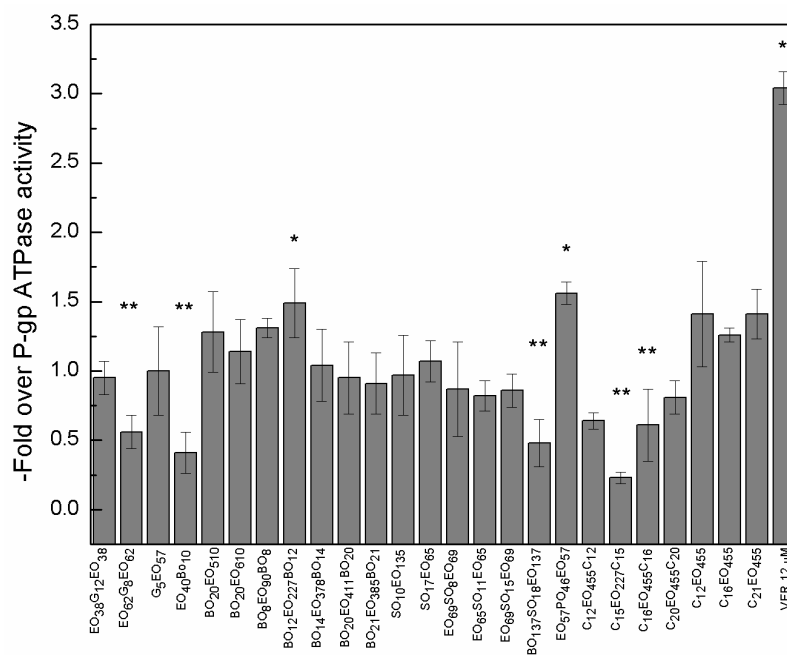


Figure 4: P-gp ATPase activity in the presence of different copolymers at a concentration of 0.2 wt. %. 12 μM VER was used as a control. * ** Statistically significant increase/decrease ($p < 0.05$) of ATPase activity when compared with VER.

Finally, to evaluate the integrity of the NCI-ADR-RES monolayers and qualitatively assess the localization and intensity of DOXO inside cells, cells preincubated with 0.2 wt. % of different copolymers (BO₁₂EO₂₂₇BO₁₂, C₁₂EO₄₅₅C₁₂, C₁₆EO₄₅₅C₁₆, EO₅₇PO₄₄EO₅₇ and EO₃₈G₁₂EO₃₈) and, then, treated with DOXO solely solutions were fixed and observed under confocal microscopy (Figure 5). Cells exposed to VER or to copolymers BO₁₂EO₂₂₇BO₁₂, EO₅₇PO₄₄EO₅₇ and C₁₆EO₄₅₅C₁₆ showed a more intense staining than the non-pretreated cells, indicating that DOXO efflux was inhibited to some extent. The relatively similar fluorescence intensity provided by the DOXO/VER, DOXO/BO₁₂EO₂₂₇BO₁₂ or DOXO/C₁₆EO₄₅₅C₁₆ systems is in agreement with the quantitative analysis of DOXO accumulation values. The observed brightest DOXO fluorescence staining when cells were pretreated with C₁₆EO₄₅₅C₁₆ would agree with the larger f_{DOXO} value compared to that achieved with VER. On the other hand, in resistant strains DOXO is usually localised in the cytoplasm and the nucleus. All the drug/copolymer samples showed the cytoplasmatic/nuclear localization of DOXO which is characteristic of cells resistant to this drug (59).

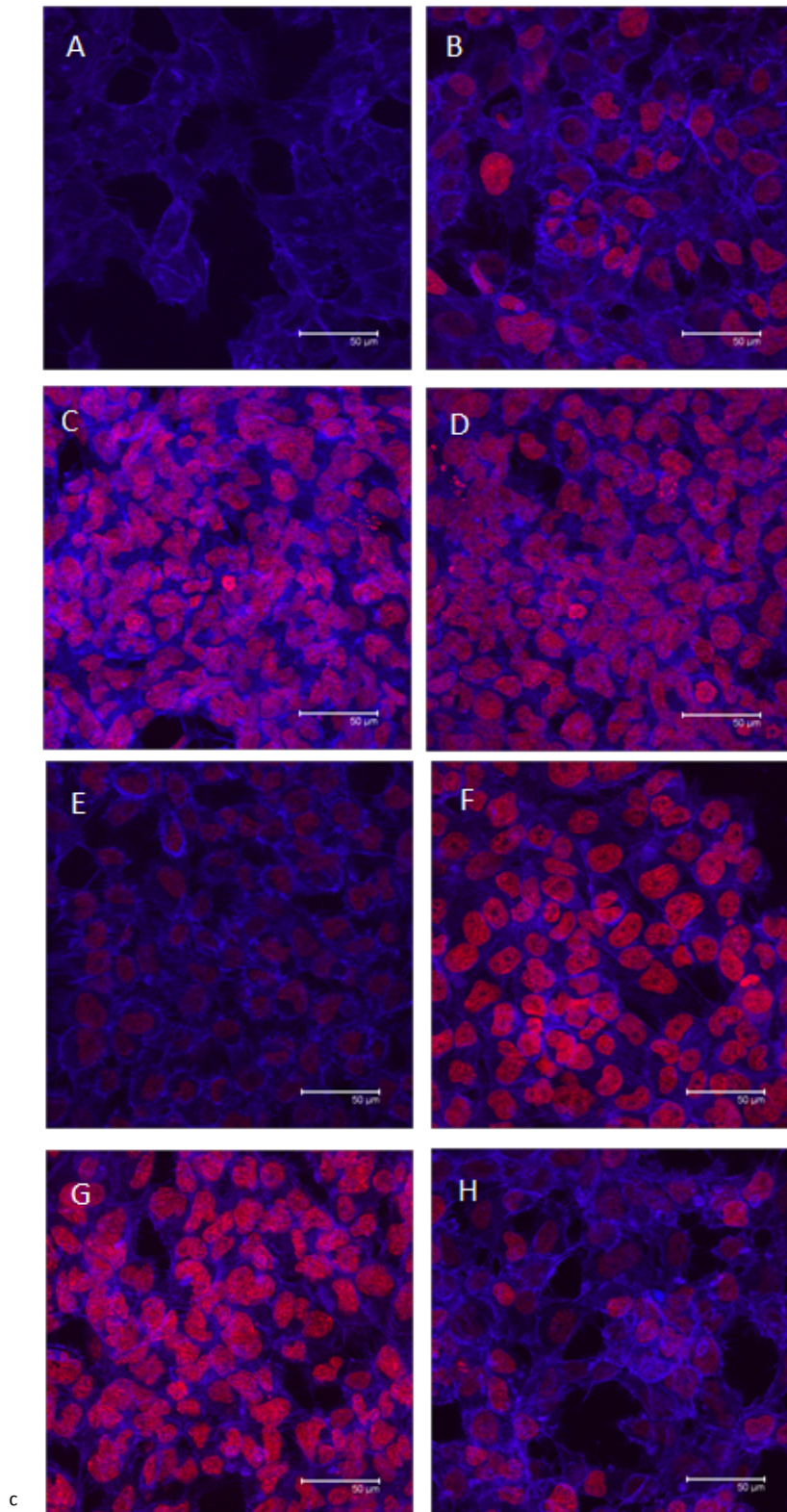


Figure 5: Confocal microscopy images of NCI-ADR-RES cells alone (A); incubated in the presence of free 50 μ M DOXO (B); pre-treated with 100 μ M VER and then incubated with 50 μ M DOXO (C); and pre-treated with 0.2 wt.% $\text{BO}_{12}\text{EO}_{227}\text{BO}_{12}$ (D), $\text{C}_{12}\text{E}_{455}\text{C}_{12}$ (E), $\text{C}_{16}\text{E}_{455}\text{C}_{16}$ (F), $\text{EO}_{57}\text{PO}_{44}\text{EO}_{57}$ (G) or $\text{EO}_{38}\text{G}_{12}\text{EO}_{38}$ (H) and then incubated with 50 μ M DOXO.

4.2.5 Conclusions

More than 30 block copolymers with diblock and triblock architecture containing different hydrophobic blocks and poly(ethylene oxide) as the common hydrophilic unit have been analysed in order to test their cytocompatibility and their potential as “active” cell response modifiers by testing their influence on the P-gp efflux pump mechanism. From the experimental data, it seems that those block copolymers bearing the most hydrophobic units in their structure (G and SO blocks) are toxic to cells, whereas those with low to intermediate hydrophobic ones display a suitable cytocompatibility. This fact highlights the role that copolymer chemical composition plays in cell survival. Viability analysis in terms of a “common” hydrophobic unit, in this case PO_{effective} units, was performed in order to check the possible influence of polymer hydrophobicity (in terms of the EO/hydrophobic unit block ratio) in cell viability and also to enable an approximate homogeneous comparison between all the different copolymers. An empirical threshold for cytotoxicity could be traced from MTT viability data at an EO/PO_{effective} value above ca. 1.5 for triblock copolymers, whereas no empirical rule was found for the diblocks. Also, the diblock copolymers appear to be more toxic to cells than their triblock counterparts, probably due to their lower EO/PO_{effective} ratios. The larger amount of diblock copolymer micelles (if compared to triblock ones) and their greater affinity for cellular membrane structures would contribute to the observed enhanced cell mortality by interfering on the cell metabolism and/or altering the cell structural integrity. On the other hand, some of the tested copolymers act as efficient inhibitors of the P-gp efflux pump promoting an enhanced DOXO accumulation inside MDR NCI-ADR-RES cells despite they do not comply the structural requirements previously stated by Batrakova *et al.*(14) to attain maximal inhibition with Pluronic® copolymers. In addition, DOXO accumulation seems to be mediated in some cases through the alteration of the P-gp ATPase activity (increasing or decreasing this activity depending on the considered copolymer), which is one of the regulation mechanisms of the pump.

4.2.6 References

1. Chiellini, E. G., H.; Braunegg, G.; Buchert, J.; Gatenholm, P.; van der Zee, M. (Eds.), *Biorelated Polymers. Sustainable Polymer Science and Technology*. 2001.
2. Yu, J. J.; Lee, H. A.; Kim, J. H.; Kong, W. H.; Kim, Y.; Cui, Z. Y.; Park, K. G.; Kim, W. S.; Lee, H. G.; Seo, S. W. *J. Drug Targeting*, **2007**, 15, 279.
3. Mitra, S.; Gaur, U.; Ghosh, P. C.; Maitra, A. N. *J. Controlled Release*, **2001**, 74, 317.
4. Bromberg, L. *J. Controlled Release*, **2008**, 128, 99.
5. Oerlemans, C.; Bult, W.; Bos, M.; Storm, G.; Nijssen, J. F.; Hennink, W. *Pharm. Res.* **2010**, 27, 2569.

6. Batrakova, E.; Lee, S.; Li, S.; Venne, A.; Alakhov, V.; Kabanov, A. *Pharm. Res.* **1999**, *16*, 1373.
7. Werle, M. *Pharm. Res.*, **2008**, *25*, 500.
8. Zastre, J. A.; Jackson, J. K.; Wong, W.; Burt, H. M. *Molecular Pharmaceutics* **2008**, *5*, 643.
9. Kabanov, A. V.; Batrakova, E. V.; Sriadibhatla, S.; Yang, Z.; Kelly, D. L.; Alakov, V. Y. *J. Controlled Release*, **2005**, *101*, 259.
10. Kopeček, J.; Kopečková, P.; Minko, T.; Lu, Z.-R. *Eur. J. Pharm. Biopharm.*, **2000**, *50*, 61.
11. Minko, T.; Batrakova, E. V.; Li, S.; Li, Y.; Pakunlu, R. I.; Alakhov, V. Y.; Kabanov, A. V. *J. Controlled Release*, **2005**, *105*, 269.
12. Kabanov, A. V.; Alakhov, V.Y. *Crit. Rev. Ther. Drug Carrier Syst.*, **2002**, *19*, 1.
13. Alvarez-Lorenzo, C.; Sosnik, A.; Concheiro, A. *Curr. Drug Targets*, **2011**, *12*, 1112.
14. Kabanov, A. V.; Batrakova, E. V.; Alakhov, V. Y. *Adv. Drug Deliv. Rev.* **2002**, *54*, 759.
15. Batrakova, E. V.; Kabanov, A. V. *J. Controlled Release* **2008**, *130*, 98.
16. Batrakova, E. V.; Li, S.; Vinogradov, S. V.; Alakhov, V. Y.; Miller, D. W.; Kabanov, A. V. *J. Pharmacol. Exp. Therap.*, **2001**, *299*, 483.
17. Batrakova, E. V.; Li, S.; Elmquist, W. F.; Miller, D. W.; Alakhov, V. Y.; Kabanov, A. V. *Br. J. Cancer*, **2001**, *85*, 1987.
18. <http://www.supratek.com/>.accessedSeptember2011
19. Booth, C.; Attwood, D. *Macromol. Rapid Commun.*, **2000**, *21*, 501.
20. Taboada, P.; Velasquez, G.; Barbosa, S.; Castelletto, V.; Nixon, S. K.; Yang, Z.; Heatley, F.; Hamley, I. W.; Ashford, M.; Mosquera, V.; Attwood, D.; Booth, C. *Langmuir*, **2005**, *21*, 5263.
21. Taboada, P.; Velasquez, G.; Barbosa, S.; Yang, Z.; Nixon, S. K.; Zhou, Z.; Heatley, F.; Ashford, M.; Mosquera, V.; Attwood, D.; Booth, C. *Langmuir*, **2006**, *22*, 7465.
22. Booth, C.; Attwood, D.; Price, C. *Phys. Chem. Chem. Phys.*, **2006**, *8*, 3612.
23. Barbosa, S.; Cheema, M. A.; Taboada, P.; Mosquera, V. J. *Phys. Chem. B*, **2007**, *111*, 10920.
24. Juárez, J.; Taboada, P.; Valdez, M. A.; Mosquera, V. *Langmuir*, **2008**, *24*, 7107.
25. Attwood, D.; Booth, C.; Yeates, S. G.; Chaibundit, C.; Ricardo, N. M. Block copolymers for drug solubilisation: relative hydrophobicities of polyether and polyester micelle-core-forming blocks. *Int. J. Pharm.*, **2007**, *345*, 35.
26. Crothers, M.; Zhou, Z.; Ricardo, N. M. P. S.; Yang, Z.; Taboada, P.; Chaibundit, C.; Attwood, D.; Booth, C. *Int. J. Pharm.*, **2005**, *293*, 91.
27. Ribeiro, M. E.; Cavalcante, I. M.; Ricardo, N. M.; Mai, S. M.; Attwood, D.; Yeates, S. G.; Booth, C. *Int. J. Pharm.*, **2009**, *369*, 196.
28. Ribeiro, M. E. N. P.; Vieira, Í. G. P.; Cavalcante, I. M.; Ricardo, N. M. P. S.; Attwood, D.; Yeates, S. G.; Booth, C. *Int. J. Pharm.*, **2009**, *378*, 211.

29. Cambón, A.; Rey-Rico, A.; Barbosa, S.; Soltero, J. F. A.; Yeates, S. G.; Brea, J.; Loza, M. I.; Alvarez-Lorenzo, C.; Concheiro, A.; Taboada, P.; Mosquera, V. J. *Controlled Release*, **2013**, 167, 68.
30. Trock, B. J.; Leonessa, F.; Clarke, R. J. *Natl. Cancer Inst.*, **1997**, 89, 917.
31. Teo, H. H.; Styring, M. G.; Yeates, S. G.; Price, C.; Booth, C. J. *Colloid Interface Sci.*, **1986**, 114, 416.
32. Chiappetta, D. A.; Alvarez-Lorenzo, C.; Rey-Rico, A.; Taboada, P.; Concheiro, A.; Sosnik, A. *Eur. J. Pharm. Biopharm.*, **2010**, 76, 24.
33. Alvarez-Lorenzo, C.; Rey-Rico, A.; Brea, J.; Loza, M. I.; Concheiro, A.; Sosnik, A. *Nanomedicine*, **2010**, 5, 1371.
34. Yang, Z.; Crothers, M.; Ricardo, N. M. P. S.; Chaibundit, C.; Taboada, P.; Mosquera, V.; Kellarakis, A.; Havredaki, V.; Martini, L.; Valder, C.; Collett, J. H.; Attwood, D.; Heatley, F.; Booth, C. *Langmuir*, **2003**, 19, 943.
35. Crothers, M.; Attwood, D.; Collett, J. H.; Yang, Z.; Booth, C.; Taboada, P.; Mosquera, V.; Ricardo, N. M. P. S.; Martini, L. G. A. *Langmuir*, **2002**, 18, 8685.
36. Cambón, A.; Alatorre-Meda, M.; Juárez, J.; Topete, A.; Mistry, D.; Attwood, D.; Barbosa, S.; Taboada, P.; Mosquera, V. J. *Colloid Interface Sci.*, **2011**, 361, 154.
37. Deng, N.-J.; Luo, Y.-Z.; Tanodekaew, S.; Bingham, N.; Attwood, D.; Booth, C. J. *Polym. Sci. Part B: Polym. Phys.*, **1995**, 33, 1085.
38. Kellarakis, A.; Havredaki, V.; Viras, K.; Mingvanish, W.; Heatley, F.; Booth, C.; Mai, S.-M. *J. Phys. Chem. B*, **2001**, 105, 7384.
39. Altinok, H.; Yu, G.-E.; Nixon, S. K.; Gorry, P. A.; Attwood, D.; Booth, C. *Langmuir*, **1997**, 13, 5837.
40. Taboada, P.; Barbosa, S.; Mosquera, V. *Langmuir* **2004**, 20, (20), 8903-8908.
41. Mistry, D.; Annable, T.; Yuan, X.-F.; Booth, C. *Langmuir*, **2006**, 22, 2986.
42. Knowles, P. R.; Stubbersfield, R. B.; Price, C. *Macromol. Symp.*, **1990**, 40, 203.
43. Park, J. C.; Park, B. J.; Lee, D. H.; Suh, H.; Kim, D. G.; Kwon, O. H. *Yonsei Med. J.*, **2002**, 43, 518.
44. Decker, T.; Lohmann-Matthes, M. L. *J. Immunol. Methods*, **1988**, 115, 61.
45. Exner, A. A.; Krupka, T. M.; Scherrer, K.; Teets, J. M. *J. Controlled Release*, **2005**, 106, 188.
46. Yang, T. F.; Chen, C. N.; Chen, M. C.; Lai, C. H.; Liang, H. F.; Sung, H. W. *Biomaterials*, **2007**, 28, 725.
47. Krupka, T. M.; Exner, A. A. *Int. J. Hyperthermia*, **2011**, 27, 663.
48. Fotakis, G.; Timbrell, J. A. *Toxicol. Lett.*, **2006**, 160, 171.
49. Snyder, E. Y.; Deitcher, D. L.; Walsh, C.; Arnold-Aldea, S.; Hartweg, E. A.; Cepko, C. L. *Cell*, **1992**, 68, 33.
50. Firestone, M. A.; Wolf, A. C.; Seifert, S. *Biomacromolecules*, **2003**, 4, 1539.
51. Lee, B.; Firestone, M. A. *Biomacromolecules*, **2008**, 9, 1541.
52. Sosnik, A.; Leung, B.; McGuigan, A. P.; Sefton, M. V. *Tissue Eng.*, **2005**, 11, 1807.
53. Rees, D. C.; Johnson, E.; Lewinson, O. *Nat. Rev. Mol. Cell Biol.*, **2009**, 10, 218.

54. Roschke, A. V.; Tonon, G.; Gehlhaus, K. S.; McTyre, N.; Bussey, K. J.; Lababidi, S.; Scudiero, D. A.; Weinstein, J. N.; Kirsch, I. R. *Cancer Res.*, **2003**, 63, 8634.
55. Perez-Tomas, R. *Curr. Med. Chem.*, **2006**, 13, 1859.
56. Cambón, A.; Rey-Rico, A.; Mistry, D.; Brea, J.; Loza, M. I.; Attwood, D.; Barbosa, S.; Alvarez-Lorenzo, C.; Concheiro, A.; Taboada, P.; Mosquera, V. *Int. J. Pharm.*, **2013**, 445, 47.
57. Batrakova, E. V.; Li, S.; Li, Y.; Alakhov, V. Y.; Kabanov, A. V. *Pharm. Res.*, **2004**, 21, 2226.
58. Litman, T.; Zeuthen, T.; Skovsgaard, T.; Stein, W. D. *Biochim. Biophys. Acta*, **1997**, 22, 169.
59. Gewirtz, D. A. *Biochem. Pharmacol.*, **1999**, 57, 727.

4.3 SUPPORTING INFORMATION FOR CYTOTOXICITY AND P-GLYCOPROTEIN INHIBITION OF BLOCK COPOLYMERS: STRUCTURE – ACTIVITY RELATIONSHIP

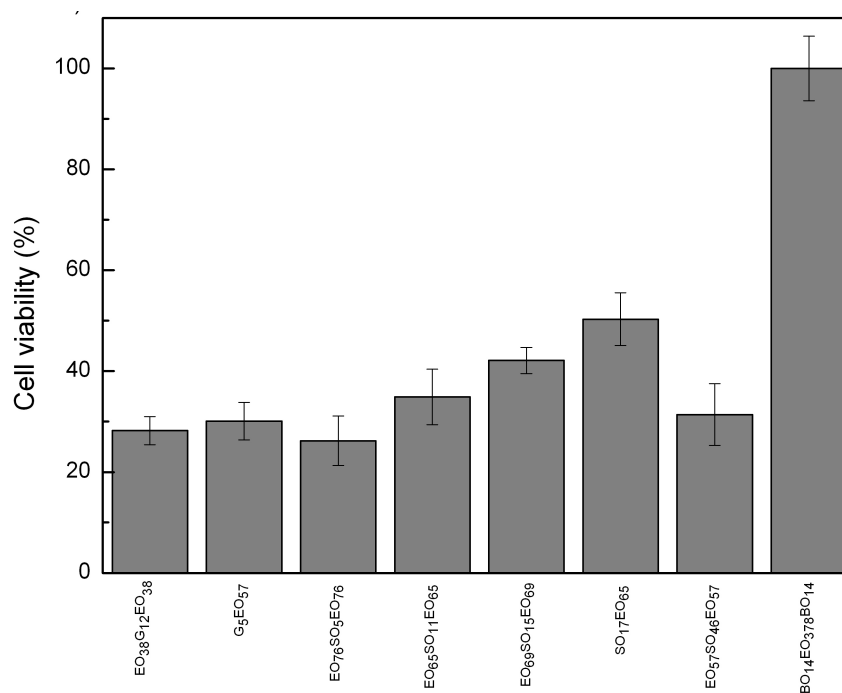


Figure S1: Cell viabilities of different block copolymers in a C17.2 murine neural stem cell line at a polymer concentration of 1.5 wt.% derived from a MTT assay.

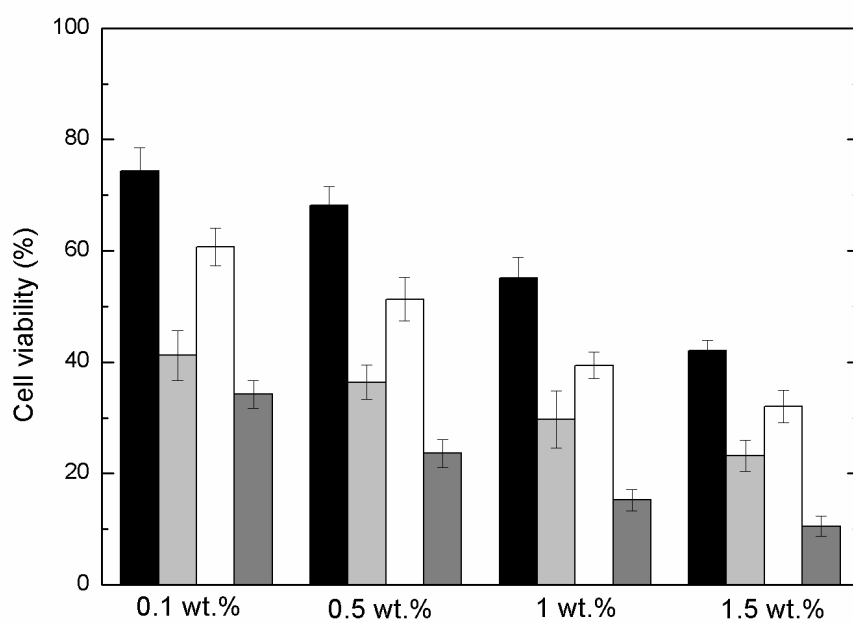


Figure S2: Effect of copolymer concentration in cell viability in a murine fibroblast BALB/3T3 clone A31 cell line for copolymers EO₆₉SO₁₅EO₆₉ (black), EO₃₈G₁₂EO₃₈ (light gray), C₁₆EO₄₅₅ (white), and EO₅₇PO₄₆EO₅₇ (gray).

CHAPTER 5

EXPERIMENTAL TECHNIQUES

5.1 SPECTROSCOPY

Spectroscopy is the part of Science that uses the materials' energy absorption/emission properties to analyze and get information of their inner structure. Briefly, spectroscopic processes rely on the fact that electromagnetic radiation (EMR) interacts with atoms and molecules in discrete ways to produce characteristic absorption or emission profiles (1). Depending on the wavelength range applied different modes can be excited, so as a consequence different experimental equipment should be used to obtain the desired information. Figure 1 shows the EM spectrum and the corresponding wavelength division.

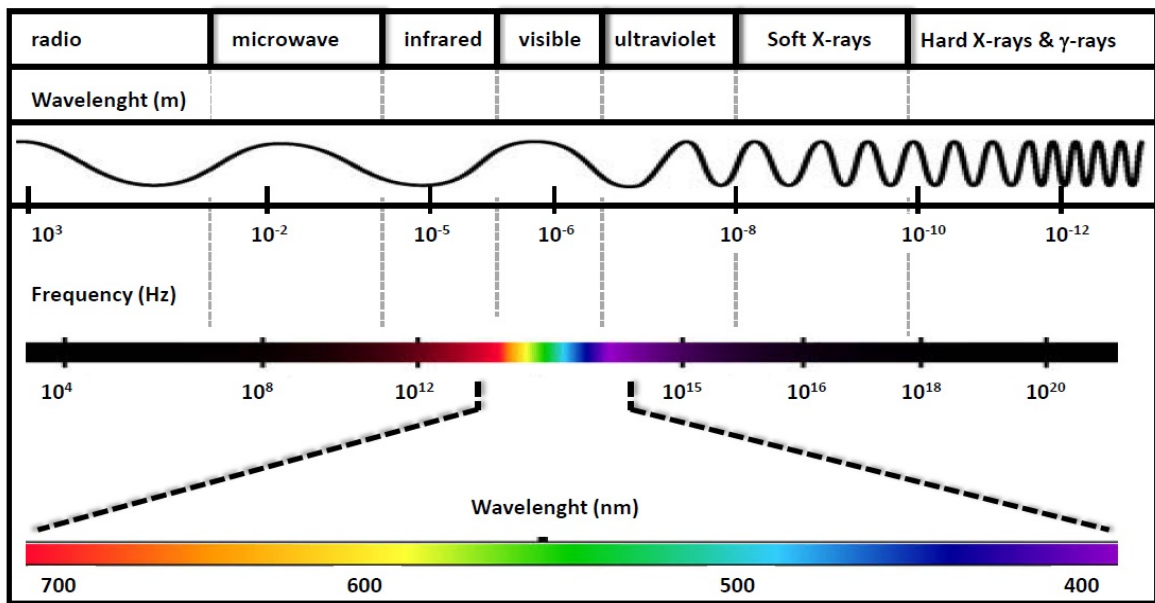


Figure 1. EM spectrum.

5.1.1 EMR and light

Electromagnetic radiation is radiant energy, which propagates in vacuum at a fixed velocity of 299.700 km/s. Its most common manifestation is in the form of heat or light, but other are X-rays, γ -rays, microwaves or radiofrequencies. The term light is used here associated to visible light, corresponding to the EMR ranging from 400 to 700 nm (see Figure 1).

As de Broglie explained in his Doctoral Thesis (2), all particles have associated a determined wave, and this brilliant idea is the first principle of Quantum Mechanics.

To explain the interaction of EMR with matter, EMR is treated as particles called photons, which are highly energetic. EMR behavior is explained using the wave theory, which defines it as a harmonic wave whose electric and magnetic fields are perpendicular to its propagation direction (see Figure 2).

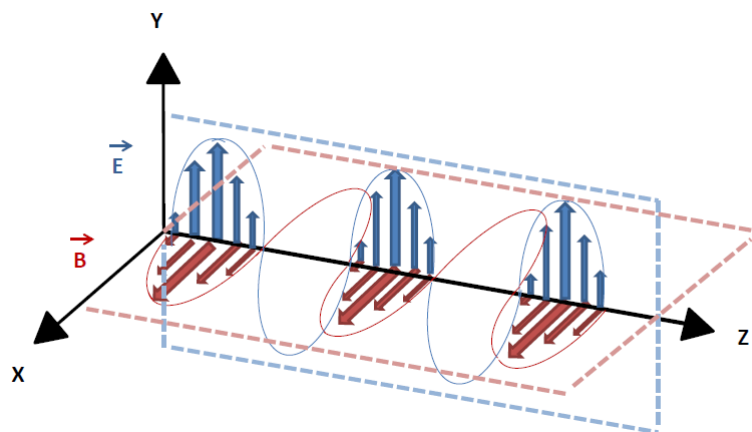


Figure 2. Electromagnetic wave.

5.1.2 Structure of matter

Each element is composed of a determined number of protons and nucleons in nuclei, and of electrons on the surface. Nucleons are attached into the nuclei by nuclear forces, whilst electrons on the shell by Coulomb forces. Both particles are fermions (i.e. they possess semi-entire spins). The laws governing the filling process of electronic orbitals are shown in Figure 3, as well as the corresponding orbitals structure and bounded orbitals. The last occupied layer is termed the valence layer. This layer is the most prompt one to interact with electromagnetic radiation. An external complete layer makes more stable the atom, while an incomplete one makes it to interact with other atoms, generating bounded orbitals (see Figure 3). In the ground state fermions occupy the lowest energetic levels, but promotion to excited states can be achieved by supplying energy. The different discrete energy levels available are an intrinsic characteristic of each element (each element has a different number of electrons and protons), and as a consequence, the study of the required energy to excite energetic levels followed by their subsequent relaxation processes to the ground state is a reliable method of analyses.

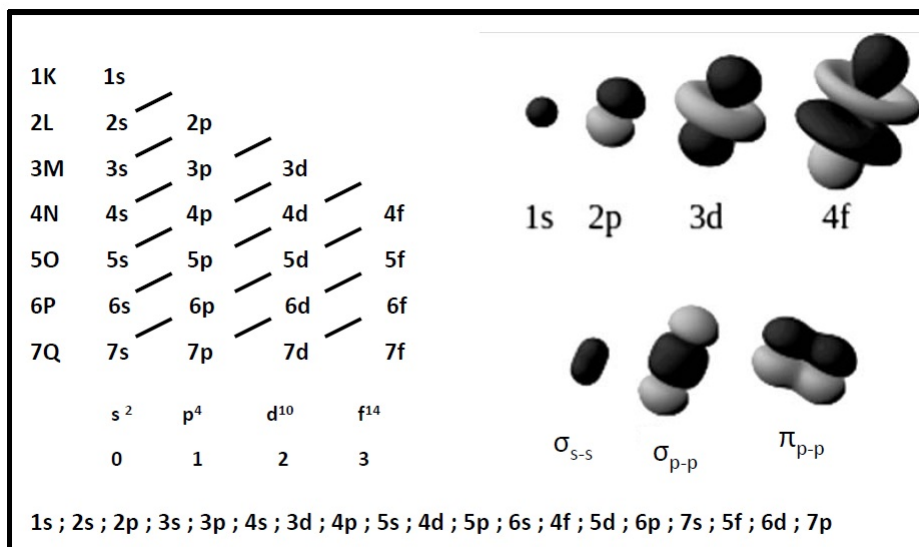


Figure 3. Filling process of electronic orbitals (left side) and their 3D structure.

In the left side of Figure 3, the procedure to fill the electronic orbitals is shown. An s orbital can be occupied by two electrons, a p one by 6, a d one by 8 and a f one by 14. At the right side of Figure 3 the different structures of several orbitals and three bounded molecular orbitals, σ_{s-s} , σ_{p-p} and π_{p-p} are shown as examples. In the case of molecules, the same rules than for atoms are applied. Besides the atomic energy levels, the atom within a molecule can rotate and vibrate with respect to each other. These vibrations and rotations also have discrete energy levels, which can be considered as being packed on top of each electronic level. In spite of the increase in complexity, the same analyses can be done, as explained later on.

5.1.3 Light interaction with matter

Light is a manifestation of energy and, as a consequence, all materials and their constituents as molecules, particles, etc, can be excited under a determined wavelength light. Energy absorption by electrons in the ground state promotes them to higher energy levels, called excited states. Once a molecule is excited by the absorption of a photon, this can return its ground state through several relaxation processes, as fluorescence emission, internal energy conversion (i.e. by heat radiation), intersystem crossing (possibly followed by phosphorescence emission), intra-molecular charge transfer and/or conformational changes. Atomic electrons can be excited and promoted to an upper level by applying the required energy amount, which usually is the difference between both levels. Depending on the applied energy and the resulting excitation and relaxation process the structure of matter can be revealed. Energy

spectra are observed as the result of the energy exchange between a material and the electromagnetic radiation. For example, if the energy is absorbed by a molecule/compound from the radiation field, an absorption spectrum is observed; meanwhile, if the energy is added to the radiation field, an emission spectrum is derived. An electromagnetic radiation may be characterized by the frequency ν , the wavelength λ , or the wave number ν . The different energetic levels and excitation/desexcitation process can be analysed, in the atomic level as well as at the molecular level. Atomic spectroscopy is related to the inherent properties of atoms, while molecular spectroscopy relates to the levels as a result of being the atoms bonded in a more complex structure. In Table 1, a summary of the main techniques based on the different excitation and relaxation processes regarding atomic excitation/relaxation process is shown.

Table 1. Different experimental techniques used in atomic spectroscopy and their associated excitation and relaxation processes (3).

Atomic spectroscopy:		
<i>Excitation</i>	<i>Relaxation</i>	<i>Experimental technique</i>
UV-Vis	Heat	Atomic spectroscopy absorption
Heat	UV-Vis	Atomic spectroscopy emission
UV-Vis	UV-Vis	Fluorescence spectroscopy
X Ray	X Ray	X Ray spectroscopy

In the same way, different molecules or compounds can be analyzed using spectroscopic methods by analyzing changes in the surrounding media of each excited particle, this means, the excitation and relaxation mechanism involving the molecules (Table 2).

Table 2. Excitation and relaxation processes and their different experimental techniques used in molecular spectroscopy.

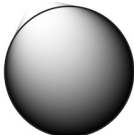
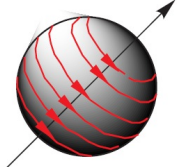

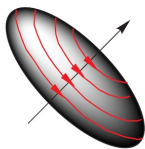
Molecular spectroscopy:	
<i>Electromagnetic radiation</i>	<i>Experimental technique</i>
Radiofrequency	Magnetic nuclear resonance spectroscopy
Microwaves	Microwaves spectroscopy
UV_visible	UV_visible spectroscopy
UV_visible	UV_visible fluorescence spectroscopy

5.2 NUCLEAR MAGNETIC RESONANCE SPECTROSCOPY

5.2.1 Nuclear Magnetic Properties

The nuclear magnetic behavior and the associated properties can be explained using classic mechanics (4). Nuclei are composed by magnetically active protons due to their charge and rotational movement about an axis, which makes them behave like small magnets. As a result, a net nucleus angular momentum is observed. Each different atom has a defined value for their angular momentum proportional to the value of \hbar , the Planck's constant, $p = I\hbar$, where p is the total angular momentum and I is the quantum number of nuclear spin ($I = 0, 1/2, 1, 3/2, 2, \dots$). Nuclei with $I \neq 0$ have a net moment and, as a result, a magnetic field is obtained, which can be assessed as a small dipolar moment (μ). Besides, if the charge distribution around the nucleus is not spherical, a new moment appear (see Table 3) ($I \geq 1$) (5-7).

Table 3. Atomic nucleus configurations owing to nuclear spin (I), angular momentum (p), magnetic moment (μ) and quadrupolar moment (Q) (4).

$I = 0$	$I = 1/2$	$I = 1$	$I > 1$
$p = 0$	$p = 1/2 h$	$p = h$	$p = I h$
$\mu = 0$	$\mu \neq 0$	$\mu \neq 0$	$\mu \neq 0$
$Q = 0$	$Q = 0$	$Q > 0$	$Q < 0$
			
$^{12}\text{C}, ^{18}\text{O}, ^{32}\text{S}$	$^1\text{H}, ^{13}\text{C}, ^{15}\text{N}, ^{19}\text{F}, ^{31}\text{P}$	$^2\text{H}, ^{14}\text{N}$	$^{17}\text{O}, ^{35}\text{Cl}$

5.2.2 Nuclear Magnetic Resonance Spectroscopy

Nuclear magnetic resonance spectroscopy (NMR) is a powerful technique extensively used to characterize polymeric atomic structures and their overall composition. The method uses a strong external magnetic field, while a broad range of radiofrequencies are applied to make nuclei enter mutual resonance. When a magnetic field is applied, the nuclear spin usually aligns in the field direction. In addition, if a specific frequency is applied nuclei gets in resonance, which means that they absorb the supplied energy. NMR spectroscopy can only be used to study atomic nuclei which have

an odd number of protons, neutrons or both, because these are the nuclear constitutive particles which possess spin. The most commonly studied nuclei are ^1H and ^{13}C , although nuclei from isotopes of many other elements (e.g. ^2H , ^6Li , ^{10}B , ^{11}B , ^{14}N , ^{15}N , ^{17}O , ^{19}F , ^{23}Na , ^{29}Si , ^{31}P , ^{35}Cl , ^{113}Cd , ^{129}Xe , ^{195}Pt) have been studied by high-field NMR spectroscopy as well (5, 6).

To get the requested information NMR uses radiowaves, which are harmless because their long wavelengths and, hence, low frequencies. Figure 4 shows a sketch of the principal components of a RMN instrument.

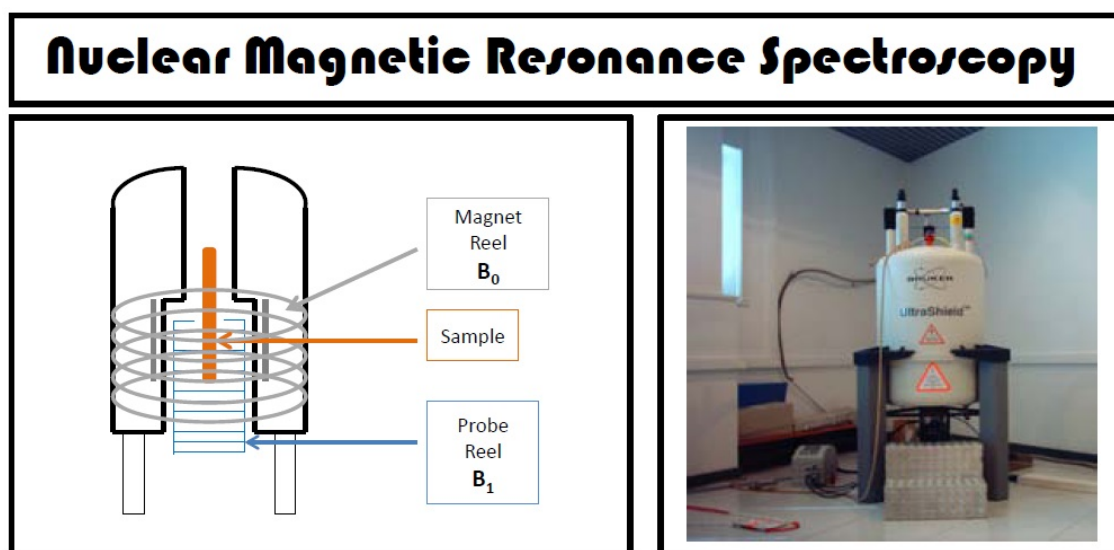


Figure 4. Left: RMN structural sketch, showing the main components of a standard equipment. Right: RMN real picture of a NMR spectrometer.

To perform a standard and simple of ^1H or ^{13}C NMR experiment, first the requested sample is dissolved in one millilitre of solvent and the resulting solution is fill in a vitreous long tube subsequently placed inside the RMN equipment. A constant magnetic field is applied while the tube is made to rotate along its longitudinal axe. In order to excite all nuclei, a brief radiofrequency pulse is applied. Such pulse covers a long range of frequencies, making the protons to absorb the necessary energy to enter resonance. Along the relaxation process nuclei emit radiation corresponding to the difference between both ground and excited states. The radiation intensity decreases with time, as shown in Figure 5. Experimental data are collected by a computer and transformed using the Fourier transform (FT-RMN) (see Figure 5) shown in Eq. 1. In this way, a time dependent function is transformed into a frequency dependent function ($w = 2\pi f$) (8).

$$F[f(t)] = f(\omega) = \int_{-\infty}^{+\infty} f(t)e^{i\omega t} dt = \int_{-\infty}^{+\infty} f(t) \cos(\omega t) dt + i \int_{-\infty}^{+\infty} f(t) \sin(\omega t) dt \quad (1)$$

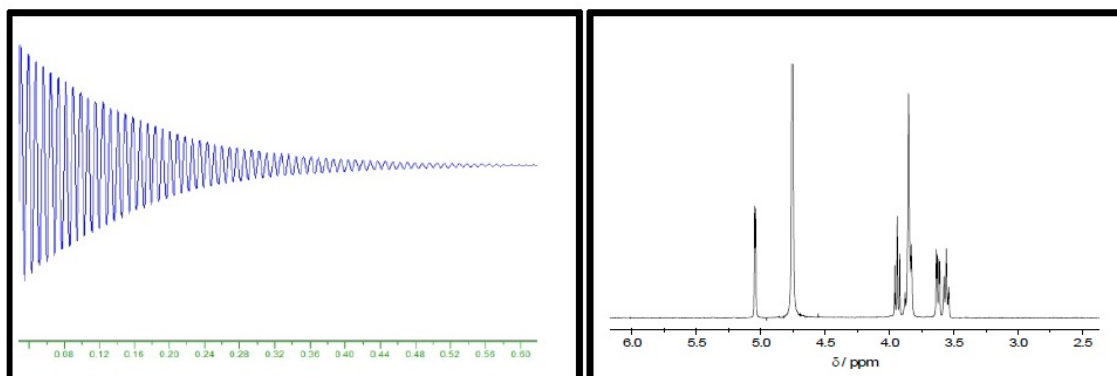


Figure 5. Left: RMN frequency spectrum. Right: ^1H RMN Fourier transform of signal on the left (5).

5.2.3 Proton RMN spectroscopy (^1H)

^1H NMR spectroscopy is a method based on the magnetic properties of the protons inside the nuclei, because they are positive charged will tend to align when a magnetic external field is applied. If only nuclei could be studied, this technique would have no incentive. Fortunately, electrons cause weak changes in the magnetic response but observable, allowing a detailed study of the electronic structure of molecules: The electronic cloud surrounding nuclei generates a small induced current in opposition to the magnetic applied field (4,9); as a result, the real magnetic field that nuclei feel is weaker than the applied external field (nuclei are shielded). Therefore, the effective field that a proton feels inside the molecule, H_{loc} is always lower than the applied external field, H_0 , so that the applied field has to be higher: $H_{ef} = H_0 - H_{loc} = H_0^*$ to get into resonance. In this way, each molecule has a distinctive combination of frequencies and applied fields that makes them to enter resonance resulting in different observable properties, that is, the frequency spectra obtained by RMN is characteristic for each nucleus (4).

The variations between magnetic nuclear resonances due to the distinct shielding of nuclei are called chemical shifts (δ , expressed in *ppm*). In practice, to measure chemical shifts a reference sample is used for comparison purposes, that is, to set the zero of the scale (6):

$$\delta(\text{ppm}) = \frac{\nu_{\text{sample}} - \nu_{\text{reference}}}{\nu_{\text{reference}}} * 10^6 \quad (2)$$

The reference compound commonly used is tetramethylsilane (TMS, $(\text{CH}_3)_4\text{Si}$) (0.0 ppm) provided that silica is less electronegative than carbon, so its methyl groups are electron-rich, that is, its protons are highly shielded. As a consequence, silica protons absorb energy at higher field intensities than common protons attached to carbon or other elements. TMS signal is, then, higher and more intense than other elements, giving a clear peak since its protons have the same chemical shift. Its signal appears at the right side of the ^1H NMR spectrum and the other species at the left side.

Most protons absorb at frequencies lower than those of TMS, which is the reason delta scale increases on the left direction corresponding to lower fields. Most of the proton signals usually vary between 0-12 ppm, while the signals originated from ^{13}C atoms vary between 0-250 ppm. As an example, δ values obtained for several proton groups are shown in Table 4.

Table 4. Values of chemical shifts for the most common proton groups (^1H) in the delta scale (5).

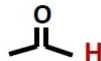
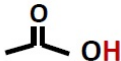
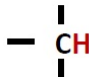
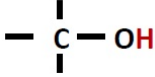
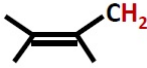
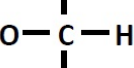
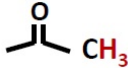
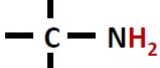
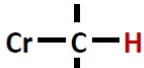
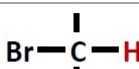
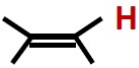
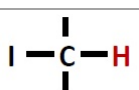
Proton structure	Chemical shift	Proton structure	Chemical shift
$-\text{CH}_3$	0.7 – 1.3		9.5 – 10.0
$-\text{CH}_2-$	1.2 – 1.4		10.0 – 12.0
	1.4 – 1.7		1.0 – 6.0
	1.5 – 2.5		3.3 – 4.0
	2.1 – 2.6		1.5 - 4.0
$-\text{C} \equiv \text{C}-\text{H}$	2.5 – 3.1		3.0 – 4.0
$\text{Ar}-\text{H}$	6.0 – 9.0		2.5 – 4.0
	4.5 – 6.5		2.0 – 4.0

Figure 6 shows the NMR spectra of a) an ethanol molecule ($\text{CH}_3\text{CH}_2\text{OH}$), and b) an ethylene molecule (CH_2CH_2) as examples. Ethanol is an alkene, this is a hydrocarbon chain bound by single bonds and, as a consequence, each ^1H peak in the NMR spectrum corresponds to a separate δ value. Ethylene is an alkane that displays an only signal at 5-

6 ppm due to its four equivalent protons. Figure 6 c) shows a real NMR spectrum of a reverse triblock PBO-PEO-PBO PBO copolymer (10).

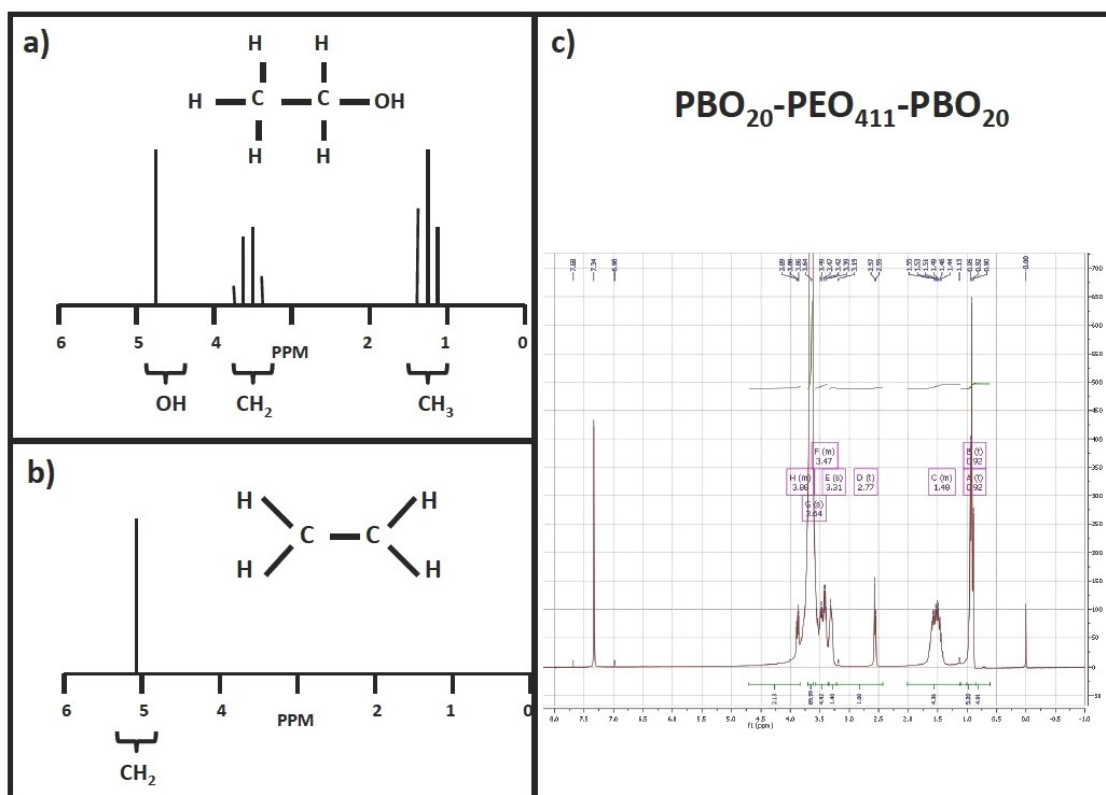


Figure 6. NMR spectra of two hydrocarbon chains: a) an ethanol molecule ($\text{CH}_3\text{CH}_2\text{OH}$), b) an ethylene molecule (CH_2CH_2) and c) a $\text{PBO}_{20}\text{PEO}_{411}\text{PBO}_{20}$ triblock copolymer chain (6).

5.3 UV-Vis SPECTROSCOPY

Ultraviolet and visible (UV-Vis) absorption spectroscopy is a technique based on the measurement of light absorbed by a sample (11). When an atom or molecule absorbs energy, electrons are promoted from their ground state to an excited state. Molecules can only absorb radiant energy in finite units or quanta, which correspond to the energy difference between the ground and excited states. This energy, E , carried by any one quantum is proportional to its frequency of oscillation, $E = h\nu = \frac{hc}{\lambda}$, where ν is the frequency, λ the related wavelength, and h the Planck's constant.

In addition to electronic excitation, the atoms within a molecule can rotate and vibrate regarding each other. These vibrations and rotations also have discrete energy levels, which can be considered as being packed on top of each electronic level. UV-Vis molecular spectroscopy describes the excitation of a valence electron of a molecule upon energy absorption from the electromagnetic radiation which is, thereby, transferred from one energy level to other more energetic one. An electronic transition consists of the promotion of an electron from a molecular orbital in the ground state to an unoccupied orbital by absorption of a photon. The molecule is, then, said to be in an excited state.

The wavelength range a spectrophotometer scans usually goes from 200 to 1100 nm. The experimental data usually are plotted as the transmitted/incident intensity ratio versus the wavelength of incident radiation.

Absorption of ultraviolet and visible light in organic molecules is restricted to certain functional groups (chromophores) that contain valence electrons of low excitation energy. The spectrum of a molecule containing these chromophores is rather complex as the superposition of atomic rotational and vibrational transitions on the electronic transitions provides a combination of overlapping lines.; hence the resulting spectrum appears as a continuous absorption band.

Ultraviolet radiation having wavelengths less than 200 nm is difficult to handle, and is seldom used as a routine tool for structural analysis. UV-Vis light causes primarily electronic excitation by promoting the outer electrons of lower orbitals to higher energy levels and, then, it is sometimes called *electronic spectroscopy*. The easily accessible part of this region (wavelengths of 200 to 800 nm) shows energy absorption only if conjugated π -electron systems are present. There are a number of possible electronic transitions, as shown in Figure 7, called $n \rightarrow \pi^*$, $\pi \rightarrow \pi^*$, $n \rightarrow \sigma^*$, $\pi \rightarrow \sigma^*$, $\sigma \rightarrow \pi^*$, and $\sigma \rightarrow \sigma^*$ (12). The energy of these electronic transitions follows, generally, next order: $n \rightarrow \pi^* < \pi \rightarrow \pi^* < n \rightarrow \sigma^* < \pi \rightarrow \sigma^* < \sigma \rightarrow \pi^* < \sigma \rightarrow \sigma^*$. Of the six transitions outlined, only the two lowest energetic ones ($n \rightarrow \pi^*$ and $\pi \rightarrow \pi^*$) are achieved by energies ranging between 200 to 800 nm. The last four types of electronic transitions required higher energy inputs, below 200 nm corresponding to the far ultraviolet region of the electromagnetic spectrum (12,13).

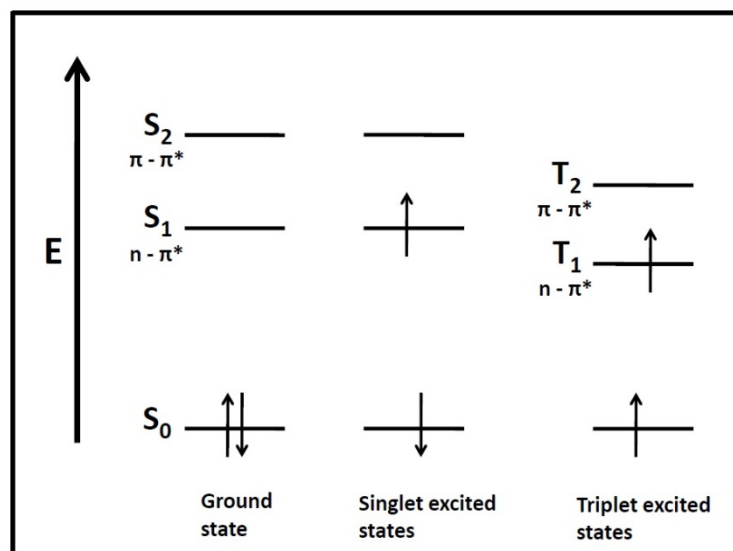


Figure 7. Scheme showing differences between ground and singlet and triplet excited states (9).

A σ orbital can be formed either from two s atomic orbitals, from one s and one p , or from two p atomic orbitals having a collinear symmetry axis. The bond formed in this way is called a σ bond. π orbitals are formed from two p atomic orbitals overlapping laterally; the resulting bond is called a π bond. For example, in ethylene ($\text{CH}_2=\text{CH}_2$) the two carbon atoms are linked by one σ and one π bond. Absorption of appropriate energy can promote, for example, one of the π electrons to an anti-bonding orbital denoted as π^* ; then, the transition is called $\pi \rightarrow \pi^*$. A molecule may also possess non-bonding electrons located on heteroatoms such oxygen or nitrogen; then, the corresponding molecular orbitals are called n orbitals. Promotion of a non-bonding electron to an anti-bonding orbital is also possible, and the associated transition is denoted by $n \rightarrow \pi^*$. Hence, molecules containing a non-bonding electron, such as oxygen, nitrogen, sulphur, or halogens, often exhibit absorption in the UV region (13).

When one of the two electrons of opposite spins (belonging to a molecular orbital of a molecule in the ground state) is promoted to a molecular orbital of higher energy, its spin is, in principle, unchanged so that the total spin quantum number ($S = \sum s_i$ with $s_i = +\frac{1}{2}$ or $s_i = -\frac{1}{2}$) is zero. Because of the multiplicities of both the ground and excited states ($M = 2S + 1$) are equal to 1, both are called *singlet states* (usually denoted S_0 for the ground state, and S_1, S_2, \dots for the excited states, see figure 5.7). The corresponding transition is called a singlet-singlet transition. A molecule in a singlet excited state may undergo conversion into a state where the promoted electron has changed its spin; as a consequence, there are two electrons with parallel spins, and

the total spin quantum number is 1, and the multiplicity is 3. Such state is called a triplet state because it corresponds to three states of equal energy. According to Hund's rule, the triplet state has lower energy than the singlet state of the same configuration (12).

The probability of transitions is also strongly influenced by bond conjugation. A conjugation enhancement brings the highest occupied and lowest unoccupied molecular orbitals closer together. The energy (ΔE) required to do this electron promotion is therefore lower, and the wavelength that provides this energy is longer correspondingly. Conjugation of double and triple bonds shifts the absorption maximum to longer wavelengths, and extending conjugation generally results in increased bathochromic (longer wavelength) and hyperchromic (greater absorbance) shifts in absorption spectra.

The solvent in which the absorbing species are dissolved also has an effect on the resulting spectrum of the species. Peaks resulting from n to π^* transitions are shifted to shorter wavelengths (blue-shifted) with increasing solvent polarity. This arises from increased solvation of the lone pair of electrons, which lowers the energy of the n orbital. Often, the opposite effect (i.e. a red-shift) is observed for π to π^* transitions. This is produced by attractive polarization forces between the solvent and the absorbing molecule, which lower the energy levels of both the excited and unexcited states. This effect is greater for the excited state, and the energy difference between the excited and unexcited states is slightly reduced, resulting in a small red-shift. This also influences n to π^* transitions but is overshadowed by the blue-shift resulting from solvation of lone electron pairs.

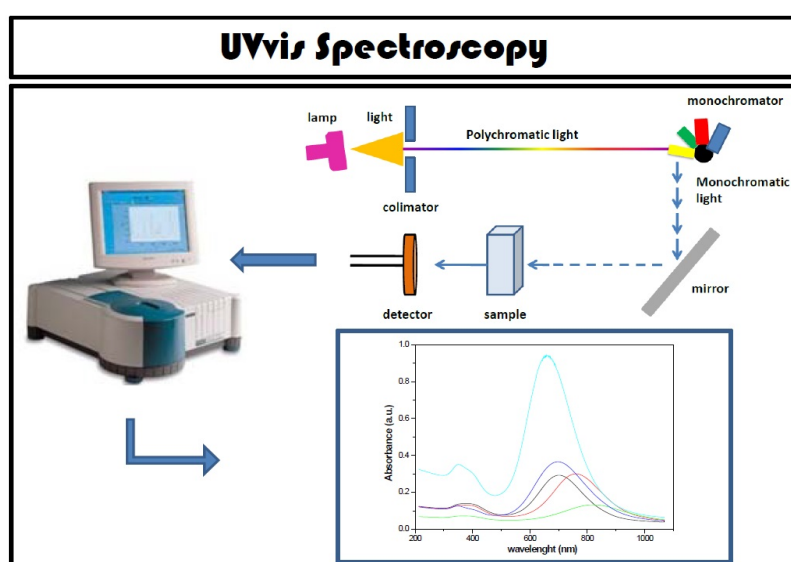


Figure 8. Scheme of UV-vis spectrometer optical path with its constitutive elements, and examples of absorbance spectra.

In summary, when sample molecules are exposed to light having an energy that matches a possible electronic transition within a molecule, some of the light energy will be absorbed as electrons are promoted to higher energy orbitals. An optical spectrometer records the wavelengths at which absorption occurs together with the extent of absorption at each wavelength. Figure 8 shows a scheme of the underlined excitation mechanism done in a spectrophotometer and the resulting information provided.

5.4 FLUORESCENCE SPECTROSCOPY

As mentioned before, energy absorption by electrons in the ground state promotes them to higher energy levels, called excited states. Once a molecule is excited by the absorption of a photon, this can return its ground state through several des-excitation processes, as fluorescence emission, internal energy conversion (i.e. by heat radiation), intersystem crossing (possibly followed by phosphorescence emission), intramolecular charge transfer and/or conformational change.

Fluorescence is a property that some materials can exhibit upon energy absorption in the wavelength range from X-ray to UV ($\lambda \sim 0.01\text{-}400\text{ nm}$); this process is followed by des-excitation in the form of light emission in the visible range ($\lambda \sim 400\text{-}700\text{ nm}$). As a consequence, there may exist a meaningful difference between absorbed and emitted energies since a high-energy photon can be absorbed whilst a low energy photon can be emitted. However, there is not a violation of the conservation law, because the energy difference is dissipated in the form of heat owing to molecular vibrations in the excited state.

Figure 9 shows the vibrational bands in absorption and fluorescence spectra. The singlet electronic states are denoted as S_0 (the fundamental electronic state), S_1 , S_2 , ... with different vibrational levels associated with each electronic state. It is important to note that energy absorption is very fast (in the order of ms) regarding all other processes (there is no concomitant shift of nuclei according to the Franck-Codon principle) (12,14). The absorption process starts from the fundamental vibrational energy level, S_0 , since most of molecules are in this state at room temperature. Absorption of a photon, hence, can bring a molecule to one of the upper vibrational levels (S_1 , S_2 , ...). Emission of photons accompanying the $S_1 \rightarrow S_0$ relaxation is called fluorescence. The transition between the ground state and the excited state (0-transition) is usually the same for absorption and fluorescence. However, the fluorescence spectrum is located at higher

wavelengths than the absorption one as a result of the energy loss in the excited state due to vibrational relaxation.

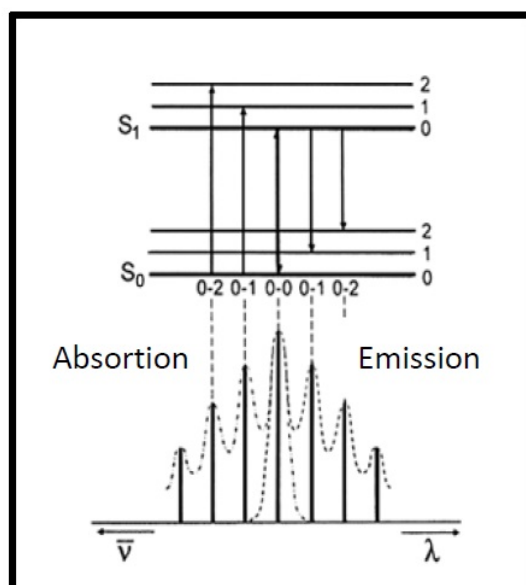


Figure 9. Scheme of the vibrational bands in absorption and fluorescence spectra (15).

According to the Stokes rule, the fluorescence emission wavelength should be always larger than that the absorption one. However, the absorption spectrum partly overlaps the fluorescence spectrum in most cases, i.e. a fraction of light is emitted at shorter wavelengths than the absorbed light. Such an observation seems to be, at first, in contradiction with the energy conservation principle. However, such energy defect is compensated by the fact that a small fraction of molecules is in a higher vibrational level in the ground state as well as in the excited state at room temperature (12, 14).

In general, differences between the vibrational levels are similar in the ground and excited states so that the fluorescence spectrum often resembles the first absorption band. The gap, expressed in wavenumber, between the maximum of the first absorption band and the fluorescence maximum is called the Stokes shift.

It should be noted that photon emission is as fast as photon absorption. However, excited molecules remain in the S_1 state for a certain time (a few tens of picoseconds to a few hundreds of nanoseconds depending on the type of molecule and its surrounding medium) before emitting a photon or undergoing other relaxation processes. Thus, after excitation of a population of molecules by a very short light pulse, the fluorescence intensity decreases exponentially with a characteristic time, reflecting the average

lifetime of the molecules in the S_1 excited state.

As a consequence of the strong influence of the local environment or surrounding medium on fluorescence emission, fluorescent molecules are currently used for physicochemical, biochemical and biological investigation. For example, fluorescent molecules are added to other systems to follow their behavior upon increases of concentration, temperature, amount of added salt, etc (14,15).

Figure 10 shows the components of a conventional spectrofluorimeter. The light source is commonly a high-pressure xenon arc lamp, which offers the advantage of a continuous emission from 250 nm to the infrared region. A monochromator is used to select the excitation wavelength. Fluorescence is collected at right angles with respect to the incident beam and detected through the monochromator by a photomultiplier. Automatic scanning of wavelengths is achieved by motorized monochromators, which are controlled by electronic devices and the computer, in which data are stored. There is an optical module which contains several parts: a sample holder, shutters, polarizers if necessary, and a beam splitter consisting of a quartz plate reflecting a few per cent of the exciting light towards a quantum counter or a photodiode. A quantum counter usually consists of a triangular cuvette which contains a concentrated solution of a dye whose fluorescence quantum yield is independent of the excitation wavelength.

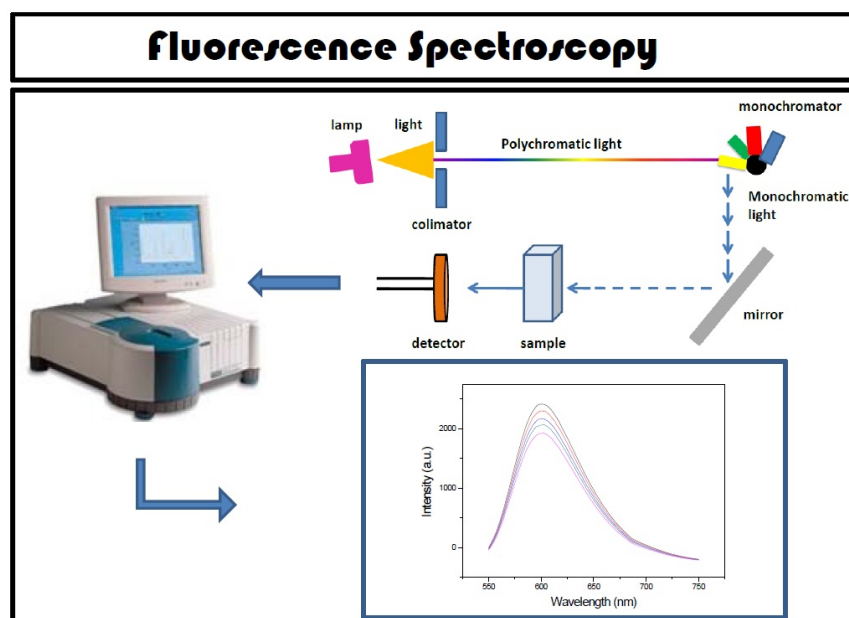


Figure 10. Spectrofluorimeter setup, fluorescence spectrophotometer and experimental curves obtained through this technique.

5.4.1 The pyrene method

Studies based on the fluorescence properties of several probes, as ethidium bromide, methylene blue, congo red, etc. has been extensively used in biophysical studies of molecular aggregates because their fluorescence is strongly dependent on the surrounding media (16,17). To analyze micellization processes, the most common dye used is pyrene due to their characteristic structure and differential behavior in several solvents. The main physico-chemical properties that make pyrene really useful as fluorophore are its long half-life as monomer and its propensity to form excimers. The absorption and emission spectrum of pyrene have been extensively studied, and the maximum values at determined wavelengths have been related to its vibrational modes, as seen in Table 5 (19).

Table 5. Relation between the principal pyrene vibrational bands at their corresponding wavelengths, λ , the frequency of vibrations, ν , the distance from the 0-0 line, the corresponding Raman assignation, and the vibrational mode with the corresponding symmetry.

<i>Peak</i>	λ , nm	ν , cm^{-1}	<i>Distancy from 0-0 line</i>	<i>Asignation (IR/Raman)</i>	<i>Vibrational mode and symmetry</i>
I	372.51	26 845	0	0 – 0	
	378.23	26 439	406	0 – 406 (R)	$a_g(\omega)$
II	378.95	26 389	456	0 – 456 (IR)	$b_{1g}(\tau)$
	379.58	26 345	500	0 – 500 (IR)	$b_{1g}(\tau)$
III	383.03	26 108	737	0 – 737 (IR)	$b_{1g}(\kappa)$
	384.00	26 042	803	0 – 803	$a_g(\kappa)$
	387.99	25 774	1071	0 – 1071 (R)	$a_g(\delta)$
IV	388.55	25 737	1108	0 – 1108 (R)	b_{1g}
	389.08	25 702	1143	0 -1143 (R)	$a_g(\delta)$
	390.42	25 613	1232	0 – 1232 (R)	$a_g(\delta)$
	391.80	25 523	1322	0 - 1322 (R)	$(a_g + b_{1g})(\kappa)$
	392.49	25 478	1367	0 – 1367 (R)	b_{1g}
	392.85	25 455	1390	0 – 1390 (R)	$a_g(\omega)$
V	393.09	25 439	1406	0 – 1406 (R)	$a_g(\omega)$
	395.34	25 295	1551	0 – 1551 (R)	a_g
	396.04	25 250	1595	0 – 1595 (R)	$b_{1g}(\omega)$

Pyrene has a characteristic five peak-spectrum, being the first and third peaks those exhibiting larger sensitivity due to their stronger dependence with the surrounding medium (Figure 11). Pyrene is mainly hydrophobic, so if added in very small amounts to a polymer solution, the micellization process of such polymer upon concentration or temperature changes can be followed. Plotting the ratio between the first and the third fluorescence peaks (I_1/I_3) versus polymer concentration, a characteristic plot is obtained. The transition zone between the two plateau regions corresponds to the concentration range where micellization occurs, termed the critical micellar concentration (CMC).

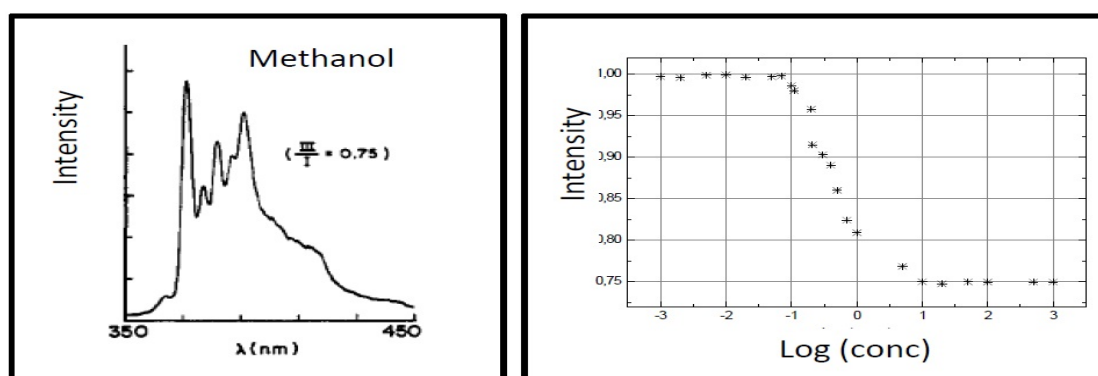


Figure 11. Left image: Fluorescence pyrene spectrum in ethanol. Right image: Plot of I_1/I_3 versus $\log(c)$ to derive the micellization region and the critical micelle concentration (18).

5.5 References

1. Thomas, O.; Burgess, C. *UV-visible Spectrophotometry of Water and Wastewater*, 2007, Elsevier BV.
2. de Broglie, L. *Foundations Phys.* **1970**, 1, 5.
3. http://www.espectrometria.com/tipos_de_espectrometra
4. *Resonancia Magnética Nuclear de Protón: Aplicaciones en Química Orgánica, Cursos en Internet del Departamento de Química Orgánica y Bio-Orgánica de la UNED.*
5. Jacobsen, N.E. *NMR Spectroscopy Explained: Simplified Theory, Applications and Examples for Organic Chemistry and Structural Biology*. 2007, Hoboken, N.J.: Wiley-Interscience.
6. Keeler, J. *Understanding NMR spectroscopy*. 2010, Chichester: Wiley.
7. Mirau, P.A., *A practical Guide to Understanding the NMR of Polymers*. 2005, Hoboken, N.J.: Wiley-Interscience.
8. Hamley, I.W., *The Physics of Block Copolymers*. Oxford science publications. 1998, Oxford: Oxford University Press.

9. Pavia, D.L., *Introduction to Spectroscopy*. 2009, Belmont, Calif.: Brooks/Cole, Cengage Learning.
10. Cambón, A.; Alatorre-Meda, M.; Juarez, J.; Topete, A.; Mistry, D.; Attwood, D.; Barbosa, S.; Taboada, P.; Mosquera, V. J. *Colloid Interface Sci.* **2011**, 361, 154.
11. *User Guidelines and Standard Operating Procedure for the Cary 50 UV-vis Spectrophotometer*, Laurier Research Instrumentation.
12. Valeur, B., *Molecular Fluorescence: Principles and Applications*. 2013, Weinheim: Wiley-VCH.
13. Bernath, P.F. *Spectra of Atoms and Molecules*. 2005, Oxford Univ. Press.
14. Van Holde, K.E.J.W.C.H.P.S., *Principles of Physical Biochemistry*. 1998, Upper Saddle River, N.J.: Prentice Hall.
15. Lakowicz, J.R., *Principles of Fluorescence Spectroscopy*. 1999, New York: Kluwer Academic.
16. Radda, G. K.; Vanderkooi, J. *Biochim. Biophys. Acta*, **1972**, 265, 509.
17. Wehry, E.L. *Modern Fluorescence Spectroscopy*. 1976, New York: Plenum Press.
18. Lianos, P.; Georghiou, S. *Photochem. Photobiol.* **1979**, 30, 355.
19. Kalyanasundaram, K.; Thomas, J.K. *J. Am. Chem. Soc.* **1977**, 99, 2039.

5.6 GEL PERMEATION CHROMATOGRAPHY

Gel permeation chromatography (GPC) is a very versatile technique used in polymer physical-chemistry. The most common uses of this technique are purification and polymer characterisation. The experimental for these processes are very simple and rely only on just making pass a polymer solution through a column full of inert colloidal beads of known porous size (Figure 12). The eluted time of the solution is directly dependent on the polymeric chain size since smaller sizes enter the porous gel beads, doing a longer route, while bigger chains/particles are not able to penetrate the gel pores and are eluted firstly after running a shorter way (20,21). Using a colloid of known size and molecular weight, as monodisperse poly(styrene), the equipment's software relates the elution time to polymer molecular weight. In this way, this technique enables to purify polymers from unreacted monomeric species during polymerization by just rejecting the slower eluted part of the injected solution through the gel column. In addition, molecular weights and polydispersity can be obtained during the same process (21).

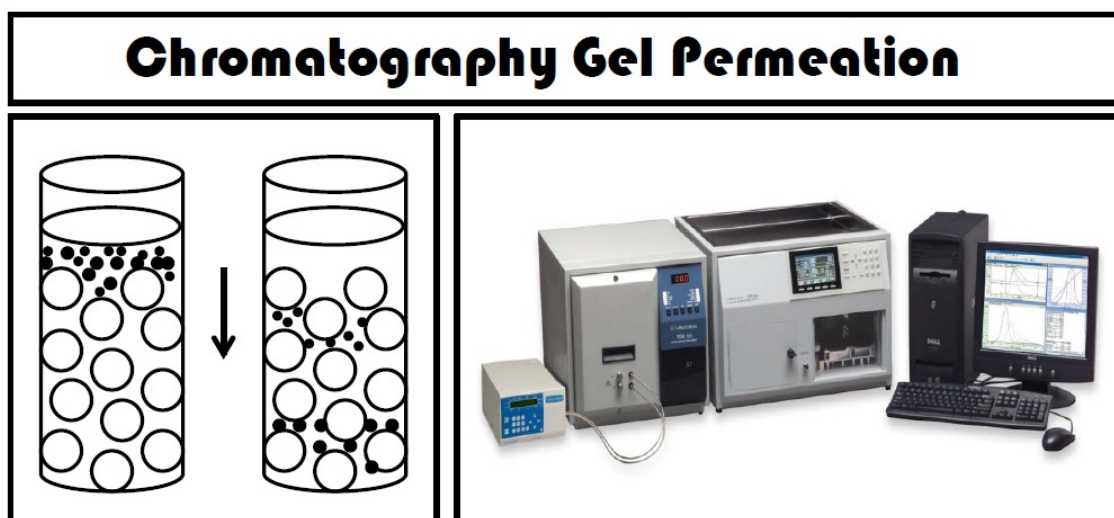


Figure 12. Left: Column separation process. Right: GPC equipment picture (21)

Molecular weights are usually expressed in averaged-weight or averaged-number whereas the polydispersity index is the ratio between them, which is the best index to determine if the polymer possesses a narrow molecular weight (22-24). Table 1 shows the equations used to calculate the molecular weights and the polydispersity index, whilst Figure 20 shows a typical GPC equipment.

Table 6. Expressions to calculate mass- and number-averages molecular weights and polydispersity index (22-23).

	<i>Symbol</i>	<i>Equation</i>
Number-averaged molecular weight	M_n	$M_n = \frac{\sum_i N_i M_i}{\sum_i N_i}$
Mass-average molecular weight	M_w	$M_w = \frac{\sum_i N_i M_i^2}{\sum_i N_i M_i}$
Polydispersity index	r	$r = \frac{M_w}{M_n}$

5.6.1 References

20. *Gel Permeation Chromatography*. 1971, M.Dekker.
21. Yau, W., *Modern Size-Exclusion Liquid Chromatography: Practice of Gel Permeation and Gel Filtration Chromatography*. 1979, New York: Wiley.
22. Feldman, D. J. *Polym. Sci.: Polym. Lett. Ed.* **1984**, 22, 673.
23. Rudin, A. *The Elements of Polymer Science and Engineering: An Introductory Text for Engineers and Chemists*. 1982, Academic Press.
24. Fried, J., *Polymer Science and Technology*. 2003, Pearson Education.

5.7 LIGHT SCATTERING

Scattering is a physical process in which a form of radiation, such as light, sound or a moving particle is forced to deviate from its trajectory by one or more localized non-uniformities in the medium through it propagates. In the case of light, it is fairly simple to understand the origin of its scattering considering it as an electromagnetic wave. Light will interact with electric charges inside a given molecule remodelling their spatial charge distribution. The quantification of this effect is reported by the polarizability (α) of the molecule/compound. The charge distribution follows the time-modulation of the electric wave vector of the incident light beam and, therefore, the molecule constitutes an oscillating dipole or electric oscillator. If the scattering process is elastic the dipole acts as an emitter of an electromagnetic wave with the same wavelength as the incident one, and which is emitted isotropically in all perpendicular directions to the oscillator as illustrated in Figure 13. The angle of observation with respect to the direction of the incident light beam is called the scattering angle, θ , and it provides a measure of the accessible length scales by a light scattering experiment (25).

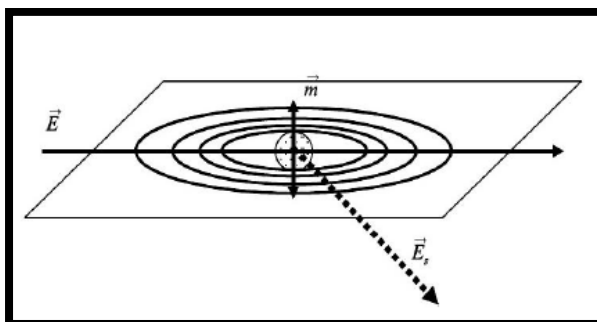


Figure 13. Oscillating dipole induced by an incident light wave, and emitting light (25).

For molecules or particles equal or larger than $\lambda/20$, being λ the wavelength of the incident radiation, several of these oscillating dipoles are created simultaneously within one given particle. As a consequence, part of the emitted light waves possesses a significant phase difference. Accordingly, interference of the scattered light emitted from such individual particles leads to a non-isotropic angular dependence of the scattered light intensity across the sample. The interference pattern of intra-particle scattered light, also called the particle form factor, is a characteristic of the geometry of the scattering particle. Hence, this parameter provides a quantitative means for the structural characterization of particles in very dilute solutions by light scattering. On the other hand, for particles smaller than $\lambda/20$, only a negligible phase difference exists

between light emitted from several scattering centres within a given particle; in this case, the detected scattered intensity will be independent on the scattering angle and it only will depend on the particle mass, which is proportional to the total number of scattering centres one particle contains. The difference in the interference pattern of light scattered by small and large particles is illustrated in Figure 14 (25).

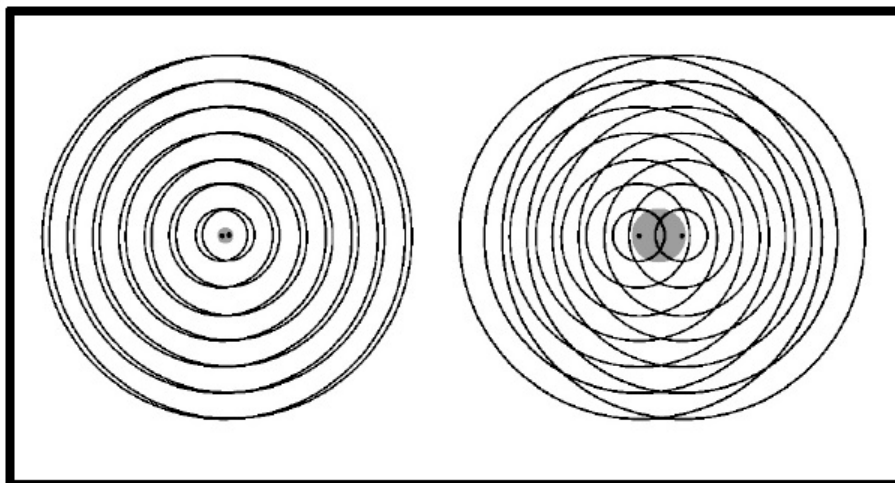


Figure 14. Interference pattern of light scattered from small particles (left) and large particles (right). For simplification, only two scattering centres are drawn (25).

5.7.1 STATIC LIGHT SCATTERING

As mentioned above, matter scatters electromagnetic waves due to the induction of an oscillating electromagnetic dipole which serves as a source for the scattered light wave. In this way, Rayleigh scattering is described in terms of three factors: the incident light of intensity I_0 , the particle (i.e. a macromolecule) which serves as an oscillating dipole, and the scattered light of intensity I . A simplified schematic model is shown in Figure 15.

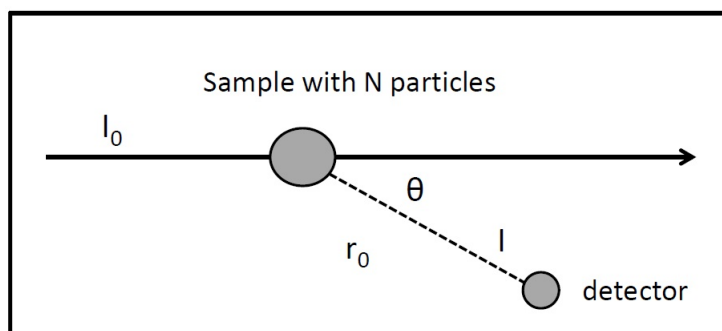


Figure 15. Sketch of a light scattering process (25).

The relation between I and I_0 for an plane-incident polarized light that reaches a particle (i.e. a macromolecule), whose size, d , is smaller than the wavelength, λ ($d \ll \lambda/20$), and considering a system of volume V containing N independent identical scattering particles, can be expressed through the Rayleigh equation (25,26).

$$\frac{I}{I_0} = \frac{N}{V} \frac{16\pi^4 \alpha^2 (1 - \cos^2 \theta)}{\lambda^4 r^2} \quad (3)$$

where α is the polarizability of the particle, r is the distance of the dipole from the observer (from the scattered light sample to the detector), and θ is the angle between the dipole axis and the line r .

The Rayleigh scattering equation is mostly directly applicable to gases, where molecules move randomly. In liquids, there exist fluctuations in particle concentration inside a volume element, which result in fluctuations of the polarizability α . Therefore, to apply the Rayleigh scattering equation to the liquid state, it is necessary to account for these fluctuations by using α . In this way, since the polarizability α depends on the dielectric permittivity ϵ , and correspondingly on the index of refraction n , then for a dilute solution α may be written as (25):

$$\alpha = \frac{V}{2\pi N} \left(\frac{dn}{dc} \right) c \quad (4)$$

where dn/dc is the differential refractive index, n , and it is an experimentally accessible quantity. Substitution of eq. 4 into eq. 3, and considering that N/V can be expressed as $N/V = cN_A/M_w$, where M_w is the molecular weight and N_A the Avogadro's number:

$$\frac{I}{I_0} = \frac{4\pi^2 \left(\frac{dn}{dc} \right)^2 M_w c (1 - \cos^2 \theta)}{\lambda^4 r^2 N_A} \quad (5)$$

Defining the Rayleigh ratio, R_θ , as the ratio: I/I_0 (see equation 3):

$$R_\theta = \frac{I_\theta}{I_0} \frac{r^2}{(1 + \cos\theta)} \quad (6)$$

the expression is reduced to $R = KcM_w$, where $K = 4\pi^2 (dn/dc)^2 / \lambda^4 N_A$.

For particles smaller than $\lambda/20$ the scattering intensity is independent on the scattering angle, and the density fluctuation from the surrounding solvent can be subtracted by considering the excess Rayleigh ratio: $\Delta R = R_{solution} - R_{solvent}$; then, the scattering intensity only depends on M_w and the osmotic pressure. For non-ideal

solutions (27), the scattering equation can be rewritten as:

$$\frac{Kc}{\Delta R} = \frac{1}{M_w} + 2A_2c + 3A_3c^2 \quad (7)$$

When $c \rightarrow 0$, the former equation can be simplified to the so-called Rayleigh-Gans-Debye relation:

$$\Delta R = KcM_w \quad (8)$$

Actually, ΔR cannot be experimentally measured since I_0 and r are unknown during the experiment. However, in a routine experiment ΔR is determined from the experimentally measured scattered intensities of the solution, $I_{solution}$, and a reference substance, I_{ref} (usually benzene or toluene) (25) which enables the derivation of their respective Rayleigh ratios. Hence, the following equation, for $\theta=90^\circ$, can be derived providing a relation between M_w and the second virial coefficient, A_2 (28,29):

$$K^*c/(S_{90} - S_{90}^s) = 1/M_w + 2A_2c + \dots \quad (9)$$

where $K^* = 4\pi^2/\lambda^4 N_A (dn/dc)^2 n_{ref}^2 / R_{ref}$ and $S_{90} = I/I_{ref}$ and $S_{90}^s = I_s/I_{ref}$. I , I_s and I_{ref} are the experimentally measured scattered intensities of the solution, solvent, and reference, respectively. For small particles at dilute concentrations eq. 9 can be reduced to:

$$K^*c/(S_{90} - S_{90}^s) = 1/M_w \quad (10)$$

For large scattering particles the intensity is no independent on the scattering angle. The scattering vector, q , provides a quantitative measure of the length scale of the static light scattering experiment:

$$q = \frac{4\pi n \sin(\theta/2)}{\lambda} \quad (11)$$

For very dilute solutions, interference between different scattering particles, the so-called structure factor, can be neglected. In this case, the angular dependence of the measured scattered intensity $I(q)$ is only caused by intraparticle interference. For dilute and semidilute solutions, to take into account the effects of particle concentration and solute-solvent interactions on the measured scattering intensity, the Zimm equation can be used :

$$Kc/R(\theta, c) = (1/M_w)(1 + q^2 R_g^2/3) + 2A_2c \quad (12)$$

In order to determine the molecular weight (M_w), the radius of gyration (R_g), and the second virial coefficient (A_2) it is necessary to prepare several dilute solutions of different concentration and measure the scattering intensities data at different scattering angles (30,31).

5.7.2 DYNAMIC LIGHT SCATTERING

In dynamic light scattering, the diffusive motion of particles in solution gives rise to fluctuations in the scattered light intensity on the microsecond timescale. This technique is one of the most popular methods used to determine particle sizes by measuring the temporal fluctuations of the scattered light intensity. Roughly, this is made by focusing a monochromatic light beam, such as a laser, on a solution with particles in Brownian motion; this causes a Doppler shift when the light “hits” the moving particle, changing the light wavelength. This change is related to the particle size (30,32).

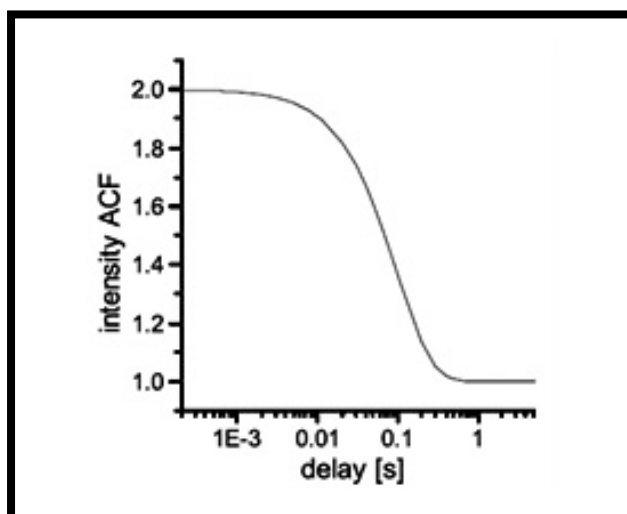


Figure 16. Illustration of an intensity autocorrelation function.

In the scope of DLS, temporal fluctuations are usually analyzed by means of the intensity autocorrelation function (ACF). In the time domain, the correlation function usually decays with time (Figure 16), and a faster dynamics leads to a faster decorrelation of the scattered intensity trace. It can be shown that for a random process the intensity ACF is the Fourier transform of the power spectrum and, therefore, DLS measurements can be equally well-performed in the spectral domain. In fact, DLS experiments were initially discussed in terms of the broadening of the spectrum peak of

monochromatic light due to Doppler shifts experienced by propagating light waves scattered by moving particles (33).

To detect the intensity fluctuation with time, a DLS system requires an autocorrelator on top of a regular SLS system, as shown in Figure 17. The pulse amplifier discriminator converts the analogic signal of the photodetector, $I(t)$, in a digitalized signal, which is further processed by the autocorrelator into the autocorrelation function.

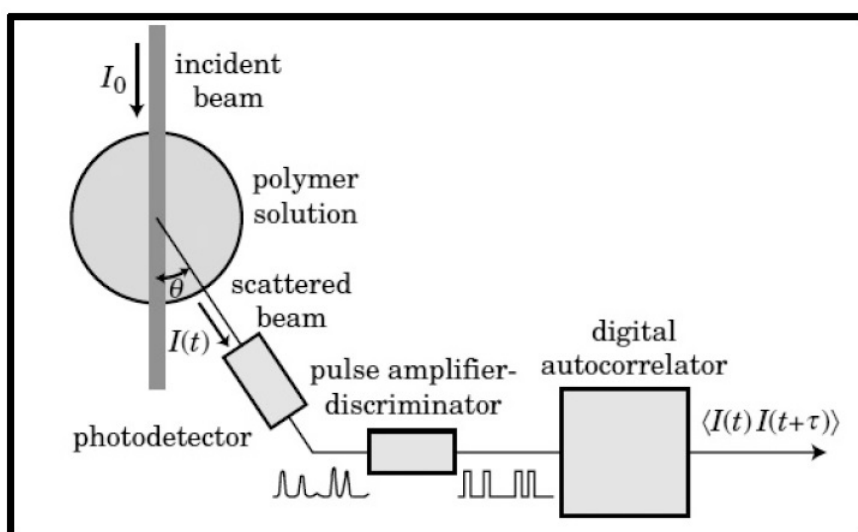


Figure 17. Sketch of a dynamic light scattering system.

Figure 18a illustrates how the intensity (I) varies with time (t). $I(t)$ fluctuates around its mean value, $\langle I \rangle$. Motions of particles (i.e. polymer molecules) and solvent molecules contribute to the change of $I(t)$ with time. This apparently noisy signal carries the information about particles motions.

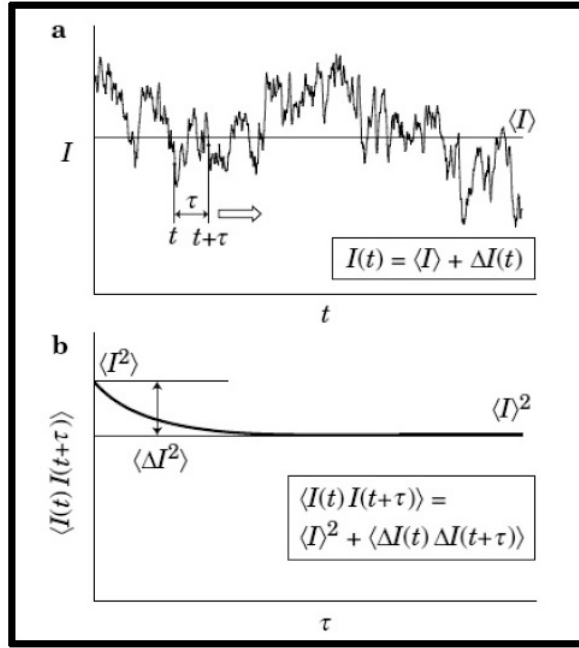


Figure 5.18. a) Light scattering intensity $I(t)$ fluctuates around its mean value $\langle I \rangle$. b) Autocorrelation function $\langle I(t)I(t + \tau) \rangle$ is obtained as the long-time average for various delay times, τ . The autocorrelation function decays from $\langle I^2 \rangle$ to $\langle I \rangle^2$ over time. The amplitude of the decaying component is $\langle \Delta I^2 \rangle$.

The autocorrelator calculates the product average of two scattering intensities $I(t)$ and $I(t + \tau)$ measured at two different times separated by a delay time, τ . The average product $\langle I(t)I(t + \tau) \rangle$ is called the correlation function of $I(t)$, or the intensity-intensity correlation function. The correlator converts $I(t)$ into $\langle I(t)I(t + \tau) \rangle$ over a long period T . Hence, we can write (25,35):

$$\langle I(t)I(t + \tau) \rangle = \lim_{T \rightarrow \infty} \frac{1}{T} \int_0^T I(t)I(t + \tau) dt \quad (13)$$

The autocorrelation function of $I(t)$ (Figure 18a) is shown in figure 5.18 b). When $\tau = 0$, $\langle I(t)I(t + \tau) \rangle = \langle I^2 \rangle$. With increasing τ , $\langle I(t)I(t + \tau) \rangle$ decays to an asymptotic level (baseline), $\langle I \rangle^2$.

Because the scattering intensity $I(t)$ fluctuates around a mean value $\langle I \rangle$, it is convenient to separate its fluctuating component, $\Delta I(t)$, as $I(t) = \langle I \rangle + \Delta I(t)$. The correlation function can be rewritten as (26):

$$\langle I(t)I(t + \tau) \rangle = \langle I \rangle^2 + \langle \Delta I(t) \Delta I(t + \tau) \rangle \quad (14)$$

Division of $\langle I(t)I(t + \tau) \rangle$ by $\langle I \rangle^2$ leads to the intensity autocorrelation function:

$$\langle I(t)I(t + \tau) \rangle / \langle I \rangle^2 = 1 + \langle \Delta I(t)\Delta I(t + \tau) \rangle / \langle I \rangle^2 = 1 + f_c g_2(\tau) \quad (15)$$

where $f_c \equiv \langle \Delta I^2 \rangle / \langle I \rangle^2$ (the coherent factor), and $g_2(\tau)$ is the normalized intensity autocorrelation function:

$$g_2(\tau) \equiv \langle \Delta I(t)\Delta I(t + \tau) \rangle / \langle \Delta I \rangle^2 \quad (16)$$

f_c depends on the coherence of the light reaching the photodetector. The measured intensity correlation function is related to the field correlation function by the Siegert's relation (34):

$$g_1(\tau) = 1 + b |g_2(\tau)|^2 \quad (17)$$

where $g_1(\tau)$, the field ACF, is:

$$g_1(\tau) = |E^*(t)E(t + \tau)| / \langle |E(t)|^2 \rangle \quad (18)$$

being $E^*(t)$ the electric field conjugate function. For monodisperse spherical particles:

$$g_1(t) = \exp(-\Gamma\tau) \quad (19)$$

where Γ is the characteristic delay rate, which is related to the translational diffusion coefficient, D , of a solute by means of the expression:

$$\Gamma = q^2 D \quad (20)$$

D is frequently used to determine the hydrodynamic radius, R_H , of the constituent particles by using the Stokes-Einstein equation (34):

$$D = \frac{k_B T}{6\pi\eta R_H} \quad (21)$$

where k_B is the Boltzmann constant, T the absolute temperature and η the liquid viscosity. The hydrodynamic radius obtained by DLS represents an ideal hard sphere

that diffuses with the same speed as the particle under examination. Actually, particles are solvated and the radius calculated from the particle diffusion corresponds to the size of the dynamic solvated particle.

5.7.3 References

25. Schärftl, W. *Light Scattering from Polymer Solutions and Nanoparticle Dispersions*. 2007, Springer.
26. Xu, R. *Particle Characterization Light Scattering Methods*. 2002, Springer.
27. Sun, S.F. *Physical Chemistry of Macromolecule: Basic Principles and Issues*. 1994, New York: Wiley.
28. Young, R.J., *Introduction to Polymers*. 1981, Chapman and Hall.
29. Huglin, M.B., *Light Scattering from Polymer Solutions*. 1972, Academic Press.
30. Holoubek, J. J. *Quant. Spectrosc. Radiat. Transfer*. **2007**, 106, 104.
31. Uchegbu, I.F.; Schätzlein, A.G., *Polymers in Drug Delivery*. 2006, CRC, Taylor & Francis.
32. Murphy, R.M. *Curr. Opin. Biotechnol.* **1997**, 8, 25.
33. Kokhanovsky, A.A. *Light Scattering Reviews 4: Single Light Scattering and Radiative Transfer*. 2009, Springer
34. Burchard, W.P.G.D., *Light Scattering from Polymers*. 1983, Springer-Verlag.

5.8 ISOTHERMAL TITRATION CALORIMETRY

Isothermal titration calorimetry (ITC) is a physical technique used to determine the thermodynamics of chemical interactions. The basis of the method rely on the fact that heat is either generated or absorbed when substances bind, so the ITC equipment directly measures the heat released or absorbed during a mixing process. The experimental setup is plotted in Figure 19 (35).

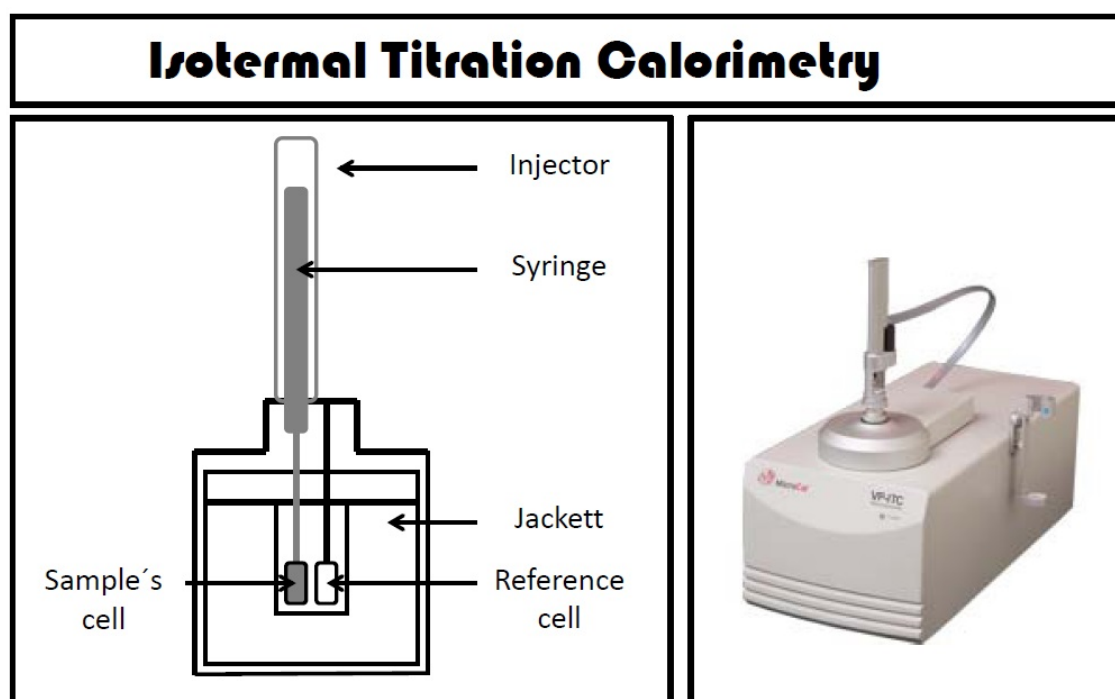


Figure 19. Right: ITC equipment. Left: Main parts of an ITC instrument: jacket, injector, sample's cell and reference cell.

Briefly, a syringe containing one solution is titrated into a cell containing a different solution. When the two solutions (or species) interact, the heat variation causes a difference in temperature respect to a reference cell. The energy that the ITC equipment apply to maintain the reference cell at the same temperature as the sample's cell is equivalent to that involved in the mixing process. The process is done in a completely isolated cell, maintaining constant both volume and pressure so that the variation in internal energy (i.e., heat) involved corresponds to the enthalpy of the system. Measurement of the enthalpy (ΔH) allows the accurate determination of binding constants (K_b), reaction stoichiometry (n) and entropy (ΔS) (36). Figure 20 shows a typical thermogram obtained by an ITC experiment.

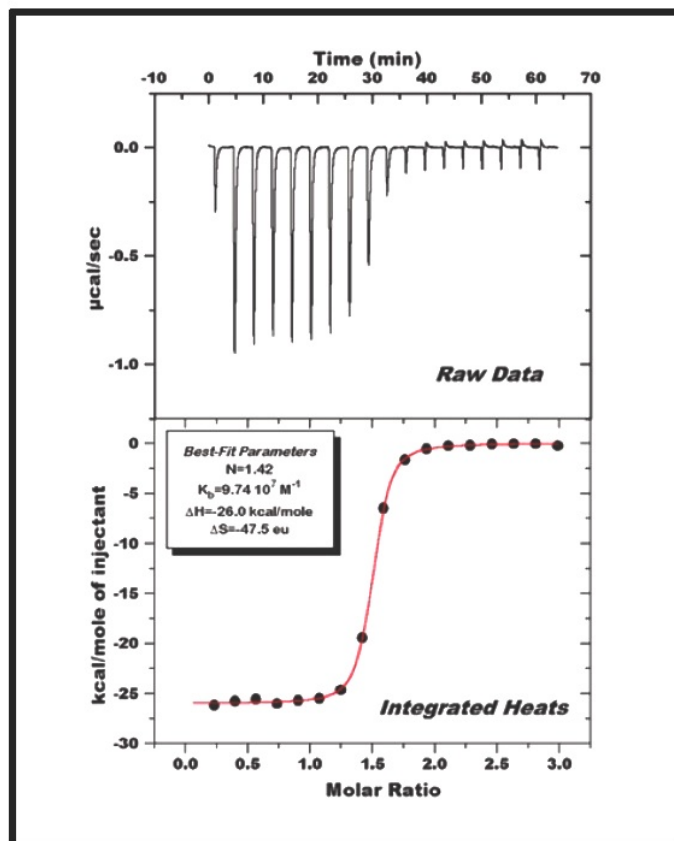


Figure 20. Typical plots of experimental ITC data. Each peak represents a heat change associated with the injection of a small volume of sample into the ITC reaction cell. Top: Raw ITC data. Bottom: Binding isotherm (35).

Thermodynamic data, specifically enthalpy (ΔH) and entropy (ΔS), reveal the forces that drive complex formation and their mechanism of action (36-38). The thermodynamic data provide information on conformational changes, hydrogen bonding, hydrophobic interactions, and charge-charge interactions of the involved species. ITC data permits to distinguish if the interaction arise from electrostatic interaction or are driven by hydrophobic forces. In addition, if the system absorbs or releases heat the process is called endothermic or exothermic, respectively.

As well as binding processes between different materials in solution, aggregation processes can also be followed by ITC due to energy changes in this type of process. For example, micellization in aqueous solution is an endothermic process that also can be followed by ITC analysis. One of the most common method consist of diluting a concentrated sample; because it is a reversible process, the demicellization test is a reliable analyses of the micellization process that permits to obtain the thermal parameters of the process.

The Origin software provides six built-in curve fitting models for ITC data analysis: one set of identical sites, two sets of identical sites, sequential binding sites, competitive binding, dissociation and enzyme assays (35). Each fitting model has a unique set of fitting parameters. For the one set of identical sites model these parameters are N (number of sites), K (binding constant in M^{-1}), and ΔH (heat change in cal/mole). A fourth parameter, ΔS (entropy change in cal/mole/deg) is calculated from ΔH and K . The model for one set of sites will work for any number of sites n if all of them have the same K and ΔH . If a macromolecule has sites with two different values of K and/or ΔH , then the model with two sets of identical sites must be used. These two models employ the following equation that incorporates the Langmuir isotherm binding equilibrium for “ i ” independent sites of association, where Q is the heat per injection, M is the macromolecule concentration, V is the volume of the cell, n_i and ΔH_i are the stoichiometry and enthalpy of interactions, respectively, and Θ_i is the fraction of ligand bound to the macromolecule (39):

$$Q = MV \sum_i n_i \Theta_i \Delta H_i \quad (22)$$

with the sub-indices “ i ” indicating the corresponding binding sites.

One can solve the last equation for Θ_i using the equilibrium equations for binding constants K_i , being X the concentration of ligand and $[X]$ the concentration of free ligand (35,39):

$$K_i = \frac{\Theta_i}{(1-\Theta_i)[X]} \quad (23)$$

$$[X] = X - M \sum_i n_i \Theta_i$$

One and two binding site are the most employed methods for analyzing ITC data.

5.8.1 References

35. *ITC Data Analysis in Origin. Tutorial Guide Version 7.0. 2004.*
36. Haines, P, *Principles of Thermal Analysis and Calorimetry*. 2002, Cambridge: Royal Society of Chemistry.
37. Kellarakis, A., Havredaki, V.; Rektas, C.J.; Booth, C. *Phys. Chem. Chem. Phys.* **2001**, 3, 5550.
38. Brown, M.E. *Handbook of Thermal Analysis and Calorimetry Principles and Practice*. 1998, Elsevier.
39. Flory, P.J. *Principles of Polymer Chemistry*. 1953, Cornell University.

5.9 SURFACE TENSION

Surface tension is a property of liquids owing to the cohesive nature of their molecules. Molecules in bulk are isotropically surrounded by neighbouring ones, which involves a zero net force over them (see Figure 21). Conversely, molecules at surfaces have at least one part of the proximal neighbours in contact to another surface, which provokes a different force balance.

By changing the surface tension of a liquid, different properties are accessible. As an example, hot water has a lower surface tension, which makes it easy to pass through the clothes fibres and obtain better results when cleaning. When adding salt or surfactants to water, the surface tension of the solution is also changed, and this is the basis of soaping.

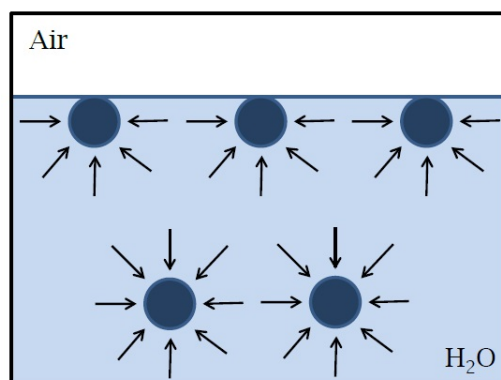


Figure 21. Surface tension in water molecules.

Surfactants have a great affinity for surfaces owing to their amphiphilic character. Hydrophilic chains tend to aggregate on surfaces, where the energy they need is lower and, as a consequence, the surface energy (or surface tension) is minimised. The same behaviour is also observed for amphiphilic polymers in solution, especially in water (see Figure 22). As the aggregation properties of polymers depend on concentration as well as surfactants do, changes in the solution structure containing polymers can be followed by surface tension measurements. The critical micelle concentration (CMC) of amphiphilic systems can be determined by measuring their surface tension (γ) as a function of concentration, being such behaviour denoted by a fairly sharp decrease in a γ vs. $\log(c)$ plot.

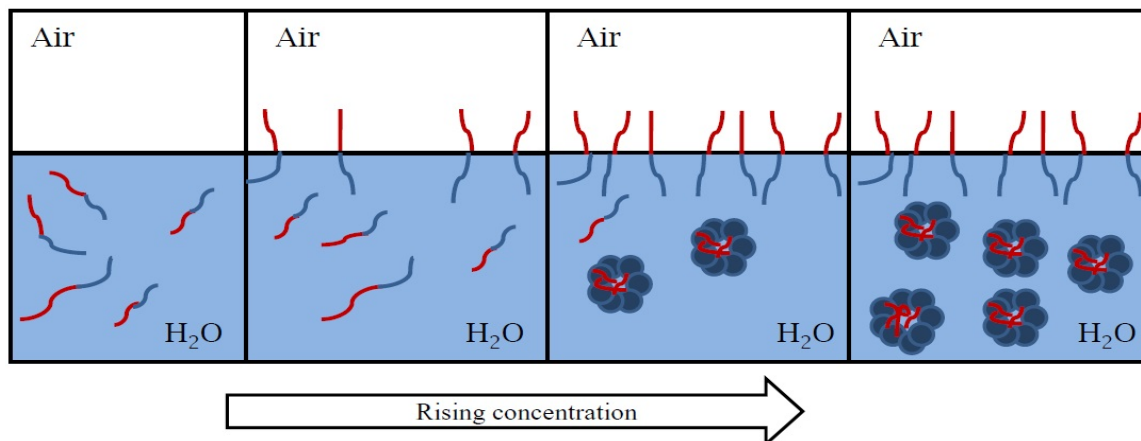


Figure 22. Behaviour of amphiphilic copolymers in water solution as the concentration raises and the corresponding change in surface tension.

There are several methods for determining the surface tension of amphiphilic polymer solutions such as the Du Noüy ring, the Wilhelmy plate, the pendant drop, the bubble pressure or the sessile drop methods (40).

5.9.1 WILHELMY PLATE METHOD

The Wilhelmy plate method measures the force (F) with which a platinum plate of known perimeter ($L = l + d$) is pulled downwards by an interface. The surface tension force, $L\gamma\cos\theta$, is equal to the weight of the liquid meniscus adsorbed onto the plate and detected by a balance (2), which can be related through the following equation:

$$w = 2(l + d)\gamma\cos\theta \quad (24)$$

where w is the meniscus' weight detected by the balance, θ is the contact angle defined by the meniscus shape on the wet platinum surface plate, l is the width and d the plate thickness, respectively (Figure 23). Considering θ very small and the plate thickness negligible compared with its width, the former expression can be simplified to:

$$w = 2\gamma l \quad (25)$$

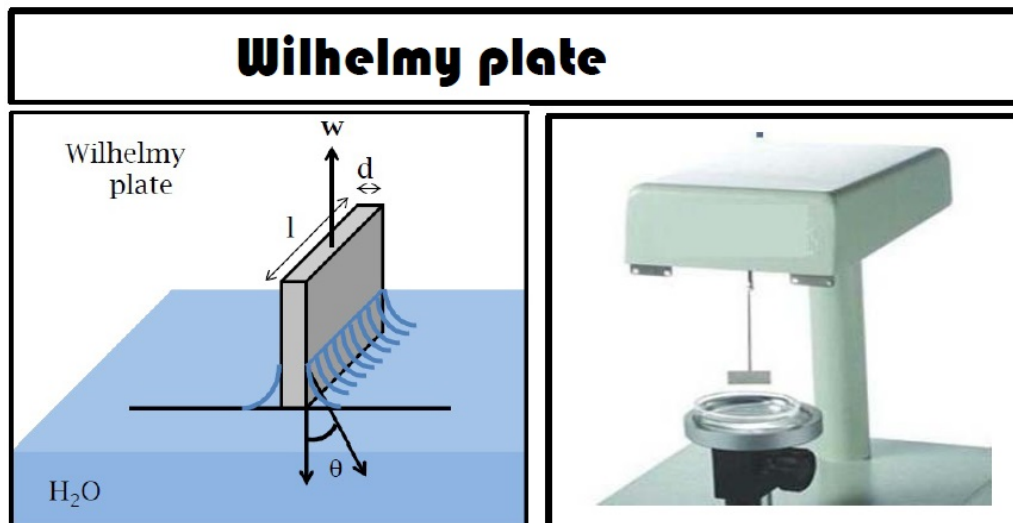


Figure 23. Left: Scheme of a surface tension experiment by means of the Wilhelmy plate in contact with an aqueous solution. Right: Wilhelmy plate instrument's picture.

5.9.2 References

40. Hamley, I.W., *Block Copolymers in Solution : Fundamentals and Applications*. 2005, John Willey & Sons.

5.10 MICROSCOPY

Microscopy is the technique that permits visualize different materials that are not within the resolution range of the naked eye (see Figure 24). Depending on the method used to obtain the images there are three different types of microscopes: optical, electronic and scanning probe ones. Optical microscope uses visible light and electronic microscope utilizes an electron beam in a vacuum line. Both of them use the reflection, refraction and diffraction properties to visualize samples and increase their size. Scanning probes consist in a solid piece performing a surface scanning of the sample to obtain a 3D image.

Optical microscopes permit to visualize samples from few to hundred microns, and they are the fastest and cheapest method. There are amazing different possible configurations of this type of microscopes, from dark and bright field microscopes to light polarized optical ones, fluorescence optical microscope and confocal microscopes, depending of the type of light signal intended to be detected (41).

Electronic microscopes permit to visualize samples from nanometer to hundred microns in size. Usually, for nanometer-sized samples a transmission electron microscope (TEM) is used while for micrometer-sized samples a scanning electron microscope (SEM) is used. TEM allows to visualize thin samples in 2D, and SEM in 3D. Apart from that, there are amazing possible configurations and several complements to these techniques that permit their use under a broad range of needs. As an example, HRTEM permits resolution in the atomic range; cryo-TEM permits visualize freezed samples; ESEM permits to visualize hydrated samples, and FESEM combines TEM and SEM properties. In addition, all of them can be provided with elemental analyses equipment (X-ray or EDX) (42).

Scanning force microscopy (SFM) permits to visualize samples from a hundred nanometers to a few microns showing their 3D shape because it makes a complete mapping in 3D. Surface mapping can be performed in contact mode (one tip continuously in contact with the surface), in tapping mode (one tip touching the surface at short-time intervals) or in non-contact mode (one tip interacting with the surface by Van der Waals forces without contacting it), and that property differences the three kinds of SFM available (43).

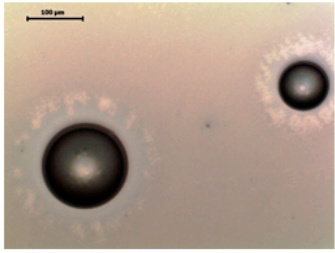
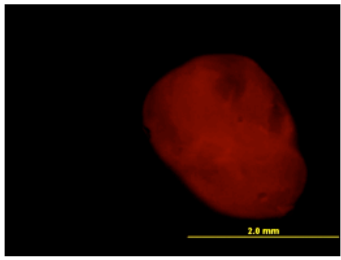
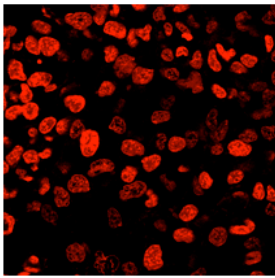
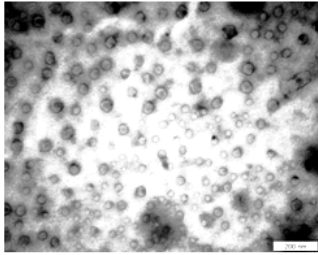
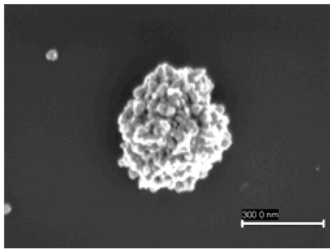
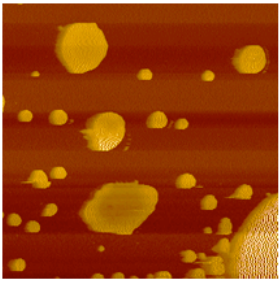
Microscopy images		
		
Optical microscopy	Fluorescence optical microscopy	Confocal optical microscopy
		
Transmission electron microscopy	Scanning electron microscopy	Atomic force microscopy

Figure 24. Images obtained by different microscopy techniques.

5.10.1 OPTICAL MICROSCOPY

Optical microscopy is referred to an equipment which uses visible light to illuminate the sample and perform an image (44,45). To enhance the image's sample, a combination of condenser lenses and diaphragms are mounted as shown in Figure 25. The magnification is limited by the light wavelength, usually being half the wavelength employed. There is a wide range of different possible configurations regarding the optical accessories included between the lenses. The most useful accessories are optical polarizers and fluorescence filters. Modern **optical microscopes** (OM) use cameras attached to a computer to imaging the samples, doing easier the image analyses (size, different species, ...) (46). A real optical microscope picture is showed in Figure 25.

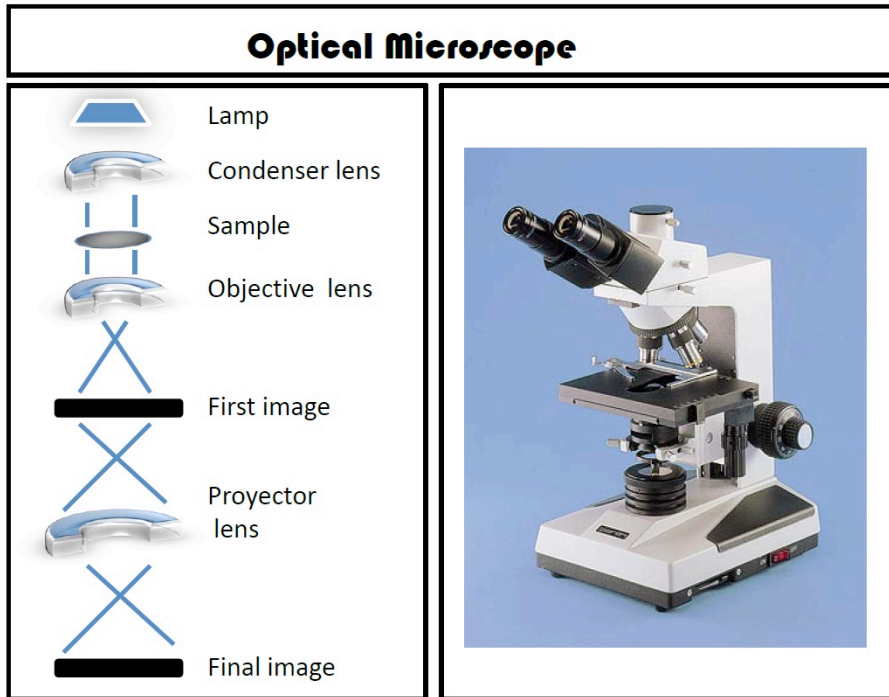


Figure 25. Left: Basic structure of an OM. Right: OM picture.

Confocal optical microscopes were designed to overcome some limitations of traditional wide-field fluorescence microscopes, where the entire specimen is light-flooded at the same time and the resulting fluorescence is detected by the photodetector or by a camera including a relatively large unfocused background area (47). To avoid this background, confocal microscopes use a laser beam and a pinhole, which accepts fluorescent photons from the illuminated and focused spot in the raster, but largely excludes fluorescence signals from objects above and below the focal plane. In addition, the laser beam is expanded to fill the back aperture of the objective forming an intense diffraction-limited spot that is scanned from side to side and from top to bottom over the specimen in a pattern called raster. This procedure is called point scanning. Fluctuations in light intensity are converted into a continuously changing voltage (an analogue signal) by the detector. The analogue signal is digitized at regular time intervals by an analogue-to-digital converter to generate pixels (digital picture elements) that are stored in an image frame buffer board and are displayed on a computer monitor. Thus, a confocal image of an object is reconstructed from photon signals and is displayed by a computer; the confocal image never exists as a real image seen by the naked eye in the microscope (Figure 26).

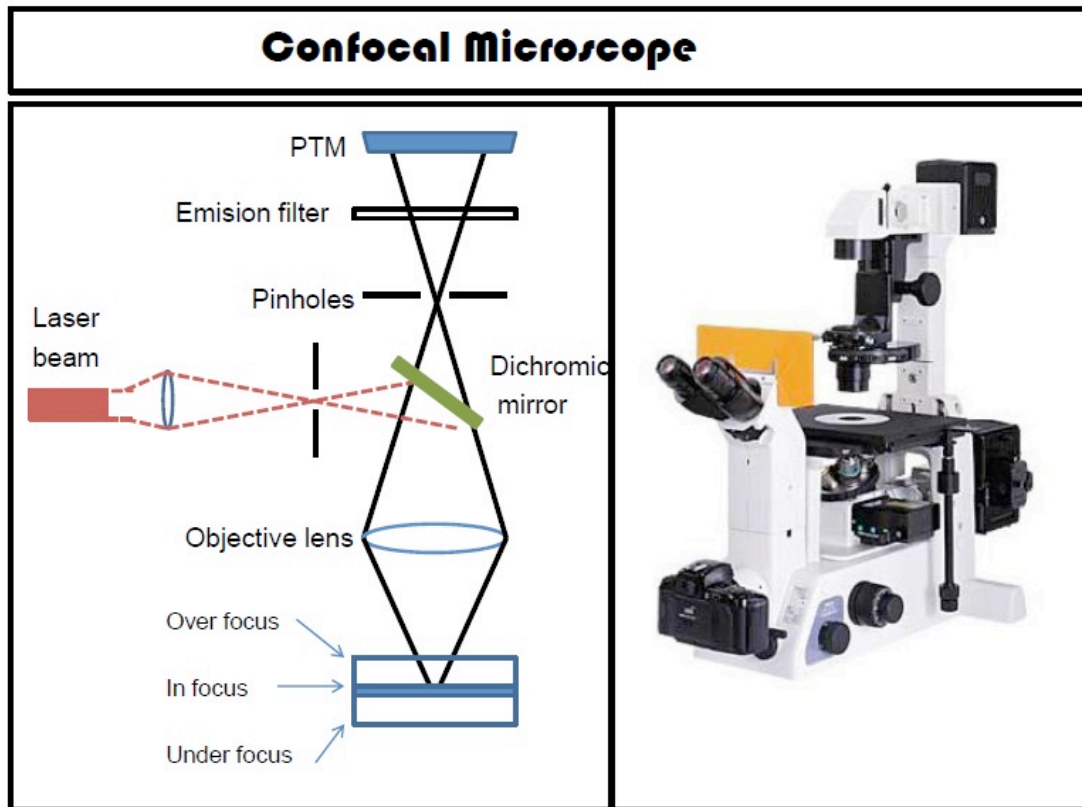


Figure 26. Left: Confocal microscope structure. Right: Confocal microscope picture.

5.10.2 ELECTRONIC MICROSCOPY

5.10.2.1 Transmission Electron Microscopy (TEM)

TEM involves the transmission of an electron beam through a sample in a high-vacuum environment. The images and their associated contrasts arise from regional differences in electron densities in such sample. TEM has a resolution of ca. 1 to 100 nm and can provide very detailed structural information about polymeric materials. The TEM specimens need to be very thin in order to enable the transmission of electron beams through the sample (42).

A transmission electron microscope (Figure 27) is constituted by an electron source (electron gun), which emits electrons travelling through the vacuum created into the microscope column. A condenser lens focus the electron beam on the sample, and several objective lenses are used to form the diffraction pattern at the back focal plane and the sample image at the image plane; there are also some intermediate lenses to

magnify the image of the diffraction screen. To obtain an improved contrasted image, an objective diaphragm is inserted in the back focal plane to select the transmitted beam. At the bottom of the microscope, the non-scattered electrons reach a fluorescent screen, which provides a contrasted image of the specimen, with a darkness distribution corresponding to its different electron densities (48).

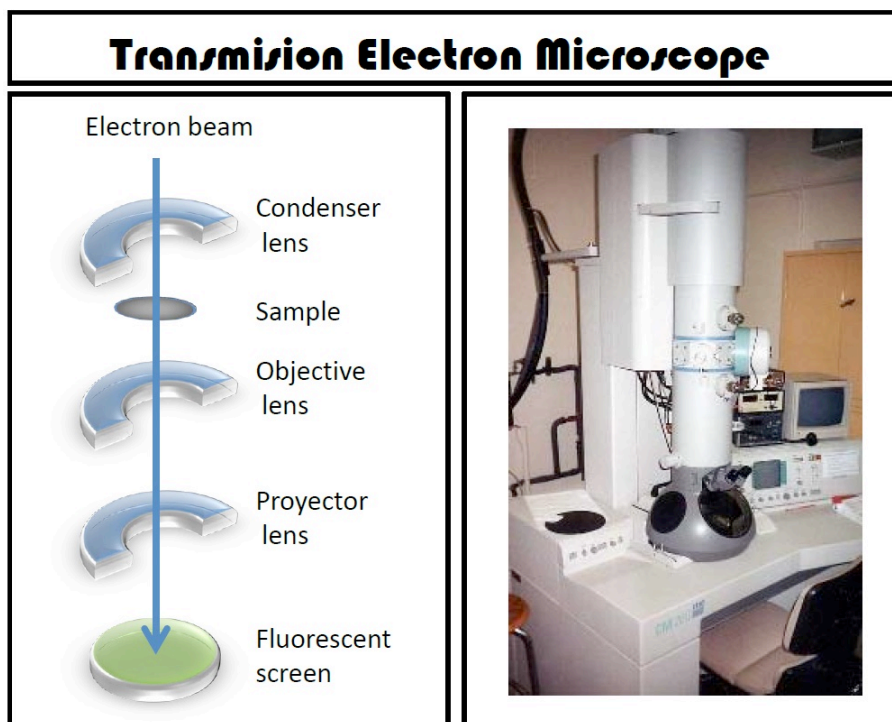


Figure 5.27. Left: TEM schematic diagram. Right: Real TEM picture.

5.10.2.2 Scanning Electron Microscopy (SEM)

SEM is another valuable electron microscopy technique for the examination and analysis of the microstructural characteristics of solid objects, with a resolution of ca. 5 nm (42). SEM can also be used to obtain compositional information of nanomaterials by coupling an electron diffraction X-ray scattering detector (49). SEM enables the observation of heterogeneous organic and inorganic materials on the mesoscopic scale. In a typical SEM experiment, an electron beam is focused to obtain a very fine spot size that is rastered over the surface, and an appropriate detector collects the electrons emitted from each point. In this way, an image having a great field depth and a remarkable three-dimensional appearance is built up line by line. The specimen is usually coated with a conducting film prior to examination to enhance the electron conductivity and, thus, improving image contrast (50).

A scanning electron microscope (Figure 28) consists of an electron gun at the top of the column, which creates a divergent electron beam. In the column, which is under high vacuum conditions, a series of magnetic apertures focuses the electron beam, and an electrostatic field drives the electrons through a small spot, called crossover, and accelerates them through the column until the sample chamber, where the electron beam interacts with the sample. The signals resulting from the beam-sample interaction are monitored. Finally, SEM constructs a virtual image from the signal emitted from the sample by scanning the electron beam line by line through a rectangular (raster) pattern on the sample surface. The scan pattern defines the area represented in the image. At any time, the beam illuminates only a single point in the pattern. As the beam moves, the signals it generates vary in strength, reflecting structural/morphological differences in the sample (51).

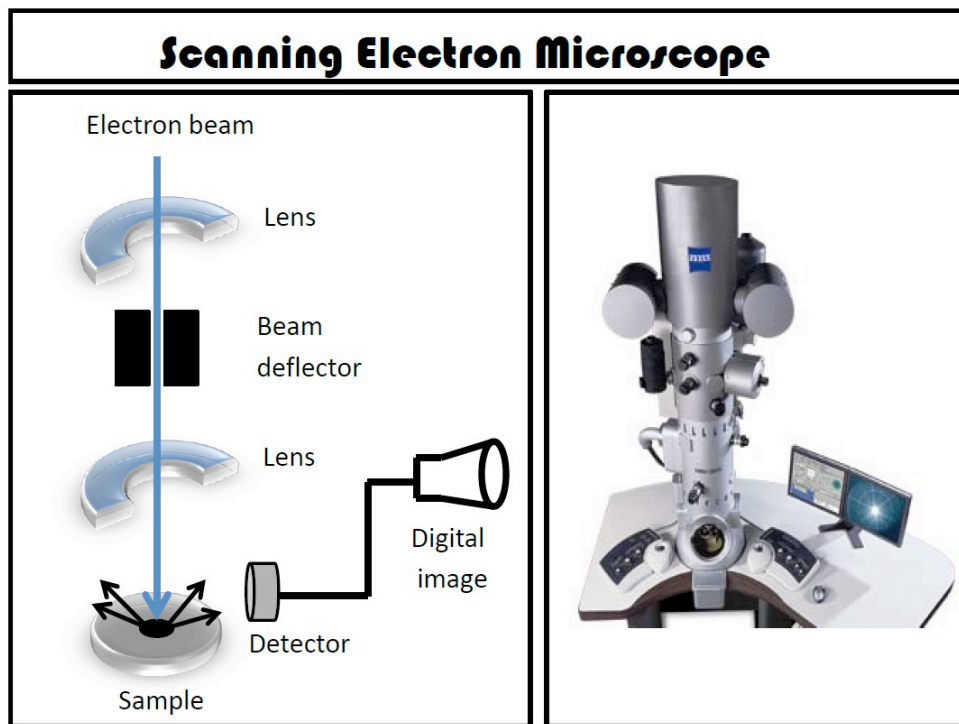


Figure 28. Left: SEM schematic diagram. Right: Real SEM picture.

5.10.3 ATOMIC FORCE MICROSCOPY (AFM)

AFM is part of a large family of instruments termed as scanning probe microscopes (SPM). The common factor in all SPM techniques is the use of a very sharp tip probe, which is scanned across a surface of interest. The interactions between the

probe and the surface are able to produce a high-resolution image of the sample (potentially up to the sub-nanometre scale) depending on the technique and sharpness of the probe tip. For AFM, the probe usually interacts directly with the surface probing the repulsive and attractive forces, which exist between the probe and the sample surface. This serves to produce a high resolution three-dimensional topographic image of the latter. The great versatility of AFM makes possible measurements in air or fluid environments rather than in high vacuum, which allows the imaging of polymeric and biological samples in their native states. In addition, it is highly adaptable, with tip probes being able to be chemically functionalised to allow quantitative measurements of interactions between many different types of materials (43).

An AFM instrument (Figure 29) consists of a sharp tip probe mounted at the apex of a flexible cantilever, made of Si or Si₃N₄. The cantilever itself or the sample surface is mounted on a piezo-crystal, which allows the position of the probe to be shifted respect to the surface. The movement in this direction is conventionally referred to as the Z-axis. The deflection of the cantilever is monitored by changes in the path of a laser light beam deflected from the upper side-end of the cantilever recorded by a photodetector (43).

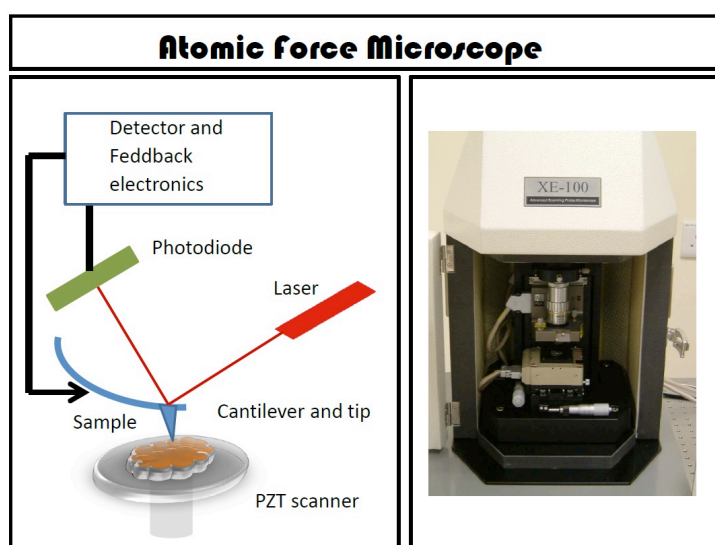


Figure 29. Left: Typical AFM setup. Right: AFM picture.

5.10.4 References

41. Herman, B.L.J.J., *Optical Microscopy: Emerging Methods and Applications*. 1993, Academic Press.
42. Murphy, D.B. *Fundamentals of Light Microscopy and Electronic Imaging*. 2001, John Wiley & Sons.

43. Bowen, W.R.H.N., *Atomic Force Microscopy in Process Engineering: Introduction to AFM for Improved Processes and Products*. 2009, Elsevier/Butterworth-Heinemann.
44. Haynes, R., *Optical Microscopy of Materials*. 1984, Springer.
45. Moorehead, W. *Scanning* **2004**, 26, 204.
46. Buffington, A. *Optical Microscopy*. 2012.
47. Corle, T.R; Kino, G.S. *Confocal Scanning Optical Microscopy and Related Imaging Systems*. 1996, Academic Press.
48. Fultz, B.H.J.M., *Transmission Electron Microscopy and Diffractometry of Materials*. 2008, Springer.
49. Kaupp, G. *Atomic Force Microscopy, Scanning Near-field Optical Microscopy and Nanoscratching Application to Rough and Natural Surfaces*. 2006, Springer.
50. Goldstein, J.Y.H., *Practical Scanning Electron Microscopy: Electron and Ion Microprobe Analysis*. 1975, Plenum Press.
51. Wells, O.C., *Scanning Electron Microscopy*. 1974, McGraw-Hill.

5.11 RHEOLOGY

Rheology involves the study of matter deformation and flow due to compressive stresses acting onto it. Particularly, it refers to the behaviour of materials when a mechanical force is applied on (52). Rheology includes three main concepts such as force, deformation and time. Irreversible flows, reversible elastic deformations or their combination (viscoelasticity) can, therefore, model and describe a rheological phenomenon under certain assumptions. The type of deformation depends on the state of matter; for example, gases and liquids will flow when a force is applied whilst solids will deform by a fixed amount and, then, back to their original shape when the force is removed. In the case of polymers, the rheological and mechanical properties affect the polymers molecular properties, such as their molecular mass, molecular mass distribution, conformation, architecture and crystallinity (53,54).

A typical rheometer measures the velocity of displacement of the moving surface and the force exerted on one of the surfaces. Most of rheometers are based on rotary motion and use one of the three following geometries (Figure 30) (52): concentric cylinder, cone and plate, and parallel disk. In most cases the same rotary instrument can use all three of these flow geometries. To generate the needed motion, they typically use actuators like a hydraulic piston or ball screws found in standard tensile testing machines for solids. Solenoids or other electromechanical actuators are often used for small amplitudes and low forces. There are two basic designs of rheometers: controlled stress ones, where the stress is applied electrically via a motor measuring the strain; and controlled strain instruments, in which a strain is imposed and the stress is computed from the deformation of a calibrated spring system (54).

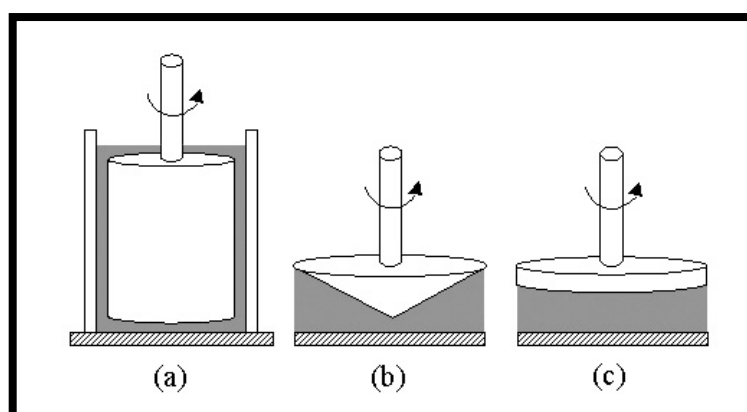


Figure 30. Schematic diagram of basic tool geometries for a rotational rheometer: a) concentric cylinder, b) cone and plate, c) parallel plate.

5.11.1 Viscoelasticity

Many materials can be classified as solid or fluids, displaying elastic and viscous behaviour, respectively. Viscoelastic materials such as polymers combine the characteristics of both elastic and viscous materials depending on the experimental time scale. Application of relatively long duration stress may cause some flow and irrecoverable deformation, while a rapid shearing would induce an elastic response in some polymeric fluids. Then, a classification of these materials should take into account the timescale of the measurement relative to the characteristic time of the material. This classification is given by the Deborah number (D_e), which is a dimensionless number that characterizes the fluidity of materials under specific flow conditions. Formally, the Deborah number is defined as the ratio of the stress relaxation time and the characteristic time scale of an observation. It incorporates both the elasticity and viscosity of the material. At low Deborah numbers, $D_e < 1$, the material behaves in a more fluid-like manner, with an associated Newtonian viscous flow. So, when $D_e = 1$ the material will display both viscous and elastic behaviour, and it is described as viscoelastic. At high Deborah numbers, $D_e > 1$, the material behavior changes to a non-Newtonian regime, increasingly dominated by elasticity and demonstrating solid-like behavior; by contrast for $D_e < 1$ the material behaves in a more fluid-like manner, with an associated Newtonian viscous flow (53,54).

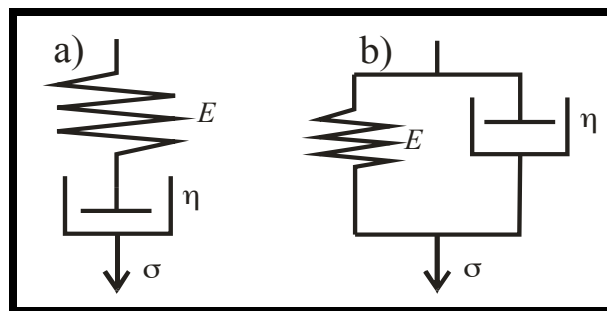


Figure 31. a) Maxwell's and b) Voigt's models.

Pure elastic solid behaviour may be exemplified by a Hook's spring, and pure viscous flow can be exemplified by the behaviour of a dashpot, which is essentially a piston moving in a cylinder of a Newtonian fluid. The use of mechanical models such as the spring and dashpot as analogues of the behaviour of real materials enables us to describe very complex experimental behaviours by simple combination of models, where the spring purely exhibits an elastic effect (as a Hookean solid), and the dashpot exhibits purely a viscous effect (as a viscous fluid). Nevertheless, the viscoelasticity

cannot be described accurately by neither spring nor dashpot alone, but a combination of both. Among all models, Maxwell's and Kelvin-Voigt's models are the most frequently used (Figure 31) (54).

As shown in Figure 31a, Maxwell suggested a simple combination of both elements, in which one spring is attached to one dashpot in series. Because the material possesses the ability to flow, some inertial relaxation will occur and less force will be required upon time to sustain the deformation. The goal in the Maxwell's model is to calculate how the stress varies with time, or expressing the stress in terms of the constant strain to describe the time-dependent modulus. When a force is acting on the Maxwell's model, the spring is downwards at $t = 0$ (in one dimensional flow), and the stress-strain relation for the spring (Hookean material) may be described by (54):

$$\sigma = \gamma G \quad (26)$$

where σ is the applied stress, γ is the strain, and G the elastic modulus. Conversely, the stress response of the dashpot with a viscous Newtonian fluid to an applied deformation rate may be described as:

$$\sigma = \eta \dot{\gamma} \quad (27)$$

where $\dot{\gamma} = d\gamma/dt$ is the strain rate and η , the viscous response of the dashpot.

In the Maxwell's element, both the spring and the dashpot support the same stress and, therefore:

$$\sigma = \sigma_{el} + \sigma_{vis} \quad (28)$$

where σ_{el} and σ_{vis} are the stresses on the spring and dashpot, respectively. However, the overall strain and the strain rates are the sum of the elemental strain and strain rates, respectively, that is:

$$\gamma = \gamma_{el} + \gamma_{vis} \quad (29)$$

$$\dot{\gamma} = \dot{\gamma}_{el} + \dot{\gamma}_{vis} \quad (30)$$

where $\dot{\gamma}_{tot}$ is the total strain rate, while $\dot{\gamma}_{el}$ and $\dot{\gamma}_{vis}$ are the strain rates of the spring and dashpot, respectively. Therefore, the total strain of the spring and dashpot at any time t is the sum of that of the spring and the dashpot. Then, for a Maxwell's model the strain rates can be written as:

$$\dot{\gamma} = \dot{\sigma}/G + \sigma/\eta \quad (31)$$

By rheometry we can measure the response of a material to an oscillating stress or strain, so it is considered as a mechanical spectroscopy. When a sample is constrained in, for example, a cone and plate assembly, an oscillating strain at a given frequency can be applied to the sample. After an initial start-up period due to a transient sample state a stress develops in direct response to the applied strain. If the strain has an oscillating value with time the stress must also be oscillating. We can represent these two wave forms as in Figure 32. The elastic and viscous effects are out of phase by an angle δ (55).

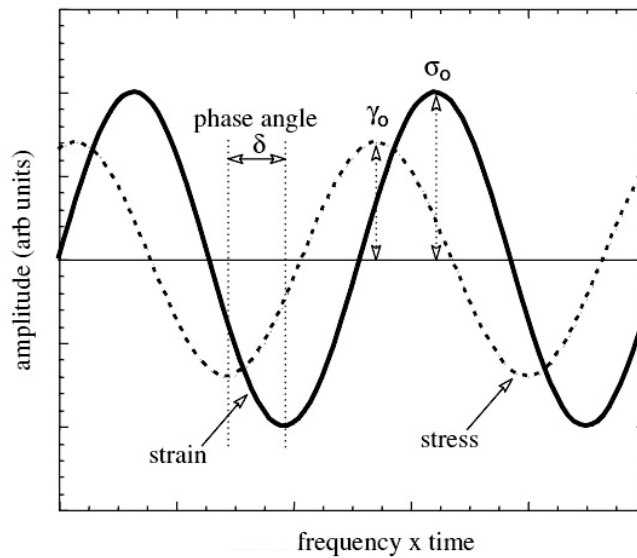


Figure 32. An oscillating strain and the stress response for a viscoelastic material.

All the information about the response of the sample at the specified frequency is contained within these wave forms. However, this information is not in a usable form. What we would really prefer is to have a few representative terms such as the relaxation time and elasticity or viscosity of the sample in order to characterize the material's properties. In order to obtain this information some mathematical operations are required. Two key constant features can be utilized:

- The first one is the maximum stress, σ , divided by the maximum strain, γ , which is constant for a given frequency ω . This ratio is called the complex modulus G^* :

$$|G^*(\omega)| = \sigma/\gamma \quad (32)$$

ω is the radial frequency, which is $2\pi f$, where f is the applied frequency

measured in Hz.

- The other feature constant with time at any given frequency is δ (rad).

These two values, G^* and δ , are characteristics of the material. It is straightforward to visualise the situation where an elastic solid is placed in a cone and plate geometry. When a tangential displacement is applied to the lower plate a strain in the sample is produced. That displacement is transmitted directly through the sample. The upper cone will react proportionally to the applied strain to give a stress response. An oscillating strain will give an oscillating stress response that is in phase with the strain, so δ will be zero. However, if we have a Newtonian liquid, the peak stress will be out of phase by $\pi/2$ rad as the peak stress is proportional to the strain rate. In summary, if we have a viscoelastic material part of the energy is stored and another part dissipated; the stored contribution will be in phase whilst the dissipated or loss contribution will be out of phase respect to the applied strain.

In order to describe the material properties as a function of frequency we need to use Eq. 33. This equation describes the relation between the stress and the strain. However, it is most convenient to express the applied sinusoidal wave in the exponential form of a complex number notation:

$$\gamma^* = \gamma_0 e^{i\omega t}; \dot{\gamma}^* = i\omega \gamma_0 e^{i\omega t} = i\omega \gamma^* \quad (33)$$

Now, the stress response lags by the phase angle δ :

$$\sigma^* = \sigma_0 e^{i(\omega t + \delta)}; \dot{\sigma}^* = i\omega \sigma_0 e^{i(\omega t + \delta)} = i\omega \sigma^* \quad (34)$$

Substituting the complex stress and strain into the constitutive equation for a Maxwell fluid, the resulting relation is given by:

$$\dot{\gamma}^* = \dot{\sigma}^*/G + \sigma^*/\eta \quad (35)$$

Using eq. 31 and 32 in eq. 33 and rearranging we have:

$$\gamma^*/G\sigma^* = 1 + G/i\omega\eta \quad (36)$$

Thus, arrangement of this expression gives the complex modulus and frequency:

$$G/G^*(\omega) = 1 + 1/i\omega\tau \quad (37)$$

or:

$$G^*(\omega) = G \left(\frac{i\omega\tau}{1+i\omega\tau} \right) \quad (38)$$

where $\tau = G/\eta$ is the characteristic relaxation time. This expression describes the variation of the complex modulus with frequency for the Maxwell model. It is normal to separate the real and imaginary components of this expression to give:

$$G^*(\omega) = G'(\omega) - iG''(\omega) \quad (39)$$

Then:

$$G'(\omega) = G \frac{(\omega\tau)^2}{1+(\omega\tau)^2} \quad (40)$$

$$G''(\omega) = G \frac{\omega\tau}{1+(\omega\tau)^2} \quad (41)$$

where $G'(\omega)$ is an in-phase elastic modulus with energy storage in the periodic deformation, called the dynamic storage modulus. $G''(\omega)$ is an out-of-phase elastic modulus associated with the energy dissipation as heat, called the dynamic loss modulus.

These expressions describe the frequency dependence of the stress with respect to the strain. It is normal to represent them as two moduli that determine the component of stress in-phase with the applied strain (storage modulus) and the component out-of-phase by 90° . In an experiment, the amplitudes of the oscillation input (γ_0) and output (σ_0) and the phase angle (δ) are measured. Therefore, each oscillatory shear flow measured at a given ω provides two independent quantities, amplitude ratio and phase angle:

$$|G^*(i\omega)| = \sigma_0/\gamma_0 = \left[(G'(\omega))^2 + (G''(\omega))^2 \right]^{1/2} \quad (42)$$

$$\tan \delta = G''(\omega)/G'(\omega) \quad (43)$$

The storage and loss moduli are subtle descriptions of the material properties of a system. These two properties are related to the phase angle and complex modulus. These are both functions of the applied frequency and represent an alternative description of the system.

$$G'(\omega) = G^*(\omega) \cos \delta, \quad G''(\omega) = G^*(\omega) \sin \delta \quad (44)$$

The phase angle changes with the frequency, from 90 degrees at low frequency to 0 degrees at the high frequency limit; thus, as the frequency increases the sample becomes more elastic, and the phase difference between the stress and the strain reduces.

5.11.2 References

52. Barnes, H.A. *A Handbook of Elementary Rheology*. 2000, University of Wales, Institute of Non-Newtonian Fluid Mechanics.
53. Goodwin, J.W.; Hughes R.W. *Rheology for Chemists: An Introduction*, RSC Publishing.
54. Guinebretière, R. *X-Ray Diffraction by Polycrystalline Materials*. 2007, Wiley.
55. Hiemenz, P.C., *Polymer Chemistry: The Basic Concepts*. 1984, CRC Press.